Localized Fast Radio Bursts Using DSA-110

Thesis by

Ge Chen

In Partial Fulfillment of the Requirements for the
Degree of
Doctor of Philosophy in Physics

CALIFORNIA INSTITUTE OF TECHNOLOGY
Pasadena, California

2024
Defended September 1, 2023

Ge Chen
ORCID: 0000-0003-2867-4544

ACKNOWLEDGEMENTS

I would like to thank my thesis supervisor Professor Vikram Ravi for taking me as a student during my third year and motivating me through the second half of PhD. His enthusiasm for astronomy and quick responses in a rapidly changing field have been inspiring. I also thank the committee members for their feedback after the candidacy in 2020, especially the advice to run the FRB journal club— I wish I had done it for a longer time and met with the committee more often.

My thesis project would have been impossible without the DSA team and the great OVRO staff. I would like to thank Dr. Casey Law for answering various software questions patiently and imposing good programming habits throughout the years. I also thank Dr. Chris Bochenek for helping me to understand the Heimdall pipeline in 2019, and thank Dr. Liam Conner for introducing the reference code for the DSA burst morphology project.

I have rotated among multiple groups before starting the thesis research at Caltech from 2016 to 2019. I would like to thank Caltech PMA for their patience with me as a wandering graduate student. I thank Professor Heather Knutson for demonstrating the most chill way of enjoying science. I thank Professor Phil Hopkins for proposing a solid project on planet formation. I thank Professor Dimitri Mawet and Professor Tom Prince for allowing me to know more about their groups.

I thank the Caltech International Student Programs (ISP), especially Laura Flower Kim and Daniel Yoder for their countless helps, including sending a letter to the US customs when I forgot to bring my I-20 while traveling abroad, helping to renew my I-20 every term in the last year, and coping with tight deadlines multiple times. Besides, the ISP organizes the sweetest orientation program for international students, holds lunch discussions throughout the year with great food and relaxing environments, and offers cultural events that introduces life and festivals in different countries. ISP is one of the most responsible, efficient and highly professional office that I've ever seen at any university, and possibly the one that cares about students the most at Caltech (unfortunately).

I thank Weiyi Tang, my best friend and Dalek Lily at Caltech for making the PhD years more colorful. Finally, none of these would have been possible without my parents. I thank my mother and father, and the rest of the bigger family, for every great moment in the past and in the future to come.

ABSTRACT

Fast Radio Bursts (FRBs) are μs– to ms- scale, energetic ($10^{40\sim46}$ erg s^{-1}) bursts detected in the radio frequency (110 MHz to 8 GHz). They primarily originate from extragalactic sources and are likely to originate from compact object sources. The exact nature of the sources and the emission mechanisms remain inconclusive.

The first FRB was not confirmed until 2007. By early 2023, over 600 FRBs have been reported, and about 40 FRBs have been associated with an individual host galaxy. The rapid growth in sample size has helped to greatly narrow down the number of source models. Neutron stars, especially magnetars, have been the most popular source candidate, although other possibilities still remain.

In this thesis, we explore a few observational methods to study the potential FRB source and host environments. In Chapter 2, we demonstrated a method to constrain the energy ratio emitted from the FRB's multiwavelength transient counterparts as compared to the FRB energy themselves. We used the existing multiwavelength transient blind survey database and the current FRB population fluence distribution to produce tighter constraints than most targeted surveys. In Chapter 3, we investigated whether or not the persistent radio source associated with FRB 121102 could be an AGN using the VLA monitoring data and a new Keck optical spectrum. We constrained the emission source radius to be $10^{17\sim18}$ cm based on the low level of variability in the VLA radio flux measurements presented in this work as compared to the Galactic scintillation theory and other published results by VLBI. We estimated the mass of the potential black hole to be $\lesssim 10^{4\sim5}M_\odot$ based on the Hα line width in the Keck spectrum. We concluded that the source is unlikely an AGN based on the size, mass, and radio luminosity, and that the persistent radio source could be explained by an isolated neutron star with a pulsar wind nebula. In Chapter 4, we showed the burst morphology of a sample of 21 FRBs detected by DSA-110 during part of the commissioning period in 2022, including 16 localized FRBs with optical spectra. We explored the potential correlation between burst morphology and host properties. We found a strong correlation between the host Hα luminosity and FRB burst energy that is likely a result of observational selection effects. We measured the scintillation timescales and found most of them close to the predicted Galactic scintillation timescales. In Chapter 5, we summarize the thesis and very briefly discussed potential extensions of the above methods for the study of FRB sources.

PUBLISHED CONTENT AND CONTRIBUTIONS

[1] Ge Chen, Vikram Ravi, and Wenbin Lu. The Multiwavelength Counterparts of Fast Radio Bursts. *ApJ*, 897(2):146, July 2020. doi: 10.3847/1538-4357/ab982b.
C. G. performed the analyses under the supervision of R. V. and L. W. B. contributed to the discussion on the SGR giant flares as FRB counterparts.

[2] Ge Chen, Vikram Ravi, and Gregg W. Hallinan. A Comprehensive Observational Study of the FRB 121102 Persistent Radio Source. *ApJ*, 958(2):185, December 2023. doi: 10.3847/1538-4357/ad02f3.
C. G. performed the analyses under the supervision of R. V. and G. W. H. provided the radio band observational data.

TABLE OF CONTENTS

LIST OF TABLES

Chapter 1

INTRODUCTION

FRBs are short ($\sim$ 10 μs to $\sim$ 10^2 ms), luminous ($10^{37\sim46}$ erg s^{-1}) radio transients whose high brightness temperature ($\sim$ 10^{35} K) indicates coherent emission. Compact objects, such as neutron stars, have been the most commonly discussed source models, yet the exact source model and emission mechanism are under debate (Section 1.2). Nevertheless, FRBs have been proposed to be unique probes of extragalactic ionized baryons, thanks to their short duration and high luminosity (Section 1.3).

By the end of 2022, over 600 FRB sources have been published [1]. One of them is associated with the galactic magnetar SGR 1935+2154, while the rest are extragalactic, as inferred from their dispersion measurement and host redshift. Over 20 FRBs have been published to associate with an individual host galaxy (Section 1.1).

1.1 Basics

1.1.1 FRB Discovery Story

The first sources of radio emission (e.g., the Milky Way, supernova remnants, radio galaxies) were steady in time. However Tony Hewish discovered in 1951-1954 that small radio sources scintillated due to changes in the earth's ionosphere and in the solar wind (interplanetary scintillation). This inspired the construction of the Interplanetary Scintillation Array (IPS Array), which later led to the discovery of pulsars from the detection of single pulses by Jocelyn Bell [1]. Single radio pulse surveys have been undertaken for decades since then with a wide range of goals— to search for pulses emitted during a supernova explosion (e.g., [2]), bursts associated with primordial black holes evaporating by the Hawking process (e.g., [3]), transient counterparts during gamma-ray bursts (GRBs) (e.g., [4]) and during soft gamma-ray (SGR) events (e.g., [5]), giant pulses emitted by Crab-like pulsars [6], and so on.

Single, non-periodic radio pulse surveys were difficult for a few reasons— (1) it requires high time and frequency resolution, yet sufficient sky coverage and sensitivity (2) they are computationally expensive, and (3) they are difficult to distinguish single pulses emitted by astrophysical sources from radio-frequency

[1] http://frbcat.org/

interference (RFI). The recent improvements in single radio pulse surveys are largely due to the improvement of modern computing power thanks to the digital hardware. In particular, 11 rotating radio transients (RRATs)— a subset of the radio pulsar population— were discovered by their short and bright single pulses in the Parkes Multibeam pulsar survey ([7])), motivating the exploration of short single pulses. Pulsar and RRAT survey instruments are naturally suitable for the discovery of short pulses such as FRBs. The luminosity-duration phase space of radio transient events can be found in several recent publications (e.g., Fig. 3 of Nimmo et al. [8]).

The first FRB (20010724) was detected from the single-pulse survey data of the Small Magellanic Cloud (SMC) taken by the Parkes telescope in 2001 [9]. The reported FRB sources has increased from $\sim$ 60 to over $\sim$600 from 2018 to early 2023, mostly thanks to The Canadian Hydrogen Intensity Mapping Experiment (CHIME). The high dispersion measures (DM) of some FRBs in some models were interpreted as due to the source, and in others due to the intergalactic medium, requiring the FRBs to be extragalactic (except for the Galactic FRB 200428). The extragalactic nature of some of the localized FRB sources were confirmed by the redshift measured from host spectra. In addition to the rapid growth in population size, our knowledge about the FRBs has been growing based on the followings— (1) improved temporal and spectral resolution (e.g., μs-scale structures, temporal-spectral drifting of pulses, polarization studies for sub-pulses at different frequencies), (2) improved localization precision and the optical observations of FRB host galaxies (e.g., host stellar population age, offset from star forming region, comparison with other transient population), (3) long-term follow up of a growing population of repeating FRBs (e.g., periodicity, DM and RM variations, bursts energy levels), (4) a few multi-wavelength counterpart detection (two sources with persistent radio counterparts and the Galactic magnetar with X-ray bursts). Some of the radio instruments that have played important roles in the FRB discovery story are summarized below in Table 1.1.

1.1.2 Signal-to-noise in Radio Transients Observations

In the search for radio transient events, the signal needs to be de-dispersed, smoothed and searched using the matched filtering method for signals above a specified noise threshold. This subsection introduces the steps and the common noises encountered in the search procedures [10, 11].

The observed width of a top-hat pulse is given by:

$$t = \sqrt{t_{intrinsic}^2(1+z)^2 + t_{samp}^2 + \Delta t_{DM}^2 + \Delta t_{\Delta DM}^2 + \tau_s^2}. \quad (1.1)$$

Here the terms under the square root are the pulse intrinsic width, the data sampling interval, the dispersive smearing in a single channel, the residual dispersive smearing across the entire band if a slightly incorrect DM were used, and the scattering broadening (Section 1.3.1), respectively.

As will be introduced in Section 1.3.1, a signal is dispersed as it propagates through the ionized IGM and ISM (Eqn. 1.19). In a channel of bandwidth $\Delta\nu$, the signal is smeared by

$$\Delta t_{DM} = \Delta\nu \frac{\partial \tau_{DM}}{\partial \nu} = 8.3 \times 10^6 \text{ DM } \Delta\nu_{MHz}\ \nu_{MHz}^{-3} \quad \text{ms}. \quad (1.2)$$

De-dispersion is a process that corrects for the frequency-dependent DM dispersion and restore the un-dispersed signal profile. De-dispersion can be done incoherently or coherently. Incoherent de-dispersion applies a time correction to each frequency channel. The accuracy of the correction is limited by the channel bandwidth as shown by Eqn. 1.2. On the other hand, coherent de-dispersion applies DM corrections on raw voltage data by modeling the dispersive effects as a filter in the Fourier domain. It is computationally more expensive but is able to entirely remove the dispersion Δt_{DM} and restore the pulse profile.

If the exact DM value were already known (e.g., a repeating FRB), the error of an incoherent de-dispersion would be given by Eqn. 1.2, and zero for a coherent de-dispersion. However, in most searches the DM value of the source is unknown, so a wide range of trial DM values need to be explored. The smearing across the entire band produced by using a slightly incorrect DM value off by ΔDM in de-dispersion is:

$$\begin{aligned} t_{\Delta DM} &= \frac{\partial \tau_{DM}}{\partial DM}\Delta DM|_{\nu 1} - \frac{\partial \tau_{DM}}{\partial DM}\Delta DM|_{\nu 2} \\ &= 4.15 \cdot 10^6 (\nu_1^{-2} - \nu_2^{-2})\Delta DM \\ &= 4.15 \cdot 10^6 \nu_c^{-2} \left((1 + \frac{N\Delta\nu}{2\nu_c})^{-2} - (1 - \frac{N\Delta\nu}{2\nu_c})^{-2} \right) \Delta DM \\ &\approx 8.3 \cdot 10^6 (N\ \Delta\nu_{MHz}) \cdot \nu_{c,MHz}^{-3} \cdot \Delta DM \quad \text{ms}. \end{aligned} \quad (1.3)$$

Here, $N\ \Delta\nu_{MHz}$ is the entire bandwidth in MHz, and $\nu_{c,MHz}$ is the central frequency. The trial step size is usually determined such that the residual smearing is below a

tolerance level ϵ as compared to the smearing effects of other effects:

$$\Delta t_{\Delta DM} = \Delta t_{DM} \frac{\Delta DM}{DM} = \epsilon \sqrt{t_{samp}^2 + \Delta t_{DM}^2 + \tau_s^2}. \quad (1.4)$$

Again, the smearing due to the non-zero channel bandwidth Δt_{DM} would be completely removed in a coherent de-dispersion.

For each trial DM, the de-dispersed signal is converted to a time series by summing up over all frequencies. For each time series, any slowly-varying baseline is removed by a running median window that smoothes the time series and distinguishes the "outliers" (fast-varying signal) from the the baseline. The baseline-removed time series is then searched for pulses above a given SNR threshold using the matched filtering method.

The optimal SNR of a top-hat pulse with intrinsic flux density S_i and de-dispersed width W_{de} is given by:

$$SNR_i = \frac{S_i}{\sigma_{s_\nu} \sqrt{W_{de}/\Delta t_{samp}}}. \quad (1.5)$$

Here, W_{de} includes all residual broadening effects not removed by the de-dispersion process. The rms noise on the flux density time series is estimated by:

$$\sigma_{s_\nu} = \frac{2 k_b T_{sys}}{\eta A_e \sqrt{N_{pol} \Delta\nu \Delta t_{samp}}}. \quad (1.6)$$

Here, T_{sys} is the system temperature of the telescope, k_b is the Boltzmann constant, η is the antenna aperture efficiency, A_e is the effective area of the telescope, N_{pol} is the number of polarization, $\Delta\nu$ is the bandwidth, and Δt_{samp} is the data sampling interval.

In the matched filtering search, each de-dispersed time series is convolved with a boxcar function of a range of trial widths. The SNR is larger when the DM value used in a de-dispersion trial is closer to the true DM, and the boxcar width is closer to the de-dispersed pulsed width. The SNR measured in the matched filtering using a boxcar width W_b is $SNR_b = SNR_i \sqrt{W_{de}/W_b}$ when $W_{de} < W_b$, and $SNR_i \sqrt{W_b/W_{de}}$ when $W_{de} > W_b$.

In the low-frequency limit ($h\nu \ll k_b T$), the specific spectral power can be approximated in terms of temperature as $P_\nu = k_b T_{sys}$, where P_ν is the spectral power per unit bandwidth, k_b is the Boltzmann constant and T_{sys} is the system temperature of the telescope. From the power, the source flux density s_ν is P_ν/A_e, where A_e is the

effective area of the telescope. The rms fluctuation of a T_{sys} measurement is given by the radiometer equation:

$$\sigma_T = \frac{T_{sys}}{\sqrt{N_{pol}\Delta\nu\Delta t_{samp}}}. \tag{1.7}$$

Here, N_{pol} is the number of polarization, $\Delta\nu$ is the bandwidth, the Δt is the data sampling interval. Combining the above three equations, the rms fluctuation on a source flux density measurement is given by Eqn. 1.6.

In general, several sources of noise power contribute to T_{sys},

$$T_{sys} = T_{cmb} + T_{rsb} + \Delta T_{source} + [1 - e^{-\tau_A}]T_{atm} + T_{spill} + T_r + ... \tag{1.8}$$

Here, $T_{cmb} \approx 2.73$k is the cosmic microwave background. T_{rsb} is the average sky brightness temperature. ΔT_{source} is the astronomical source of an observation, and it is usually much lower than T_{sys}. $[1 - e^{-\tau_A}]T_{atm}$ is the atmospheric emission in the telescope beam. T_{spill} comes from the spillover radiation primarily from the ground. T_r is the noise produced by the radiometer itself.

1.1.3 Localization with Interferometers

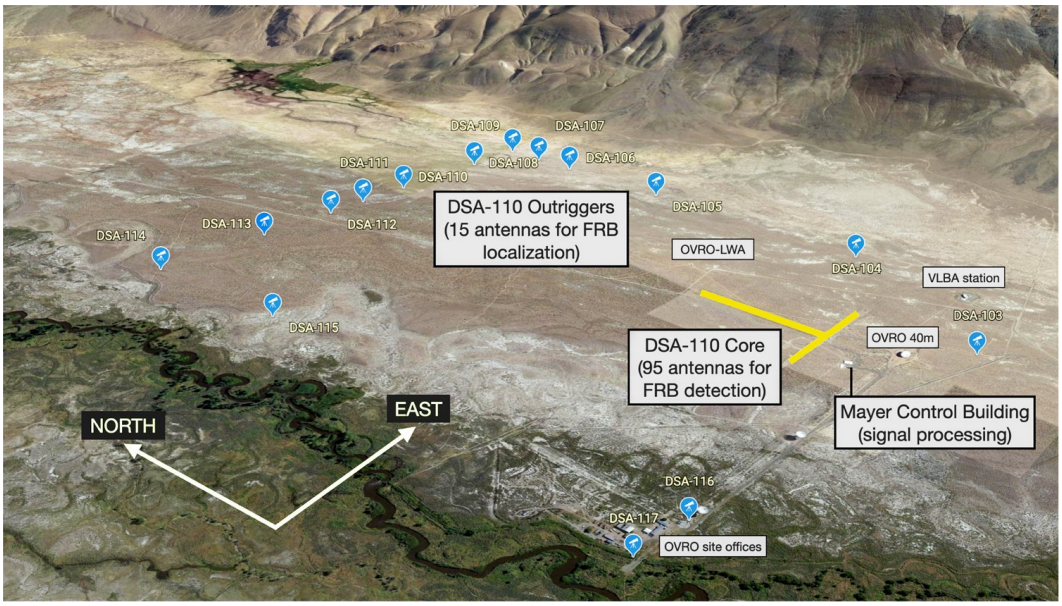

Figure 1.1: The DSA-110 configuration (www.deepsynoptic.org/instrument).

Although DM provides a rough estimation of a FRB's distance, spectroscopic redshift is a more direct measurement. This requires that the FRB can be associated with a single host galaxy. The localization of FRBs is achieved by radio interferometers, and the techniques for probabilistic association with candidate host galaxies

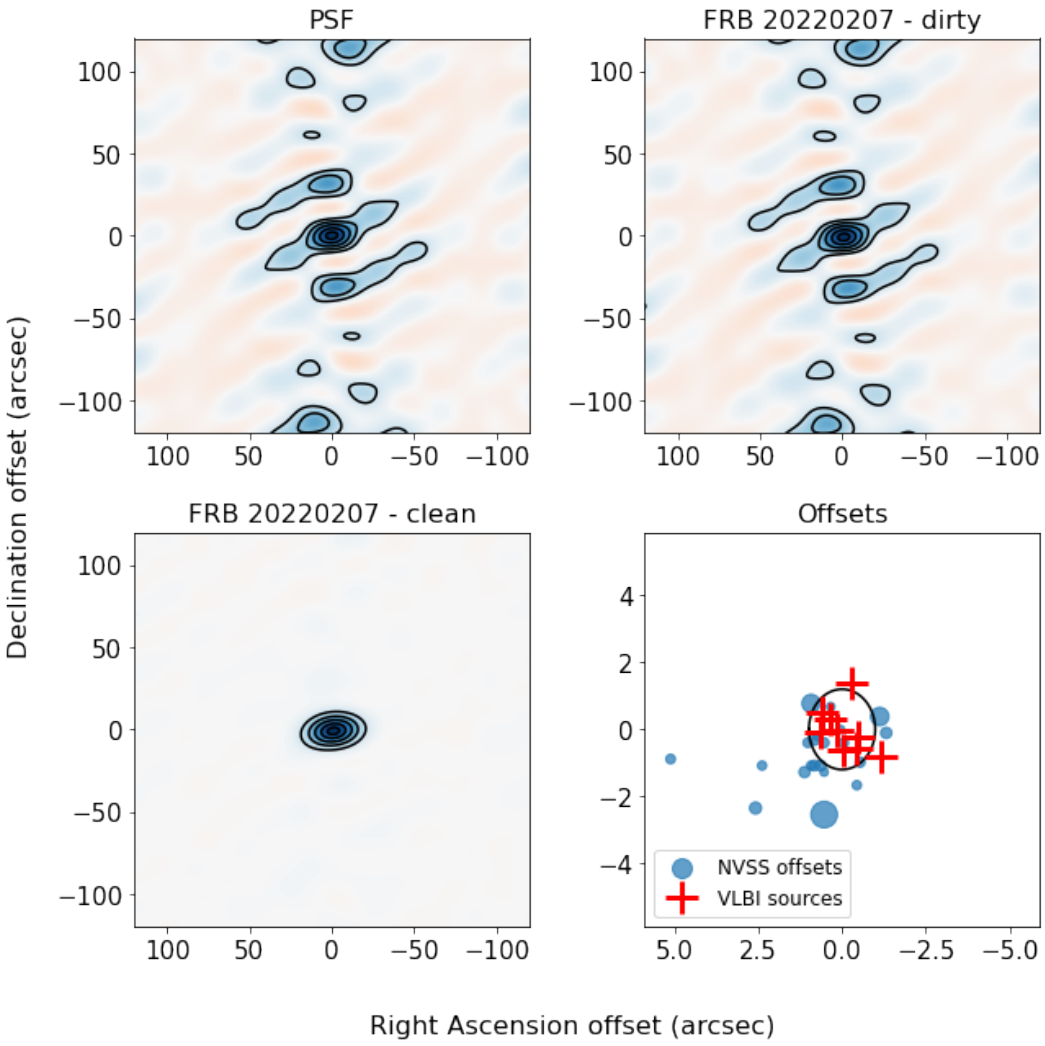

Figure 1.2: The DSA-110 localization precision for one FRB as an example.

have been discussed in several works (e.g., the "PATH" paper 2021). This section introduces the basics of radio interferometry and aperture synthesis.

A radio interferometer is an array of single telescopes. Each telescope points to the same direction and measures the complex E-field vector of the incoming radio wave. The E-field vectors measured by each pair of telescopes are multiplied and then averaged over Δt by correlators. The output is called visibility:

$$V_{ij} = \int I(\hat{s}) e^{-i2\pi \vec{b}\cdot\hat{s}/\lambda} d\Omega. \tag{1.9}$$

Here, $I(\hat{s})$ is the sky brightness in the direction $\hat{s}$ for a slightly extended source, $\vec{b}$ is the baseline vector from antenna i to antenna j. The signal travels an additional distance of $\vec{b}\cdot\hat{s}$ to reach the second antenna, giving a phase difference of $2\pi\vec{b}\cdot\hat{s}/\lambda$.

The visibility of a monochromatic light from one pair of telescopes would be evenly-spaced constructive and destructive interference "fringes," just like those seen in the Young's double slit experiment. Moreover, the image center (phase referencing center) can be shifted to a position that is different from the pointing direction of the dishes by adding an extra delay in the correlator.

For a single telescope dish with diameter D observing a signal with wavelength λ, the "resolution," or the prime beam FWHM, is $\theta_{\rm p} \sim \lambda/{\rm D}$. A typical resolution in the L-band ($1 \sim 2$ GHz) of a large single-dish telescope is a couple of arcminutes (e.g., FAST D $\approx$ 300 m), and of a small single dish is a couple of degrees (e.g., DSA-110 D $\approx$ 4.5 m). For an array of small dishes whose longest baseline is b, the synthesized beam FWHM would be $\theta_{\rm s} \sim \lambda/{\rm b}$. For example, the longest base line of the Very Long Baseline Array (VLBA) is over 8000 km, giving a synthesized beam FWHM of a few milliarcseconds in the L-band. A transient signal can be detected from the visibility difference of two images at different epochs, and the source can be localized by being detected in one (or a few, when side lobes are significant) synthesized beam(s).

In principle, the localization precision's FWHM is:

$$\sigma_\theta \approx 1.22\,\frac{\lambda}{\rm b}\frac{1}{\rm SNR}\frac{1}{\cos(\theta)}. \tag{1.10}$$

Here, λ is the wavelength, b is the longest baseline, SNR is the signal-to-noise ratio and θ is the zenith angle of this detection.

The Deep Synoptic Array (DSA) is a radio interferometer located at the Owens Valley Radio Observatory (OVRO). Each dish has a diameter of $\sim$ 4.5 m, and each antenna has a receiver spanning the band of 1280 to 1530 MHz. During the commissioning stage in 2022, a 63-antenna deployment that contains 48 antennas on the east-west arm of the "Tee" and all of the 15 outriggers was used. The complete stage, DSA-110, contains 95 antennas on the "Tee" for searching, and 15 outrigger antennas with a baseline of $\sim$ 2.5 km for localization (Fig. 1.1). A source detected at zenith at the central frequency (λ = 0.21 m, b $\sim$ 2.5 km) has a precision FWHM of:

$$\sigma_\theta \approx \frac{21.4''}{\rm SNR}. \tag{1.11}$$

In principle, a 8-σ detection could be localized to a sub-arcsecond precision radius. As an example, Fig. 1.2 shows the localization of one FRB during the commissioning

period.

In practice, the above precision is compromised by several factors such as pointing errors, distortion and thermal expansion of the telescope structures, direction-dependent phase differences, antenna electronic noises, variations of the Earth atmosphere, and so on. Some of the errors can be corrected by further calibrations. For example, Michilli et al. [12] perform an empirical calibration by measuring the location of 15 sources with known positions and fit them with a calibration model.

1.2 FRB sources and Emission Mechanisms

1.2.1 Physical constraints on FRB sources

The source models are expected to explain the following observational constraints—

- Timescale: FRBs are typically $\sim$ ms pulses. The duration of observed FRBs ranges from $\sim 10^{-2}$ ms to $\sim 10^{2}$ ms, though an accurate intrinsic width distribution is difficult to determine due to multiple unresolvable propagation effects that attenuate and broaden the pulses and due to instrumental selection effects (e.g., the searching resolution). As high-resolution baseband data becomes available, ultra-fast (a few tens of nanoseconds to μs) variations have been detected in a few FRBs (e.g., FRB 191221 [13]). It is unclear whether or not those are create by the same mechanism as the Crab Pulsar's "nano-shots" (ns-scale features in giant pulses), which have been suggested to be produced by magnetic re-connection events in the magnetosphere.

- Compactness: ms-scale pulses imply a compact emission region of $R \sim cW_i \sim 10^2$ to 10^3 km (ignoring relativistic beaming), where W_i is the redshift-corrected burst duration measured by, e.g., burst morphology modeling.

- Luminosity and Energy budget: the isotropic observed FRB luminosity ranges from $\sim 10^{38}$ to $\sim 10^{46}$ erg s^{-1}, requiring an isotropic energy of 10^{35} to $\sim 10^{43}$ ergs.

- Brightness temperature and Emission mechanism: brightness temperature is the temperature at which a black body would emit the same intensity as a source. FRBs satisfy the Rayleigh–Jeans regime criterion ($h\nu \lll kT$), in which the black body intensity is $I_\nu \approx 2\nu^2 kT_b/c^2$. For non-relativistic FRB sources of width W_i, the projected emission area is $\pi(cW_i)^2$, and

$$T_b \sim 10^{35}\ \mathrm{K}\left(\frac{f_\nu}{\mathrm{Jy}}\right)\left(\frac{\nu}{\mathrm{GHz}}\right)^{-2}\left(\frac{W_i}{\mathrm{ms}}\right)^{-2}\left(\frac{D_L}{\mathrm{GPc}}\right)^{2}.$$

(e.g., [14]). In general, the range of brightness temperature observed in FRBs requires coherent emission mechanisms.

- Spectral: FRBs have been detected from 110 MHz [15] to 8 GHz [16]. FRB spectra are unlikely to be simple power-laws and they show various spectral indices [9, 17]. Most repeaters have narrow-banded spectra (e.g. Chime/Frb Collaboration et al. [18] present a sample of 25 repeaters and most of them have bandwidths of 50 to 200 MHz).

- Multi-wavelength counterpart: Two FRBs (121102, 20190520B) have been reported to have persistent radio counterparts [19, 20]. The counterpart of FRB 121102 has a flat spectrum from 11 GHz down to at least 400 MHz. The galactic FRB 200428A has been associated with magnetar SGR 1935+2154) and has been observed to have hard X-ray transient counterparts [21], CHIME, HXMT).

- Repetition, periodicity, and drifting: it remains uncertain whether or not all FRBs repeat, but repeating FRBs have been observed in over 20 sources, so at least some FRBs are produced by non-catastrophic events. In fact, most FRBs are likely repeaters since the observed FRB event rate by CHIME has exceeded the event rate of supernovae, one of the most promising catastrophic FRB source candidates [22]. Moreover, FRB 180916 has been found to recur at a period of $\approx$ 16 days, [21], FRB 121102 may have a period of 160 days despite some missing active windows [23], and FRB 191221 has been reported to have a period of $\sim$ 0.216 s [13] Proposed models for periods of several days include binary systems, rotating magnetars or magnetar procession. The sub-second periodicity could be explained by phenomena in neutron star magnetospheres, but not the external shock models, for which it is difficult to have such a short, and constant period. Finally, downwards drifting of frequency with time (the "sad trombones") in single pulses have been seen in several repeaters, providing clues for the mechanism and geometry of the coherent emission regions in some of the FRBs (e.g., height above a neutron star surface), though upward drifting of frequency with time has also been reported in a few bursts from the active repeater 20201124A [24].

- Rate: FRBs are estimated to occur $\sim 10^3$ sky^{-1} day^{-1} [11]. [22] estimate that the volumetric rate of FRB sources is R > 2.4×10^5 Gpc^{-3} yr^{-1} based on the CHIME sample and assuming that each of the one-off FRB event is

from a different source, DM_{host} = 50 and the Milky Way halo DM has a flat probability distribution function between $50 \sim 80\,\mathrm{pc\,cm^{-3}}$. In comparison, the birth rate of popular FRB source models, such as magnetars, can be estimated from the volumetric rate of core-collapse supernovae ($\sim 10^5\ \mathrm{Gpc^{-3}yr^{-1}}$), although additional formation channels, such as merger-induced or accretion-induced collapse, could be the source of additional FRB sources observed in older stellar populations.

- Host types and location: by early 2023, over 20 FRBs had been reported to be associated with individual galaxies. These FRBs have been found to reside in diverse galaxy types and local environments (e.g., [25–28]). Although most FRBs have been detected in star-forming galaxies as expected by the popular magnetar source models, a few FRBs are not— for example, FRB 20200120E has been associated with an aged globular cluster in M81 [29], and 20220509G is located within an early-type quiescent galaxy [30]. In addition to the diversity of their host galaxies' star forming histories, some FRBs with sub-arcsecond localization have been reported to be offset from the star-forming region in their hosts, and the offset is too large to be explained by typical natal kicks, or binary formation recoil. Those requires different source formation channels.

- "Local" environment: The observed FRBs are estimated to have local DMs from few to $\sim 10^3$ pc cm^{-3} and local RMs from few to $\sim 10^5$ rad m^{-2}, indicating potentially different local environments. In a few repeaters, the DM and RM have been found to change over time. For example, the large and changing DM and RM in FRB 121102 could be related to a magnetized and dynamic local environment.

- Polarization: Most FRBs have been observed to be highly polarized. Most, but not all, repeaters have been found to be linearly polarized (though repeater FRB20201124A has circular polarization), and one-off events have more diverse polarization states. In some FRBs the polarization position angle has been found to vary within a pulse or between different pulses of a repeater.

The small emission region, large burst energy and the requirement of coherent emission motivate source models involving compact objects (e.g., [31, 32]). The most commonly discussed models include isolated Neutron stars, magnetars, as

well as neutron stars or black holes interacting with the environment or with their companion in a binary / many-body system (e.g., Fig. 3 of BingZhang 2020 [31]).

In general, there are two main classes of FRB models distinguished by the location of the emission.

- "Close-in": FRBs are produced within the magnetosphere of a compact body (e.g., Neutron star, black hole) by plasma maser effects or by coherent curvature radiation from electron-positron bunches radiating in phase.
- "Far-away": FRBs are created far away above the surface of a compact body by the synchrotron maser process from particles accelerated by an ultra-relativistic shock initiated by flares in a magnetized plasma environment (e.g., flares from reconnection in a neutron star magnetosphere).

One interesting feature to potentially distinguish the two class of models is the polarization angle (PA). For example, Luo et al. [33] report diverse polarization angle swings among 15 bursts from the repeating FRB 180301, and argue that the observed swing is consistent with close-in curvature radiation models where FRBs originate in the magnetosphere, while it disfavors the far-away synchrotron maser models where FRBs are produced in relativistic shocks far above the magnetosphere. PA variations originate from the B-field configurations along the line-of-sight being swept by the FRBs radiation beam. In the close-in models, a simple rotating-vector dipole B-field model predicts an 's' or 'inverse s' shaped PA variation, a straight B-field line along the line of sight predicts a constant PA, and a complicated B-field configuration can produce diverse PA swings. In the far-away models, the coherent radiation relies on a highly ordered B-field configuration in the upstream medium, which is in tension with the observed PA swing that requires a complicated configurations varying non-monotonically with the radius.

In addition to an isolated compact body as the FRB source, several works have proposed that FRBs can be produced during the interaction between a compact object and its environment or companion. For example, the "cosmic comb" model involves a regular pulsar magnetosphere being "combed" by a nearby strong plasma stream from, for example, an active galactic nucleus (AGN) flare or stellar flares from a companion star. The stream initiates magnetic reconnection events, which produce FRBs by curvature-radiation processes within the magnetosphere. Moreover, to explain the observed periodicity and activity windows of FRBs 180916 and 121102,

models argue that these FRBs could originate from highly eccentric binary system (or perturbed three-body system) where mass transfer occurs periodically around the orbital periastron from a stellar companion to a compact object. Coherent emission can be produced, for example, within the relativistic jet of a black hole undergoing super-Eddington accretion.

1.2.2 Neutron star population, magnetars

As introduced in the previous subsection, the observed features of FRBs favour compact sources such as neutron stars or black holes. In particular, one class of neutron stars— magnetars— have been the most commonly discussed source candidate, as motivated by the X-ray bursts detected during the FRB-like events from the Galactic magnetar SGR 1935+2154. Moreover, several of the FRB emission models are developed from neutron star emission models. This subsection briefly introduce some of the neutron star demography and highlight some of the magnetars properties (e.g., [34–36]).

Neutron stars are compact stars born in core-collapse supernovae and supported by the neutron degeneracy pressure. The canonical neutron star model has $R \sim 10$ km and $M \sim 1.4 M_\odot$. They are believed to be composed of free Neutrons as well as a small fraction of protons and electrons, though their internal structures and states remain highly uncertain. The observed neutron stars population is diverse (e.g., Fig. 3 of Gotthelf et al. 2013 [37]), and the most well-understood sources of power are rotation, accretion, and magnetic field.

The first observed class of neutron stars are pulsars— highly magnetized, rotating neutron stars whose magnetic and rotational axes are misaligned and the beam(s) of radiation along the magnetic axis periodically sweeps through the Earth. Pulsars have been observed to spin rapidly (1.4 ms $\sim$ 8s). They are known to be highly magnetized as measured from, for example, cyclotron resonance in their X-ray spectra. In the simple magnetic dipole toy model, the characteristic B-field at the equator is estimated to be:

$$B = 3.2 \times 10^{19} \sqrt{P\dot{P}}. \tag{1.12}$$

Here, P and $\dot{P}$ are the spin period and spin-down rate, respectively, which can be measured from long-term observations. A rotating magnetic dipole radiates and spins down (magnetic braking), giving a characteristic age for pulsars:

$$\tau_c \approx \frac{P}{2\dot{P}}. \tag{1.13}$$

Fig. 3 of Gotthelf et al. 2013 [37] shows an P-$\dot{\text{P}}$ diagram of the observed neutron stars. The rotation of the highly-magnetized star induces a strong electric field. The electric force drags charged particles out of the pulsar surface and form a plasma sphere surrounding the pulsar surface, called the "magnetosphere." In certain region(s) of the magnetosphere, charged particles are accelerated to relativistic energies and produce radiations. In the radio band, the observed high brightness temperature requires coherent emission mechanisms. The most commonly discussed ones are antenna, maser and relativistic plasma emission processes. In the high energy band, possible emission mechanisms may include synchrotron, curvature and inverse Compton scattering processes.

Isolated radio pulsars (black dots in Fig. 3 of Gotthelf et al. 2013 [37]) are believed to be powered by their rotational energy, which is represented by the spin-down luminosity:

$$\dot{\text{L}_{\text{sd}}} = \frac{\text{d}}{\text{dt}}(\frac{1}{2}\text{I}\omega^2) = 4 \times 10^{31} \left(\frac{\dot{\text{P}}_{-15}}{\text{P}_1}\right) \quad \text{erg/s}. \tag{1.14}$$

Here, P_{-15} is in the unit of 10^{-15} s/s and P is in the unit of seconds. The radio emission is expected to turn off once the pulsar spins down to the region below a "death line" (Fig. 3 of Gotthelf et al. 2013 [37], at which the accelerating potential within the relevant region(s) of the magnetosphere is insufficient to initiate a pair cascade process.

Though isolated pulsars turn off as they age, neutron stars in binary systems can regain energy and momentum from their just-evolved companions during the Roche Lobe mass transfer process. The neutron star can be spun up to a few $\sim$ tens of milliseconds (mostly in the lower-left of Fig. 3 of Gotthelf et al. 2013 [37]), depending on the life-time of their companion. The binary evolution theory of these "recycled" millisecond pulsars (MSP) have been confirmed by the observations of X-ray emissions from the accretion dick, and the swings between X-ray and radio pulsations. In addition, MSPs have also been found without any companion, in highly eccentric binary systems or in triple systems, indicating other possible "recycling" processes.

Magnetars are a class of young ($\lesssim$ years) neutron stars with high B-field ($\text{B} \gtrsim 5 \times 10^{13}$ G; upper-right of Fig. 3 of Gotthelf et al. 2013 [37]) as compared with typical radio pulsars ($\text{B} \sim 10^{12}$ G). They represent $\gtrsim$ 10% of the Neutron star population but show some of the most dramatic behaviors. They are observed as soft γ-ray repeaters ("SGRs") and anomalous X-ray pulsars ("AXPs") and have

X-ray luminosities greater than their spin-down luminosities (Eqn. 1.14). Their emission activities are believed to be powered by their magnetic energy. About 30 magnetars have been detected [2], with all of them found in the Galactic plane, and some associated with supernova remnant shells, consistent with their young spin-down ages, given the measured proper motion velocity of $\sim$ 200 km/s (e.g. [38]). Magnetars have been proven to be high-B radio pulsars in quiescent (e.g., [39]).

Magnetars are temporally highly variable. They are often found by their X-ray and γ-ray transient events: bursts, outbursts and giant flares. Bursts (a few milliseconds to seconds) are the most common transient events seen in Magnetars. A typical burst is $\sim$ 100-ms-long with a peak luminosity of $10^{36\sim43}$ erg s^{-1}, followed by a tail of several minutes. Outbursts consist of an X-ray flux raise (of a factor of $\times 10 \sim 10^3$) lasting for weeks to months and peaks up to $\sim 10^{36}$ erg s^{-1}, followed by a few-month-long tail / afterglow, and accompanied with short X-ray bursts and radiative anomalies. Giant flares are rare and energetic— the observed ones peak at $10^{44\sim47}$ erg s^{-1} in the X-ray, and can release an energy of 10^{46} ergs within $\sim$ 0.2 s (e.g., Hurley+2005). These events are potentially connected with the production of FRBs due to their high energy budgets. Frequent glitches (spin-up) and strong glitches recovery have been noticed during transient events. Correlated emissions in the optical, IR and radio bands have been seen in a few magnetars during their X-ray transient events (e.g., FRB 200428 [40, 41]). In addition to the three types of transient events, some magnetars emit persistently ($\gtrsim 10^{33}$ erg s^{-1}), while others don't ("transient magnetars").

The spectra of persistent magnetars in quiescence can be approximated as a blackbody plus a power-law component in the soft X-ray, and turns up above $\sim$ 10 keV. The energy and spectral parameters are highly rotational-phase-dependent. The spectra of transient magnetars in quiescence can be approximated as a pure blackbody in the soft X-ray, similar with high-B radio pulsars. The spectra of magnetar bursts and giant flares are initially much harder than those of magnetars in quiescence, and soften afterwards. Magnetar spectra are nearly flat in the radio band.

The rich phenomenons of Magnetars are powered by their magnetic energy. The B-field evolves internally as the Magnetar ages through ambipolar diffusion and Hall drift, which increases crustal stresses and trigger "starquakes." The sudden displacement of the crust releases magnetic energy and twists the magnetosphere to an unstable state. The unstable magnetosphere releases a large fraction of its twist

[2] https://www.physics.mcgill.ca/ pulsar/magnetar/main.html

energy and produces a giant flare in a short time scale and then reconnects its B-field lines. Additionally, it could gradually release the rest of the twist energy to power persistent non-thermal emissions.

Magnetars could be formed in multiple channels (e.g., [35]), which is consistent with the diversity of observed FRB hosts assuming magnetars were their sources. The most common formation channel may be core-collapse supernovea as the origin of most neutron stars. This channel is consistent with FRBs observed in young, star forming host galaxies. In addition, magnetars could also be formed by accretion- or merger- induced collapse in a binary system [29], which could account for the FRBs found in the old star populations. The correlation between FRB properties (e.g., energy level, temporal features) and host stellar population age may help to test the formation channel hypotheses.

1.2.3 Emission mechanisms

Two classes of coherent emission mechanisms have been proposed for FRBs: synchrontron maser and curvature radiation of bunched particles.

- Synchrontron Maser: Microwave Amplification by Stimulated Emission of Radiation, or Maser, has been observed in many astrophysical sources. [42] consider a system of leptons with three discrete energy levels: γmc^2 and $\gamma mc^2 \pm h\nu$. As an electrons at the intermediate energy γmc^2 is stimulated by an incident photon with the correct energy $h\nu$, it either jump to the higher energy level $\gamma mc^2 + h\nu$ (absorption) or drop to the lower level $\gamma mc^2 - h\nu$ and emit two photons with the same frequency ν (stimulated emission). The two emitted photons then stimulate two new leptons at the intermediate energy level to emit four photons, and so on, producing a chain of stimulated emissions at the same phase and frequency, coherently amplifying the incident radiation. This negative absorption requires a "population inversion"—more leptons are at the higher energy levels than the lower ones, as opposite to the Boltzmann distribution of systems at thermal equilibrium. Specifically, synchrotron maser process occurs in magnetized plasma where the lepton's synchrotron frequency is close to the incident photons frequency. The emitting leptons are required to have a population inversion in energies and a narrow pitch-angle below $1/\gamma$. *"These conditions are possible in an ultra-relativistic (bulk Lorentz factor $\Gamma \gg 1$) radiative shock driven into a significantly magnetized plasma (magnetization parameter $\sigma \gtrsim 10^{-3}$); the*

shock is mediated by Larmor-rotating charges, which results in the population inversion within the shock."[43] This scenario is possible in a wide range of source models. For example, [44] proposed a model where *"Magnetar flares eject ultra-relativistic ion-electron shells that are supersonic into the surrounding magnetized trans-relativistic ion-electron plasma released by previous flares. The forward shock creates a population inversion and enables the synchrotron maser process, which results in narrowly peaked coherent radio emission putatively responsible for FRBs."*[43] For another example, [45] apply the synchrotron maser shock mechanism to a binary system with a stellar mass black hole undergoing super-Eddington accretion from its companion star. The accretion generates short-lived relativistic outflows into the magnetized upstream plasma released by the pre-existing jets, producing periodic FRBs at the timescale of the binary system's orbit or the procession of the accretion funnel.

- Curvature: The coherent curvature emission mechanism for FRBs requires bunched relativistic leptons in curved / twisted, strong ($\gtrsim 10^{10}$ G) magnetic fields. The particles are accelerated along the B-field and grouped to have the same oscillatory phase (in space and momentum), producing coherent emissions. The required "bunches" could be formed by two-stream plasma instability, magnetic reconnection events, or magnetic braking of a deferentially rotating object. While the synchrontron maser emission mechanism applies to various sources and locations, coherent curvature radiation occur most naturally in the magnetosphere near the neutron stars / magnetars surface—most of the source models involves FRBs formed within the magnetosphere of highly magnetized neutron stars / magnetars to account for the short timescale and high energy budgets of FRBs. For example, [14] describes a model where *"counter-streaming* $e^{\pm}$ *plasma inside the twisted magnetosphere of a magnetar rapidly clumps due to the two-stream instability. When magnetic reconnection occurs near the magnetar surface, these clumps are accelerated along magnetic field lines and radiate coherently."*[43] Another type of examples involve small bodies (e.g., comets, asteroids, planet fragments) falls onto the neutron stars surface and produce coherent curvature radiation as they travels through the magnetosphere [46].

1.2.4 Multi-wavelength counterparts

Until early 2023, the only reported multi-wavelength transient association with FRB comes from the galactic magnetar SGR 1935+2154. X-ray transients have been detected together with the FRB-like events 200428, although later observations of SGR 1935+2154 show that most of its X-ray transients are not associated with FRB-like events [47]. Multi-wavelength and / or gravitational wave (GW) transient FRB counterparts have been predicted by several catastrophic-type FRB models (e.g., binary mergers, compact objects collapse) and a few non-catastrophic ones predict (see Chapter 2 for an extended discussion).

In the far-away models, [44] predict that the forward shock which produces the coherent emission also dissipates most of its energy in a synchrotron "afterglow," resulting in detectable high-energy transient counterpart. Alternatively, if the upstream medium were made of electrons and positrons instead of electrons and ions, a weak optical counterpart is possible. More recently, [45] predict an observable transient optical / IR counterpart similar with that of a dusty common envelope transient or luminous red nova.

In the close-in models, [48] described a model that could explain the X-ray burst associated with the FRB-like event from the galactic magnetar SGR 1935+2154. In this model, FRBs are produced within the neutron star magnetosphere through curvature radiation by particle clumps in the charge starvation region near the magnetic poles. The X-ray

Until early 2023, two persistent radio counterparts have been associated with FRBs 121102 and 20190520B. They are both highly-active repeaters with large RMs ($10^{4\sim5}$ rad m^2). These features have been commonly explained by synchrontron radiation from relativistic particles within a dense and highly-magnetized environment at the source's vicinity, such as a supernova remnant (SNR) or pulsar wind nebula (PWN).

1.3 Propagation Effects

FRBs are potential cosmic probes for a range of studies. For example, FRBs might be used to study the distributions of ionized baryons in the IGM and the CGMs (e.g., [49]), to measure the history of reionization (e.g., [50]), to constrain cosmological parameters (e.g., [51]) and the CMB optical depth (e.g., [52]), to measure the extragalactic B-fields (e.g., [53]), to test the equivalence principle (e.g., [54]) and the photon mass (e.g., [55]), to study the cosmic web (e.g., [56]), and so

on. However, most of the proposals rely on a good understanding of the propagation effects.

1.3.1 Basic

Signals from extragalactic FRBs travel through varies mediums to reach the telescopes. It is important to understand the propagation effects for two reasons—to separate intrinsic FRB phenomenons from propagation effects, and to derive properties of the mediums from the observed propagation effects.

Before reaching the radio telescopes, light from an extragalactic FRB propagates through the local surounding environment of its source, the host ISM and CGM / halo, the IGM, potentially the intervening galaxies, the Milky way halo and ISM, as well as the interplanetary medium of our Solar system and the Earth ionosphere. The major radio propagation effects for FRBs are summarized below [36].

1.3.1.1 Dispersion Measurement (DM)

The dispersion measurement (DM) is defined as the electron number density integrated along the propagation path:

$$\mathrm{DM} = \int_0^{\mathrm{d}} \mathrm{n_e ds}. \tag{1.15}$$

For extragalactic sources like FRBs, the observed DM is usually composed of the following components (e.g., [57]):

$$\mathrm{DM_{obs}} = \frac{\mathrm{DM_{host}} + \mathrm{DM_{local}}}{1 + \mathrm{z_{frb}}} + \frac{\mathrm{DM_{ICM}}}{1 + \mathrm{z_c}} + \mathrm{DM_{IGM}} + \mathrm{DM_{MW,halo\&CGM}} + \mathrm{DM_{MW,ISM}}. \tag{1.16}$$

- $\mathrm{DM_{host}}$: the FRB host galaxy could provide a DM of $\sim 10^0 \sim 10^3$, depending on the type of galaxy and, the location of the FRB source within the galaxy, and our viewing angle. Typically, the contribution ranges from a few ten 's to a couple of hundreds (e.g., [58]). The uncertainty of the host DM is estimated determined by the uncertainties of the Milky Way DM contributions.

- $\mathrm{DM_{local}}$: the local environment of the FRB source contribute a DM of $\sim 10^0 \sim 10^3$, depending on FRB source models.

- $\mathrm{DM_{ICM}}$: if the FRB is discovered within a galaxy cluster, the hot plasma in the intracluster medium contribute to the total DM (e.g., [59]).

- DM_{IGM}: The exact relation between the intergalactic medium DM and redshift remain uncertain and depends on the line of sight. The average cosmic DM for a flat universe at redshift z is estimated to be (e.g., [49]):

$$\langle DM_{cosmic} \rangle = \int_0^z \frac{c\bar{n_e}(z)dz}{H_0(1+z)^2\sqrt{\Omega_m(1+z)^3+\Omega_\Lambda}}. \tag{1.17}$$

  Here, the mean ion density $\bar{n_e} = f_d\rho_d(z)m_p^{-1}(1 - Y_{He}/2)$, where f_d is the fraction of cosmic baryons in ionized diffuse gas, $\rho_d(z) = \Omega_b\rho_{c,0}(1+z)^3$ is the baryon mass density at redshift z for a critical universe whose mass density today is $\rho_{c,0} = 3H_0^2/8\pi G$, m_p is the mass of proton and $Y_{He} = 0.25$ is the Helium mass fraction. $\Omega_b = 0.0486$, $\Omega_m = 0.3075$ and $\Omega_\Lambda = 0.6910$ are the mass fraction of baryon, matter and dark energy, respectively [60]. The uncertainty of the IGM DM is due to cosmic variance.

- $DM_{MW,\,halo\&CGM}$: the halo and CGM of the Milky Way contributes about $\sim 10 \sim 10^2$ cm^3 pc, depending on the halo states [57].

- $DM_{MW,\,ISM}$: the Milky Way ISM could contribute $\sim 10^0 \sim 10^3$ cm^3 pc, depending on the line of sight (e.g., [61, 62]). The uncertainty of the Milky Way contribution is estimated to be negligible at higher galactic latitude ($b > 20^o$), and is $\sim 20\%$ near the galactic plane ([61, 62]).

For unlocalized FRBs, the extragalactic DM can be used to estimate their distances. For localized FRBs, the distance is directly measured from the host redshift, making it possible to separate the host DM contribution from the total. This helps to understand the host environment as well as its relation to the evolution channels of the FRB sources.

DM is informative, but how is it measured? Plasma is a dispersive medium since its index of refraction is frequency-dependent and greater than one. A signal that travels through plasma mediums, such as the ionized intergalactic medium (IGM) or an interstellar medium (ISM), is delayed by

$$\tau = \frac{2\pi e^2}{cm_e\omega^2}\int n_e ds. \tag{1.18}$$

Here, Ω is the angular frequency of the signal. Equations 1.15 and 1.18 indicate that high-frequency signal arrives ahead of low-frequency signal by

$$\tau = 4.15 \left((\frac{\nu_{\rm low}}{\rm GHz})^{-2} - (\frac{\nu_{\rm high}}{\rm GHz})^{-2} \right) \frac{\rm DM}{\rm cm^{-3}\ pc}\ {\rm ms}. \tag{1.19}$$

Here, $\nu_{\rm high}$, $\nu_{\rm low}$ are the frequencies of the high- and the low- frequency signals. Therefore, DM can be measured by modelling this frequency-dependent time delay into the dynamic spectrum. In addition, the dispersion needs to be removed using the above relation in a process called the "de-dispersion" in order to restore the intrinsic signal profile. The detailed de-dispersion steps have been introduced in Section 1.1.2.

1.3.1.2 Scattering

In ionized plasma medium, the temporal and angular broadening of signals due to multi-path propagation is called "scattering." The broadening are frequency-dependent since photons are refracted in the plasma. The exact relation depends on the nature and the location of the scattering medium. For example, the scattering medium of most extragalactic sources could be approximated as a single, thin screen with gaussian fluctuations in the free electron column density (e.g., [63]). In this model, the plasma phase $\phi \propto \nu^{-1}$, the angular broadening scales with frequency as:

$$\theta \propto \nu^{-2}, \tag{1.20}$$

and the delay time depends on frequency as:

$$\tau \propto \nu^{-4}. \tag{1.21}$$

If the scattering screen were Kolmogorov turbulence, $\tau \propto \nu^{-4.4}$.

The observed scattering timescale $\tau_{\rm obs}$ usually consists of the following components:

$$\tau_{\rm obs} = \frac{\tau_{\rm host} + \tau_{\rm local}}{(1 + {\rm z_{frb}})^3} + \tau_{\rm MW,halo\&CGM} + \tau_{\rm MW,ISM}. \tag{1.22}$$

In the first term, the power of three is a combination of two effects: $(1 + {\rm z})^{-1}$ from time dilation and $(1 + {\rm z})^4$ from the fact that $\nu_{\rm rest} = \nu_{\rm obs}(1 + {\rm z})$ and $\tau_{\rm host}$ happened at the rest frame, assuming $\tau \propto \nu^{-4}$. Scattering from the IGM and the ICM are usually negligible due to the lack of turbulent medium.

In general, it is common to describe the distribution of the free electron column density along the line of sight by the "scattering measurement" (SM) defined as [64]:

$$\mathrm{SM} = \int_0^{\mathrm{d}} \mathrm{C}_{\mathrm{n_e}}^2(\mathrm{l})\mathrm{dl}. \tag{1.23}$$

Here, $\mathrm{C}_{\mathrm{n_e}}^2(\mathrm{l})$ describes the clumpiness or turbulence of the free electrons per unit length. Note that the scattering measurement is sensitive to the location of the screen— $\mathrm{SM} \propto (\mathrm{s}(1-\mathrm{s}))^{-5/6}$ (e.g., Eqn. 10 of [65]), where s is the distance between the scattering screen and the observer.

1.3.1.3 Scintillation

Scintillation has been observed from compact and distant sources, such as FRBs and pulsars, as their signal propagate through plasma medium. In ionized medium, the fluctuations in the electron density lead to variations of the refractive index, which change the phase of the wavefront. When the multi-path radiation from the same source combines coherently, the source scintillates. Scintillation can be detected from spectral modulation, since the frequency-dependent multi-path radiation combines coherently. Scintillation could also be found from flux density temporal variation, when there were relative motions between the source, the medium and the observer.

For extragalactic sources, the Milky Way is the major sintillating medium, and can often be approximated as a thin scattering screen at a distant D from the observer. One characteristic property of the screen is the first Fresnel scale:

$$\mathrm{r_F} = \sqrt{\frac{\lambda \mathrm{D}}{2\pi}}, \tag{1.24}$$

which is the transverse length at which the phase of a wavefront with wavelength λ changes by one radian due to the geometric path length difference, assuming that $\mathrm{D} \gg \lambda$. Another feature of the scattering screen is $\mathrm{r_0}$, the transverse scale at which phase changes by one radian due to the random fluctuations. Based on the relation of these two scales, scattering is divided into the weak regime ($\mathrm{r_0} \gg \mathrm{r_F}$) and the strong regime ($\mathrm{r_0} \ll \mathrm{r_F}$).

In the weak regime, the signal is only weakly deflected, and the image is slightly focused or defocused on the observer's plane. Scintillation occurs when the source size is less than the 1st Fresnel scale, and is smeared out if the source were larger.

In the strong regime, the screen generates a large variation in phase over the 1st Fresnel scale. There are two main types of scintillation behaviors— refractive and diffractive. Refractive scintillation is caused by light beams travelling through relatively large-scale inhomogeneities that are equivalent with lens. The observed flux variability is slow ($\sim$ days) and broad-band.

In contrast, diffractive scintillation is produced by interference effects between light beams passing through small-scale inhomogeneities. The variations are fast ($\sim$ hours) and narrow-band. The diffractive scintillation bandwidth is frequency-dependent (e.g., [66]):

$$\Delta\nu \propto \nu^{22/5}. \tag{1.25}$$

1.3.1.4 Faraday Rotation and B-field

Faraday rotation occurs when a polarized wave propagate through a magnetized plasma. A linearly polarized wave can be decomposed into a right-hand and a left-hand circular polarized components. In a magnetized plasma, the index of refraction has different values for the right-hand and the left-hand polarized waves, making the former to propagate faster than the later. As a result, as a linearly polarized plane wave travels across a magnetized plasma medium, the plane of polarization rotates as (e.g., [11]):

$$\Delta\Theta = \omega^2 \mathrm{RM}, \tag{1.26}$$

where the rotational measurement RM is given by:

$$\mathrm{RM} = \frac{e^2}{2\pi m_e^2 c^4 \omega} \int_0^d n_e \, B_{\parallel} ds \approx 8.1 \times 10^5 \int_0^d \frac{n_e}{\mathrm{cm}^{-3}} \frac{B_{\parallel}}{\mathrm{Gauss}} \frac{ds}{\mathrm{pc}} \quad \mathrm{rad\ m}^{-2}. \tag{1.27}$$

Like the observed DM, the observed $\mathrm{RM_{obs}}$ from an extragalactic FRB is composed of multiple components:

$$\mathrm{RM_{obs}} = \mathrm{RM_{MW}} + \mathrm{RM_{IGM}} + \frac{\mathrm{RM_{ICM}}}{(1+z_{\mathrm{ICM}})^2} + \frac{\mathrm{RM_{host}} + \mathrm{RM_{local}}}{(1+z_{\mathrm{frb}})^2}. \tag{1.28}$$

- $|\mathrm{RM_{MW}}|$: The galactic RM contribution along a LoS is predicted by models such as the `NE2001` [61] and measured using polarized radio sources (e.g., [67]). $|\mathrm{RM_{MW}}|$ is $\sim$ 100 rad m^{-2} within a few tens of degrees around the galactic plane and $\sim$ 10 rad m^{-2} at high galactic altitude . The B-field is $\sim$ 0.1 to $\sim$ 1 μG.

- $|RM_{IGM}|$: Usually believed to be negligible $\sim$ 10 rad m^{-2} as compared to the other contributions (e.g., [56]).

- $|RM_{ICM}|$: Until early 2023, only two FRBs have been localized to galaxy clusters [59]. The $|RM_{ICM}|$ of FRB 20220509 is estimated to be $\approx$ 120 rad m^{-2}, corresponding to a B-field of $\sim$ 1 to $\sim$ 10 μG. The observed $|RM_{ICM}|$ is consistent with the magneto-hydrodynamical simulations (MHD) results of $\approx \pm 200$ rad m^{-2} (e.g., [68]).

- $|RM_{host} + RM_{local}|$: varies by several orders of magnitude among the reported FRBs, and some of them change over time. For example, the observed total RM of FRB 121102 is $\sim 10^5$ rad m^{-2} and has been reported to decrease by about 15% per year within 2.5 years [69]. The large RM value obviously cannot be explained by the other contributors above, and the variation has been explained as a dense, dynamic plasma environment around the FRB source [70]. Most of other FRBs have much lower observed RM from a few hundreds to negligible.

If the DM and the RM were produced by the same region, the average B-field along the line of sight could be estimated by:

$$< B_{\parallel} >= \frac{RM}{8.1 \times 10^5\ DM} \quad \text{Gauss.} \tag{1.29}$$

Here, DM is in cm^{-3} pc, RM is in rad m^{-2}.

1.3.1.5 Polarization

Until mid-2023, most repeating FRBs are reported to be highly linearly polarized (e.g., [16, 70, 71]), and only a couple of repeating sources have been reported to have significant portions of circular polarization (e.g., FRB 20201124A [72]). The one-off FRBs are linearly-, circularly- or non- polarized (e.g., [71]), but most of them are highly linearly polarized. The polarization angle have been reported to vary within individual burst and between pulses in some FRBs (e.g., [33]), providing clues on the emission locations relative to the magnetosphere and the configurations of the B-fields.

1.3.2 Galactic ISM model and halo

Extragalactic FRB signals travel through our Milky way before reaching the telescopes. Our Milky Way is a spiral galaxy with a total stellar mass of $M_* \sim 10^{11}\ M_\odot$.

It is composed of a bulge (R $\sim$ 1 kpc), a thick stellar disk (half light radius $R_{eff} \sim 5$ kpc, scale height H $\sim$ 1 kpc), a thin gas disk ($R_{eff} \sim 10$ kpc, H $\sim$ 100 pc), and a circumgalactic halo ($R_{vir} \sim 200$ kpc) composed of dark matter, gas and stars.

The ISM is cold and ionized with a typical electron density of $n_e \sim 0.03$ cm^{-3} (e.g., Ables and Manchester 1976). Most of the galactic ISM resides in the thin and the thick discs, the spiral arms, and the galactic center / bulge. The galactic ISM free electron along a LoS are often estimated using models such as `NE2001` [61, 73] and `YMW16` [62], which are mostly based on radio pulsar surveys results. These model can be used to estimate the galactic DM, scattering, scintillation and rotation measure for a given line of sight (LoS). The galactic B-field and rotation measure are also predicted by a few other models (e.g., [74, 75]). Localized nearby FRBs help to refine the galactic free electron distribution. For example, the recent DM value of FRB 220319 show that the DM_{ISM} along the LoS of 220319 are overestimated using the `NE2001` and the `YMW16` models [76].

The circumgalactic halo is dominated by dark matter ($\sim 10^{12} M_\odot$), but also contains a small amount of gas (a few ten's percents of the galactic gas mass) and stars (a few percents of the galactic stellar mass). The halo has a viralized radius of $R_{vir} \sim 200$ kpc, a viralized velocity of $\sim$ 200 km/s, and a viralized temperature of $\sim 10^5$ to 10^6 K. The Magellannic clouds and several satellite galaxies also reside inside the halo.

Several models have been proposed to describe the gas distribution in the galactic halo. For example, some of those models numerically simulate the gas distribution based on the dark matter density profile within the halo [77], as well as the hydrodynamic relaxation of the gas and the modifications due to feedback processes ([78–81]). For the galactic halo DM contribution, [57] estimate that the hot (T$\sim 10^6$-10^7 K) halo gas a DM contribute of $\approx$ 50-80 pc cm^{-3} based on the X-ray and far UV absorption lines of highly ionized oxygen. They also find that the cool halo gas (T$\sim 10^4$ K) has negligible DM contribution based on the HI 21 cm emission observations and assume an ionization fraction of $x_{HI} = 0.3$.

1.3.3 IGM, CGM, and ICM

Nearly 90% of the baryons reside in the IGM and CGMs and are of great interest for galaxy evolution and cosmology studies. For example, the baryonic mass distributions in the IGM can be used to probe the cosmological structure formation histories (e.g., [82, 83]) and the amount of ionized IGM baryons at different redshift reveals the history of reionization. In addition, the phases of the IGM and the CGMs feature

the environments in which galaxies were formed and trace the baryonic matters and the ionizing photons ejected by the galaxies as they evolve. The CGM helps to understand the feedback processes in galaxy evolution.

The IGM evolves with redshift [84]. Every roughly, during the reionization epoch (between z $\sim$ 11 and z $\sim$ 6.5), radiations from galaxies photoionize most of the neutral Hydrogen (and later Helium) atoms in the IGM and heats the IGM from $\sim$ a few 10^3 k to $\sim$ 10^5 k. In intermediate redshift (z of 2 $\sim$ 5), the IGM has a mean density of $\sim$ a few cm^{-3} and a temperature of $\sim$ 10^4 k. In relatively low redshift ($z \lesssim 2$), structure formation shocks heat up $\sim$ 50% of the IGM baryons to the hot / warm ionized phases ($10^{5\sim7}$ k). Meanwhile, the IGM becomes more diffused ($10^{-6} \sim 10^{-4}$ cm^{-3}) due to cosmological expansion.

In general, it is easier to probe the cool and dense gases than the hot and diffused ones. The column densities of elements in a gas cloud can be inferred from the curve of growth using their spectral absorption lines widths. In a moderately-ionized cool/ warm gas, a wide range of possible absorption lines are available, while in a highly-ionized hot gas, the choice is limited as more atoms are already in the highly-excited states. In the past, warm and hot ionized IGM / CGM have been observed mostly from X-ray (emission / absorption lines, total X-ray luminosity) and the Sunyaev-Zeld'ovich Effect (SZE) in the millimeter and sub-millimeter bands. The SZE effect is observed by the change of brightness of the CMB behind hot plasma due to Compton Scattering. FRB provides a new probe to the ionized plasma in all temperatures.

The observation is difficult around the reionization epoch since (1) there is no bright background sources and (2) fewer photons can be collected due to the high redshift.

In the intermediate redshift, the ionized HI and HeII in the IGM can be effectively measured by the Lyα forest due to (1) the suitable gas density range and relatively cool temperature, (2) the abundance of bright background quasars, and since (3) the Lyα line is redshifted into the optical band. Metal absorption lines, such as Si[II][III] and O[II][III], can also be used to infer the redshifts of the Lyα absorbers.

At lower redshift, Lyα becomes less effective since the IGM is more diffused and the optical depth is too low ($\tau = 0.016(1 + z)^{1.1}$ at z < 1.2, cite Meiksin 2006). Moreover, it is more difficult to probe baryons in the shock-heated HIM as less absorptive features are available (the "missing baryons problem"). In addition, X-ray observation could by limited by the emissivity, which is temperature-dependent.

For CGMs and ICM, the observational methods and difficulties are similar. For high redshift CGMs, spectra of multiple galaxies with similar properties and redshift could be stacked to increase the SNR of the spectroscopic measurements.

While most of the current observational methods measure baryons in neutral or lower energy states in the IGM / CMGs, FRBs can be used to probe the total ionized baryon mass in all temperatures along the LoS. For FRBs localized to a single host galaxies, the source distance can be measured from the host's spectroscopic redshift, producing good estimations of the DM-z relation [28]. Cautions have to be taken since (1) the precision of widely-used models such as `NE2001` or `YMW16` also vary by location, (2) overall $\mathrm{DM_{host}}$ might be estimated from some of the host features, but the location of the FRB source within the host is difficult to measure and so is the portion of $\mathrm{DM_{host}}$ in the foreground of the FRB, and (3) DM contribution from intervening galaxy and ICM needs to be considered.

References

[1] A. Hewish, S. J. Bell, J. D. H. Pilkington, P. F. Scott, and R. A. Collins. Observation of a Rapidly Pulsating Radio Source. *Nature*, 217(5130):709–713, February 1968. doi: 10.1038/217709a0.

[2] Stirling A. Colgate and Peter D. Noerdlinger. Coherent Emission from Expanding Supernova Shells. *ApJ*, 165:509, May 1971. doi: 10.1086/150918.

[3] S. Phinney and J. H. Taylor. A sensitive search for radio pulses from primordial black holes and distant Supernovae. *Nature*, 277(5692):117–118, January 1979. doi: 10.1038/277117a0.

[4] S. Cortiglioni, N. Mandolesi, G. Morigi, A. Ciapi, P. Inzani, and G. Sironi. A Systematic Search for Radio Pulses Associated with Gamma-Ray Bursts. *Ap&SS*, 75(1):153–161, March 1981. doi: 10.1007/BF00651392.

[5] David J. Nice. Radio Pulses along the Galactic Plane. *ApJ*, 513(2):927–932, March 1999. doi: 10.1086/306898.

[6] Simon Johnston and Roger W. Romani. Giant Pulses from PSR B0540-69 in the Large Magellanic Cloud. *ApJ*, 590(2):L95–L98, June 2003. doi: 10.1086/376826.

[7] M. A. McLaughlin, A. G. Lyne, D. R. Lorimer, M. Kramer, A. J. Faulkner, R. N. Manchester, J. M. Cordes, F. Camilo, A. Possenti, I. H. Stairs, G. Hobbs, N. D'Amico, M. Burgay, and J. T. O'Brien. Transient radio bursts from rotating neutron stars. *Nature*, 439(7078):817–820, February 2006. doi: 10.1038/nature04440.

[8] K. Nimmo, J. W. T. Hessels, F. Kirsten, A. Keimpema, J. M. Cordes, M. P. Snelders, D. M. Hewitt, R. Karuppusamy, A. M. Archibald, V. Bezrukovs, M. Bhardwaj, R. Blaauw, S. T. Buttaccio, T. Cassanelli, J. E. Conway, A. Corongiu, R. Feiler, E. Fonseca, O. Forssén, M. Gawroński, M. Giroletti, M. A. Kharinov, C. Leung, M. Lindqvist, G. Maccaferri, B. Marcote, K. W. Masui, R. Mckinven, A. Melnikov, D. Michilli, A. G. Mikhailov, C. Ng, A. Orbidans, O. S. Ould-Boukattine, Z. Paragi, A. B. Pearlman, E. Petroff, M. Rahman, P. Scholz, K. Shin, K. M. Smith, I. H. Stairs, G. Surcis, S. P. Tendulkar, W. Vlemmings, N. Wang, J. Yang, and J. P. Yuan. Burst timescales and luminosities as links between young pulsars and fast radio bursts. *Nature Astronomy*, 6:393–401, February 2022. doi: 10.1038/s41550-021-01569-9.

[9] D. R. Lorimer, M. Bailes, M. A. McLaughlin, D. J. Narkevic, and F. Crawford. A Bright Millisecond Radio Burst of Extragalactic Origin. *Science*, 318(5851): 777, November 2007. doi: 10.1126/science.1147532.

[10] J. M. Cordes and M. A. McLaughlin. Searches for Fast Radio Transients. *ApJ*, 596(2):1142–1154, October 2003. doi: 10.1086/378231.

[11] E. Petroff, J. W. T. Hessels, and D. R. Lorimer. Fast radio bursts. *A&A Rev.*, 27(1):4, May 2019. doi: 10.1007/s00159-019-0116-6.

[12] D. Michilli, K. W. Masui, R. Mckinven, D. Cubranic, M. Bruneault, C. Brar, C. Patel, P. J. Boyle, I. H. Stairs, A. Renard, K. Bandura, S. Berger, D. Breitman, T. Cassanelli, M. Dobbs, V. M. Kaspi, C. Leung, J. Mena-Parra, Z. Pleunis, L. Russell, P. Scholz, S. R. Siegel, S. P. Tendulkar, and K. Vanderlinde. An Analysis Pipeline for CHIME/FRB Full-array Baseband Data. *ApJ*, 910(2): 147, April 2021. doi: 10.3847/1538-4357/abe626.

[13] Bridget C. Chime/Frb Collaboration, Andersen, Kevin Bandura, Mohit Bhardwaj, P. J. Boyle, Charanjot Brar, Daniela Breitman, Tomas Cassanelli, Shami Chatterjee, Pragya Chawla, Jean-François Cliche, Davor Cubranic, Alice P. Curtin, Meiling Deng, Matt Dobbs, Fengqiu Adam Dong, Emmanuel Fonseca, B. M. Gaensler, Utkarsh Giri, Deborah C. Good, Alex S. Hill, Alexander Josephy, J. F. Kaczmarek, Zarif Kader, Joseph Kania, Victoria M. Kaspi, Calvin Leung, D. Z. Li, Hsiu-Hsien Lin, Kiyoshi W. Masui, Ryan McKinven, Juan Mena-Parra, Marcus Merryfield, B. W. Meyers, D. Michilli, Arun Naidu, Laura Newburgh, C. Ng, Anna Ordog, Chitrang Patel, Aaron B. Pearlman, Ue-Li Pen, Emily Petroff, Ziggy Pleunis, Masoud Rafiei-Ravandi, Mubdi Rahman, Scott Ransom, Andre Renard, Pranav Sanghavi, Paul Scholz, J. Richard Shaw, Kaitlyn Shin, Seth R. Siegel, Saurabh Singh, Kendrick Smith, Ingrid Stairs, Chia Min Tan, Shriharsh P. Tendulkar, Keith Vanderlinde, D. V. Wiebe, Dallas Wulf, and Andrew Zwaniga. Sub-second periodicity in a fast radio burst. *Nature*, 607(7918):256–259, July 2022. doi: 10.1038/s41586-022-04841-8.

[14] Wenbin Lu and Pawan Kumar. On the radiation mechanism of repeating fast radio bursts. *MNRAS*, 477(2):2470–2493, June 2018. doi: 10.1093/mnras/sty716.

[15] Z. Pleunis, D. Michilli, C. G. Bassa, J. W. T. Hessels, A. Naidu, B. C. Andersen, P. Chawla, E. Fonseca, A. Gopinath, V. M. Kaspi, V. I. Kondratiev, D. Z. Li, M. Bhardwaj, P. J. Boyle, C. Brar, T. Cassanelli, Y. Gupta, A. Josephy, R. Karuppusamy, A. Keimpema, F. Kirsten, C. Leung, B. Marcote, K. W. Masui, R. Mckinven, B. W. Meyers, C. Ng, K. Nimmo, Z. Paragi, M. Rahman, P. Scholz, K. Shin, K. M. Smith, I. H. Stairs, and S. P. Tendulkar. LOFAR Detection of 110-188 MHz Emission and Frequency-dependent Activity from FRB 20180916B. *ApJ*, 911(1):L3, April 2021. doi: 10.3847/2041-8213/abec72.

[16] V. Gajjar, A. P. V. Siemion, D. C. Price, C. J. Law, D. Michilli, J. W. T. Hessels, S. Chatterjee, A. M. Archibald, G. C. Bower, C. Brinkman, S. Burke-Spolaor, J. M. Cordes, S. Croft, J. Emilio Enriquez, G. Foster, N. Gizani, G. Hellbourg, H. Isaacson, V. M. Kaspi, T. J. W. Lazio, M. Lebofsky, R. S. Lynch, D. MacMahon, M. A. McLaughlin, S. M. Ransom, P. Scholz, A. Seymour, L. G. Spitler, S. P. Tendulkar, D. Werthimer, and Y. G. Zhang. Highest Frequency Detection of FRB 121102 at 4-8 GHz Using the Breakthrough Listen Digital Backend at the Green Bank Telescope. *ApJ*, 863(1):2, August 2018. doi: 10.3847/1538-4357/aad005.

[17] L. G. Spitler, P. Scholz, J. W. T. Hessels, S. Bogdanov, A. Brazier, F. Camilo, S. Chatterjee, J. M. Cordes, F. Crawford, J. Deneva, R. D. Ferdman, P. C. C. Freire, V. M. Kaspi, P. Lazarus, R. Lynch, E. C. Madsen, M. A. McLaughlin, C. Patel, S. M. Ransom, A. Seymour, I. H. Stairs, B. W. Stappers, J. van Leeuwen, and W. W. Zhu. A repeating fast radio burst. *Nature*, 531(7593): 202–205, March 2016. doi: 10.1038/nature17168.

[18] Chime/Frb Collaboration, Bridget C. Andersen, Kevin Bandura, Mohit Bhardwaj, P. J. Boyle, Charanjot Brar, Tomas Cassanelli, S. Chatterjee, Pragya Chawla, Amanda M. Cook, Alice P. Curtin, Matt Dobbs, Fengqiu Adam Dong, Jakob T. Faber, Mateus Fandino, Emmanuel Fonseca, B. M. Gaensler, Utkarsh Giri, Antonio Herrera-Martin, Alex S. Hill, Adaeze Ibik, Alexander Josephy, Jane F. Kaczmarek, Zarif Kader, Victoria Kaspi, T. L. Landecker, Adam E. Lanman, Mattias Lazda, Calvin Leung, Hsiu-Hsien Lin, Kiyoshi W. Masui, Ryan McKinven, Juan Mena-Parra, Bradley W. Meyers, D. Michilli, Cherry Ng, Ayush Pandhi, Aaron B. Pearlman, Ue-Li Pen, Emily Petroff, Ziggy Pleunis, Masoud Rafiei-Ravandi, Mubdi Rahman, Scott M. Ransom, Andre Renard, Ketan R. Sand, Pranav Sanghavi, Paul Scholz, Vishwangi Shah, Kaitlyn Shin, Seth Siegel, Kendrick Smith, Ingrid Stairs, Jianing Su, Shriharsh P. Tendulkar, Keith Vanderlinde, Haochen Wang, Dallas Wulf, and Andrew Zwaniga. CHIME/FRB Discovery of 25 Repeating Fast Radio Burst Sources. *ApJ*, 947(2):83, April 2023. doi: 10.3847/1538-4357/acc6c1.

[19] S. Chatterjee, C. J. Law, R. S. Wharton, S. Burke-Spolaor, J. W. T. Hessels, G. C. Bower, J. M. Cordes, S. P. Tendulkar, C. G. Bassa, P. Demorest, B. J. Butler, A. Seymour, P. Scholz, M. W. Abruzzo, S. Bogdanov, V. M. Kaspi, A. Keimpema, T. J. W. Lazio, B. Marcote, M. A. McLaughlin, Z. Paragi, S. M. Ransom, M. Rupen, L. G. Spitler, and H. J. van Langevelde. A direct localization of a fast radio burst and its host. *Nature*, 541(7635):58–61, January 2017. doi: 10.1038/nature20797.

[20] C. H. Niu, K. Aggarwal, D. Li, X. Zhang, S. Chatterjee, C. W. Tsai, W. Yu, C. J. Law, S. Burke-Spolaor, J. M. Cordes, Y. K. Zhang, S. K. Ocker, J. M. Yao, P. Wang, Y. Feng, Y. Niino, C. Bochenek, M. Cruces, L. Connor, J. A. Jiang, S. Dai, R. Luo, G. D. Li, C. C. Miao, J. R. Niu, R. Anna-Thomas, J. Sydnor, D. Stern, W. Y. Wang, M. Yuan, Y. L. Yue, D. J. Zhou, Z. Yan, W. W. Zhu, and B. Zhang. A repeating fast radio burst associated with a persistent radio source. *Nature*, 606(7916):873–877, June 2022. doi: 10.1038/s41586-022-04755-5.

[21] Chime/Frb Collaboration, M. Amiri, B. C. Andersen, K. M. Bandura, M. Bhardwaj, P. J. Boyle, C. Brar, P. Chawla, T. Chen, J. F. Cliche, D. Cubranic, M. Deng, N. T. Denman, M. Dobbs, F. Q. Dong, M. Fandino, E. Fonseca, B. M. Gaensler, U. Giri, D. C. Good, M. Halpern, J. W. T. Hessels, A. S. Hill, C. Höfer, A. Josephy, J. W. Kania, R. Karuppusamy, V. M. Kaspi, A. Keimpema, F. Kirsten, T. L. Landecker, D. A. Lang, C. Leung, D. Z. Li, H. H. Lin, B. Marcote, K. W. Masui, R. McKinven, J. Mena-Parra, M. Merryfield, D. Michilli, N. Milutinovic, A. Mirhosseini, A. Naidu, L. B. Newburgh, C. Ng, K. Nimmo, Z. Paragi, C. Patel, U. L. Pen, T. Pinsonneault-Marotte, Z. Pleunis, M. Rafiei-Ravandi, M. Rahman, S. M. Ransom, A. Renard, P. Sanghavi, P. Scholz, J. R. Shaw, K. Shin, S. R. Siegel, S. Singh, R. J. Smegal, K. M. Smith, I. H. Stairs, S. P. Tendulkar, I. Tretyakov, K. Vanderlinde, H. Wang, X. Wang, D. Wulf, P. Yadav, and A. V. Zwaniga. Periodic activity from a fast radio burst source. *Nature*, 582(7812):351–355, June 2020. doi: 10.1038/s41586-020-2398-2.

[22] Vikram Ravi. The prevalence of repeating fast radio bursts. *Nature Astronomy*, 3:928–931, July 2019. doi: 10.1038/s41550-019-0831-y.

[23] K. M. Rajwade, M. B. Mickaliger, B. W. Stappers, V. Morello, D. Agarwal, C. G. Bassa, R. P. Breton, M. Caleb, A. Karastergiou, E. F. Keane, and D. R. Lorimer. Possible periodic activity in the repeating FRB 121102. *MNRAS*, 495(4):3551–3558, July 2020. doi: 10.1093/mnras/staa1237.

[24] D. J. Zhou, J. L. Han, B. Zhang, K. J. Lee, W. W. Zhu, D. Li, W. C. Jing, W. Y. Wang, Y. K. Zhang, J. C. Jiang, J. R. Niu, R. Luo, H. Xu, C. F. Zhang, B. J. Wang, J. W. Xu, P. Wang, Z. L. Yang, and Y. Feng. FAST Observations of an Extremely Active Episode of FRB 20201124A: I. Burst Morphology. *Research in Astronomy and Astrophysics*, 22(12):124001, December 2022. doi: 10.1088/1674-4527/ac98f8.

[25] David Eichler. Nanolensed Fast Radio Bursts. *ApJ*, 850(2):159, December 2017. doi: 10.3847/1538-4357/aa8b70.

[26] Vikram Ravi, Nicholas Battaglia, Sarah Burke-Spolaor, Shami Chatterjee, James Cordes, Gregg Hallinan, Casey Law, T. Joseph W. Lazio, Kiyoshi Masui, Matthew McQuinn, Julian B. Muñoz, Nipuni Palliyaguru, J. Xavier Prochaska, Andrew Seymour, Harish Vedantham, and Yong Zheng. Fast Radio Burst Tomography of the Unseen Universe. *BAAS*, 51(3):420, May 2019.

[27] J. Xavier Prochaska, Jean-Pierre Macquart, Matthew McQuinn, Sunil Simha, Ryan M. Shannon, Cherie K. Day, Lachlan Marnoch, Stuart Ryder, Adam Deller, Keith W. Bannister, Shivani Bhandari, Rongmon Bordoloi, John Bunton, Hyerin Cho, Chris Flynn, Elizabeth K. Mahony, Chris Phillips, Hao Qiu, and Nicolas Tejos. The low density and magnetization of a massive galaxy halo exposed by a fast radio burst. *Science*, 366(6462):231–234, Oct 2019. doi: 10.1126/science.aay0073.

[28] B. Marcote, K. Nimmo, J. W. T. Hessels, S. P. Tendulkar, C. G. Bassa, Z. Paragi, A. Keimpema, M. Bhardwaj, R. Karuppusamy, V. M. Kaspi, C. J. Law, D. Michilli, K. Aggarwal, B. Andersen, A. M. Archibald, K. Bandura, G. C. Bower, P. J. Boyle, C. Brar, S. Burke-Spolaor, B. J. Butler, T. Cassanelli, P. Chawla, P. Demorest, M. Dobbs, E. Fonseca, U. Giri, D. C. Good, K. Gourdji, A. Josephy, A. Yu. Kirichenko, F. Kirsten, T. L. Landecker, D. Lang, T. J. W. Lazio, D. Z. Li, H. H. Lin, J. D. Linford, K. Masui, J. Mena-Parra, A. Naidu, C. Ng, C. Patel, U. L. Pen, Z. Pleunis, M. Rafiei-Ravandi, M. Rahman, A. Renard, P. Scholz, S. R. Siegel, K. M. Smith, I. H. Stairs, K. Vanderlinde, and A. V. Zwaniga. A repeating fast radio burst source localized to a nearby spiral galaxy. *Nature*, 577(7789):190–194, Jan 2020. doi: 10.1038/s41586-019-1866-z.

[29] M. Bhardwaj, B. M. Gaensler, V. M. Kaspi, T. L. Landecker, R. Mckinven, D. Michilli, Z. Pleunis, S. P. Tendulkar, B. C. Andersen, P. J. Boyle, T. Cassanelli, P. Chawla, A. Cook, M. Dobbs, E. Fonseca, J. Kaczmarek, C. Leung, K. Masui, M. Mnchmeyer, C. Ng, M. Rafiei-Ravandi, P. Scholz, K. Shin, K. M. Smith, I. H. Stairs, and A. V. Zwaniga. A Nearby Repeating Fast Radio Burst in the Direction of M81. *ApJ*, 910(2):L18, April 2021. doi: 10.3847/2041-8213/abeaa6.

[30] Kritti Sharma, Jean Somalwar, Casey Law, Vikram Ravi, Morgan Catha, Ge Chen, Liam Connor, Jakob T. Faber, Gregg Hallinan, Charlie Harnach, Greg Hellbourg, Rick Hobbs, David Hodge, Mark Hodges, James W. Lamb, Paul Rasmussen, Myles B. Sherman, Jun Shi, Dana Simard, Reynier Squillace, Sander Weinreb, David P. Woody, and Nitika Yadlapalli. Deep Synoptic Array science: A massive elliptical host among two galaxy-cluster fast radio bursts. *arXiv e-prints*, art. arXiv:2302.14782, February 2023. doi: 10.48550/arXiv.2302.14782.

[31] Bing Zhang. The physical mechanisms of fast radio bursts. *Nature*, 587(7832): 45–53, November 2020. doi: 10.1038/s41586-020-2828-1.

[32] Bing Zhang. The Physics of Fast Radio Bursts. *arXiv e-prints*, art. arXiv:2212.03972, December 2022. doi: 10.48550/arXiv.2212.03972.

[33] R. Luo, B. J. Wang, Y. P. Men, C. F. Zhang, J. C. Jiang, H. Xu, W. Y. Wang, K. J. Lee, J. L. Han, B. Zhang, R. N. Caballero, M. Z. Chen, X. L. Chen, H. Q. Gan, Y. J. Guo, L. F. Hao, Y. X. Huang, P. Jiang, H. Li, J. Li, Z. X. Li, J. T. Luo, J. Pan, X. Pei, L. Qian, J. H. Sun, M. Wang, N. Wang, Z. G. Wen, R. X. Xu, Y. H. Xu, J. Yan, W. M. Yan, D. J. Yu, J. P. Yuan, S. B. Zhang, and Y. Zhu. Diverse polarization angle swings from a repeating fast radio burst source. *Nature*, 586 (7831):693–696, October 2020. doi: 10.1038/s41586-020-2827-2.

[34] Victoria M. Kaspi and Michael Kramer. Radio Pulsars: The Neutron Star Population & Fundamental Physics. *arXiv e-prints*, art. arXiv:1602.07738, February 2016. doi: 10.48550/arXiv.1602.07738.

[35] Victoria M. Kaspi and Andrei M. Beloborodov. Magnetars. *ARA&A*, 55(1): 261–301, August 2017. doi: 10.1146/annurev-astro-081915-023329.

[36] D. R. Lorimer and M. Kramer. *Handbook of Pulsar Astronomy*, volume 4. 2004.

[37] E. V. Gotthelf, J. P. Halpern, and J. Alford. The Spin-down of PSR J0821-4300 and PSR J1210-5226: Confirmation of Central Compact Objects as Anti-magnetars. *ApJ*, 765(1):58, March 2013. doi: 10.1088/0004-637X/765/1/58.

[38] Mareki Honma, Takumi Nagayama, Kazuma Ando, Takeshi Bushimata, Yoon Kyung Choi, Toshihiro Handa, Tomoya Hirota, Hiroshi Imai, Takaaki Jike, Mi Kyoung Kim, Osamu Kameya, Noriyuki Kawaguchi, Hideyuki Kobayashi, Tomoharu Kurayama, Seisuke Kuji, Naoko Matsumoto, Seiji Manabe, Takeshi Miyaji, Kazuhito Motogi, Akiharu Nakagawa, Hiroyuki Nakanishi, Kotaro Niinuma, Chung Sik Oh, Toshihiro Omodaka, Tomoaki Oyama, Nobuyuki Sakai, Katsuhisa Sato, Mayumi Sato, Katsunori M. Shibata, Satoshi Shiozaki, Kazuyoshi Sunada, Yoshiaki Tamura, Yuji Ueno, and Aya Yamauchi. Fundamental Parameters of the Milky Way Galaxy Based on VLBI astrometry. *PASJ*, 64:136, December 2012. doi: 10.1093/pasj/64.6.136.

[39] Anne M. Archibald, Victoria M. Kaspi, Margaret A. Livingstone, and Maura A. McLaughlin. No Detectable Radio Emission from the Magnetar-Like Pulsar in Kes 75. *ApJ*, 688(1):550–554, November 2008. doi: 10.1086/591661.

[40] V. S. Dhillon, T. R. Marsh, S. P. Littlefair, C. M. Copperwheat, R. D. G. Hickman, P. Kerry, A. J. Levan, N. Rea, C. D. J. Savoury, N. R. Tanvir, R. Turolla, and K. Wiersema. The first observation of optical pulsations from a soft gamma repeater: SGR 0501+4516. *MNRAS*, 416(1):L16–L20, September 2011. doi: 10.1111/j.1745-3933.2011.01088.x.

[41] R. M. Shannon and S. Johnston. Radio properties of the magnetar near Sagittarius a* from observations with the australia telescope compact array. *MNRAS*, 435:L29–L32, August 2013. doi: 10.1093/mnrasl/slt088.

[42] Gabriele Ghisellini and Roland Svensson. The synchrotron and cyclo-synchrotron absorption cross-section. *MNRAS*, 252:313–318, October 1991. doi: 10.1093/mnras/252.3.313.

[43] Ge Chen, Vikram Ravi, and Wenbin Lu. The Multiwavelength Counterparts of Fast Radio Bursts. *ApJ*, 897(2):146, July 2020. doi: 10.3847/1538-4357/ab982b.

[44] Brian D. Metzger, Ben Margalit, and Lorenzo Sironi. Fast radio bursts as synchrotron maser emission from decelerating relativistic blast waves. *MNRAS*, 485(3):4091–4106, May 2019. doi: 10.1093/mnras/stz700.

[45] Navin Sridhar, Brian D. Metzger, Paz Beniamini, Ben Margalit, Mathieu Renzo, Lorenzo Sironi, and Konstantinos Kovlakas. Periodic Fast Radio Bursts from Luminous X-ray Binaries. *ApJ*, 917(1):13, August 2021. doi: 10.3847/1538-4357/ac0140.

[46] Bing Zhang. A "Cosmic Comb" Model of Fast Radio Bursts. *ApJ*, 836(2): L32, February 2017. doi: 10.3847/2041-8213/aa5ded.

[47] Lin Lin, Ersin Göğüş, Oliver J. Roberts, Matthew G. Baring, Chryssa Kouveliotou, Yuki Kaneko, Alexander J. van der Horst, and George Younes. Fermi/GBM View of the 2019 and 2020 Burst Active Episodes of SGR J1935+2154. *ApJ*, 902(2):L43, October 2020. doi: 10.3847/2041-8213/abbefe.

[48] Wenbin Lu, Pawan Kumar, and Bing Zhang. A unified picture of Galactic and cosmological fast radio bursts. *MNRAS*, 498(1):1397–1405, October 2020. doi: 10.1093/mnras/staa2450.

[49] J. P. Macquart, J. X. Prochaska, M. McQuinn, K. W. Bannister, S. Bhandari, C. K. Day, A. T. Deller, R. D. Ekers, C. W. James, L. Marnoch, S. Osłowski, C. Phillips, S. D. Ryder, D. R. Scott, R. M. Shannon, and N. Tejos. A census of baryons in the Universe from localized fast radio bursts. *Nature*, 581(7809): 391–395, May 2020. doi: 10.1038/s41586-020-2300-2.

[50] Tetsuya Hashimoto, Tomotsugu Goto, Ting-Yi Lu, Alvina Y. L. On, Daryl Joe D. Santos, Seong Jin Kim, Ece Kilerci Eser, Simon C. C. Ho, Tiger Y. Y. Hsiao, and Leo Y. W. Lin. Revealing the cosmic reionization history with fast radio bursts in the era of Square Kilometre Array. *MNRAS*, 502(2):2346–2355, April 2021. doi: 10.1093/mnras/stab186.

[51] Anthony Walters, Amanda Weltman, B. M. Gaensler, Yin-Zhe Ma, and Amadeus Witzemann. Future Cosmological Constraints From Fast Radio Bursts. *ApJ*, 856(1):65, March 2018. doi: 10.3847/1538-4357/aaaf6b.

[52] A. Fialkov and A. Loeb. Constraining the CMB optical depth through the dispersion measure of cosmological radio transients. *J. Cosmology Astropart. Phys.*, 2016(5):004, May 2016. doi: 10.1088/1475-7516/2016/05/004.

[53] F. Vazza, M. Brüggen, P. M. Hinz, D. Wittor, N. Locatelli, and C. Gheller. Probing the origin of extragalactic magnetic fields with Fast Radio Bursts. *MNRAS*, 480(3):3907–3915, November 2018. doi: 10.1093/mnras/sty1968.

[54] Robert Reischke, Steffen Hagstotz, and Robert Lilow. Probing primordial non-Gaussianity with fast radio bursts. *Phys. Rev. D*, 103(2):023517, January 2021. doi: 10.1103/PhysRevD.103.023517.

[55] Luca Bonetti, John Ellis, Nikolaos E. Mavromatos, Alexander S. Sakharov, Edward K. Sarkisyan-Grinbaum, and Alessandro D. A. M. Spallicci. Photon mass limits from fast radio bursts. *Physics Letters B*, 757:548–552, June 2016. doi: 10.1016/j.physletb.2016.04.035.

[56] V. Ravi, R. M. Shannon, M. Bailes, K. Bannister, S. Bhandari, N. D. R. Bhat, S. Burke-Spolaor, M. Caleb, C. Flynn, A. Jameson, S. Johnston, E. F. Keane, M. Kerr, C. Tiburzi, A. V. Tuntsov, and H. K. Vedantham. The magnetic field and turbulence of the cosmic web measured using a brilliant fast radio burst. *Science*, 354(6317):1249–1252, December 2016. doi: 10.1126/science.aaf6807.

[57] J. Xavier Prochaska and Yong Zheng. Probing Galactic haloes with fast radio bursts. *MNRAS*, 485(1):648–665, May 2019. doi: 10.1093/mnras/stz261.

[58] E. Petroff, J. W. T. Hessels, and D. R. Lorimer. Fast radio bursts at the dawn of the 2020s. *A&A Rev.*, 30(1):2, December 2022. doi: 10.1007/s00159-022-00139-w.

[59] Liam Connor, Vikram Ravi, Morgan Catha, Ge Chen, Jakob T. Faber, James W. Lamb, Gregg Hallinan, Charlie Harnach, Greg Hellbourg, Rick Hobbs, David Hodge, Mark Hodges, Casey Law, Paul Rasmussen, Jack Sayers, Kritti Sharma, Myles B. Sherman, Jun Shi, Dana Simard, Jean Somalwar, Reynier Squillace, Sander Weinreb, David P. Woody, and Nitika Yadlapalli. Deep Synoptic Array science: Two fast radio burst sources in massive galaxy clusters. *arXiv e-prints*, art. arXiv:2302.14788, February 2023. doi: 10.48550/arXiv.2302.14788.

[60] Planck Collaboration, P. A. R. Ade, N. Aghanim, M. Arnaud, M. Ashdown, J. Aumont, C. Baccigalupi, A. J. Banday, R. B. Barreiro, J. G. Bartlett, N. Bartolo, E. Battaner, R. Battye, K. Benabed, A. Benoît, A. Benoit-Lévy, J. P. Bernard, M. Bersanelli, P. Bielewicz, J. J. Bock, A. Bonaldi, L. Bonavera, J. R. Bond, J. Borrill, F. R. Bouchet, F. Boulanger, M. Bucher, C. Burigana, R. C. Butler, E. Calabrese, J. F. Cardoso, A. Catalano, A. Challinor, A. Chamballu, R. R. Chary, H. C. Chiang, J. Chluba, P. R. Christensen, S. Church, D. L. Clements, S. Colombi, L. P. L. Colombo, C. Combet, A. Coulais, B. P. Crill,

A. Curto, F. Cuttaia, L. Danese, R. D. Davies, R. J. Davis, P. de Bernardis, A. de Rosa, G. de Zotti, J. Delabrouille, F. X. Désert, E. Di Valentino, C. Dickinson, J. M. Diego, K. Dolag, H. Dole, S. Donzelli, O. Doré, M. Douspis, A. Ducout, J. Dunkley, X. Dupac, G. Efstathiou, F. Elsner, T. A. Enßlin, H. K. Eriksen, M. Farhang, J. Fergusson, F. Finelli, O. Forni, M. Frailis, A. A. Fraisse, E. Franceschi, A. Frejsel, S. Galeotta, S. Galli, K. Ganga, C. Gauthier, M. Gerbino, T. Ghosh, M. Giard, Y. Giraud-Héraud, E. Giusarma, E. Gjerløw, J. González-Nuevo, K. M. Górski, S. Gratton, A. Gregorio, A. Gruppuso, J. E. Gudmundsson, J. Hamann, F. K. Hansen, D. Hanson, D. L. Harrison, G. Helou, S. Henrot-Versillé, C. Hernández-Monteagudo, D. Herranz, S. R. Hildebrandt, E. Hivon, M. Hobson, W. A. Holmes, A. Hornstrup, W. Hovest, Z. Huang, K. M. Huffenberger, G. Hurier, A. H. Jaffe, T. R. Jaffe, W. C. Jones, M. Juvela, E. Keihänen, R. Keskitalo, T. S. Kisner, R. Kneissl, J. Knoche, L. Knox, M. Kunz, H. Kurki-Suonio, G. Lagache, A. Lähteenmäki, J. M. Lamarre, A. Lasenby, M. Lattanzi, C. R. Lawrence, J. P. Leahy, R. Leonardi, J. Lesgourgues, F. Levrier, A. Lewis, M. Liguori, P. B. Lilje, M. Linden-Vørnle, M. López-Caniego, P. M. Lubin, J. F. Macías-Pérez, G. Maggio, D. Maino, N. Mandolesi, A. Mangilli, A. Marchini, M. Maris, P. G. Martin, M. Martinelli, E. Martínez-González, S. Masi, S. Matarrese, P. McGehee, P. R. Meinhold, A. Melchiorri, J. B. Melin, L. Mendes, A. Mennella, M. Migliaccio, M. Millea, S. Mitra, M. A. Miville-Deschênes, A. Moneti, L. Montier, G. Morgante, D. Mortlock, A. Moss, D. Munshi, J. A. Murphy, P. Naselsky, F. Nati, P. Natoli, C. B. Netterfield, H. U. Nørgaard-Nielsen, F. Noviello, D. Novikov, I. Novikov, C. A. Oxborrow, F. Paci, L. Pagano, F. Pajot, R. Paladini, D. Paoletti, B. Partridge, F. Pasian, G. Patanchon, T. J. Pearson, O. Perdereau, L. Perotto, F. Perrotta, V. Pettorino, F. Piacentini, M. Piat, E. Pierpaoli, D. Pietrobon, S. Plaszczynski, E. Pointecouteau, G. Polenta, L. Popa, G. W. Pratt, G. Prézeau, S. Prunet, J. L. Puget, J. P. Rachen, W. T. Reach, R. Rebolo, M. Reinecke, M. Remazeilles, C. Renault, A. Renzi, I. Ristorcelli, G. Rocha, C. Rosset, M. Rossetti, G. Roudier, B. Rouillé d'Orfeuil, M. Rowan-Robinson, J. A. Rubiño-Martín, B. Rusholme, N. Said, V. Salvatelli, L. Salvati, M. Sandri, D. Santos, M. Savelainen, G. Savini, D. Scott, M. D. Seiffert, P. Serra, E. P. S. Shellard, L. D. Spencer, M. Spinelli, V. Stolyarov, R. Stompor, R. Sudiwala, R. Sunyaev, D. Sutton, A. S. Suur-Uski, J. F. Sygnet, J. A. Tauber, L. Terenzi, L. Toffolatti, M. Tomasi, M. Tristram, T. Trombetti, M. Tucci, J. Tuovinen, M. Türler, G. Umana, L. Valenziano, J. Valiviita, F. Van Tent, P. Vielva, F. Villa, L. A. Wade, B. D. Wandelt, I. K. Wehus, M. White, S. D. M. White, A. Wilkinson, D. Yvon, A. Zacchei, and A. Zonca. Planck 2015 results. XIII. Cosmological parameters. *A&A*, 594:A13, September 2016. doi: 10.1051/0004-6361/201525830.

[61] J. M. Cordes and T. J. W. Lazio. NE2001.I. A New Model for the Galactic Distribution of Free Electrons and its Fluctuations. *arXiv e-prints*, art. astro-ph/0207156, July 2002. doi: 10.48550/arXiv.astro-ph/0207156.

[62] J. M. Yao, R. N. Manchester, and N. Wang. A New Electron-density Model for Estimation of Pulsar and FRB Distances. *ApJ*, 835(1):29, January 2017. doi: 10.3847/1538-4357/835/1/29.

[63] R. W. Romani, R. Narayan, and R. Blandford. Refractive effects in pulsar scintillation. *MNRAS*, 220:19–49, May 1986. doi: 10.1093/mnras/220.1.19.

[64] James M. Cordes and T. J. Lazio. Interstellar Scattering Effects on the Detection of Narrow-Band Signals. *ApJ*, 376:123, July 1991. doi: 10.1086/170261.

[65] Dana Simard and Vikram Ravi. Scintillation Can Explain the Spectral Structure of the Bright Radio Burst from SGR 1935+2154. *ApJ*, 899(1):L21, August 2020. doi: 10.3847/2041-8213/abaa40.

[66] Mark A. Walker. Interstellar scintillation of compact extragalactic radio sources. *MNRAS*, 294:307–311, February 1998. doi: 10.1046/j.1365-8711.1998.01238.x.

[67] A. R. Taylor, J. M. Stil, and C. Sunstrum. A Rotation Measure Image of the Sky. *ApJ*, 702(2):1230–1236, September 2009. doi: 10.1088/0004-637X/702/2/1230.

[68] Hans Böhringer, Gayoung Chon, and Philipp P. Kronberg. The Cosmic Large-Scale Structure in X-rays (CLASSIX) Cluster Survey. I. Probing galaxy cluster magnetic fields with line of sight rotation measures. *A&A*, 596:A22, November 2016. doi: 10.1051/0004-6361/201628873.

[69] G. H. Hilmarsson, D. Michilli, L. G. Spitler, R. S. Wharton, P. Demorest, G. Desvignes, K. Gourdji, S. Hackstein, J. W. T. Hessels, K. Nimmo, A. D. Seymour, M. Kramer, and R. Mckinven. Rotation Measure Evolution of the Repeating Fast Radio Burst Source FRB 121102. *ApJ*, 908(1):L10, February 2021. doi: 10.3847/2041-8213/abdec0.

[70] D. Michilli, A. Seymour, J. W. T. Hessels, L. G. Spitler, V. Gajjar, A. M. Archibald, G. C. Bower, S. Chatterjee, J. M. Cordes, K. Gourdji, G. H. Heald, V. M. Kaspi, C. J. Law, C. Sobey, E. A. K. Adams, C. G. Bassa, S. Bogdanov, C. Brinkman, P. Demorest, F. Fernandez, G. Hellbourg, T. J. W. Lazio, R. S. Lynch, N. Maddox, B. Marcote, M. A. McLaughlin, Z. Paragi, S. M. Ransom, P. Scholz, A. P. V. Siemion, S. P. Tendulkar, P. van Rooy, R. S. Wharton, and D. Whitlow. An extreme magneto-ionic environment associated with the fast radio burst source FRB 121102. *Nature*, 553(7687):182–185, January 2018. doi: 10.1038/nature25149.

[71] Myles B. Sherman, Liam Connor, Vikram Ravi, Casey Law, Ge Chen, Morgan Catha, Jakob T. Faber, Gregg Hallinan, Charlie Harnach, Greg Hellbourg, Rick Hobbs, David Hodge, Mark Hodges, James W. Lamb, Paul Rasmussen, Kritti Sharma, Jun Shi, Dana Simard, Jean Somalwar, Reynier Squillace, Sander Weinreb, David P. Woody, and Nitika Yadlapalli. Deep Synoptic

Array Science: Polarimetry of 25 New Fast Radio Bursts Provides Insights into their Origins. *arXiv e-prints*, art. arXiv:2308.06813, August 2023. doi: 10.48550/arXiv.2308.06813.

[72] P. Kumar, R. M. Shannon, M. E. Lower, S. Bhandari, A. T. Deller, C. Flynn, and E. F. Keane. Circularly polarized radio emission from the repeating fast radio burst source FRB 20201124A. *MNRAS*, 512(3):3400–3413, May 2022. doi: 10.1093/mnras/stac683.

[73] J. M. Cordes and T. J. W. Lazio. NE2001. II. Using Radio Propagation Data to Construct a Model for the Galactic Distribution of Free Electrons. *arXiv e-prints*, art. astro-ph/0301598, January 2003.

[74] Xiao-Hui Sun and Wolfgang Reich. The Galactic halo magnetic field revisited. *Research in Astronomy and Astrophysics*, 10(12):1287–1297, December 2010. doi: 10.1088/1674-4527/10/12/009.

[75] L. Fauvet, J. F. Macías-Pérez, T. R. Jaffe, A. J. Banday, F. X. Désert, and D. Santos. Expected constraints on the Galactic magnetic field using Planck data. *A&A*, 540:A122, April 2012. doi: 10.1051/0004-6361/201016349.

[76] Vikram Ravi, Morgan Catha, Ge Chen, Liam Connor, James M. Cordes, Jakob T. Faber, James W. Lamb, Gregg Hallinan, Charlie Harnach, Greg Hellbourg, Rick Hobbs, David Hodge, Mark Hodges, Casey Law, Paul Rasmussen, Kritti Sharma, Myles B. Sherman, Jun Shi, Dana Simard, Jean J. Somalwar, Reynier Squillace, Sander Weinreb, David P. Woody, and Nitika Yadlapalli. Deep Synoptic Array science: a 50 Mpc fast radio burst constrains the mass of the Milky Way circumgalactic medium. *arXiv e-prints*, art. arXiv:2301.01000, January 2023. doi: 10.48550/arXiv.2301.01000.

[77] Julio F. Navarro, Carlos S. Frenk, and Simon D. M. White. A Universal Density Profile from Hierarchical Clustering. *ApJ*, 490(2):493–508, December 1997. doi: 10.1086/304888.

[78] Ariyeh H. Maller and James S. Bullock. Multiphase galaxy formation: high-velocity clouds and the missing baryon problem. *MNRAS*, 355(3):694–712, December 2004. doi: 10.1111/j.1365-2966.2004.08349.x.

[79] William G. Mathews and J. Xavier Prochaska. Circumgalactic Oxygen Absorption and Feedback. *ApJ*, 846(2):L24, September 2017. doi: 10.3847/2041-8213/aa8861.

[80] Yakov Faerman, Amiel Sternberg, and Christopher F. McKee. Massive Warm/Hot Galaxy Coronae as Probed by UV/X-Ray Oxygen Absorption and Emission. I. Basic Model. *ApJ*, 835(1):52, January 2017. doi: 10.3847/1538-4357/835/1/52.

[81] Drummond Fielding, Eliot Quataert, Michael McCourt, and Todd A. Thompson. The impact of star formation feedback on the circumgalactic medium. *MNRAS*, 466(4):3810–3826, April 2017. doi: 10.1093/mnras/stw3326.

[82] M. Viel, E. Branchini, R. Cen, J. P. Ostriker, S. Matarrese, P. Mazzotta, and B. Tully. Tracing the warm-hot intergalactic medium in the local Universe. *MNRAS*, 360(3):1110–1122, July 2005. doi: 10.1111/j.1365-2966.2005.09097.x.

[83] Uroš Seljak, Alexey Makarov, Patrick McDonald, Scott F. Anderson, Neta A. Bahcall, J. Brinkmann, Scott Burles, Renyue Cen, Mamoru Doi, James E. Gunn, Željko Ivezić, Stephen Kent, Jon Loveday, Robert H. Lupton, Jeffrey A. Munn, Robert C. Nichol, Jeremiah P. Ostriker, David J. Schlegel, Donald P. Schneider, Max Tegmark, Daniel E. Berk, David H. Weinberg, and Donald G. York. Cosmological parameter analysis including SDSS Lyα forest and galaxy bias: Constraints on the primordial spectrum of fluctuations, neutrino mass, and dark energy. *Phys. Rev. D*, 71(10):103515, May 2005. doi: 10.1103/PhysRevD.71.103515.

[84] Matthew McQuinn. The Evolution of the Intergalactic Medium. *ARA&A*, 54: 313–362, September 2016. doi: 10.1146/annurev-astro-082214-122355.

Instrument	Type	Recent feature (Until Jan. 2023)	Future
CHIME	Interforemeter	600+ FRBs reported	Outriggers
ASKAP	Interforemeter	$\approx$ 20 localized FRBs	
DSA-110	Interforemeter	15+ localized FRBs in 2022 (commissioning)	DSA-2000
MeerKAT	Interforemeter	MeerLICHT(optical telescope) co-pointing	
VLA	Interforemeter		
VLBI	Interforemeter		
FAST	Single-dish (D=500m)	Sensitive to faint repeaters	More dishes
Arecibo	Single-dish (D=305m)	Sensitive to faint repeaters	NA
Parkes	Single-dish (D=64m)	Sensitive to faint repeaters	
STARE 2	Single-antenna	Large FoV, good for very bright events	Galactic Radio Explorer (GReX)

Table 1.1: Summary of Recent Radio Instrument in the FRBs Discovery Story

Chapter 2

MULTIWAVELENGTH COUNTERPARTS OF FAST RADIO BURSTS

The work presented in this chapter can be found at:

- Ge Chen, Vikram Ravi and Wenbin Lu. The multiwavelength counterparts of fast radio bursts. *Published in the Astrophysical Journal*, 2020

2.1 Abstract

The engines that produce extragalactic fast radio bursts (FRBs), and the mechanism by which the emission is generated, remain unknown. Many FRB models predict prompt multi-wavelength counterparts, which can be used to refine our knowledge of these fundamentals of the FRB phenomenon. However, several previous targeted searches for prompt FRB counterparts have yielded no detections, and have additionally not reached sufficient sensitivity with respect to the predictions. In this work, we demonstrate a technique to estimate the ratio, η, between the energy outputs of FRB counterparts at various wavelengths and the radio-wavelength emission. Our technique combines the fluence distribution of the FRB population with results from several wide-field blind surveys for fast transients from the optical to the TeV bands. We present constraints on η that improve upon previous observations even in the case that all unclassified transient events in existing surveys are FRB counterparts. In some scenarios for the FRB engine and emission mechanism, we find that FRB counterparts should have already been detected, thus demonstrating that our technique can successfully test predictions for η. However, it is possible that FRB counterparts are lurking amongst catalogs of unclassified transient events. Although our technique is robust to the present uncertainty in the FRB fluence distribution, its ultimate application to accurately estimate or bound η will require the careful analysis of all candidate fast-transient events in multi-wavelength survey data sets.

2.2 Introduction

Fast radio bursts (FRBs) are short ($\sim$ ms) and luminous ($\sim 10^{42}$ erg s^{-1}) radio pulses detected at extragalactic distances. There have been nearly a hundred FRBs reported

[1], and the estimated rate is $\sim 10^3$ sky^{-1} day^{-1} [2]. Five FRB sources have been directly associated with host galaxies, revealing a range of galaxy classes, and source environments [3–7]. Repeat bursts have been observed from 20 FRB sources [8–12], indicating that at least some FRBs originate from non-catastrophic events [see also 13]. The exact FRB emission mechanism(s) and engine(s) remain elusive.

The high brightness temperatures ($\sim 10^{35}$ K) of FRBs require a coherent emission process. Although several astrophysical coherent emission mechanisms are identified with Galactic sources [14], these mechanisms encounter difficulties with the energy scales of FRBs. Two classes of mechanisms have been proposed for FRBs [although see, e.g., 15]: synchrotron masers [e.g., 16–20] and coherent curvature radiation [e.g., 21, 22]. Synchrotron masers require a population inversion in the emitting lepton energy and pitch-angle distribution. This is generally thought to be possible in an ultra-relativistic (bulk Lorentz factor $\Gamma \gg 1$) radiative shock driven into a significantly magnetized plasma (magnetization parameter $\sigma \gtrsim 10^{-3}$); the shock is mediated by Larmor-rotating charges, which results in the population inversion within the shock. The curvature-radiation mechanism instead scales ideas for the generation of pulsar radio emission to FRB energy scales, invoking coherently radiating bunches of relativistic ($\Gamma \sim 30$) leptons accelerated by magnetic reconnection events. These radiation processes are discussed in the context of several progenitor models. The majority of these models involve highly magnetized neutron stars / magnetars, because the short durations and high luminosities of FRBs require compact, active engines with large energy budgets and emission-region field strengths of $\gtrsim 10^{10}$ G.

Several classes of FRB models (emission mechanism and/or engine) predict prompt multi-wavelength counterparts, and specify the ratio between the energy emitted by the counterpart and by the FRB. Synchrotron masers initiated by ultra-relativistic shocks are accompanied by synchrotron emission from fast-cooling shock-heated electrons that cascades through the γ-ray and X-ray bands on sub-second timescales, or perhaps through the optical/NIR bands in the case of an electron-positron plasma upstream of the shock [20]. Specific luminosities comparable to or greater than the FRB luminosities are predicted for the higher-energy emission. Additionally, although the curvature-radiation mechanism does not naturally produce multi-wavelength emission, the mechanism may be triggered by events that do radiate across the electromagnetic spectrum [e.g., the cosmic comb model; 23].

We define the ratio between the energy radiated by an FRB event in a given electro-

magnetic band and in the radio band as

$$\eta(\nu_c) = \frac{F_{Band}}{F_{Radio}} \approx \frac{\nu_{1,Band} \cdot F_{\nu,Band}}{\nu_{1,Radio} \cdot F_{\nu Radio}}. \quad (2.1)$$

Here, ν_c is the central frequency of the band of interest, F_{Radio} and F_{Band} are the band-integrated fluences in the band of interest and the radio band, respectively, $F_{\nu,Radio}$ and $F_{\nu,Band}$ are the specific fluences, and $\nu_{1,Band}$ and $\nu_{1,Radio}$ are the lower-frequency bounds of these two bands. The commonly-made approximation in the second step [24] assumes that the bands span natural-logarithmic frequency intervals, but is accurate in general when the specific fluence scales as $F_\nu \propto \nu^{-2}$, and the band upper-frequency bound ν_2 is much greater than the lower bound ν_1. We also define a fluence ratio as

$$\eta_\nu(\nu_c) = \frac{F_{\nu,Band}}{F_{\nu,Radio}}. \quad (2.2)$$

In this work, we consider how constraints on η and η_ν based on the possible detection, or non-detection, of multiwavelength FRB counterparts can test FRB models.

Until December 2019, no FRB multi-wavelength counterpart has been confirmed. Most previous observational constraints on η are derived from searches for multi-wavelength transient emissions that are close to the FRBs in both time and location (see Section 2.6.2 for references). It is also possible to search for multi-wavelength transient events that are close to the FRBs in location only, but at any time.

In this work, we explore a third method: a blind search of the whole sky for unclassified multi-wavelength transient events at any time. Several surveys across the optical and high-energy bands explore the sky with sub-second time resolution. We develop and demonstrate a method to estimate η by combining relevant multi-wavelength survey parameters with the fluence distribution of the currently observed FRB population. This method can only directly constrain η when the statistics of unclassified short-duration transient events are published. However, these statistics are rarely published. We therefore compare constraints derived assuming no multi-wavelength FRB counterparts have been detected with predictions from FRB emission models. We find in several scenarios that existing surveys are likely / unlikely to have already detected FRB counterparts. For some surveys, we also consider the case where a fraction of their unclassified events are indeed FRB counterparts to derive upper bounds on η.

We propose our method for three reasons. First, a blind search for counterparts is meaningful since some models predict cases where the radio emission from an FRB

is non-detectable while the counterpart is. For example, Metzger et al. [20] show that high-energy counterpart emission may escape a dense medium surrounding the source even when the radio emission is subject to the obscuring effects of scattering and absorption. Second, it is reasonable to make use of the statistical properties of FRBs. The estimated FRB rate above $F_{\nu,0} \sim 2$ Jy ms is $R_0 \approx 1.7 \times 10^3$ sky^{-1}day^{-1} [2], sufficiently large to be treated as a common events for relatively large telescopes scanning across most of the sky in a blind survey [25]. Third, we will show that our technique provides stronger constraints than previous multi-wavelength observations in the current situation wherein no counterpart has been detected.

We explain the method to estimate the band-to-radio energy ratio η in Section 2.3, introduce the surveys under consideration in Section 2.4, and show our calculations and results in Section 2.5. In Section 4.4, we compare our results with theoretical predictions made by leading FRB emission models. We also compare our results with previous observational constraints, and discuss observational strategies for future blind searching. We conclude in Section 4.5.

2.3 Methods

We adopt the broken power-law specific-fluence cumulative distribution function (CDF) estimated using the Australian Square Kilometre Array Pathfinder (ASKAP) and Parkes FRB samples [26]:

$$R(F_\nu) = \int_F^\infty r(F'_\nu) dF'_\nu, \tag{2.3a}$$

$$= R_0 \left(\frac{F_\nu}{F_{\nu,0}}\right)^{\alpha_1} \quad (F_{\nu,\min} < F_\nu < F_{\nu,b}), \tag{2.3b}$$

$$= R_b \left(\frac{F_\nu}{F_{\nu,b}}\right)^{\alpha_2} \quad (F_\nu > F_{\nu,b}). \tag{2.3c}$$

Here, $R(F_\nu)$ is the FRB rate (in the usual units of sky^{-1} day^{-1}) above a given fluence threshold F_ν in the radio band, $r(F_\nu)$ is the differential fluence distribution function, $\alpha_1 = -1.18$, $\alpha_2 = -2.2$, $F_{\nu,\min}$ is the (observationally unconstrained) fluence cut-off in the radio-band, $F_{\nu,0} \sim 2$ Jy ms is the fluence completeness threshold for the Parkes FRB searches [27], $R_0 \approx 1.7 \times 10^3$ sky^{-1} day^{-1} is the estimated rate above $F_{\nu,0}$ [2], $F_{\nu,b}$ is the fluence break which we choose to be 15 Jy ms, and $R_b \approx 171$ sky^{-1} day^{-1} is the rate above F_b calculated from Eq. (A.1b).

We assume that in any other emission band the fluence CDF, $\tilde{R}$, has the same functional form as R, except with a shift in abscissa (i.e., horizontally), and a

re-normalization:

$$\tilde{\mathrm{R}}\left(\mathrm{F}_\nu\right) = \mathrm{R}\left(\frac{\mathrm{F}_\nu}{\eta_\nu}\right). \tag{2.4}$$

We use properties of multi-wavelength surveys to estimate η_ν by calculating the degree to which the distribution needs to be shifted in its abscissa to achieve the same detection rate in two different bands.

We now describe how estimates of η and η_ν are made. Suppose that a transient survey has a field of view (FOV) of Ω steradians, effectively lasts for n days, and has not detected any FRB counterpart. The survey operates at frequencies from ν_1 to ν_2, with a center frequency of ν_c. Our method involves the following steps:

1. Convert the instrumental detection sensitivity threshold to an energy flux, f_0.

   - If the photon flux threshold f_ph is specified, we calculate f_0 using the specifications of each instrument and the weighted average photon frequency $\langle\nu\rangle$ in this band, assuming a typical photon index of –2 (i.e. a spectral index of –1; see e.g., [28])[1]:

$$\begin{aligned} \mathrm{f}_0 &= \mathrm{f}_\mathrm{ph} \cdot \mathrm{h}\langle\nu\rangle, \\ &= \mathrm{f}_\mathrm{ph} \cdot \mathrm{h}\, \frac{\int_{\nu_1}^{\nu_2} \mathrm{d}\nu\ \nu^{-2}\ \nu}{\int_{\nu_1}^{\nu_2} \mathrm{d}\nu\ \nu^{-2}}, \\ &= \mathrm{f}_\mathrm{ph} \cdot \mathrm{h}\, \frac{\ln(\nu_2/\nu_1)}{\nu_1^{-1} - \nu_2^{-1}}. \end{aligned} \tag{2.5}$$

   - If we know the limiting magnitude m,

$$\mathrm{f}_0 = 10^{-0.4\mathrm{m}} \cdot \nu_1 \cdot \mathrm{f}_{\nu,\mathrm{m0}}. \tag{2.6}$$

     Here, $\mathrm{f}_{\nu,\mathrm{m0}}$ is the specific energy flux of an object with zero magnitude in that band and magnitude system [30–32].

2. Scale the detection limiting energy flux f_0 according to a timescale $\Delta\mathrm{t}$. Specifically, if the survey has an automatic self-trigger algorithm for burst candidates,

[1] This assumption yields larger estimates for η than if a steeper photon index was assumed (see Section 2.5). Some previous studies [e.g., 29] assume steeper photon indices.

we use the trigger timescale(s) t_{trig}. Otherwise, we use the nominal instrumental time resolution t_{res}. Since the signal to noise ratio SNR $\propto \Delta t^{1/2}$, the detection flux threshold $f_0 \propto \Delta t^{-1/2}$. (Note that if the burst duration $t_{burst} < \Delta t$, the corresponding intrinsic burst flux needs to be higher than f_0. Otherwise, they are the same.)

3. Compute the fluence thresholds of the burst in the band of interest.

   - If $t_{burst} < \Delta t$, the band-integrated burst fluence limit is $F_{0,Band} = f_0 \cdot \Delta t$.
   - Otherwise, Δt is too short for the burst. One should either choose a different timescale or bin adjacent time samples.

   The specific fluence threshold is $F_{\nu,0,Band} \approx F_{0,Band}/\nu_1$. In addition, we require that the number of photons received within the timescale (Δt) by the telescope's effective collecting area (A) is at least one. When this is not satisfied, we replace the photon flux threshold f_{ph} (step 1) with 1 photon Δt^{-1} A^{-1}, and repeat the previous steps.

4. Calculate the event-rate upper bound in this survey if no candidate were detected:
$$R(F_{\nu,0,Band}) \leq \frac{3}{n}\frac{4\pi}{\Omega}\ sky^{-1}\ d^{-1}. \tag{2.7}$$
A non-detection means a Poisson single-sided upper limit of 3 at the 95% confidence level [33]. Alternatively, if there were x candidate events in this survey, the event rate would be
$$R = \frac{x}{n}\frac{4\pi}{\Omega}\ sky^{-1}\ d^{-1}. \tag{2.8}$$

5. Solve for the radio band fluence threshold $F_{\nu,0,Radio}$ that would have produced the same rate R using Eqn.A.1.

6. Find the fluence ratios:
$$\eta_\nu(\nu_c) \leq F_{\nu,0,Band}/F_{\nu,0,Radio}, \tag{2.9}$$
and
$$\eta(\nu_c) \leq F_{0,Band}/F_{0,Radio} \approx \frac{F_{0,Band}/\nu_{1,Band}}{F_{0,Radio}/\nu_{1,Radio}}. \tag{2.10}$$
Here, $F_{\nu,0,Band}$ and $F_{\nu,0,Radio}$ have been found in steps 3 and 5, respectively.

2.4 Existing Surveys

We demonstrate the application of the methods outlined above using existing high time resolution transient surveys from the near-infrared (NIR) band up to the TeV-band. Following model predictions (see Section 4.4), we assume that FRB counterparts are fast transient events shorter than $\sim$ a few minutes. In this work, we only focus on surveys with short cadences ($\lesssim$ 2 minutes), large fields of view (FOVs), and relatively high sensitivities.

Table 2.1 lists the survey instruments considered in this work. The survey durations are counted until October 1, 2019. We assume full-time operation since the launch date for space missions, and a typical average observation time of 8 hours per day since the operation date for ground-based instruments. We adopt the detection threshold used by each instrument, although some of them correspond to different statistical SNRs, as each survey could have different false-positive rates. We list the threshold corresponding to the given timescale, unless specified otherwise. We increase the detection threshold of *MAGIC* and Fermi/ LAT (at the lower timescale) to 2.4×10^{-11} and 7×10^{-8} photon cm^{-2} s^{-1}, respectively, to satisfy the requirement that at least one photon is received within the timescales by the corresponding telescopes (step 3).

The timescales are chosen differently for the high energy and the optical bands. All of the high-energy surveys selected in this work have been designed to be sensitive to GRB-like transient events ($\sim$0.1 s to $\sim$100 s). Each survey has its own transient-candidate self-trigger algorithm that runs on board commensally with observations using a range of trial trigger timescales. In addition, it is also possible to manually search the survey data afterwards for candidate events using different algorithms and timescales. For *Fermi*/LAT, we adopt the timescales optimized for FRB-counterpart searching [44], since the on-board trigger only responds to very bright bursts due to the high cosmic ray rate.[2] For the other high-energy surveys, we list the trial timescales used by the corresponding self-trigger algorithms. In the optical band, we use the nominal time resolutions for all instruments.

2.5 Results

We estimate η for each survey/instrument (Table 2.1) following the steps introduced in Section 2.3. Table 2.2 and Fig. 2.1 summarize the results. In Section 2.5.1, we make the assumption that no counterpart has been detected to demonstrate the power

[2] Personal communication with Dr. Nicola Omodei.

of our technique. In Section 2.5.2, we investigate the implications of assuming that counterparts exist among the unclassified transient events in some surveys.

2.5.1 Band-to-radio fluence ratios assuming non-detections

In Table 2.2, we list 95% confidence upper limits on the rate of FRB counterparts and on η for each survey. We use a reference frequency of $\nu_{1,\mathrm{Radio}} = 1.182$ GHz (the lower limit of the Parkes radio band) to convert the specific fluence into the band-integrated radio fluence (in step 6). We assume that the counterpart duration t_{burst} is shorter than the timescale Δt for all instruments (in step 3 above), and discuss the alternative case in Section 4.4. For surveys with multiple timescales, we scale the flux and fluence following steps 2 and 3 using the **shortest** and the **longest** timescales. We list the corresponding results in two rows in Table 2.2, and plot both ratios in Fig. 2.1 (a).

Our results are robust within order of magnitude to a selection of variations in the fluence distribution model in Eqn. A.1 [45]. We vary the broken power-law indices α_1 and α_2 by ± 0.7 and find that the results change by 46% ($\alpha_1 = -0.48$), 86% ($\alpha_1 = -1.88$), 92% ($\alpha_2 = -1.5$), and 270% ($\alpha_2 = -2.9$), respectively. We also use a single power-law fluence distribution model with an index of –1.5, and find that the results change by less than 88%. However, our results are sensitive to the choice of the photon index in the γ-ray band. In step 1, we assume a Crab-like photon index of 2 to calculate the energy flux limit from the photon flux limit for *MAGIC*, *Fermi*/ LAT and GBM. We vary the photon index to –2.5 and –1.5 and find that the resulting fluence ratios decrease / increase by 70% and one order-of-magnitude, respectively. There is little theoretical guidance on what range of photon indices is reasonable for FRB counterparts, but the example of GRBs suggests that photon indices > –2 are expected below peak energies (in νF_ν spectra) of typically 100 keV – 1 MeV, and photon indices < –2 are expected above the peak energies [46].

2.5.2 What if FRB counterparts have been detected?

No compelling candidate FRB counterpart at any wavelength has been reported until the end of 2019. However, we cannot exclude the possibility that some unclassified short transient events found in existing surveys could be associated with FRBs. It is beyond the scope of this paper to estimate what fraction of them might be FRB counterparts, but we will investigate the results assuming the extreme case where all of them are FRB counterparts. We show the results in Table 2.2 (within parentheses) and Fig. 2.1 (b) (dashed lines).

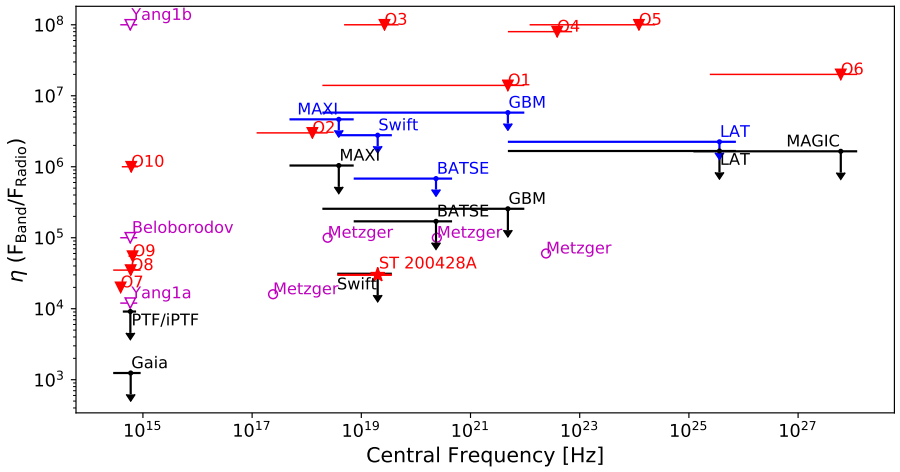

(a) Our 95% confidence upper limits assuming non-detection using the **shortest** timescales (solid black lines) and the **longest** timescales (solid blue lines).

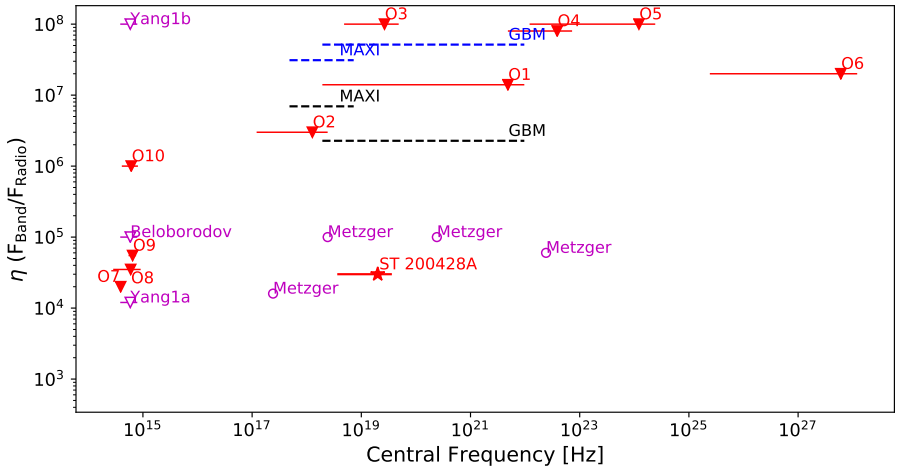

(b) Our nominal upper limits assuming that all of the unclassified events in the trigger catalogs were FRB counterparts, using the **shortest** (dashed black lines) and the **longest** (dashed blue lines) timescales.

Figure 2.1: Constraints on the band-integrated fluence ratios from our results **using the shortest and the longest timescales (black and blue lines, respectively; see section 2.5)**, previous model predictions (the hollow magenta markers are circles for predicted values, and triangles for predicted upper limits; see section 2.6.1) and previous observations (**filled red star and triangles;** 'O1' to 'O10' each represents the upper limit from Scholz ('O1' and 'O2'), Anumurlapudi, Yamasaki, Casentini, MAGIC Collaboration, Hardy, Wevers, Andreoni and Richmond, respectively; see section 2.6.2)

In the *Fermi*/GBM trigger catalog [3] to the end of 2019, there were 7045 triggered events, and 370 of them were marked as "uncertain classification." We discuss two limiting cases for these unclassified short transient events. First, if none of them were FRB counterparts, the results would be the same as those of Section 2.5.1. Second, if all of them were FRB counterparts, we estimate η using the method as in Section 2.3. Using the **shortest** trigger timescale as an example, steps 1 to 3 remain the same, so the *Fermi*/GBM fluence limit is still 1.02×10^{18} Jy ms Hz. In step 4, the rate is now estimated as $\mathrm{R} = \frac{370}{4132\ \mathrm{days}} \frac{4\pi\ \mathrm{sky}^{-1}}{8} = 0.14\ \mathrm{day}^{-1}\mathrm{sky}^{-1}$, ~ 100 times larger than the upper limit assuming non-detection. In the radio band, the fluence threshold that would have produced the new detection rate is 380 Jy ms, or 4.49×10^{11} Jy ms Hz. Hence, $\eta = \frac{1.02\times10^{18}}{4.49\times10^{11}} \approx 2.27 \times 10^{6}$, $\sim$ 10 times higher than our result in Section 2.5.1.

In the *MAXI* trigger catalog[4] between 2011 April 18 and 2020 January 28, 168 events were classified as "either GRB or unknown X-ray transient". If all of them were FRB counterparts, the rate would be $\mathrm{R} = \frac{168}{3207\ \mathrm{days}} \frac{4\pi\ \mathrm{sky}^{-1}}{0.0731} = 9.00\ \mathrm{day}^{-1}\mathrm{sky}^{-1}$. The radio fluence that could have produced the same rate would be 6.76×10^{10} Jy ms Hz, and the fluence ratio would be $\eta = \frac{4.70\times10^{17}}{6.76\times10^{10}} \approx 6.95 \times 10^{6}$, $\sim$ 7 times higher than our previous result.

In the optical band, we only use the most constraining result (from *Gaia*) in the following comparison with model predictions and previous observations. No unclassified fast *Gaia* transient has been reported[5], so we tentatively maintain the non-detection assumption for *Gaia* in our results. This may change as more *Gaia* data are searched for unclassified fast transients.

2.6 Discussion

We have developed and demonstrated a technique to estimate the ratios between FRB energy output in the radio band, and in various bands from the near-IR to γ-rays. Preliminary results based on published surveys for fast transients (Table 2.1) are presented in Table 2.2 and Fig. 2.1 in two extreme cases: assuming either that no FRB counterpart has been detected, or assuming that all unclassified fast transients are FRB counterparts. Our method uses the statistical properties of the observed FRB population, while most of the previous observational estimations are based

[3] https://heasarc.gsfc.nasa.gov/db-perl/W3Browse/w3hdprods.pl

[4] https://gcn.gsfc.nasa.gov/maxi_grbs.html

[5] [47] develop a method to search the *Gaia* data for fast transients between tens of seconds to hours. They find four events produced by stellar flares in 23.5 square degrees of sky.

on multi-wavelength observations at the locations of individual FRB events. In this section, we will compare our results with theoretical predictions and previous observations, and briefly discuss possible future FRB counterpart search strategies.

2.6.1 Comparison to theoretical predictions

The two leading FRB emission mechanisms are the synchrotron maser and coherent curvature radiation. We first compare our high-energy results with predictions from these two types of models, as well as a class of models generally involving contemporaneous high-energy flares, and the cosmic comb model. We then compare our optical results with model predictions made under five scenarios. Finally, we conclude by calculating the model-predicted counterpart detection rate for some of the existing surveys (Table 2.3). This section is partly intended as a pedagogical resource for future studies of FRB multi-wavelength counterparts.

2.6.1.1 Metzger et al. model

Synchrotron masers have been widely discussed as an astrophysical coherent emission process (e.g., [48, 49]), and one common variation is coherent emission from synchrotron masers produced by ultrarelativistic shock in magnetized plasmas (e.g., [50], [16], [19], [51], [20], [52]). [20] describe a model using the particle-in-cell (PIC) simulation results for maser emission and the dynamics of self-similar shock deceleration. Magnetar flares eject ultra-relativistic ion-electron shells that are supersonic into the surrounding magnetized trans-relativistic ion-electron plasma released by previous flares. The forward shock creates a population inversion and enables the synchrotron maser process, which results in narrowly peaked coherent radio emission putatively responsible for FRBs. The same forward shock, however, primarily dissipates energy through a synchrotron "afterglow" that will result in observable high-energy counterparts. The model predicts that the observed counterpart luminosity is $L_\gamma \sim 10^{45}$– 10^{46} erg s^{-1} with a duration of ~ 0.1 – 10 ms in the MeV–GeV band, and $L_X \sim 10^{42}$ – 10^{53} erg s^{-1} with a duration of $\sim$ 0.1–1 s in the keV band. A weak optical counterpart is possible if the upstream plasma were composed of electrons and positrons rather than electrons and ions; we do not consider any resulting quantitative predictions here. We convert the above predictions to fluence ratios η, which can be directly compared with our results. Assuming a typical FRB of duration 1 ms initiated by a flare of energy $\sim 10^{44}$ erg, the results of [20] imply ratios of 6×10^4, 10^5, 10^5 and 2×10^4 for a counterpart whose band starts from 100 MeV, 1 MeV, 10 keV and 1 keV, respectively (hollow magenta circles in

Fig 2.1).

2.6.1.2 Beloborodov model

Meanwhile, [51] proposes that the synchrotron maser is formed instead when the magnetar giant flares launch ultra-relativistic blast waves ($\Gamma \gtrsim 10^3$) into the relativistic ($\Gamma \sim 10^2$), persistent magnetar wind outflow, which consists of $e^{\pm}$. A bright optical counterpart occurs only when the blast wave strikes a hot wind bubble in the slow ion tail of a previous flare. The optical flash is estimated to have a duration of $\sim$ 1 s and an energy upper limit of $\sim 10^{44}$ erg. The optical-to-radio fluence ratio would be $\eta \lesssim 10^5$ using the average FRB 121102 burst energy of 10^{39} erg [53], and $\eta \sim 10^3$ using the FRB energy corresponding to the strongest explosion, which produces the brightest optical flash in their model. The former is shown in Fig. 2.1 to compare with our results, since our technique utilizes the statistical features of the entire FRB population. The latter prediction could be comparable to results of simultaneous multi-wavelength observations of individual events. Note that in this model many FRBs do not have optical counterparts, since only strong magnetar flares may have significant ion tails.

2.6.1.3 Soft gamma-ray repeater (SGR) giant flares as FRB counterparts

More generally, in many FRB models the emission processes are initiated by SGR giant flares. The energy released by giant flares is typically specified in the γ-ray band, where the *Fermi*/GBM survey suggests constraints ranging between $\eta \lesssim 10^5$ (0.1-s counterparts, assuming no extant detections) and $\eta \sim 10^7$ (100-s counterparts, assuming all unclassified events are giant flares). These constraints can be used to test the hypothesis that each giant flare corresponds to an FRB.

Following Ofek [54], the rate of giant flares in the Milky Way, which hosts four SGRs, is $\lesssim 0.002\,\mathrm{yr}^{-1}$ for energies $E_{SGR} > 4 \times 10^{46}$ erg (this rate is based on an analysis of extragalactic giant-flare candidates), and $\sim 0.1\,\mathrm{yr}^{-1}$ for energies $E_{SGR} > 2 \times 10^{44}$ erg (Poisson errors neglected; this rate is derived from the Milky Way alone). Ofek [54] derives the number of SGRs in a given galaxy by comparing its core-collapse supernova rate with that of the Milky Way, which is justified given the short lifetimes (O(kyr)) of active SGRs. As the overall star-formation rate is a reasonable proxy for the core-collapse supernova rate [55], we can derive the (local) volumetric rate of giant flares by scaling the Milky Way rate by the ratio of the local star-formation rate density [$0.015\,\mathrm{M}_\odot\,\mathrm{yr}^{-1}\,\mathrm{Mpc}^{-3}$; 55] and the

Milky Way star-formation rate [$1.9\,M_\odot\,yr^{-1}$; 56]. For $E_{SGR} > 4\times10^{46}$ erg and $E_{SGR} > 2\times10^{44}$ erg, the volumetric giant flare rates are $\lesssim 2\times10^4\,Gpc^{-3}\,yr^{-1}$ and $\sim 8\times10^5\,Gpc^{-3}\,yr^{-1}$, respectively. If each giant flare produces an FRB, these volumetric rates correspond to estimates of the FRB volumetric rates for radio-band energy releases $E_{FRB} = E_{SGR}/\eta$ (e.g., $E_{FRB} = 4\times10^{39}$ erg and $E_{FRB} = 2\times10^{37}$ erg respectively for $\eta = 10^7$). The volumetric rate of FRBs in the local Universe inferred from the Canadian Hydrogen Intensity Mapping Experiment (CHIME) is $\sim 10^5\,Gpc^{-3}\,yr^{-1}$ [13], approximately above an energy threshold of 2×10^{37} erg s^{-1}.[6] Thus, contrary to previous studies [13, 57], the giant-flare rate may in fact be too high to explain the FRB rate. This result would be strengthened if the value of η is substantially lower than the conservative upper bound of 10^7 derived herein. We note, however, that all rate estimates above are subject to severe Poisson errors, and that this analysis will require significant refinement before firm conclusions can be drawn.

A similar analysis can be applied to any multiwavelength event that triggers an FRB. This is of particular relevance to the "cosmic comb" model, where a regular pulsar magnetosphere is "combed" by a nearby strong plasma stream with a ram pressure higher than the magnetic pressure in the magnetosphere. The stream triggers magnetic reconnection that accelerates particles within the magnetosphere, which produce coherent emission by the curvature-radiation or cyclotron instability mechanisms. On the one hand, when the plasma stream comes from nearby energetic events, such as active galactic nucleus (AGN) flares, those events should be detected as FRB counterparts. On the other hand, when the stream comes from closer but less luminous events, such as stellar flares from a companion star, no detectable counterpart would occur.

2.6.1.4 Curvature radiation

Another commonly discussed coherent emission process is curvature radiation (e.g., [22]; [58]). For example, [58] propose a model where counter-streaming $e^\pm$ plasma inside the twisted magnetosphere of a magnetar rapidly clumps due to the two-stream instability. When magnetic reconnection occurs near the magnetar surface, these clumps are accelerated along magnetic field lines and radiate coherently. The model predicts fluence ratios of $\eta \sim 1$ in all bands, so there would be no detectable FRB counterpart.

[6] An energy of $E_{FRB} \sim 2\times10^{37}$ erg corresponds to a 2 Jy ms burst detected by CHIME at 100 Mpc.

2.6.1.5 Fast optical bursts associated with FRBs

We compare our most constraining result from *Gaia* ($\eta \lesssim 10^3$, assuming non-detection and using the *Gaia* time resolution of 4.5 s) with predictions made by [59]. These authors investigate the detectability of the "fast optical bursts" (FOBs) associated with FRBs in two broad cases and five specific scenarios. We convert them to the constraints on the optical-to-radio fluence ratios assuming an FRB of 1-ms duration (hollow magenta triangles in Fig. 2.1).

Case 1 FOB formed by inverse Compton scattering between the FRB photons and ambient electrons.

a. OB and FRB both formed in the pulsar magnetosphere ($10^{-7} \lesssim \eta \lesssim 10^4$, $t_{FOB} \sim 1$ ms).

b. FOB formed in a surrounding nebula, and FRB near the neutron star ($\eta \lesssim 10^8$, $t_{FOB} \sim$ a few $\times$ 10 s).

c. FRB formed by synchrotron maser mechanism and FOB formed by inverse Compton scattering between the maser electrons and the FRB photons ($\eta \lesssim 0.38$, $t_{FOB} \sim 1$ ms).

Case 2 FOB and FRB formed by the same emission mechanism.

a. Curvature radiation by particle bunches ($\eta \lesssim 3.8 \times 10^{-5}$, $t_{FOB} \sim 1$ ms).

b. Synchrotron maser ($\eta \lesssim 3.8 \times 10^{-4}$, $t_{FOB} \sim 1$ ms).

We omit case 1(c) and case 2 in Fig. 2.1 as they are too low to compare with any existing optical telescope. Compared with our *Gaia* result, the upper limits predicted by cases 1(a) and 1(b) are greater by $\sim$ 1 and 5 orders of magnitude, while predictions of the other three scenarios are **lower by** $\sim$ 4, 8 and 7 orders of magnitude, respectively. Hence, a detection of FRB counterparts by *Gaia* (or indeed any other optical telescope) would rule out case 1(c) and case 2, and it might be able to rule out case 1(a) if the observed fluence ratio lies between $\sim 10^4$ and 10^8.

2.6.1.6 How many multi-wavelength FRB counterparts should blind surveys detect?

Finally, we estimate the counterpart detection rate from each model (Table 2.3) by combining the model-predicted η with the observed FRB fluence distribution.

For example, the theoretical counterpart duration at 1 MeV (2.4×10^{20} Hz) from the [20] model is $\sim$ 50 ms. The **shortest** trigger timescale of *Fermi*/GBM **and CGRO/ BATSE** above 50 ms are both 64 ms. At this timescale, the band-integrated fluence threshold is $F_{0,GBM} = 2 \times 10^{18}$ Jy ms Hz (**7.6×10^{17} for BATSE**), and $F_{\nu,0,GBM} \approx \frac{2\times10^{18} \text{ Jy ms Hz}}{2.4\times10^{20} \text{ Hz}} \approx 8.4\times10^{-3}$ Jy ms (**3.1×10^{-3} for BATSE**). The model predicts that $\eta_\nu \approx 4.1 \times 10^{-7}$ at $\nu_1 = 1$ MeV, so the expected counterpart rate above $F_{\nu,0,GBM}$ in the GBM-band would be $\tilde{R}(F_\nu) = R(\frac{F_{\nu,0,GBM}}{\eta_\nu}) = R(2.1 \times 10^4 \text{ Jy ms}) \approx 2.13\times10^{-5}$ sky^{-1} day^{-1} (Equations 2.7 and A.1c; 1.9×10^{-4} **for BATSE**). On average, *Fermi*/GBM is expected to detect one such event per $\langle n \rangle \approx (2.13 \times 10^{-5})^{-1}(\frac{4\pi}{8 \text{ sr}}) \approx 7.36 \times 10^4$ days (**5.3×10^3 for BATSE**). By comparing $\langle n \rangle$ with the relevant survey durations n (the last two columns in Table 2.3), it is unlikely that *Fermi*/ LAT, GBM **or BATSE** have already detected any counterparts events, or will detect one in the near future, according to the prediction of Metzger et al. [20].

As another example, we interpolate the Metzger et al. [20] predictions to 100 keV and conservatively assume a 1-s duration counterpart in the *Swift*/ BAT band **(and the *CGRO*/ BATSE band)** with $\eta_\nu \approx 4.1 \times 10^{-6}$. At this timescale, $F_{\nu,0,BAT} \approx 4.18 \times 10^{-2}$ Jy ms, and the expected counterpart rate in that band would be $R(\frac{4.18\times10^{-2} \text{ Jy ms}}{4.1\times10^{-6}}) = R(10^4 \text{ Jy ms}) \approx 10^{-4}$ sky^{-1} day^{-1}, and $\langle n \rangle \approx 8.95 \times 10^4$ days. *Swift*/ BAT is not expected to have detected any FRB counterpart based on this model, unless the counterpart duration at 100 keV is significantly shorter ($\lesssim$ 64 ms).

We cannot comment on the predictions from Beloborodov [19] and Yang et al. [59], as their models only indicate the lower limits to $\langle n \rangle$.

2.6.1.7 Caveat emptor

Cautions should be taken in the comparisons described above. First, our technique relies on a homogeneous FRB population distribution, and the synchrotron-maser and curvature-radiation models may not be able to explain so far non-repeating FRBs. Although it has been argued that all FRB sources repeat in their lifetimes [13], some sources are clearly more active than the others and it is not yet clear whether or not they belong to the same population groups. Second, the high-energy counterpart could be either the giant flare that initiates the FRB emission processes or the afterglow, or both, but their contributions are observationally indistinguishable. Third, it might be difficult to distinguish intrinsic emissions from propagation effects, since any dense intervening medium has different attenuation effects on different

wavelengths. For example, in the model of Metzger et al. [20], it is unclear whether the keV photons would escape from supernova ejecta shells surrounding the proposed magnetars, or get absorbed by the neutral gas on the FRB timescale [60]. This ambiguity makes it difficult to constrain the model based on the non-detection of X-ray counterparts. Fourth, in this work we only focus on surveys with cadences less than 2 minutes, but longer-duration counterparts may also be possible [e.g., 61]. In this case, sensitive surveys on these longer timescales should also be considered.

A further issue is that the brightest FRB sources may in fact be missed by some of the multi-wavelength surveys, because of the sparsity of these FRBs on the sky. Consider the possibility that the nearest FRB sources are the brightest [62]. The nearest sources might be missed by surveys using telescopes with small fields of view that are restricted to certain portions of the sky. Our technique assumes that FRBs are uniformly distributed over the sky region scanned by a survey, which is likely true for distant FRBs, but may not be true for nearby FRBs or those near the Galactic plane. Although over time, the anisotropic distribution would be averaged out by successive surveys, this issue may result in erroneously low estimates of η. However, this effect is mitigated by our incorporation of Poisson error in Step 4 in Section 2.3, in the case of multi-wavelength non-detections. It is also not a major issue for our analysis of the surveys with cataloged unidentified detections (*Fermi*/GBM, MAXI), because they cover the full sky besides the Galactic plane.

2.6.2 Comparison to other observations

As is evident from Figure 2.1, our technique generally provides stronger constraints on η than previous observations. We consider a selection of previous observational results in turn.

Some high-energy transient surveys have been blindly searched for FRB counterpart candidates without using knowledge of individual FRB events. Yamasaki et al. [63] (O4 in Figure 2.1) performed a blind search for γ-ray flashes (duration 1 to 10 ms) using the 7-year *Fermi*/LAT data. No event is found after removing flashes associated with known steady γ-ray sources and false events produced by the diffuse background. They found a γ-ray to radio fluence ratio of $\eta \lesssim (4.2 \sim 12) \times 10^7$ by modeling FRBs as standard candles with a power-law γ-ray spectrum and estimating the comoving FRB rate density using the nine FRB detected by then. In comparison, our technique adopts a model-independent FRB population distribution based on

a directly measurable quantity (fluence) and a significantly larger sample ($\sim$ 50). Using our technique, we find $\eta \lesssim 1.7 \times 10^6$ (100 ms) based on the non-detection in the 7-year of *Fermi*/LAT data.

In the optical band, we estimate η from a few survey sub-datasets that have been blindly searched for fast transients. Wevers et al. [47] (O8 in Figure 2.1) develop a method to blindly search the *Gaia* Photometric Science Alerts data base for fast transients between tens of seconds to hours. They demonstrate the method on a trial data set that spans $\sim$ 23.5 deg^2 of sky and has been repeatedly scanned for 40 to 50 times. Four events produced by stellar flares are found but no unclassified event is detected. The non-detection implies a optical-to-radio-band fluence ratio of $\eta \lesssim 4 \times 10^4$ using our technique. In addition, Andreoni et al. [64] (O9 in Figure 2.1) specifically search for extragalactic fast optical transients with durations down to 70 s using the Dark Energy Camera as part of the Deeper Wider Faster programme. The g-band limiting magnitude of one single exposure (20 s) is $\sim$ 23 mag (AB), the FOV is 2.52 deg^2 and the total observation time of their data set is 25.76 hours. Four events with uncertain classifications are detected, but no γ-ray signal or FRB is found within $\pm$ 1 day near these transients. Using our technique, the optical-to-radio-band fluence ratio is $\eta \lesssim 6 \times 10^4$. Finally, Richmond et al. [65] (O10 in Figure 2.1) find no transients with durations from 1.5 s to 11.5 s using the *Tomo-e Gozen* wide-field CMOS mosaic camera data (limiting magnitude V=15.6) with a control time of 177,502 deg^2 sec. The non-detection implies that $\eta \lesssim 10^6$ using our technique.

Most previous constraints on η are based on counterpart searches in the sky region of individual FRB events, either contemporaneous or not. We summarize them below and show some of the stronger constraints in Fig. 2.1.

A one-second-long X-ray counterpart was detected during the recent FRB event ST 200428A from the Galactic magnetar SGR 1935+2154 [66, 67]. Based on the X-ray observations of [68], [66] estimated that the band-integrated fluence ratio $F_X/F_{radio} \sim 3 \times 10^4$ (red star in Fig. 2.1), about one order-of-magnitude lower than our result based on the non-detection in the blind search of *Swift*/BAT for a one-second-long burst in a similar energy band.

MAGIC Collaboration et al. [69] (O6 in Figure 2.1) conducted simultaneous observations of the repeating FRB 121102 using the Arecibo telescope and MAGIC (100 GeV–50 TeV, and the optical band). Five FRBs were detected during this time (mean fluence $\sim$ 2 Jy ms), but no simultaneous or persistent counterparts were found

by MAGIC. This implies that $F_{>100GeV}/F_{Arecibo} \lesssim 2\times10^{7}$ for a 10-ms counterpart, and $F_{optical}/F_{Arecibo} \lesssim 4\times10^{3}$ for a 1-ms counterpart.

[70] (O5 in Figure 2.1) searched the AGILE archival data for MeV–GeV counterparts of two repeating FRB sources. They find no prompt emission and estimate a band-integrated fluence ratio of $F_{MeV}/F_{Radio} \lesssim 10^{8}$, assuming ms-scale emissions in the MeV band.

Cunningham et al. [44] found no prompt high energy counterpart with durations between 0.1 and 100 s for a sample of 23 FRBs in the *Fermi*/GBM, *Fermi*/LAT and *Swift* data. They estimate the fluence ratio to be $\eta \lesssim 10^{7-12}$ for the timescale of 0.1 s (and $\eta \lesssim 10^{8-13}$ for 100 s).

Anumarlapudi et al. [71] (O3 in Figure 2.1) find no prompt X-ray counterpart for a sample of 42 FRBs in the *AstroSat*/CZTI data (20–200 keV) and estimate the fluence ratio to be $F_X/F_{Radio} \lesssim 10^{8-10}$.

[72] (O1 and O2 in Figure 2.1) present simultaneous observations of the repeating FRB 121102 using the XMM-*Newton*, *Chandra*, and *Fermi*/GBM telescopes along with several radio telescopes. They found 12 radio bursts and no contemporaneous counterpart emission. They estimate that $\eta \lesssim 4\times10^{8}$ in the *Fermi*/GBM band and $\eta \lesssim 3\times10^{6}$ in the X-ray band (0.5– 10 keV) assuming bursts of < 700 ms. In addition, they find no X-ray counterpart in the sky region at anytime during these observations. Using the fluence distribution of radio bursts from FRB 121102, they estimate that $\eta \lesssim 5\times10^{7}$ in the *XMM-Newton* band (0.1– 15 keV) and $\eta \lesssim 10^{8}$ in the Chandra band (0.5– 7 keV), assuming 5-ms X-ray bursts.

[73] (O7 in Figure 2.1) conducted simultaneous observations of FRB 121102 using the high-speed optical camera ULTRASPEC on the Thai national telescope, and the Effelsberg radio telescope. They detected 13 radio events and no prompt optical counterparts. They compared the median radio fluence of those bursts with the optical detection limit and find $F_{\nu,767nm}/F_{\nu,1.4GHz} \lesssim 0.077$, corresponding to a band-integrated fluence ratio of $\eta \lesssim 2\times10^{4}$.

Finally, in a class of FRB models, the emission processes are initiated by SGR giant flares. Tendulkar et al. [29] estimate that $F_{\nu,1.4GHz}/F_{\gamma} \lesssim 10^{7}$ Jy ms erg^{-1} cm^{2} for a 10-ms radio fluence based on the radio non-detection of a γ-ray giant flare from the magnetar SGR 1806-20. Their results imply $\eta = F_{\gamma}/F_{radio} \gtrsim 10^{10}$, which is inconsistent with our γ-ray upper limits and thus in tension with the idea that SGR flares generally produce FRBs. This outcome is consistent with the discussion in

Section 2.6.1.3.

2.6.3 Future searching strategies

In the absence of FRB counterpart detections, η can be constrained from either simultaneous multi-wavelength and radio searches, or blind searches combined with the FRB population (considered in this paper). The observational strategies are slightly different in these two cases, given the nature of the FRB fluence distribution.

First, we emphasize that simultaneous radio and multi-wavelength searches are only worthwhile if they probe to lower values of η than existing blind multi-wavelength searches. In a simultaneous counterpart search with non-detection, the upper limit to $\eta \propto f_0 \cdot \Delta t$. Here, Δt is the timescale and f_0 is the corresponding detection flux threshold. The FOV (Ω) makes no difference. The total observation duration (L) is also irrelevant, until the next FRB occurs.

In contrast, in a blind search where no counterpart is found, the upper limit on η also depends on L and Ω. The counterpart rate upper bound $R \propto L^{-1} \cdot \Omega^{-1}$ (step 4 in section 2.3). Using the broken power law fluence distribution, the radio fluence threshold that would have produced the same rate R is $F_{\nu,0,\mathrm{Radio}} \propto R^{1/\alpha} \propto L^{-1/\alpha} \cdot \Omega^{-1/\alpha}$. Meanwhile, the fluence threshold in the band of the counterpart is $F_{\nu,0,\mathrm{Band}} \propto f_0 \cdot \Delta t$. Therefore,

$$\begin{aligned} \eta &\propto f_0 \cdot \Delta t \cdot \Omega^{1/\alpha} \cdot L^{1/\alpha}, \\ &\propto 10^{-0.4\ m} \cdot \Delta t \cdot \Omega^{1/\alpha} \cdot L^{1/\alpha}. \end{aligned} \tag{2.11}$$

Here, m is the absolute magnitude, and α is the power-law index of the fluence distribution (Eqn. A.1). Assuming non-detection or low counterpart detection rate, the power-law index of the ASKAP FRB sample ($\alpha_2 = -2.2$) is more relevant than that of the Parkes ($\alpha_1 = -1.18$), since the former describes events with rate below $R_b \approx 170\ \mathrm{sky}^{-1}\ \mathrm{day}^{-1}$ (Eqn. A.1c), and the latter describes more common events (Eqn. A.1b). Using α_2, $\eta \propto f_0 \cdot \Delta t \cdot \Omega^{-0.45} \cdot L^{-0.45}$, so one could enhance the constraint on η by one order of magnitude by lowering the detection flux threshold by 10 times, using a 10 times shorter timescale, or increasing the FOV or survey duration by 158 times (15 times if using α_1).

Nonetheless, there may be reasons to also require large fields of view or survey areas. If counterpart events are rare in the local Universe, a significant number of nearby galaxies would need to be included in a blind search.

2.7 Conclusions

We have developed and demonstrated a technique to estimate η — the ratio between the energy emitted by the multi-wavelength counterparts of FRBs and FRBs themselves — by combining existing multi-wavelength fast transient surveys with the fluence distribution of the FRB population. The extremely large fields of view and observation durations of surveys from the optical to the TeV bands, combined with the high all-sky rate of FRBs, mean that the locations of several FRBs undetected by radio telescopes have likely been observed by telescopes across the electromagnetic spectrum. We use the properties of several multi-wavelength surveys (listed in Table 2.1) to constrain η under the assumption that no FRB counterparts have been detected, and in some cases to estimate η under the assumption that all unclassified transient events are FRB counterparts (Table 2.2 and Figure 2.1). We conclude the following:

1. Even our most conservative constraints / estimates for η are lower than several existing results, which are largely based on targeted observations of known FRB locations, coordinated between multiple telescopes.

2. The FRB models proposed by Metzger et al. [20] and Beloborodov [51], which involve synchrotron masers initiated by shocks driven by young-magnetar flares, are closest to our constraints on η. In some scenarios, *Gaia* should have already detected several FRB counterparts. FRB counterparts may be found amongst unclassified transient events. This demonstrates the power of our technique to address FRB model predictions. However, in the high-energy bands, surveys by the *Fermi* and *Swift* satellites are not likely to have detected FRB counterparts unless the photon indices are significantly steeper than –2.

3. Our technique can also be used to test predictions for multi-wavelength emission that is associated with but not directly caused by FRBs. For example, we find evidence that the volumetric rate of magnetar giant flares that emit a factor of $\eta = 10^7$ larger energies in γ-rays than FRBs do in the radio band is over an order of magnitude higher than the FRB volumetric rate (Section 2.6.1.3).

4. The apparent rarity of multiwavelength FRB counterparts, and correspondingly likely low values of η, implies that future multiwavelength surveys are likely to only detect counterparts to the brightest FRBs. Given the steepness of the FRB fluence distribution at the bright end [26], future blind surveys

searching for FRB counterparts should prioritize sensitivity, and the ability to probe appropriately short timescales, over field of view and survey duration.

Although our results are robust to uncertainties in the FRB fluence distribution, the future application of our technique to better constrain FRB models will require a careful analysis of unclassified transient events in existing survey data sets. In addition, we assume a homogeneous population of FRB sources, which may not be the case, and it is also possible that some (e.g., soft X-ray, or blue optical) FRB counterparts are absorbed or scattered in dense surrounding media. Multi-wavelength observations of nearby individual sources [e.g., 74–76] are a complementary means to address the nature of the FRB engine and emission mechanism.

References

[1] E. Petroff, E. D. Barr, A. Jameson, E. F. Keane, M. Bailes, M. Kramer, V. Morello, D. Tabbara, and W. van Straten. FRBCAT: The Fast Radio Burst Catalogue. *PASA*, 33:e045, Sep 2016. doi: 10.1017/pasa.2016.35.

[2] S. Bhandari, E. F. Keane, E. D. Barr, A. Jameson, E. Petroff, S. Johnston, M. Bailes, N. D. R. Bhat, M. Burgay, S. Burke-Spolaor, M. Caleb, R. P. Eatough, C. Flynn, J. A. Green, F. Jankowski, M. Kramer, V. Venkatraman Krishnan, V. Morello, A. Possenti, B. Stappers, C. Tiburzi, W. van Straten, I. Andreoni, T. Butterley, P. Chand ra, J. Cooke, A. Corongiu, D. M. Coward, V. S. Dhillon, R. Dodson, L. K. Hardy, E. J. Howell, P. Jaroenjittichai, A. Klotz, S. P. Littlefair, T. R. Marsh, M. Mickaliger, T. Muxlow, D. Perrodin, T. Pritchard, U. Sawangwit, T. Terai, N. Tominaga, P. Torne, T. Totani, A. Trois, D. Turpin, Y. Niino, R. W. Wilson, A. Albert, M. André, M. Anghinolfi, G. Anton, M. Ardid, J. J. Aubert, T. Avgitas, B. Baret, J. Barrios-Martí, S. Basa, B. Belhorma, V. Bertin, S. Biagi, R. Bormuth, S. Bourret, M. C. Bouwhuis, H. Brânzaș, R. Bruijn, J. Brunner, J. Busto, A. Capone, L. Caramete, J. Carr, S. Celli, R. Cherkaoui El Moursli, T. Chiarusi, M. Circella, J. A. B. Coelho, A. Coleiro, R. Coniglione, H. Costantini, P. Coyle, A. Creusot, A. F. Díaz, A. Deschamps, G. De Bonis, C. Distefano, I. Di Palma, A. Domi, C. Donzaud, D. Dornic, D. Drouhin, T. Eberl, I. El Bojaddaini, N. El Khayati, D. Elsässer, A. Enzenhöfer, A. Ettahiri, F. Fassi, I. Felis, L. A. Fusco, P. Gay, V. Giordano, H. Glotin, T. Gregoire, R. Gracia-Ruiz, K. Graf, S. Hallmann, H. van Haren, A. J. Heijboer, Y. Hello, J. J. Hernández-Rey, J. Hößl, J. Hofestädt, C. Hugon, G. Illuminati, C. W. James, M. de Jong, M. Jongen, M. Kadler, O. Kalekin, U. Katz, D. Kießling, A. Kouchner, M. Kreter, I. Kreykenbohm, V. Kulikovskiy, C. Lachaud, R. Lahmann, D. Lefèvre, E. Leonora, S. Loucatos, M. Marcelin, A. Margiotta, A. Marinelli, J. A. Martínez-Mora, R. Mele, K. Melis, T. Michael, P. Migliozzi, A. Moussa, S. Navas, E. Nezri, M. Organokov, G. E. Păvălaș, C. Pellegrino, C. Perrina, P. Piattelli, V. Popa,

T. Pradier, L. Quinn, C. Racca, G. Riccobene, A. Sánchez-Losa, M. Saldaña, I. Salvadori, D. F. E. Samtleben, M. Sanguineti, P. Sapienza, F. Schüssler, C. Sieger, M. Spurio, Th Stolarczyk, M. Taiuti, Y. Tayalati, A. Trovato, D. Turpin, C. Tönnis, B. Vallage, V. Van Elewyck, F. Versari, D. Vivolo, A. Vizzocca, J. Wilms, J. D. Zornoza, and J. Zúñiga. The SUrvey for Pulsars and Extragalactic Radio Bursts - II. New FRB discoveries and their follow-up. *MNRAS*, 475(2):1427–1446, Apr 2018. doi: 10.1093/mnras/stx3074.

[3] S. Chatterjee, C. J. Law, R. S. Wharton, S. Burke-Spolaor, J. W. T. Hessels, G. C. Bower, J. M. Cordes, S. P. Tendulkar, C. G. Bassa, P. Demorest, B. J. Butler, A. Seymour, P. Scholz, M. W. Abruzzo, S. Bogdanov, V. M. Kaspi, A. Keimpema, T. J. W. Lazio, B. Marcote, M. A. McLaughlin, Z. Paragi, S. M. Ransom, M. Rupen, L. G. Spitler, and H. J. van Langevelde. A direct localization of a fast radio burst and its host. *Nature*, 541(7635):58–61, Jan 2017. doi: 10.1038/nature20797.

[4] K. W. Bannister, A. T. Deller, C. Phillips, J. P. Macquart, J. X. Prochaska, N. Tejos, S. D. Ryder, E. M. Sadler, R. M. Shannon, S. Simha, C. K. Day, M. McQuinn, F. O. North-Hickey, S. Bhandari, W. R. Arcus, V. N. Bennert, J. Burchett, M. Bouwhuis, R. Dodson, R. D. Ekers, W. Farah, C. Flynn, C. W. James, M. Kerr, E. Lenc, E. K. Mahony, J. O'Meara, S. Osłowski, H. Qiu, T. Treu, V. U, T. J. Bateman, D. C. J. Bock, R. J. Bolton, A. Brown, J. D. Bunton, A. P. Chippendale, F. R. Cooray, T. Cornwell, N. Gupta, D. B. Hayman, M. Kesteven, B. S. Koribalski, A. MacLeod, N. M. McClure-Griffiths, S. Neuhold, R. P. Norris, M. A. Pilawa, R. Y. Qiao, J. Reynolds, D. N. Roxby, T. W. Shimwell, M. A. Voronkov, and C. D. Wilson. A single fast radio burst localized to a massive galaxy at cosmological distance. *Science*, 365(6453): 565–570, Aug 2019. doi: 10.1126/science.aaw5903.

[5] V. Ravi, M. Catha, L. D'Addario, S. G. Djorgovski, G. Hallinan, R. Hobbs, J. Kocz, S. R. Kulkarni, J. Shi, H. K. Vedantham, S. Weinreb, and D. P. Woody. A fast radio burst localized to a massive galaxy. *Nature*, 572(7769):352–354, Aug 2019. doi: 10.1038/s41586-019-1389-7.

[6] J. Xavier Prochaska, Jean-Pierre Macquart, Matthew McQuinn, Sunil Simha, Ryan M. Shannon, Cherie K. Day, Lachlan Marnoch, Stuart Ryder, Adam Deller, Keith W. Bannister, Shivani Bhandari, Rongmon Bordoloi, John Bunton, Hyerin Cho, Chris Flynn, Elizabeth K. Mahony, Chris Phillips, Hao Qiu, and Nicolas Tejos. The low density and magnetization of a massive galaxy halo exposed by a fast radio burst. *Science*, 366(6462):231–234, Oct 2019. doi: 10.1126/science.aay0073.

[7] B. Marcote, K. Nimmo, J. W. T. Hessels, S. P. Tendulkar, C. G. Bassa, Z. Paragi, A. Keimpema, M. Bhardwaj, R. Karuppusamy, V. M. Kaspi, C. J. Law, D. Michilli, K. Aggarwal, B. Andersen, A. M. Archibald, K. Bandura, G. C. Bower, P. J. Boyle, C. Brar, S. Burke-Spolaor, B. J. Butler, T. Cassanelli,

P. Chawla, P. Demorest, M. Dobbs, E. Fonseca, U. Giri, D. C. Good, K. Gourdji, A. Josephy, A. Yu. Kirichenko, F. Kirsten, T. L. Landecker, D. Lang, T. J. W. Lazio, D. Z. Li, H. H. Lin, J. D. Linford, K. Masui, J. Mena-Parra, A. Naidu, C. Ng, C. Patel, U. L. Pen, Z. Pleunis, M. Rafiei-Ravandi, M. Rahman, A. Renard, P. Scholz, S. R. Siegel, K. M. Smith, I. H. Stairs, K. Vanderlinde, and A. V. Zwaniga. A repeating fast radio burst source localized to a nearby spiral galaxy. *Nature*, 577(7789):190–194, Jan 2020. doi: 10.1038/s41586-019-1866-z.

[8] L. G. Spitler, P. Scholz, J. W. T. Hessels, S. Bogdanov, A. Brazier, F. Camilo, S. Chatterjee, J. M. Cordes, F. Crawford, J. Deneva, R. D. Ferdman, P. C. C. Freire, V. M. Kaspi, P. Lazarus, R. Lynch, E. C. Madsen, M. A. McLaughlin, C. Patel, S. M. Ransom, A. Seymour, I. H. Stairs, B. W. Stappers, J. van Leeuwen, and W. W. Zhu. A repeating fast radio burst. *Nature*, 531(7593): 202–205, Mar 2016. doi: 10.1038/nature17168.

[9] M. Amiri, K. Bandura, M. Bhardwaj, P. Boubel, M. M. Boyce, P. J Boyle, C. . Brar, M. Burhanpurkar, T. Cassanelli, P. Chawla, J. F. Cliche, D. Cubranic, M. Deng, N. Denman, M. Dobbs, M. Fandino, E. Fonseca, B. M. Gaensler, A. J. Gilbert, A. Gill, U. Giri, D. C. Good, M. Halpern, D. S. Hanna, A. S. Hill, G. Hinshaw, C. Höfer, A. Josephy, V. M. Kaspi, T. L. Landecker, D. A. Lang, H. H. Lin, K. W. Masui, R. Mckinven, J. Mena-Parra, M. Merryfield, D. Michilli, N. Milutinovic, C. Moatti, A. Naidu, L. B. Newburgh, C. Ng, C. Patel, U. Pen, T. Pinsonneault-Marotte, Z. Pleunis, M. Rafiei-Ravandi, M. Rahman, S. M. Ransom, A. Renard, P. Scholz, J. R. Shaw, S. R. Siegel, K. M. Smith, I. H. Stairs, S. P. Tendulkar, I. Tretyakov, K. Vanderlinde, and P. Yadav. A second source of repeating fast radio bursts. *Nature*, 566(7743): 235–238, Jan 2019. doi: 10.1038/s41586-018-0864-x.

[10] B. C. Andersen, K. Bandura, M. Bhardwaj, P. Boubel, M. M. Boyce, P. J. Boyle, C. Brar, T. Cassanelli, P. Chawla, D. Cubranic, M. Deng, M. Dobbs, M. Fandino, E. Fonseca, B. M. Gaensler, A. J. Gilbert, U. Giri, D. C. Good, M. Halpern, A. S. Hill, G. Hinshaw, C. Höfer, A. Josephy, V. M. Kaspi, R. Kothes, T. L. Landecker, D. A. Lang, D. Z. Li, H. H. Lin, K. W. Masui, J. Mena-Parra, M. Merryfield, R. Mckinven, D. Michilli, N. Milutinovic, A. Naidu, L. B. Newburgh, C. Ng, C. Patel, U. Pen, T. Pinsonneault-Marotte, Z. Pleunis, M. Rafiei-Ravandi, M. Rahman, S. M. Ransom, A. Renard, P. Scholz, S. R. Siegel, S. Singh, K. M. Smith, I. H. Stairs, S. P. Tendulkar, I. Tretyakov, K. Vanderlinde, P. Yadav, and A. V. Zwaniga. CHIME/FRB Discovery of Eight New Repeating Fast Radio Burst Sources. *ApJ*, 885(1): L24, Nov 2019. doi: 10.3847/2041-8213/ab4a80.

[11] Pravir Kumar, R. M. Shannon, Stefan Osłowski, Hao Qiu, Shivani Bhandari, Wael Farah, Chris Flynn, Matthew Kerr, D. R. Lorimer, J. P. Macquart, Cherry Ng, C. J. Phillips, Danny C. Price, and Renée Spiewak. Faint Repetitions from a Bright Fast Radio Burst Source. *ApJ*, 887(2):L30, Dec 2019. doi: 10.3847/2041-8213/ab5b08.

[12] E. Fonseca, B. C. Andersen, M. Bhardwaj, P. Chawla, D. C. Good, A. Josephy, V. M. Kaspi, K. W. Masui, R. Mckinven, D. Michilli, Z. Pleunis, K. Shin, S. P. Tendulkar, K. M. Bandura, P. J. Boyle, C. Brar, T. Cassanelli, D. Cubranic, M. Dobbs, F. Q. Dong, B. M. Gaensler, G. Hinshaw, T. L. Land ecker, C. Leung, D. Z. Li, H. H. Lin, J. Mena-Parra, M. Merryfield, A. Naidu, C. Ng, C. Patel, U. Pen, M. Rafiei-Ravandi, M. Rahman, S. M. Ransom, P. Scholz, K. M. Smith, I. H. Stairs, K. Vanderlinde, P. Yadav, and A. V. Zwaniga. Nine New Repeating Fast Radio Burst Sources from CHIME/FRB. *arXiv e-prints*, art. arXiv:2001.03595, Jan 2020.

[13] Vikram Ravi. The prevalence of repeating fast radio bursts. *Nature Astronomy*, 3:928–931, Jul 2019. doi: 10.1038/s41550-019-0831-y.

[14] D. B. Melrose. Coherent emission mechanisms in astrophysical plasmas. *Reviews of Modern Plasma Physics*, 1(1):5, December 2017. doi: 10.1007/s41614-017-0007-0.

[15] Yuri Lyubarsky. Fast radio bursts from reconnection in magnetar magnetosphere. *arXiv e-prints*, art. arXiv:2001.02007, Jan 2020.

[16] Yu. Lyubarsky. A model for fast extragalactic radio bursts. *MNRAS*, 442: L9–L13, Jul 2014. doi: 10.1093/mnrasl/slu046.

[17] G. Ghisellini. Synchrotron masers and fast radio bursts. *MNRAS*, 465(1): L30–L33, Feb 2017. doi: 10.1093/mnrasl/slw202.

[18] Eli Waxman. On the Origin of Fast Radio Bursts (FRBs). *ApJ*, 842(1):34, Jun 2017. doi: 10.3847/1538-4357/aa713e.

[19] Andrei M. Beloborodov. A Flaring Magnetar in FRB 121102? *ApJ*, 843(2): L26, Jul 2017. doi: 10.3847/2041-8213/aa78f3.

[20] Brian D. Metzger, Ben Margalit, and Lorenzo Sironi. Fast radio bursts as synchrotron maser emission from decelerating relativistic blast waves. *MNRAS*, 485(3):4091–4106, May 2019. doi: 10.1093/mnras/stz700.

[21] J. M. Cordes and Ira Wasserman. Supergiant pulses from extragalactic neutron stars. *MNRAS*, 457(1):232–257, Mar 2016. doi: 10.1093/mnras/stv2948.

[22] Pawan Kumar, Wenbin Lu, and Mukul Bhattacharya. Fast radio burst source properties and curvature radiation model. *MNRAS*, 468(3):2726–2739, Jul 2017. doi: 10.1093/mnras/stx665.

[23] Bing Zhang. A "Cosmic Comb" Model of Fast Radio Bursts. *ApJ*, 836(2): L32, Feb 2017. doi: 10.3847/2041-8213/aa5ded.

[24] N. Gehrels. Use of νF_ν spectral energy distributions for multiwavelength astronomy. *Nuovo Cimento B Serie*, 112B(1):11–15, January 1997.

[25] H. K. Vedantham, V. Ravi, K. Mooley, D. Frail, G. Hallinan, and S. R. Kulkarni. On Associating Fast Radio Bursts with Afterglows. *ApJ*, 824(1):L9, June 2016. doi: 10.3847/2041-8205/824/1/L9.

[26] C. W. James, R. D. Ekers, J. P. Macquart, K. W. Bannister, and R. M. Shannon. The slope of the source-count distribution for fast radio bursts. *MNRAS*, 483 (1):1342–1353, Feb 2019. doi: 10.1093/mnras/sty3031.

[27] E. F. Keane and E. Petroff. Fast radio bursts: search sensitivities and completeness. *MNRAS*, 447(3):2852–2856, March 2015. doi: 10.1093/mnras/stu2650.

[28] W. B. Atwood, A. A. Abdo, M. Ackermann, W. Althouse, B. Anderson, M. Axelsson, L. Baldini, J. Ballet, D. L. Band, G. Barbiellini, J. Bartelt, D. Bastieri, B. M. Baughman, K. Bechtol, D. Bédérède, F. Bellardi, R. Bellazzini, B. Berenji, G. F. Bignami, D. Bisello, E. Bissaldi, R. D. Blandford, E. D. Bloom, J. R. Bogart, E. Bonamente, J. Bonnell, A. W. Borgland , A. Bouvier, J. Bregeon, A. Brez, M. Brigida, P. Bruel, T. H. Burnett, G. Busetto, G. A. Caliandro, R. A. Cameron, P. A. Caraveo, S. Carius, P. Carlson, J. M. Casandjian, E. Cavazzuti, M. Ceccanti, C. Cecchi, E. Charles, A. Chekhtman, C. C. Cheung, J. Chiang, R. Chipaux, A. N. Cillis, S. Ciprini, R. Claus, J. Cohen-Tanugi, S. Condamoor, J. Conrad, R. Corbet, L. Corucci, L. Costamante, S. Cutini, D. S. Davis, D. Decotigny, M. DeKlotz, C. D. Dermer, A. de Angelis, S. W. Digel, E. do Couto e Silva, P. S. Drell, R. Dubois, D. Dumora, Y. Edmonds, D. Fabiani, C. Farnier, C. Favuzzi, D. L. Flath, P. Fleury, W. B. Focke, S. Funk, P. Fusco, F. Gargano, D. Gasparrini, N. Gehrels, F. X. Gentit, S. Germani, B. Giebels, N. Giglietto, P. Giommi, F. Giordano, T. Glanzman, G. Godfrey, I. A. Grenier, M. H. Grondin, J. E. Grove, L. Guillemot, S. Guiriec, G. Haller, A. K. Harding, P. A. Hart, E. Hays, S. E. Healey, M. Hirayama, L. Hjalmarsdotter, R. Horn, R. E. Hughes, G. Jóhannesson, G. Johansson, A. S. Johnson, R. P. Johnson, T. J. Johnson, W. N. Johnson, T. Kamae, H. Katagiri, J. Kataoka, A. Kavelaars, N. Kawai, H. Kelly, M. Kerr, W. Klamra, J. Knödlseder, M. L. Kocian, N. Komin, F. Kuehn, M. Kuss, D. Landriu, L. Latronico, B. Lee, S. H. Lee, M. Lemoine-Goumard, A. M. Lionetto, F. Longo, F. Loparco, B. Lott, M. N. Lovellette, P. Lubrano, G. M. Madejski, A. Makeev, B. Marangelli, M. M. Massai, M. N. Mazziotta, J. E. McEnery, N. Menon, C. Meurer, P. F. Michelson, M. Minuti, N. Mirizzi, W. Mitthumsiri, T. Mizuno, A. A. Moiseev, C. Monte, M. E. Monzani, E. Moretti, A. Morselli, I. V. Moskalenko, S. Murgia, T. Nakamori, S. Nishino, P. L. Nolan, J. P. Norris, E. Nuss, M. Ohno, T. Ohsugi, N. Omodei, E. Orlando, J. F. Ormes, A. Paccagnella, D. Paneque, J. H. Panetta, D. Parent, M. Pearce, M. Pepe, A. Perazzo, M. Pesce-Rollins, P. Picozza, L. Pieri, M. Pinchera, F. Piron, T. A. Porter, L. Poupard, S. Rainò, R. Rando, E. Rapposelli, M. Razzano, A. Reimer, O. Reimer, T. Reposeur, L. C. Reyes, S. Ritz, L. S. Rochester, A. Y. Rodriguez, R. W. Romani, M. Roth, J. J. Russell, F. Ryde, S. Sabatini, H. F. W. Sadrozinski, D. Sanchez, A. Sand er, L. Sapozhnikov, P. M. Saz Parkinson, J. D. Scargle, T. L. Schalk, G. Scolieri, C. Sgrò, G. H. Share, M. Shaw, T. Shimokawabe, C. Shrader, A. Sierpowska-

Bartosik, E. J. Siskind, D. A. Smith, P. D. Smith, G. Spandre, P. Spinelli, J. L. Starck, T. E. Stephens, M. S. Strickman, A. W. Strong, D. J. Suson, H. Tajima, H. Takahashi, T. Takahashi, T. Tanaka, A. Tenze, S. Tether, J. B. Thayer, J. G. Thayer, D. J. Thompson, L. Tibaldo, O. Tibolla, D. F. Torres, G. Tosti, A. Tramacere, M. Turri, T. L. Usher, N. Vilchez, V. Vitale, P. Wang, K. Watters, B. L. Winer, K. S. Wood, T. Ylinen, and M. Ziegler. The Large Area Telescope on the Fermi Gamma-Ray Space Telescope Mission. *ApJ*, 697 (2):1071–1102, Jun 2009. doi: 10.1088/0004-637X/697/2/1071.

[29] Shriharsh P. Tendulkar, Victoria M. Kaspi, and Chitrang Patel. Radio Nondetection of the SGR 1806-20 Giant Flare and Implications for Fast Radio Bursts. *ApJ*, 827(1):59, August 2016. doi: 10.3847/0004-637X/827/1/59.

[30] M. S. Bessell, F. Castelli, and B. Plez. Model atmospheres broad-band colors, bolometric corrections and temperature calibrations for O - M stars. *A&A*, 333:231–250, May 1998.

[31] Zsolt Frei and James E. Gunn. Generating Colors and K Corrections From Existing Catalog Data. *AJ*, 108:1476, October 1994. doi: 10.1086/117172.

[32] M. Fukugita, T. Ichikawa, J. E. Gunn, M. Doi, K. Shimasaku, and D. P. Schneider. The Sloan Digital Sky Survey Photometric System. *AJ*, 111:1748, April 1996. doi: 10.1086/117915.

[33] N. Gehrels. Confidence Limits for Small Numbers of Events in Astrophysical Data. *ApJ*, 303:336, Apr 1986. doi: 10.1086/164079.

[34] J. Aleksić, S. Ansoldi, L. A. Antonelli, P. Antoranz, A. Babic, P. Bangale, M. Barceló, J. A. Barrio, J. Becerra González, W. Bednarek, E. Bernardini, B. Biasuzzi, A. Biland, M. Bitossi, O. Blanch, S. Bonnefoy, G. Bonnoli, F. Borracci, T. Bretz, E. Carmona, A. Carosi, R. Cecchi, P. Colin, E. Colombo, J. L. Contreras, D. Corti, J. Cortina, S. Covino, P. Da Vela, F. Dazzi, A. De Angelis, G. De Caneva, B. De Lotto, E. de Oña Wilhelmi, C. Delgado Mendez, A. Dettlaff, D. Dominis Prester, D. Dorner, M. Doro, S. Einecke, D. Eisenacher, D. Elsaesser, D. Fidalgo, D. Fink, M. V. Fonseca, L. Font, K. Frantzen, C. Fruck, D. Galindo, R. J. García López, M. Garczarczyk, D. Garrido Terrats, M. Gaug, G. Giavitto, N. Godinović, A. González Muñoz, S. R. Gozzini, W. Haberer, D. Hadasch, Y. Hanabata, M. Hayashida, J. Herrera, D. Hildebrand , J. Hose, D. Hrupec, W. Idec, J. M. Illa, V. Kadenius, H. Kellermann, M. L. Knoetig, K. Kodani, Y. Konno, J. Krause, H. Kubo, J. Kushida, A. La Barbera, D. Lelas, J. L. Lemus, N. Lewandowska, E. Lindfors, S. Lombardi, F. Longo, M. López, R. López-Coto, A. López-Oramas, A. Lorca, E. Lorenz, I. Lozano, M. Makariev, K. Mallot, G. Maneva, N. Mankuzhiyil, K. Mannheim, L. Maraschi, B. Marcote, M. Mariotti, M. Martínez, D. Mazin, U. Menzel, J. M. Miranda, R. Mirzoyan, A. Moralejo, P. Munar-Adrover, D. Nakajima, M. Negrello, V. Neustroev, A. Niedzwiecki, K. Nilsson, K. Nishijima, K. Noda, R. Orito, A. Overkemping, S. Paiano, M. Palatiello, D. Paneque, R. Paoletti,

J. M. Paredes, X. Paredes-Fortuny, M. Persic, J. Poutanen, P. G. Prada Moroni, E. Prandini, I. Puljak, R. Reinthal, W. Rhode, M. Ribó, J. Rico, J. Rodriguez Garcia, S. Rügamer, T. Saito, K. Saito, K. Satalecka, V. Scalzotto, V. Scapin, C. Schultz, J. Schlammer, S. Schmidl, T. Schweizer, S. N. Shore, A. Sillanpää, J. Sitarek, I. Snidaric, D. Sobczynska, F. Spanier, A. Stamerra, T. Steinbring, J. Storz, M. Strzys, L. Takalo, H. Takami, F. Tavecchio, L. A. Tejedor, P. Temnikov, T. Terzić, D. Tescaro, M. Teshima, J. Thaele, O. Tibolla, D. F. Torres, T. Toyama, A. Treves, P. Vogler, H. Wetteskind, M. Will, and R. Zanin. The major upgrade of the MAGIC telescopes, Part II: A performance study using observations of the Crab Nebula. *Astroparticle Physics*, 72:76–94, January 2016. doi: 10.1016/j.astropartphys.2015.02.005.

[35] Charles Meegan, Giselher Lichti, P. N. Bhat, Elisabetta Bissaldi, Michael S. Briggs, Valerie Connaughton, Roland Diehl, Gerald Fishman, Jochen Greiner, Andrew S. Hoover, Alexand er J. van der Horst, Andreas von Kienlin, R. Marc Kippen, Chryssa Kouveliotou, Sheila McBreen, W. S. Paciesas, Robert Preece, Helmut Steinle, Mark S. Wallace, Robert B. Wilson, and Colleen Wilson-Hodge. The Fermi Gamma-ray Burst Monitor. *ApJ*, 702(1):791–804, Sep 2009. doi: 10.1088/0004-637X/702/1/791.

[36] Scott D. Barthelmy, Louis M. Barbier, Jay R. Cummings, Ed E. Fenimore, Neil Gehrels, Derek Hullinger, Hans A. Krimm, Craig B. Markwardt, David M. Palmer, Ann Parsons, Goro Sato, Masaya Suzuki, Tadayuki Takahashi, Makota Tashiro, and Jack Tueller. The Burst Alert Telescope (BAT) on the SWIFT Midex Mission. *Space Sci. Rev.*, 120(3-4):143–164, Oct 2005. doi: 10.1007/s11214-005-5096-3.

[37] Masaru Matsuoka, Kazuyoshi Kawasaki, Shiro Ueno, Hiroshi Tomida, Mitsuhiro Kohama, Motoko Suzuki, Yasuki Adachi, Masaki Ishikawa, Tatehiro Mihara, Mutsumi Sugizaki, Naoki Isobe, Yujin Nakagawa, Hiroshi Tsunemi, Emi Miyata, Nobuyuki Kawai, Jun Kataoka, Mikio Morii, Atsumasa Yoshida, Hitoshi Negoro, Motoki Nakajima, Yoshihiro Ueda, Hirotaka Chujo, Kazutaka Yamaoka, Osamu Yamazaki, Satoshi Nakahira, Tetsuya You, Ryoji Ishiwata, Sho Miyoshi, Satoshi Eguchi, Kazuo Hiroi, Haruyoshi Katayama, and Ken Ebisawa. The MAXI Mission on the ISS: Science and Instruments for Monitoring All-Sky X-Ray Images. *PASJ*, 61:999, Oct 2009. doi: 10.1093/pasj/61.5.999.

[38] Timo Prusti, JHJ De Bruijne, Anthony GA Brown, A Vallenari, C Babusiaux, CAL Bailer-Jones, U Bastian, M Biermann, Dafydd Wyn Evans, L Eyer, et al. The gaia mission. *Astronomy & Astrophysics*, 595:A1, 2016.

[39] Nicholas M. Law, Shrinivas R. Kulkarni, Richard G. Dekany, Eran O. Ofek, Robert M. Quimby, Peter E. Nugent, Jason Surace, Carl C. Grillmair, Joshua S. Bloom, Mansi M. Kasliwal, Lars Bildsten, Tim Brown, S. Bradley Cenko, David Ciardi, Ernest Croner, S. George Djorgovski, Julian van Eyken, Alexei V. Filippenko, Derek B. Fox, Avishay Gal-Yam, David Hale, Nouhad Hamam,

George Helou, John Henning, D. Andrew Howell, Janet Jacobsen, Russ Laher, Sean Mattingly, Dan McKenna, Andrew Pickles, Dovi Poznanski, Gustavo Rahmer, Arne Rau, Wayne Rosing, Michael Shara, Roger Smith, Dan Starr, Mark Sullivan, Viswa Velur, Richard Walters, and Jeff Zolkower. The Palomar Transient Factory: System Overview, Performance, and First Results. *PASP*, 121(886):1395, Dec 2009. doi: 10.1086/648598.

[40] L. Mankiewicz, T. Batsch, A. Castro-Tirado, H. Czyrkowski, A. Cwiek, M. Cwiok, R. Dabrowski, M. Jelínek, G. Kasprowicz, A. Majcher, A. Majczyna, K. Malek, K. Nawrocki, L. Obara, R. Opiela, L. W. Piotrowski, M. Siudek, M. Sokolowski, R. Wawrzaszek, G. Wrochna, M. Zaremba, and A. F. Żarnecki. Pi of the Sky full system and the new telescope. In *Revista Mexicana de Astronomia y Astrofisica Conference Series*, volume 45 of *Revista Mexicana de Astronomia y Astrofisica Conference Series*, page 7, Dec 2014.

[41] A. Cwiek, L. Mankiewicz, T. Batsch, A. Castro-Tirado, H. Czyrkowski, M. Cwiok, R. Dabrowski, M. Jelínek, G. Kasprowicz, A. Majcher, K. Małek, K. Nawrocki, L. Obara, R. Opiela, L. W. Piotrowski, M. Siudek, M. Sokolowski, R. Wawrzaszek, G. Wrochna, M. Zaremba, and A. F. Zarnecki. *Pi of the Sky robotic observatories in Chile and Spain*, volume 9290 of *Society of Photo-Optical Instrumentation Engineers (SPIE) Conference Series*, page 92900T. 2014. doi: 10.1117/12.2076052.

[42] A. Biryukov, G. Beskin, S. Karpov, S. Bondar, E. Ivanov, E. Katkova, A. Perkov, and V. Sasyuk. The first light of Mini-MegaTORTORA wide-field monitoring system. *Baltic Astronomy*, 24:100–108, January 2015. doi: 10.1515/astro-2017-0208.

[43] Nicholas M. Law, Octavi Fors, Jeffrey Ratzloff, Philip Wulfken, Dustin Kavanaugh, David J. Sitar, Zachary Pruett, Mariah N. Birchard, Brad N. Barlow, Kipp Cannon, S. Bradley Cenko, Bart Dunlap, Adam Kraus, and Thomas J. Maccarone. Evryscope Science: Exploring the Potential of All-Sky Gigapixel-Scale Telescopes. *PASP*, 127(949):234, Mar 2015. doi: 10.1086/680521.

[44] Virginia Cunningham, S. Bradley Cenko, Eric Burns, Adam Goldstein, Amy Lien, Daniel Kocevski, Michael Briggs, Valerie Connaughton, M. Coleman Miller, Judith Racusin, and Matthew Stanbro. A Search for High-energy Counterparts to Fast Radio Bursts. *ApJ*, 879(1):40, Jul 2019. doi: 10.3847/1538-4357/ab2235.

[45] J. P. Macquart and RD Ekers. FRB event rate counts - II. Fluence, redshift, and dispersion measure distributions. *MNRAS*, 480(3):4211–4230, November 2018. doi: 10.1093/mnras/sty2083.

[46] R. D. Preece, M. S. Briggs, R. S. Mallozzi, G. N. Pendleton, W. S. Paciesas, and D. L. Band. The Synchrotron Shock Model Confronts a "Line of Death" in the BATSE Gamma-Ray Burst Data. *ApJ*, 506(1):L23–L26, October 1998. doi: 10.1086/311644.

[47] Thomas Wevers, Peter G. Jonker, Simon T. Hodgkin, Zuzanna Kostrzewa-Rutkowska, Diana L. Harrison, Guy Rixon, Gijs Nelemans, Maroussia Roelens, Laurent Eyer, Floor van Leeuwen, and Abdullah Yoldas. The fast transient sky with Gaia. *MNRAS*, 473(3):3854–3862, Jan 2018. doi: 10.1093/mnras/stx2625.

[48] Masahiro Hoshino and Jonathan Arons. Preferential positron heating and acceleration by synchrotron maser instabilities in relativistic positron-electron-proton plasmas. *Physics of Fluids B*, 3(3):818–833, March 1991. doi: 10.1063/1.859877.

[49] Killian Long and Asaf Pe'er. Synchrotron Maser from Weakly Magnetized Neutron Stars as the Emission Mechanism of Fast Radio Bursts. *ApJ*, 864(1): L12, September 2018. doi: 10.3847/2041-8213/aada0b.

[50] A. Bruce Langdon, Jonathan Arons, and Claire E. Max. Structure of relativistic magnetosonic shocks in electron-positron plasmas. *Phys. Rev. Lett.*, 61(7): 779–782, August 1988. doi: 10.1103/PhysRevLett.61.779.

[51] Andrei M. Beloborodov. Blast Waves from Magnetar Flares and Fast Radio Bursts. *arXiv e-prints*, art. arXiv:1908.07743, August 2019.

[52] Ben Margalit, Brian D. Metzger, and Lorenzo Sironi. Constraints on the Engines of Fast Radio Bursts. *arXiv e-prints*, art. arXiv:1911.05765, November 2019.

[53] C. J. Law, M. W. Abruzzo, C. G. Bassa, G. C. Bower, S. Burke-Spolaor, B. J. Butler, T. Cantwell, S. H. Carey, S. Chatterjee, J. M. Cordes, P. Demorest, J. Dowell, R. Fender, K. Gourdji, K. Grainge, J. W. T. Hessels, J. Hickish, V. M. Kaspi, T. J. W. Lazio, M. A. McLaughlin, D. Michilli, K. Mooley, Y. C. Perrott, S. M. Ransom, N. Razavi-Ghods, M. Rupen, A. Scaife, P. Scott, P. Scholz, A. Seymour, L. G. Spitler, K. Stovall, S. P. Tendulkar, D. Titterington, R. S. Wharton, and P. K. G. Williams. A Multi-telescope Campaign on FRB 121102: Implications for the FRB Population. *ApJ*, 850(1):76, November 2017. doi: 10.3847/1538-4357/aa9700.

[54] Eran O. Ofek. Soft Gamma-Ray Repeaters in Nearby Galaxies: Rate, Luminosity Function, and Fraction among Short Gamma-Ray Bursts. *ApJ*, 659(1): 339–346, April 2007. doi: 10.1086/511147.

[55] Piero Madau and Mark Dickinson. Cosmic Star-Formation History. *ARA&A*, 52:415–486, August 2014. doi: 10.1146/annurev-astro-081811-125615.

[56] Laura Chomiuk and Matthew S. Povich. Toward a Unification of Star Formation Rate Determinations in the Milky Way and Other Galaxies. *AJ*, 142(6):197, December 2011. doi: 10.1088/0004-6256/142/6/197.

[57] S. R. Kulkarni, E. O. Ofek, J. D. Neill, Z. Zheng, and M. Juric. Giant Sparks at Cosmological Distances? *ApJ*, 797(1):70, December 2014. doi: 10.1088/0004-637X/797/1/70.

[58] Wenbin Lu and Pawan Kumar. On the radiation mechanism of repeating fast radio bursts. *MNRAS*, 477(2):2470–2493, Jun 2018. doi: 10.1093/mnras/sty716.

[59] Yuan-Pei Yang, Bing Zhang, and Jian-Yan Wei. How Bright Are Fast Optical Bursts Associated With Fast Radio Bursts? *ApJ*, 878(2):89, Jun 2019. doi: 10.3847/1538-4357/ab1fe2.

[60] Ben Margalit, Brian D. Metzger, Edo Berger, Matt Nicholl, Tarraneh Eftekhari, and Raffaella Margutti. Unveiling the engines of fast radio bursts, superluminous supernovae, and gamma-ray bursts. *MNRAS*, 481(2):2407–2426, December 2018. doi: 10.1093/mnras/sty2417.

[61] E. Petroff, M. Bailes, E. D. Barr, B. R. Barsdell, N. D. R. Bhat, F. Bian, S. Burke-Spolaor, M. Caleb, D. Champion, P. Chandra, G. Da Costa, C. Delvaux, C. Flynn, N. Gehrels, J. Greiner, A. Jameson, S. Johnston, M. M. Kasliwal, E. F. Keane, S. Keller, J. Kocz, M. Kramer, G. Leloudas, D. Malesani, J. S. Mulchaey, C. Ng, E. O. Ofek, D. A. Perley, A. Possenti, B. P. Schmidt, Yue Shen, B. Stappers, P. Tisserand , W. van Straten, and C. Wolf. A real-time fast radio burst: polarization detection and multiwavelength follow-up. *MNRAS*, 447(1):246–255, Feb 2015. doi: 10.1093/mnras/stu2419.

[62] R. M. Shannon, J. P. Macquart, K. W. Bannister, R. D. Ekers, C. W. James, S. Osłowski, H. Qiu, M. Sammons, A. W. Hotan, M. A. Voronkov, R. J. Beresford, M. Brothers, A. J. Brown, J. D. Bunton, A. P. Chippendale, C. Haskins, M. Leach, M. Marquarding, D. McConnell, M. A. Pilawa, E. M. Sadler, E. R. Troup, J. Tuthill, M. T. Whiting, J. R. Allison, C. S. Anderson, M. E. Bell, J. D. Collier, G. Gürkan, G. Heald, and C. J. Riseley. The dispersion-brightness relation for fast radio bursts from a wide-field survey. *Nature*, 562(7727):386–390, October 2018. doi: 10.1038/s41586-018-0588-y.

[63] Shotaro Yamasaki, Tomonori Totani, and Norita Kawanaka. A blind search for prompt gamma-ray counterparts of fast radio bursts with Fermi-LAT data. *MNRAS*, 460(3):2875–2880, August 2016. doi: 10.1093/mnras/stw1206.

[64] I. Andreoni, J. Cooke, S. Webb, A. Rest, T. Pritchard, M. Caleb, S. W. Chang, W. Farah, A. Lien, A. Möller, M. E. Ravasio, T. M. C. Abbott, S. Bhandari, A. Cucchiara, C. Flynn, F. Jankowski, E. F. Keane, T. J. Moriya, C. A. Onken, A. Parthasarathy, D. C. Price, E. Petroff, S. Ryder, D. Vohl, and C. Wolf. Probing the extragalactic fast transient sky at minute time-scales with DECam. *MNRAS*, 491(4):5852–5866, February 2020. doi: 10.1093/mnras/stz3381.

[65] Michael W. Richmond, Masaomi Tanaka, Tomoki Morokuma, Shigeyuki Sako, Ryou Ohsawa, Noriaki Arima, Nozomu Tominaga, Mamoru Doi, Tsutomu

Aoki, Ko Arimatsu, Makoto Ichiki, Shiro Ikeda, Yoshifusa Ita, Toshihiro Kasuga, Koji S. Kawabata, Hideyo Kawakita, Naoto Kobayashi, Mitsuru Kokubo, Masahiro Konishi, Hiroyuki Maehara, Hiroyuki Mito, Takashi Miyata, Yuki Mori, Mikio Morii, Kentaro Motohara, Yoshikazu Nakada, Shin-Ich, Hiroki Onozato, Yuki Sarugaku, Mikiya Sato, Toshikazu Shigeyama, Takao Soyano, Hidenori Takahashi, Ataru Tanikawa, Ken'ichi Tarusawa, Seitaro Urakawa, Fumihiko Usui, Junichi Watanabe, Takuya Yamashita, and Makoto Yoshikawa. An optical search for transients lasting a few seconds. *arXiv e-prints*, art. arXiv:1910.11343, Oct 2019.

[66] Christopher D. Bochenek, Vikram Ravi, Konstantin V. Belov, Gregg Hallinan, Jonathon Kocz, Shri R. Kulkarni, and Dan L. McKenna. A fast radio burst associated with a Galactic magnetar. *arXiv e-prints*, art. arXiv:2005.10828, May 2020.

[67] B. C. Andersen, K. M. Band ura, M. Bhardwaj, A. Bij, M. M. Boyce, P. J. Boyle, C. Brar, T. Cassanelli, P. Chawla, T. Chen, J. F. Cliche, A. Cook, D. Cubranic, A. P. Curtin, N. T. Denman, M. Dobbs, F. Q. Dong, M. Fandino, E. Fonseca, B. M. Gaensler, U. Giri, D. C. Good, M. Halpern, A. S. Hill, G. F. Hinshaw, C. Höfer, A. Josephy, J. W. Kania, V. M. Kaspi, T. L. Landecker, C. Leung, D. Z. Li, H. H. Lin, K. W. Masui, R. Mckinven, J. Mena-Parra, M. Merryfield, B. W. Meyers, D. Michilli, N. Milutinovic, A. Mirhosseini, M. Münchmeyer, A. Naidu, L. B. Newburgh, C. Ng, C. Patel, U. L. Pen, T. Pinsonneault-Marotte, Z. Pleunis, B. M. Quine, M. Rafiei-Ravandi, M. Rahman, S. M. Ransom, A. Renard, P. Sanghavi, P. Scholz, J. R. Shaw, K. Shin, S. R. Siegel, S. Singh, R. J. Smegal, K. M. Smith, I. H. Stairs, C. M. Tan, S. P. Tendulkar, I. Tretyakov, K. Vanderlinde, H. Wang, D. Wulf, and A. V. Zwaniga. A bright millisecond-duration radio burst from a Galactic magnetar. *arXiv e-prints*, art. arXiv:2005.10324, May 2020.

[68] A. Ridnaia, D. Svinkin, D. Frederiks, A. Bykov, S. Popov, R. Aptekar, S. Golenetskii, A. Lysenko, A. Tsvetkova, M. Ulanov, and T. Cline. A peculiar hard X-ray counterpart of a Galactic fast radio burst. *arXiv e-prints*, art. arXiv:2005.11178, May 2020.

[69] MAGIC Collaboration, V. A. Acciari, S. Ansoldi, L. A. Antonelli, A. Arbet Engels, C. Arcaro, D. Baack, Babić, A. , B. Banerjee, P. Bangale, U. Barres de Almeida, J. A. Barrio, J. Becerra González, W. Bednarek, E. Bernardini, A. Berti, J. Besenrieder, W. Bhattacharyya, C. Bigongiari, A. Biland, O. Blanch, G. Bonnoli, R. Carosi, G. Ceribella, A. Chatterjee, S. M. Colak, P. Colin, E. Colombo, J. L. Contreras, J. Cortina, S. Covino, P. Cumani, V. D'Elia, P. da Vela, F. Dazzi, A. de Angelis, B. de Lotto, M. Delfino, J. Delgado, F. di Pierro, A. Domínguez, D. Dominis Prester, D. Dorner, M. Doro, S. Einecke, D. Elsaesser, V. Fallah Ramazani, A. Fattorini, A. Fernández-Barral, G. Ferrara, D. Fidalgo, L. Foffano, M. V. Fonseca, L. Font, C. Fruck, S. Gallozzi, R. J. García López, M. Garczarczyk, M. Gaug,

P. Giammaria, Godinović, N. , D. Guberman, D. Hadasch, A. Hahn, T. Hassan, J. Herrera, J. Hoang, D. Hrupec, S. Inoue, K. Ishio, Y. Iwamura, H. Kubo, J. Kushida, Kuveždić, D. , A. Lamastra, D. Lelas, F. Leone, E. Lindfors, S. Lombardi, F. Longo, M. López, A. López-Oramas, C. Maggio, P. Majumdar, M. Makariev, G. Maneva, M. Manganaro, K. Mannheim, L. Maraschi, M. Mariotti, M. Martínez, S. Masuda, D. Mazin, M. Minev, J. M. Miranda, R. Mirzoyan, E. Molina, A. Moralejo, V. Moreno, E. Moretti, V. Neustroev, A. Niedzwiecki, M. Nievas Rosillo, C. Nigro, K. Nilsson, D. Ninci, K. Nishijima, K. Noda, L. Nogués, S. Paiano, J. Palacio, D. Paneque, R. Paoletti, J. M. Paredes, G. Pedaletti, P. Peñil, M. Peresano, M. Persic, P. G. Prada Moroni, E. Prand ini, I. Puljak, J. R. Garcia, W. Rhode, M. Ribó, J. Rico, C. Righi, A. Rugliancich, L. Saha, T. Saito, K. Satalecka, T. Schweizer, J. Sitarek, Šnidarić, I. , D. Sobczynska, A. Somero, A. Stamerra, M. Strzys, Surić, T. , F. Tavecchio, P. Temnikov, Terzić, T. , M. Teshima, N. Torres-Albà, S. Tsujimoto, G. Vanzo, M. Vazquez Acosta, I. Vovk, J. E. Ward, M. Will, D. Zarić, B. Marcote, L. G. Spitler, J. W. T. Hessels, K. Kashiyama, K. Murase, V. Bosch-Ramon, D. Michilli, and A. Seymour. Constraining very-high-energy and optical emission from FRB 121102 with the MAGIC telescopes. *MNRAS*, 481(2):2479–2486, December 2018. doi: 10.1093/mnras/sty2422.

[70] C. Casentini, F. Verrecchia, M. Tavani, A. Ursi, L. A. Antonelli, A. Argan, G. Barbiellini, A. Bulgarelli, P. Caraveo, M. Cardillo, P. W. Cattaneo, A. Chen, E. Costa, I. Donnarumma, M. Feroci, A. Ferrari, F. Fuschino, M. Galli, A. Giuliani, C. Labanti, F. Lazzarotto, P. Lipari, F. Longo, F. Lucarelli, M. Marisaldi, A. Morselli, F. Paoletti, N. Parmiggiani, A. Pellizzoni, G. Piano, M. Pilia, C. Pittori, and S. Vercellone. AGILE Observations of Two Repeating Fast Radio Bursts with Small Intrinsic Dispersion Measure. *arXiv e-prints*, art. arXiv:1911.10189, Nov 2019.

[71] Akash Anumarlapudi, Varun Bhalerao, Shriharsh P. Tendulkar, and Arvind Balasubramanian. Prompt X-ray emission from Fast Radio Bursts — Upper limits with AstroSat. *arXiv e-prints*, art. arXiv:1911.00537, Nov 2019.

[72] P. Scholz, S. Bogdanov, J. W. T. Hessels, R. S. Lynch, L. G. Spitler, C. G. Bassa, G. C. Bower, S. Burke-Spolaor, B. J. Butler, S. Chatterjee, J. M. Cordes, K. Gourdji, V. M. Kaspi, C. J. Law, B. Marcote, M. A. McLaughlin, D. Michilli, Z. Paragi, S. M. Ransom, A. Seymour, S. P. Tendulkar, and R. S. Wharton. Simultaneous X-Ray, Gamma-Ray, and Radio Observations of the Repeating Fast Radio Burst FRB 121102. *ApJ*, 846(1):80, Sep 2017. doi: 10.3847/1538-4357/aa8456.

[73] L. K. Hardy, V. S. Dhillon, L. G. Spitler, S. P. Littlefair, R. P. Ashley, A. De Cia, M. J. Green, P. Jaroenjittichai, E. F. Keane, P. Kerry, M. Kramer, D. Malesani, T. R. Marsh, S. G. Parsons, A. Possenti, S. Rattanasoon, and D. I. Sahman. A search for optical bursts from the repeating fast radio burst FRB 121102. *MNRAS*, 472(3):2800–2807, Dec 2017. doi: 10.1093/mnras/stx2153.

[74] C. Casentini, F. Verrecchia, M. Tavani, A. Ursi, L. A. Antonelli, A. Argan, G. Barbiellini, A. Bulgarelli, P. Caraveo, M. Cardillo, P. W. Cattaneo, A. Chen, E. Costa, I. Donnarumma, M. Feroci, A. Ferrari, F. Fuschino, M. Galli, A. Giuliani, C. Labanti, F. Lazzarotto, P. Lipari, F. Longo, F. Lucarelli, M. Marisaldi, A. Morselli, F. Paoletti, N. Parmiggiani, A. Pellizzoni, G. Piano, M. Pilia, C. Pittori, and S. Vercellone. AGILE Observations of Two Repeating Fast Radio Bursts with Low Intrinsic Dispersion Measures. *ApJ*, 890(2):L32, February 2020. doi: 10.3847/2041-8213/ab720a.

[75] M. Pilia, M. Burgay, A. Possenti, A. Ridolfi, V. Gajjar, A. Corongiu, D. Perrodin, G. Bernardi, G. Naldi, G. Pupillo, F. Ambrosino, G. Bianchi, A. Burtovoi, P. Casella, C. Casentini, M. Cecconi, C. Ferrigno, M. Fiori, K. C. Gendreau, A. Ghedina, G. Naletto, L. Nicastro, P. Ochner, E. Palazzi, F. Panessa, A. Papitto, C. Pittori, N. Rea, G. A. Rodriguez Castillo, V. Savchenko, G. Setti, M. Tavani, A. Trois, M. Trudu, M. Turatto, A. Ursi, F. Verrecchia, and L. Zampieri. The lowest frequency Fast Radio Bursts: Sardinia Radio Telescope detection of the periodic FRB 180916 at 328 MHz. *arXiv e-prints*, art. arXiv:2003.12748, March 2020.

[76] M. Tavani, F. Verrecchia, C. Casentini, M. Perri, A. Ursi, L. Pacciani, C. Pittori, A. Bulgarelli, G. Piano, M. Pilia, G. Bernardi, A. Addis, L. A. Antonelli, A. Argan, L. Baroncelli, P. Caraveo, P. W. Cattaneo, A. Chen, E. Costa, G. Di Persio, I. Donnarumma, Y. Evangelista, M. Feroci, A. Ferrari, V. Fioretti, F. Lazzarotto, F. Longo, A. Morselli, F. Paoletti, N. Parmiggiani, A. Trois, S. Vercellone, G. Naldi, G. Pupillo, G. Bianchi, and S. Puccetti. Gamma-Ray and X-Ray Observations of the Periodic-Repeater FRB 180916 During Active Phases. *arXiv e-prints*, art. arXiv:2004.03676, April 2020.

Table 2.1: Existing Surveys and Instruments.

Instrument	Band	Effective duration (days)	Detection threshold	Timescales	FOV
MAGIC [a]	50 GeV–50 TeV	**613**	7.6×10^{-12} photons cm^{-2} s^{-1} [l]	e.g., 10 ms	4.8 sq. deg.
Fermi/LAT[b]	20 MeV–300 GeV	4132	3×10^{-9}photons cm^{-2} s^{-1} [m]	0.1 s to 100 s	2.4 sr
Fermi/GBM[c]	8 keV–40 MeV	4132	0.74 photons cm^{-2} s^{-1}	16 ms to 8.192 s	> 8 sr
***CGRO*/BATSE**[d]	30 keV–1.9 MeV	3348	3×10^{-8} erg cm^{-2} s^{-1}	64 ms to 1.024 s	4π sr
SWIFT/BAT[e]	15–150 keV	5344	$\sim 10^{-8}$ erg cm^{-2} s^{-1}	4 ms to 32 s	1.4 sr
MAXI/GSC[f]	2–30 keV	3729	$\sim 7 \times 10^{-10}$ erg cm^{-2} s^{-1}	1 s to 30 s	$1.5^{o} \times 160^{o}$
Gaia[g]	330–1050 nm	2112	G=20.6 mag (Vega)	4.5 s	$0.85^{o} \times 0.66^{o}$
PTF/iPTF[h]	$\approx$ 400–700 nm	973	R $\approx$ 20.6 (AB)	60 s	$\approx$ 8 sq. deg.
Pi of the Sky[i]	$\approx$ 320–900 nm	756	V=12 mag (assume Vega)	10 s	6400 sq. deg.
MMT-9[j]	$\approx$ 400–800 nm	644	V=11 mag (assume Vega)	0.128 s	900 sq. deg.
Evryscope[k]	$\approx$ 400–700 nm	533	V=16.4 mag (assume Vega)	120 s	8660 sq. deg.

a Aleksić et al. [34]. Major Atmospheric Gamma Imaging Cherenkov telescopes (MAGIC) consists of two Imaging Atmospheric Cherenkov telescopes. One has been operating since April 2005, the other since 2009 Fall, and both were upgraded in 2012 summer. Here we calculate the duration from September 2009 and assume **4-hour observation per day**.

b [28] and https://fermi.gsfc.nasa.gov. The Fermi Gamma-Ray Space Telescope (FGST), was launched on June 11, 2008.

c [35] and https://fermi.gsfc.nasa.gov. The threshold is for a pulse in the band of 50–300 keV and 1 s peak.

d **https://heasarc.gsfc.nasa.gov/docs/cgro/cgro/. The Burst And Transient Source Experiment (BATSE) on the Compton Gamma Ray Observatory (CGRO) was in operation from April 2000 to June 2009. The threshold was for a 1-s burst.**

e [36]. The BAT monitor archive begins on February 12, 2005. The threshold is for a $\sim$ 1 s peak.

f [37]. MAXI was launched on 2009 July 16. The threshold corresponds to one International Space Station orbit, in which an objects stay in the FOV for at least 45 s. For the timescales, we ignore those $\geq$ one scan as they are too long for a ms-scale transient.

g [38]; https://www.cosmos.esa.int/web/gaia; and http://www.astro.utu.fi/~cflynn/galdyn/lecture10.html. The spacecraft was launched on 19 December 2013.

h [39]. Operating from March 2009 to February 2017.

i [40] and [41]. The full system started to operate in July 2013. Assume the Vega magnitude system.

j Biryukov et al. [42]; Mini-MegaTORTORA. The high time resolution started to operate in June 2014. Assume the Vega magnitude system.

k [43]. The Evryscope-South started to operate since May 2015. We do not include Evryscope-North since it started operations in 2019. Assume the Vega magnitude system.

l The sensitivity corresponds to a 50-hour observation of a point source with Crab-nebula-like spectrum above 104 GeV. However, we increase the threshold to 2.4×10^{-11} photons cm^{-2} s^{-1} to satisfy the requirements that at least one photon is received within 10 ms by the *MAGIC* effective collecting area of 10^{9} cm^{2}.

m The detection threshold corresponds to a one-year survey at high latitude and > 100 MeV, assuming a source photon spectral index of –2. However, for the **shortest** timescale of 0.1 s, we increase the threshold to 7×10^{-8} photons cm^{-2} s^{-1} to satisfy the requirements that at least one photon is received within 0.1 s by the *Fermi*/LAT effective collecting area of 8000 cm^{2}.

Table 2.2: Results.

Instrument	ν_c (Hz)	Flux threshold f_0 (erg cm^{-2} s^{-1})	Fluence threshold F_0 (Jy ms Hz)	Rate[a] (sky^{-1} d^{-1})	η_ν	η[a]
MAGIC	6.05×10^{27}	5.54×10^{-8}	5.54×10^{16}	**42**	$\mathbf{1.61 \times 10^{-10}}$	$\mathbf{1.65 \times 10^{6}}$
Fermi/LAT	3.63×10^{25}	3.85×10^{-7}	3.85×10^{18}	3.80×10^{-3}	4.07×10^{-7}	1.67×10^{6}
		5.19×10^{-10}	5.19×10^{18}		5.49×10^{-7}	2.25×10^{6}
Fermi/GBM	4.84×10^{21}	6.39×10^{-7}	1.02×10^{18}	1.14×10^{-3} (0.14)	1.56×10^{-4}	2.56×10^{5} (2.27×10^{6})
		2.82×10^{-8}	2.31×10^{19}		3.54×10^{-3}	5.79×10^{6} (5.15×10^{7})
***CGRO*/BATSE**	2.33×10^{20}	1.19×10^{-7}	7.59×10^{17}	8.96×10^{-4}	2.77×10^{-5}	1.70×10^{5}
		2.96×10^{-8}	3.04×10^{18}		1.11×10^{-4}	6.81×10^{5}
Swift/BAT	1.99×10^{19}	1.58×10^{-7}	6.32×10^{16}	5.04×10^{-3}	1.01×10^{-5}	3.11×10^{4}
		1.77×10^{-9}	5.66×10^{18}		9.07×10^{-4}	2.78×10^{6}
MAXI/GSC	3.87×10^{18}	4.70×10^{-9}	4.70×10^{17}	1.38×10^{-1} (9.00)	2.54×10^{-3}	1.04×10^{6} (6.95×10^{6})
		7.00×10^{-10}	2.10×10^{18}		1.14×10^{-2}	4.65×10^{6} (3.11×10^{7})
Gaia	5.97×10^{14}	6.13×10^{-14}	2.76×10^{13}	1.04×10^{2}	5.15×10^{-3}	1.24×10^{3}
PTF/iPTF	5.89×10^{14}	7.92×10^{-14}	4.77×10^{14}	15.9	2.52×10^{-2}	9.13×10^{3}
Pi of the Sky	6.35×10^{14}	2.00×10^{-10}	2.00×10^{17}	2.56×10^{-2}	7.30×10^{-1}	1.06×10^{5}
MMT-9	5.62×10^{14}	5.65×10^{-10}	7.23×10^{15}	2.13×10^{-1}	6.16×10^{-2}	1.95×10^{4}
Evryscope	5.89×10^{14}	4.47×10^{-12}	5.36×10^{16}	2.68×10^{-2}	1.55×10^{-1}	5.63×10^{4}

a Rate and η results outside parentheses assume no FRB-counterpart detection (Section 2.5.1), and are to be interpreted as 95%-confidence upper limits. Results in parentheses assume that all unclassified short transients were FRB counterparts (Section 2.5.2), and are thus to be interpreted as nominal upper limits.

Table 2.3: Theoretical Predictions and Expected Counterpart Rate

Model	Band	$t_{Counterpart}$	η_ν	η	Instrument	Timescale[a]	Rate (sky^{-1} day^{-1})	$\langle n \rangle$ [b] (days)	Survey Duration [c] (days)
Metzger	ν_1=100 MeV	~ 3 ms	$\sim 2.8 \times 10^{-9}$	$\sim 6.0 \times 10^{4}$	*Fermi*/LAT	0.1 s	2.29×10^{-6}	2.29×10^{6}	4132
Metzger	ν_1=1 MeV	~ 50 ms	$\sim 4.1 \times 10^{-7}$	$\sim 10^{5}$	*Fermi*/GBM	64 ms	2.13×10^{-5}	7.36×10^{4}	4132
					***CGRO*/BATSE**	64 ms	1.89×10^{-4}	5.30×10^{3}	3348
Metzger	ν_1=100 keV[d]	~ 1 s	$\sim 4.1 \times 10^{-6}$	$\sim 10^{5}$	*Swift*/ BAT	1.024 s	10^{-4}	8.95×10^{4}	5344
					***CGRO*/BATSE**	1.024 s	8.94×10^{-6}	1.12×10^{5}	3348
Metzger	ν_1=10 keV	~ 1 s	$\sim 4.1 \times 10^{-5}$	$\sim 10^{5}$	*Fermi*/GBM	1.024 s	1.01×10^{-6}	1.55×10^{6}	4132
Beloborodov	Optical	~ 1 s	$\lesssim 2.0 \times 10^{-1}$	$\lesssim 10^{5}$	*Gaia*	4.5 s	$\lesssim 6.31 \times 10^{5}$	$\gtrsim 1.17 \times 10^{-1}$	2112
Yang 1a[e]	Optical	~ 1 ms	$\lesssim 2.0 \times 10^{-2}$	$\lesssim 1.2 \times 10^{4}$	*Gaia*	4.5 s	$\lesssim 3.98 \times 10^{3}$	$\gtrsim 18$	2112
			$\gtrsim 1.7 \times 10^{-13}$	$\gtrsim 1.2 \times 10^{-7}$	*Gaia*	4.5 s	$\gtrsim 1.76 \times 10^{-21}$	$\lesssim 4.18 \times 10^{25}$	
Yang 1b	Optical	~ a few ×10 s	$\lesssim 1.7 \times 10^{2}$	$\lesssim 10^{8}$	*Gaia*	≈45 s	$\lesssim 1.40 \times 10^{11}$	$\gtrsim 5.27 \times 10^{-7}$	2112
Yang 1c	Optical	~ 1 ms	$\lesssim 6.6 \times 10^{-7}$	$\lesssim 3.8 \times 10^{-1}$	*Gaia*	4.5 s	$\lesssim 5.51 \times 10^{-7}$	$\gtrsim 1.34 \times 10^{11}$	2112
Yang 2a	Optical	~ 1 ms	$\lesssim 6.6 \times 10^{-11}$	$\lesssim 3.8 \times 10^{-5}$	*Gaia*	4.5 s	$\lesssim 8.73 \times 10^{-16}$	$\gtrsim 8.43 \times 10^{19}$	2112
Yang 2b	Optical	~ 1 ms	$\lesssim 6.6 \times 10^{-10}$	$\lesssim 3.8 \times 10^{-4}$	*Gaia*	4.5 s	$\lesssim 1.38 \times 10^{-13}$	$\gtrsim 5.32 \times 10^{17}$	2112

a The **shortest** instrumental timescale above the theoretical counterpart duration.
b The expected number of days to detect one single counterpart using the corresponding instrument (Poisson errors neglected).
c Same as the effective duration in Table 2.1.
d η interpolated between 1 MeV and 10 keV.
e e.g., "1a" refers to case 1, scenario (a) in the model (Section 2.6.1).

Chapter 3

A COMPREHENSIVE OBSERVATIONAL STUDY OF THE FRB 121102 PERSISTENT RADIO SOURCE

The work presented in this chapter can be found at:

- Ge Chen, Vikram Ravi and Gregg W. Hallinan. A comprehensive observational study of the FRB 121102 persistent radio source. *Published in the Astrophysical Journal*, 2023.

ABSTRACT

FRB 121102 is the first fast radio burst source to be spatially associated with a persistent radio source (QRS121102), the nature of which remains unknown. We constrain the physical size of QRS121102 by measuring its flux-density variability with the VLA from 12 to 26 GHz. Any such variability would likely be due to Galactic refractive scintillation, and would require the source radius to be $\lesssim 10^{17}$ cm at the host-galaxy redshift. We found the radio variability lower than the scintillation theory predictions for such a small source, leaving open the possibility for non-AGN models for QRS121102. In addition, we roughly estimated the mass of any potential supermassive black hole (BH) associated with QRS121102 from the line width of the host-galaxy Hα emission using a new optical spectrum from the Keck Observatory. The line width indicates a supermassive BH mass of $\lesssim 10^{4\sim5}$ $M_{\odot}$, too low for the observed radio luminosity and X-ray luminosity constraints, if QRS121102 were an AGN. Finally, some dwarf galaxies that host supermassive black holes may be the stripped cores of massive galaxies during the tidal interactions with companion systems. We find no nearby galaxy at the same redshift as the QRS121102 host from low-resolution Keck spectra, or from the PanSTARRS catalog. In conclusion, we find no evidence supporting the hypothesis that QRS121102 is an AGN. We instead argue that the inferred size, and the flat radio spectrum, favors a plerion interpretation. We urge continued broadband radio monitoring of QRS121102 to search for long-term evolution.

3.1 Introduction

Fast radio bursts (FRBs) are a class of transient phenomena wherein energies $\gtrsim 10^{35}$ erg are released on timescales $\ll 1$ s at radio wavelengths (e.g., [2]). The progenitor and emission processes of FRBs remain uncertain. Hundreds of FRB sources have been reported, and over 20 of them have been found to repeat (e.g., [3]). Repeaters and non-repeaters are reported to show statistically different characters (luminosity, pulse width, temporal-spectral structures, etc.), yet it remains unclear whether or not they originate from two distinct populations. FRB 121102 was the first repeater detected [4, 5], and so far one of the most extensively studied FRB sources. The bursts are found to have a $\sim$ 160-day periodicity [6], and the source has been localized within a star forming region of a low-metallicity dwarf galaxy at a redshift of 0.19273 [7–9], giving a luminosity distance of 971 Mpc (using the recent Planck results implemented in *astropy*: $H_0 = 67.4$ km s^{-1} kpc^{-1}, $\Omega_m = 0.315$, $\Omega_\Lambda = 0.685$; [10]).

FRB 121102 is one of only two FRBs reported to be spatially associated with persistent radio emission of unknown origin [9, 11]. In the case of FRB 121102, the centroid of the persistent emission is within 12 mas (40 pc; 95% confidence level) from the FRB source. The emission shows a flat spectrum from $\sim$ 400 MHz to $\sim$ 6 GHz (flux density ≈ 200 μJy), and decreases at higher frequencies (166 ± 9, 103 ± 7 and 66 ± 7 μJy at 10, 15 and 22 GHz, respectively) [12, 13]. It remains unresolved by very long baseline interferometry (VLBI) at 5 GHz, indicating a radius below $\sim$ 0.2 mas, or $\sim 10^{18}$ cm (0.35 pc) at the host-galaxy redshift [9]. A flux-density amplitude modulation of $\sim$ 30% has been reported at 3 GHz [12], consistent with refractive scintillation by the Milky Way interstellar medium (ISM) (e.g., [14, 15]). No X-ray counterpart has been detected with XMM-Newton and Chandra [12].

If we remain agnostic regarding models for the origin of FRBs, a compact radio source like that associated with FRB 121102, with a luminosity of $\sim 2 \times 10^{29}$ erg s^{-1} Hz^{-1}, would most likely be ascribed to AGN activity. Several AGN-like radio sources of similar luminosities have been reported to be hosted by dwarf galaxies (e.g., [16, 17]). Although Tendulkar et al. [9] has found the host-galaxy optical spectrum to be consistent with intense star formation based on the BPT diagnostics [18], it is rare but not unheard of [at the $\sim$ 0.1% level; 19] for galaxies classified as star forming according to BPT diagnostics to host radio-loud AGN. This may be substantially more common among the dwarf galaxy population: the majority of the Reines et al. [16] sample of dwarf galaxies with optical spectra

hosting candidate radio AGN are classified as star forming on BPT diagrams. The radio source associated with FRB 121102 is too compact and too luminous to be associated with star-formation activity [12]. Other possible origins include a supernova afterglow powered by interaction with a dense circum-stellar medium [20], the afterglow of a long-duration gamma-ray burst (e.g., [21]), and an extreme pulsar wind nebula (PWN; e.g., [22]).

In this paper, we investigate the nature of the persistent radio source associated with FRB 121102 ("QRS121102" hereafter) using new data from the Karl G. Jansky Very Large Array (VLA) and the Low Resolution Imaging Spectrometer (LRIS) at the Keck Observatory. We adopt the host redshift of 0.19273 [9] for all relevant calculations hereafter. In Section 3.2, we describe the observations. In Section 4.3, we first measure the flux-density modulation of QRS121102 in the K-band (18 to 26 GHz) and the Ku-band (12 to 18 GHz), where refractive scintillation is expected to produce larger modulations than previously observed at 5 GHz. We also separately investigate the hypothesis that QRS121102 is powered by a supermassive or intermediate-mass black hole (BH) using a medium-resolution LRIS spectrum, and evaluate whether or not the host galaxy belongs to a galaxy group using the low-resolution LRIS spectra. In Section 4.4, we first constrain the size of QRS121102 by comparing its flux-density modulation with that predicted by scattering theory. In addition, we compare the AGN population with our dynamical BH mass estimation, stellar mass estimation, and radio and X-ray luminosity constraints. We conclude in Section 4.5 that an AGN hypothesis for QRS121102 is unlikely.

3.2 Observations

3.2.1 VLA radio observations

We have observed the persistent radio source (QRS121102) in the VLA K-band (18 to 26 GHz) and Ku-band (12 to 18 GHz) using the C configuration. The channel width was 2 MHz and the integration time was 3 s for the K-band observations and 2 s for the Ku-band observations. The observations include six epochs from 2017 May 29 to 2017 August 10 (Table 3.1). In each epoch, the observation started with a single scan of the primary calibrator 3C147 (Field 0) for flux scale and bandpass calibration, and then a few cycles of the phase calibrator 1 J0555+3948 (Field 1), phase calibrator 2 J0518+3306 (Field 2), and QRS121102 (Field 3) (Table 3.2).

3.2.2 Keck optical observations

The optical spectra used in this work were obtained using Keck/LRIS. We obtained two types of observations. One, with medium spectral resolution, was used to measure the spectral width of the Hα emission line associated with the FRB 121102 host galaxy. The other, with low spectral resolution, used two slit orientations to obtain spectra of galaxies immediately adjacent to the FRB 121102 host.

The medium resolution spectrum of the FRB 121102 host was obtained on October 12, 2018 using the 1.0" longslit and the D560 dichroic. The red side used the grating with 1200 lines/mm blazed at 7500 Å and targeted the Hα emission.

Low resolution spectra of the host and nearby sources were obtained on 2017 January 26 using the 1.5" long slit and the 560 dichroic. The grating used on the red side has 400 lines / mm blazed at 8500 Å, covering wavelength from about 5462 Å to 10318 Å, with a dispersion of 1.86 Å/pixel. We estimate the spectral resolution to be ~ 4 Å (1σ) from the weighted average width of the four isolated skylines (5577.0 Å, 5898.0 Å, 6315.7 Å, 7257.4 Å). On the blue side the grism has 600 lines / mm blazed at 4000 Å, covering wavelengths from 3122 Å to 5603 Å. Standard stars were observed for the flux response calibration, arc-lamp spectra were obtained for the wavelength calibration, and bias frames were taken for the bias-subtraction. The flat field was generated using dome flats.

3.3 Data Analysis and Results

3.3.1 VLA flux density measurements

In this section, we describe how we measure the radio flux density of QRS121102 in each epoch.

The visibility data were calibrated and imaged using CASA following the standard procedures (task names shown in parentheses).[1] In the calibration, the VLA antenna positions were updated (*gencal*). The primary calibrator 3C147 was used to find the absolute scale of the gain amplitudes by referring to the standard flux density (*setjy*), and to correct for the instrumental delay and the complex antenna-response variation with frequency (*bandpass*). The complex gain solutions (both amplitude and phase) were obtained from the phase calibrator 1, J0555+3948, that is $\sim 8^{\rm o}$ apart from QRS121102 (CASA task *gaincal*), and the gain amplitudes were properly-scaled using the absolute scale just obtained using 3C147 (*fluxscale*). All calibration

[1]The Common Astronomy Software Applications (CASA) is a software package developed by the NRAO.

solutions were then applied (*applycal*) to QRS121102, as well as the fainter phase calibrator 2, J0518+3306 ($\sim 2^{o}$ away from QRS121102). After calibration, potential radio frequency interference (RFI) and internally generated signals were removed by flagging out narrow-banded spikes in the spectra (*flagdata*). In epoch 3, one scan of QRS121102 was removed as it was several times brighter than the others (within 30 minutes apart) due to strong RFI, or perhaps a passing cloud.

The calibrated visibility data were binned to 20 s and 500 kHz to speed up synthesis imaging using the CASA task (*split*). The data were gridded and Fourier transformed and the synthesized beam was deconvolved (*tclean*). The FWHM of the synthesized beam was $\sim 1.5''$ (major axis) $\times 1.2''$ (minor axis) in the Ku-band and $\sim 1.3''$ (major axis) $\times 0.9''$ (minor axis) in the K-band in C configuration. Our images were created using a small cell size of $0.1'' \times 0.1''$ and a Briggs robust weighting of 0.5 [23].

We measured the flux density of each source from the images by fitting each with a 2-D Gaussian model (*imfit*; Fig.3.1). We obtained the flux density of those point sources (based on the criterion implemented by the CASA *imfit* task) from the peak, and of the others from the integrated flux density within each fitting region. Uncertainties were calculated by propagation of errors of the 2D fitting model. Table 3.1 lists the results and Fig. 3.2 shows the flux density light curves in both bands.

The angular size of QRS121102 has been reported to be under ~ 0.2 mas at 5 GHz as measured by the Very-long-baseline interferometry (VLBI) [8]. It is expected to be unresolved in our observations, where the beam FWHM is ~ 1.4" in the Ku-band and ~ 0.9" in the K-band. In our images, the 2D Gaussian fitting results show that QRS121102 is a point source in all but epoch 3, where the image is marginally resolved as 1.13 ± 0.61 arcsec along the major axis and 0.49 ± 0.22 arcsec along the minor axis (FWHM, deconvolvd from beam). This is likely due to the remaining phase errors in the calibration solution, as the image of phase calibrator 2 J0518+3306 appears highly distorted. The errors were removed by phase-only self-calibration in field 2, but not in field 3, for reasons outlined below.

In field 3, our observations of QRS121102 were affected by a bright source, NVSS J053153+331014, that is ≈ 1.8' (twice of the primary beam FWHM in the Ku-band) away from the pointing center (QRS121102) and over one order-of-magnitude brighter (≈ 3 mJy in flux density before correcting for primary-beam attenuation). To reduce the associated errors, we performed self-calibration (phase only) for NVSS J053153+331014 and QRS121102 simultaneously. We also tried to remove the flux density contribution from NVSS J053153+331014 modeled from self-calibration,

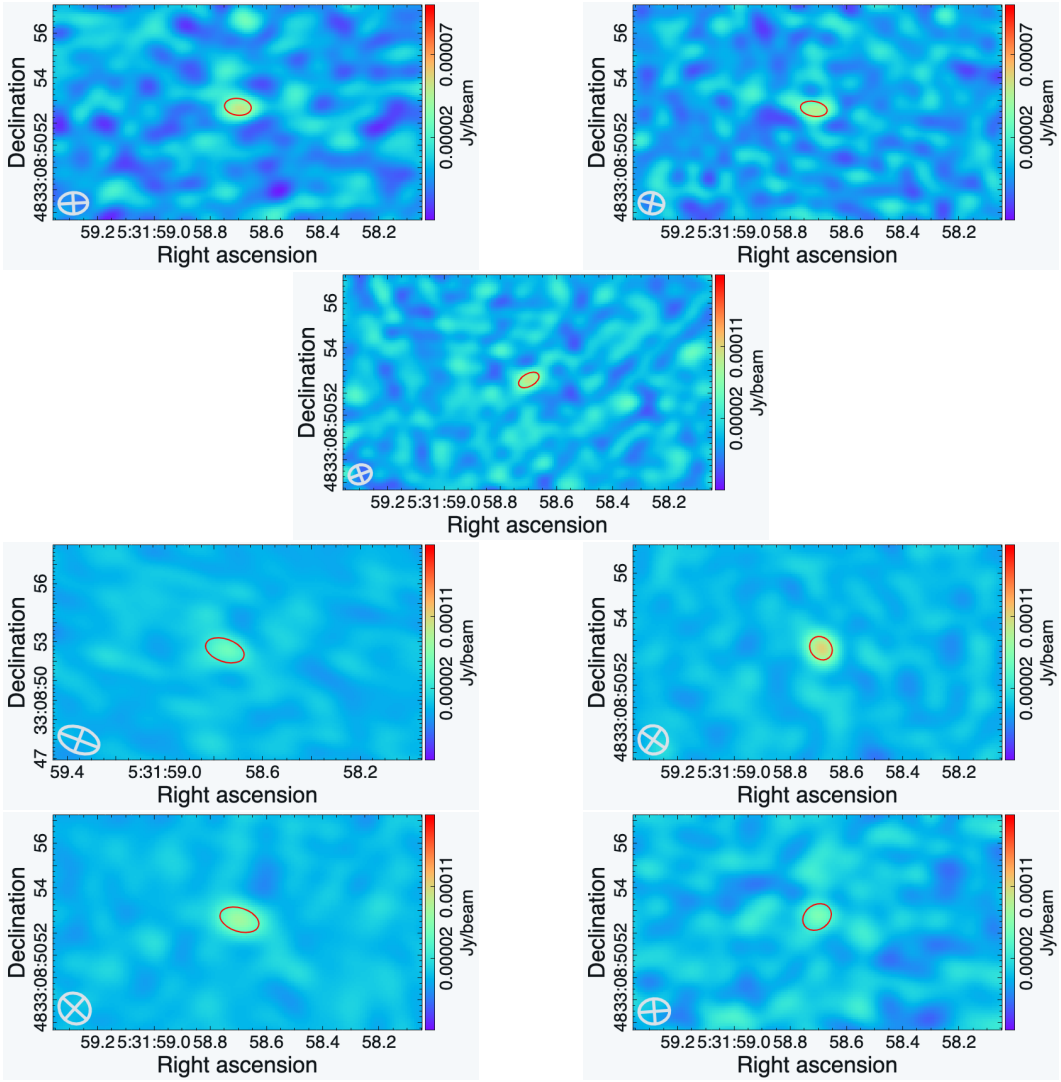

Figure 3.1: VLA images (in J2000 coordinates) of QRS121102 in seven epochs, with band indicated in parentheses. The color scale represents flux density in Jy / beam (see color bar). The open light gray circle (on the bottom left of each image) shows the synthesized beam size (1σ) and the red circle shows the 1σ 2D Gaussian fitting results convolved with the synthesized beam. The position angles of the best fit results are consistent with those of the clean beams within 1σ in all cases where the source is unresolvable.

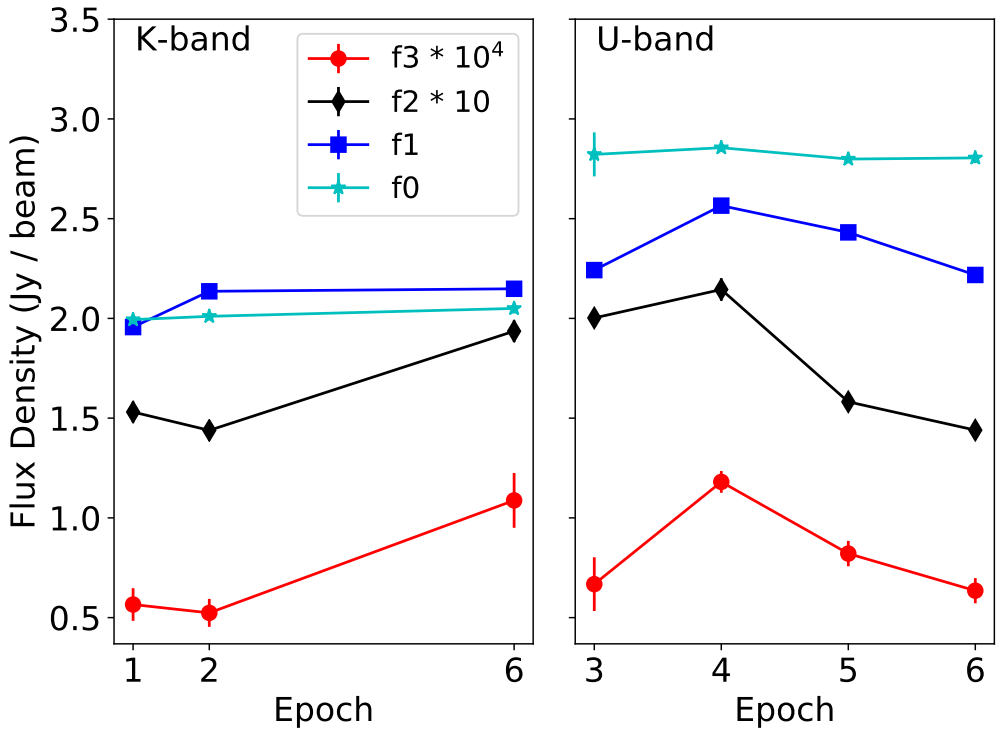

Figure 3.2: Flux density light curve of the K-band (left) and the Ku-band (right). f3, f2, f1 and f0 represents the flux density of QRS121102 (solid red circle), the phase calibrator 2 (solid black diamond), the phase calibrator 1 (solid blue square) and the prime calibrator (cyan stars), respectively. f3 and f2 are scaled by 10^4 and 10 times for display. Details of the observations are shown in Tables 3.1, 3.2.

and then subtract the model visibility from the corrected visibility data. Neither attempt made a significant improvement on the image of QRS121102, since self-calibration failed to correct the beam model error far away from the pointing center.

In addition, there might be remaining calibration errors since the flux densities of the two phase calibrators, J0555+3948 and J0518+3306, also vary by $\sim$ 4% and $\sim$ 10% throughout the epochs in each band (Fig. 3.2). The variations are likely not intrinsic to the source for two reasons. (1) J0555+3948 has been reported to vary by 2.0% on a time scale of 251 days at 33 GHz and 3.4% on a time scale of 293 days at 16 GHz [24]. It is unlikely to show a greater variability on a timescale of days, as been observed in this work (e.g., epochs 3, 4, 5). (2) More importantly, the flux density light curve of QRS121102 shows a moderate positive correlation with that of J0555+3948, and a strong positive correlation with that of J0518+3306, with a correlation coefficient of 0.67 and 0.91, respectively. To reduce potential calibration errors, in each epoch we re-scaled the flux density measurements of QRS121102 by

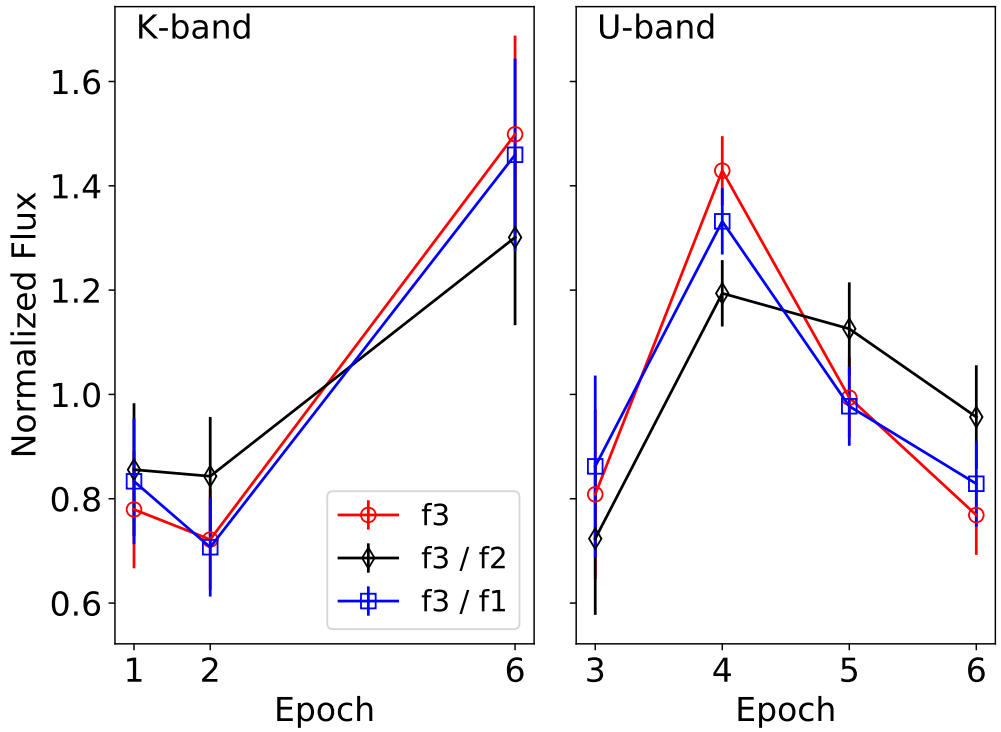

Figure 3.3: Normalized (and scaled) flux density light curve of the K-band (left) and the Ku-band (right). f3, f2 and f1 represents the flux density of QRS121102, the phase calibrator 2 and the phase calibrator 1, respectively. Red open circles (f3) show the normalized flux density of QRS121102, black open diamonds (f3/f2) show the flux density of QRS121102 divided by those of the phase calibrator 2 and then normalized to average at unity, and blue open squares (f3/f1) are the flux density of QRS121102 divided by those of the phase calibrator 1 and then normalized to average at unity.

those of the two phase calibrators (Fig. 3.3). We adopt the flux density scaled by J0518+3306 (phase calibrator 2) thereafter, since it has a smaller angular separation from QRS121102.

3.3.2 Keck/LRIS Medium Resolution Spectral Analysis

The LRIS data were processed using the LRIS automated reduction pipeline (LPipe; [25]) following standard procedures: subtract the bias, make flat fields and apply flat-field correction, remove cosmic ray pixels, model and remove sky lines, perform wavelength calibration by referring to the arc lamp spectra, and determine the flux response function by observing standard reference stars. The processed 2D spectrum targets the Hα emission.

The width of the Hα emission line is produced by multiple effects [26]—

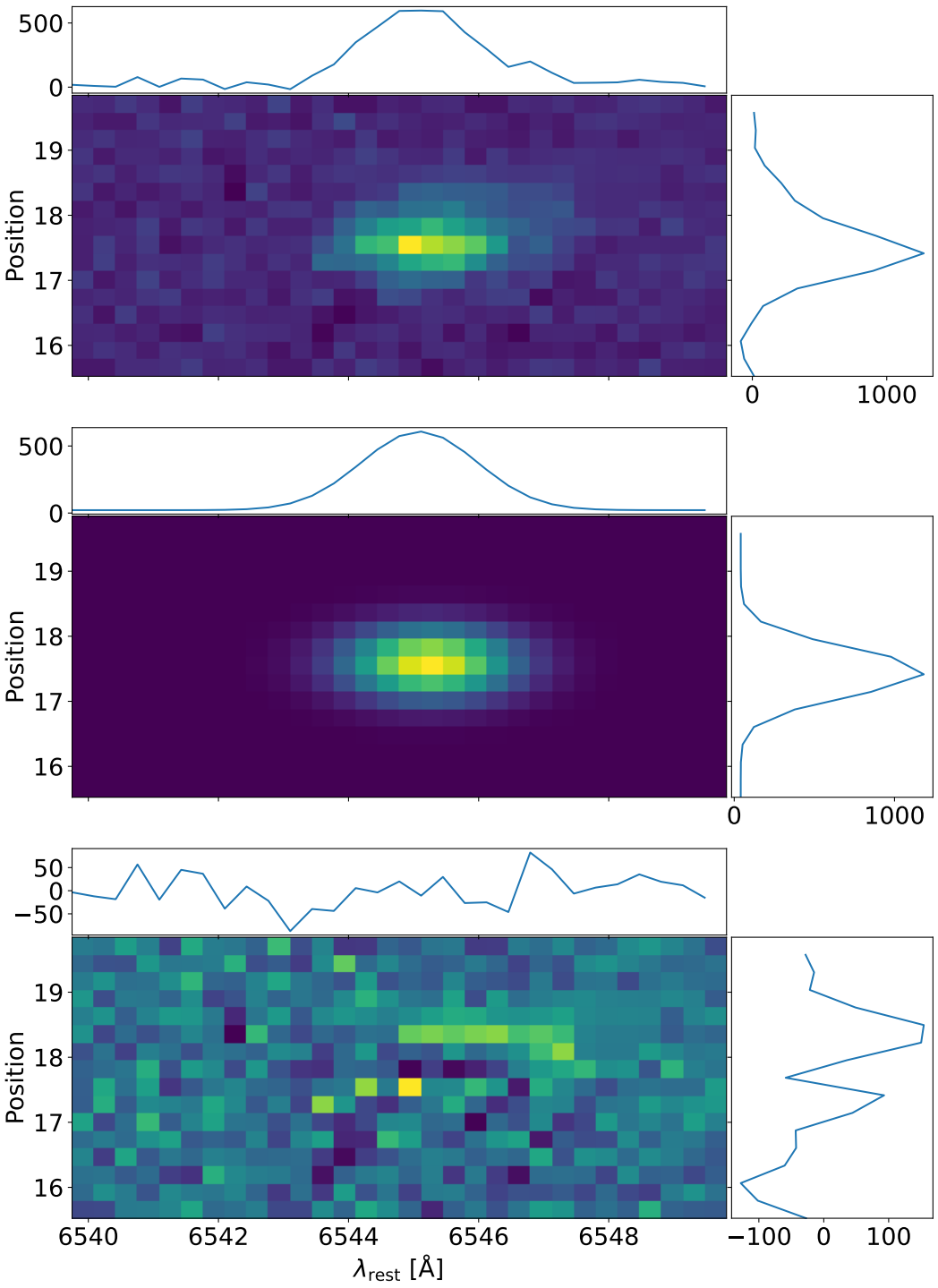

Figure 3.4: 2D medium resolution LRIS spectrum of the host galaxy of FRB 121102. Wavelength has been converted to the rest frame using the previously reported redshift of z = 0.19273 [9]. Top to bottom panels are the observed 2D spectrum, the 2D fitting model and the residual (data–model), respectively. On the top and right of each panel are plots of the data collapsed along the wavelength axis and position axis, respectively.

- dynamical velocity dispersion due to gravity,
- instrumental broadening,
- random thermal motions,
- natural broadening,
- turbulent motions.

In this section, we test the hypothesis that QRS121102 is associated with an AGN by using the velocity dispersion to roughly constrain the mass of a potential supermassive BH. The velocity dispersion is estimated from the Hα line width.

The Hα emission line width of the host is determined by fitting the rest-frame 2D spectrum with a 2D Gaussian function whose rotation angle is fixed at zero, plus a constant offset. We convert the observed 2D spectrum of the host into the rest-frame wavelength using a previously reported redshift of 0.19273 [9]. The width (1σ) of the emission line is 0.9316 ± 0.0026 Å when combining all four exposures, and 0.8947 ± 0.0015 Å after removing the two exposures polluted by the nearby cosmic rays (Fig. 3.4). A bright pixel at the center of the Hα emission is seen in the residual (bottom panel of Fig. 3.4), but no extended structure that might impact the emission width result is found.

We then determine the width of the instrumental broadening effects by collapsing the 2D spectrum into 1D and fitting each of the three isolated sky lines in the field with a 1D Gaussian function plus an offset. The instrumental spectral broadening width is given by the weighted mean of the three sky lines' 1-σ widths (0.638725 ± 0.000039 Å). The natural broadening width of the Hα line is known to be 0.46 mÅ (e.g., [26]). The 1-σ width of the line is 0.6265 ± 0.0021 Å after quadratically removing the instrumental and natural broadening effects.

The rest frame line width of a Maxwellian velocity distribution (i.e., Gaussian along the line-of-sight) is given by [26]:

$$\frac{\Delta\nu}{\nu_0} = \frac{1}{c}\left(\sigma_v^2 + \frac{2kT}{m_H} + v_{turb}^2\right)^{1/2}. \tag{3.1}$$

Here, $\Delta\nu$ Hz is the rest-frame line width (1σ) in frequency and $\nu_0 = 4.57 \times 10^{14}$ Hz is the frequency of the Hα emission in vacuum. σ_v is the velocity dispersion due to gravity, $\sqrt{2kT/m_H} \approx 12.8$ km/s is the most probable thermal velocity assuming

a gas temperature of 10^4 K (e.g., [27]). v_{turb}, the turbulent velocity, is weakly constrained to be $\lesssim 10^3$ km/s as inferred from the scattering measurements of FRB 121102 (Table 2 of [28]). We ignored its contribution and find an upper limit of $\sigma_v \lesssim 30$ km s^{-1}.

Assuming that the FRB 121102 host galaxy has a central BH, we estimate its mass using the empirical M-σ relation reported in recent literature. The BH mass is $7.8^{+8.2}_{-5.2} \times 10^4 M_\odot$ using the relation derived from a sample of 88 AGN covering a stellar velocity dispersion σ_* of 30 – 268 km s^{-1} ([29], error bars calculated from the intrinsic scatter found in the relation). A consistent BH mass of $8.8^{16.2}_{-5.8} \times 10^4 M_\odot$ is found using the relation based on 93 low-mass active galaxies ([30], σ_* from 31 to 138 km/s). Other reports show similar results, though an extrapolation of the M-σ relation is required as the sampled objects cover higher σ_*: the mass is $4.2^{+7.5}_{-2.7} \times 10^4 M_\odot$ (error bars from the intrinsic scatter in the relation) based on a sample of 49 BH mass dynamical measurements in spiral galaxies, S0 galaxies and elliptical budges (σ = 67–385 km s^{-1}; [31]), and $\sim 10^4 M_\odot$ from 72 similar objects (σ = 75 – 347 km s^{-1}; [32, 33]). Finally, we note that the measured velocity dispersion is lower than any of those measured from a sample of 35 tidal disruption events host galaxies (σ > 43 km/s) reported by [34, 35]. This suggests that the BH mass in the FRB 121102 host is lower than the BH masses of the tidal disruption event galaxy sample.

We consider two potential errors in our BH mass estimation. First, the Hα velocity dispersion measurement may not be suitable for the dynamical analysis. The BH mass is usually estimated from the stellar velocity dispersion measured from multiple absorption lines from an optical or IR spectrum. In our observation, these stellar absorption line widths were unavailable due to the limited SNR. Instead, we infer the velocity dispersion from the line width of a single compact Hα emission region (radius < 0″.24 at 1σ, [36]) that is offset from the stellar continuum centroid of the galaxy by $0''.29 \pm 0''.05$ [9]. The Hα line width reveals the dynamics of the partially ionized warm star forming gas formed in discrete clouds. If the gas pervades in the galaxy, it is expected to have larger velocity dispersion than the stars due to turbulent motions and provide an upper limit to the BH mass. However, the Hα region is isolated to one part of the host and may not represent the global gas dynamics in the host. This could lead to systematic errors as reported in the dynamical analyses of galaxies with irregular gas and dust distributions [37].

However, the dynamical mass implied by the Hα velocity dispersion is comparable

to the stellar mass of the FRB 121102 host galaxy inferred using the optical/IR spectral energy distribution. We assume that the system is virialized for an order-of-magnitude estimation. In an ellipsoid, the kinetic energy is dominated by random motions. The virial theorem gives a total stellar mass of $M_* \sim \sigma_v^2 R_{eff}/G \sim 10^8 M_\odot$, adopting a half-light-radius of R_{eff} = 0.68 kpc [7]. In a pure rotational disk (e.g., disk of a spiral galaxy), a comparable value is expected. The inferred mass is consistent with the stellar mass reported by Bassa et al. [7] from a spectral energy distribution fit ($(1.3 \pm 0.4) \times 10^8 M_\odot$). This suggests that the velocity dispersion may be useful for the dynamical BH mass estimation. We also note that QRS121102 is spatially associated with the Hα emission region.

Second, the M-σ relations could be less reliable at our velocity dispersion for two reasons. (1) Most reports derive the empirical M-σ relation based on a sample of more massive galaxies with larger stellar velocity dispersions. It is unclear how well the relation extends to lower velocity dispersions. (2) Even in the few reports that cover velocity dispersions down to 30 km/s, the M-σ relation is still less reliable due to the larger uncertainty in the empirical mass-luminosity (M-L) relation at the lower end. To derive the M-σ relation, the dynamical mass of the BHs were estimated using the virial relation, where the virial radius is either measured directly from reverberation mapping (e.g., [38]) or indirectly from the empirical M-L relation that was derived from the reverberation mapped AGN. At the low-mass end, few AGN have been reverberation mapped, so an extrapolation of the M-L relation has to be made in the BH mass estimations, introducing extra uncertainty to the resulting M-σ relation. The M-σ relation might be flatter at the lower-mass end based on a few intermediate mass BHs in the sample (e.g., [29]), although the flattening is inconclusive without reverberation mapping results of the lower-mass BHs.

We validate our BH mass estimation result by comparing to the empirical BH-galaxy mass correlation. Reines and Volonteri [39] measure the correlation between galaxy stellar mass and BH mass based on a sample of 341 AGN host galaxies, including a sub-sample of dwarf galaxies [40]. They find that $\log(M_{BH}/M_\odot) = 7.45 + 1.05 \log\left(M_*/10^{11} M_\odot\right)$, with a scatter of 0.55 dex. A stellar mass of $10^8 M_\odot$ gives an AGN BH mass of $10^{4\sim5} M_\odot$ (1σ uncertainty assuming log-normal mass distribution), consistent with our BH mass estimation.

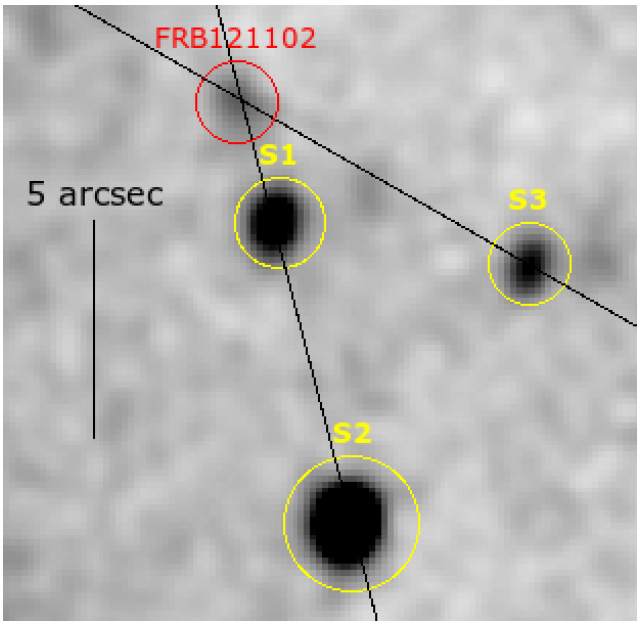

Figure 3.5: Locations of the host, the slits and the sources in the low resolution Keck/LRIS observation. The slit orientations are shown as black lines. Spectra were extracted for each of sources S1, S2, and S3, together with the FRB 121102 host. The background image is an LRIS R-band exposure, as presented in Tendulkar et al. [9]

3.3.3 Keck/LRIS Low Resolution Spectral Analysis

Data were obtained with two longslit orientations (shown in Fig. 3.5). The LRIS data were bias subtracted, flattened, cosmic-ray removed, skyline subtracted and flux calibrated using the LPipe [25]. The LPipe wavelength calibration failed on the red side, since the arc lamps spectrum missed too many of the expected reference lines. We calibrated the wavelength manually by fitting the sky spectra to six isolated, bright skylines. We then selected all nearby sources for which reliable spectra could be extracted— two sources near the host on slit 1 (S1, S2) and one on slit 2 (S3) (Fig. 3.5).

In this section, we evaluate whether or not the host and its nearby sources belong to the same galaxy group. The redshift of each spectrum was estimated as follows. The procedures were also tested on several SDSS spectra and yield results within 1% of the known redshift values.

1. Remove strong sky line features and data near the boundaries of the wavelength coverage.

2. Interpolate and smooth the spectrum using a 1D Gaussian kernel (σ = 3 Å) to reduce random high-frequency noise. The kernel width was chosen such

that it is narrower than the spectral line width at 8000 Å ($1\sigma \sim 5$ Å) for a typical galactic velocity dispersion of $\sim$ 200 km/s (e.g., [41]). Somewhat different kernel width choices (1Å, 3Å, 5 Å) do not change the redshift results significantly.

3. Fit for the continuum and subtract from the spectrum. The fit was done using the *Astropy* package *specutils*, which removes spikes using a median filter and fits the spike-removed spectrum with a list of models using the Levenberg-Marquardt algorithm.

4. Extract a 60-Å-long segment of spectrum centered at each typical galaxy absorption (or emission) line and stack them. We considered the following absorption lines as they are near the visible wavelength at a redshift of ~ 0 to 1: the Balmer series, Ca K&H (3934.777, 3969.588), the G-band (4305.61), Mg (5176.7), Na (5895.6), and Ca[II] (8500.36, 8544.44, 8664.52). We ignored emission lines since none of our sources show significant emission features. The segment width of 60 Å was chosen such that it were able to include at last the $\pm 5\sigma$ region of a spectral line broadened by a typical galactic vlocity dispersion of 200 km/s (e.g., [41]), but not too wide to contain multiple lines.

5. Compare the amplitude of the stacked segment at a grid of trial redshift values. In this work, the best estimation occurs at the deepest valley since we only considered absorption lines.

For S1, we find z $\approx$ 0.5796 and inspect absorptive features at the wavelengths of the Ca H&K, Mg, Hγ and possibly the G-band. For S2, we find z $\approx$ 0.4471 and see absorptive features at the wavelengths of the Ca K, the G-band, Na, and potentially Hα. For S3, a few weak lines (the Ca H, Mg and Na) indicate that this source might be close to S2 in redshift, but we were unable to reach a conclusion due to the low SNR. We find no significant spectral feature at the expected wavelengths assuming that S3 were at the host redshift. None of the three sources is likely to be at the same redshift as the host of FRB 121102.

3.4 Discussion

3.4.1 Does QRS121102 scintillate?

3.4.1.1 Scattering theory predictions

Compact sources scintillate as their wavefronts propagate through an inhomogeneous ionized medium. Within the medium, fluctuations in the electron density lead

to variations of the refractive index, which change the phase of the wavefront. The fluctuations can be described by the phase structure function defined as the phase difference of two points separated by a distance x:

$$D_\varphi(x) = \langle[\varphi(x + x_0) - \varphi(x)]\rangle_{x_0} \propto x^\alpha. \tag{3.2}$$

Here, α is 5/3 for Kolmogorov turbulence [42]. We adopt a Kolmogorov turbulence assumption in our calculations thereafter. When there are relative motions between the source, the medium and the observer, the fluctuations cause temporal variations in the observed flux density.

One important scale of the scattering medium is r_0, the transverse radius (on the observer's plane) at which the phase changes by one radian ($D_\phi(r_0) = 1$) due to the ISM free electron inhomogeneity. r_0 can be related to σ_θ, the root mean square of the angle of arrival for a point source at distance D:

$$r_0 = \frac{\lambda}{\sqrt{2}\pi\sigma_\theta}, \tag{3.3}$$

$$\sigma_\theta^2 = \int_0^D dx\, \eta(x) \left(\frac{x}{D}\right)^2. \tag{3.4}$$

Here, x is the source-observer axis. $\eta(x)$ is the mean square of the scattering angle per unit length along the line of sight.

In general, $\eta(x)$ is determined by the wavelength λ, the scattering measurement (SM) and the inner scale of the spatial power spectrum of the electron density fluctuation in the turbulent medium. The specific relation depends on the geometry and the power spectrum (e.g., see [43] for details).

For extragalactic sources, scattering is dominated by the Milky Way ISM, which can often be approximated as a thin scattering screen at a distance D from the observer (e.g., [14]). In Eqn. 3.4, the integration becomes a Delta function at the distance of the galactic ISM screen.

Another characteristic scale of the scattering medium is the Fresnel scale (e.g., [44]):

$$\begin{aligned} r_F &= \sqrt{\frac{\lambda D}{2\pi}}, \\ &= 1.23 \times 10^9 \text{ m} \left(\frac{D}{1 \text{ kpc}}\right)^{1/2} \left(\frac{\nu}{1 \text{ GHz}}\right)^{-1/2}, \end{aligned} \tag{3.5}$$

which is the transverse length (on the observer's plane) at which the phase of a wavefront with wavelength λ changes by one radian due to the geometric path length difference, assuming that $D \gg \lambda$.

Based on the relation of these two scales (Eqn's 3.3, 3.5), scattering is divided into the weak regime ($r_0 \gg r_F$) and the strong regime ($r_0 \ll r_F$). The transitional frequency, ν_0, is defined as the frequency at which $r_0 \sim r_F$ for an extragalactic source. In the NE2001 electron density model (Cordes and Lazio 45, 46), the ν_0 for plane waves emitted by far-away sources is given by (adopted from Eqn. 17 of Cordes and Lazio 45):

$$\nu_0 \approx 318 \text{ GHz } (\xi \frac{r_0}{r_F})^{10/17} \, (\frac{SM}{1 \text{ kpc m}^{-20/3}})^{6/17} \, (\frac{D_{eff}}{1 \text{ kpc}})^{5/17}. \tag{3.6}$$

Here, $\xi = 1/\sqrt{2\pi}$ is the fresnel scale definition factor. $SM = \int_0^D ds \; C_{n_e}^2(s)$ is the scattering measure and $C_{n_e}^2$ describes the strength of the free electron density fluctuations along the line of sight. We adopt a SM of 0.00614 kpc $m^{-20/3}$ based on the NE2001 model along the line of sight.

$$D_{eff} = \frac{\int_0^D ds \; s \; C_{n_e}^2}{\int_0^D ds \; C_{n_e}^2}$$

is the effective path length through medium. We find $D_{eff} \approx 2$ kpc, as calculated using NE2001 by $D(SM - SM_\tau/6 - SM_\theta/3)/SM$, where we use D = 30 kpc for extragalactic sources, $SM_\tau = \int ds(s/D)(1 - s/D)C_{n_e}^2 \approx 0.0023$ kpc $m^{-20/3}$ and $SM_\theta = \int ds(1 - s/D)C_{n_e}^2 \approx 0.016$ kpc $m^{-20/3}$. We estimate that $\nu_0 = 38$ GHz along the line of sight of FRB121102 ($l \approx 175^o$, $b \approx -0.2^o$). Our observations were taken at frequencies (12 to 26 GHz) below ν_0, so they all belong to the strong scattering regime.

In the strong scattering regime, there are two main types of scintillation behaviors: refractive and diffractive. We summarize the predicted scintillation behaviors below based on Romani et al. [14] and Walker [15].

Refractive scintillation is caused by large-scale ($\gg r_F$) ISM inhomogeneities. The observed flux density variability is slow and broad-band. For Kolmogorov turbulence, the angular radius of the apparent scattering disc at frequency ν is [15]

$$\begin{aligned} \theta_r &= \theta_{F0} \left(\frac{\nu_0}{\nu}\right)^{11/5}, \\ &= 1.32 \; \mu\text{as} \left(\frac{D}{1 \text{ kpc}}\right)^{1/2} \left(\frac{\nu_0}{\nu}\right)^{11/5}. \end{aligned} \tag{3.7}$$

Here, θ_{F0} is the angular size of the first Fresnel zone at the transitional frequency ν_0:

$$\theta_{F0} = \sqrt{\frac{c}{2\pi\nu_0 D}} = 8.11 \; \mu\text{as} \left(\frac{D}{1 \text{ kpc}}\right)^{1/2} \left(\frac{\nu_0}{1 \text{ GHz}}\right)^{-1/2}. \tag{3.8}$$

The observed flux density of a compact source smaller than θ_r varies on a refractive time-scale of [15]

$$\begin{aligned} t_r &\sim \frac{2r_r}{v}, \\ &= \frac{2r_{F_0}}{v}\left(\frac{\nu_0}{\nu}\right)^{11/5}, \\ &\approx \frac{2\times(2\times10^8\ \mathrm{m})}{50\ \mathrm{km\ s^{-1}}}\left(\frac{\nu_0}{\nu}\right)^{11/5}, \\ &\sim 2\ \mathrm{hours}\left(\frac{\nu_0}{\nu}\right)^{11/5}. \end{aligned} \tag{3.9}$$

We assume a typical relative transverse velocity of 50 km/s [47] , an ISM scattering screen distance of 1 kpc from the observer, and using the diameter of the apparent scattering disc at frequency ν as the length scale. In this work, modulation index is defined as the weighted root-mean-square (rms) fractional variation:

$$m_p = \frac{1}{\langle f\rangle}\sqrt{\frac{\sum_i w_i(f_i-\langle f\rangle)^2}{\sum_i w_i}}. \tag{3.10}$$

Here, f_i is the flux density of the i-th epoch, $w_i = 1/\sigma_{f_i}^2$ is the weight calculated from the measurement uncertainty σ_{f_i}, and $\langle f\rangle$ is the weighted mean flux density. The modulation index of a source smaller than θ_r is given by [15]

$$m_p = \left(\frac{\nu}{\nu_0}\right)^{17/30}. \tag{3.11}$$

When the point source approximation fails ($\theta_s > \theta_r$, where θ_s is the source angular radius), the modulation index reduces as $m = m_p(\theta_r/\theta_s)^{7/6}$ and the variability timescale increases as $t = t_r(\theta_s/\theta_r)$.

Table 3.4 lists the predicted θ_r (Eqn.3.7), t_r (Eqn.3.9) and m_p (Eqn.3.11) using the central frequency of each band, and assuming a point source. We do not predict the substantially larger effects of diffractive scintillation because, as will be seen below, we observe significantly less modulation than expected due to refractive scintillation alone. We calculate θ_r (Eqn's 3.7, 3.8) using a distance D ranging from 100 pc to 10 kpc (Fig. 3.6), and list the θ_r corresponding to a nominal distance of 1 kpc ($\sim$ galactic scale height) in Table 3.4. For scattering media dominated by a steeper fluctuation spectrum, the expected values of m_p, t_r and θ_r would be greater [42].

In contrast, diffractive scintillation is produced by interference effects between light rays passing through small-scale ($\ll r_F$) ISM inhomogeneities. The variations are

fast ($t_d \sim 2(\nu/\nu_0)^{6/5} \sim 5$ hours at $\nu = 18$ GHz) and narrow-band ($\Delta\nu \approx \nu(\nu/\nu_0)^{17/5} \approx$ 1 GHz at $\nu = 18$ GHz). This is beyond the scope of this paper.

3.4.1.2 Comparison between the flux density measurements and predictions

In the following analyses, we analyze two types of flux density measurements in each band—

- The normalized flux density measurements of QRS121102 ("f3" in Table 3.5).
- The flux density measurements of QRS121102 divided by those of J0518+3306 and then normalized ("f3/f2" in Table 3.5). The scaling is justified for two reasons. (1) The phase calibrators J0518+3306 (and J0518+3306) are not expected to scintillate, since the constraints on their angular radii and the observed flux densities would require a brightness temperature exceeding the inverse Compton catastrophe threshold — $\gtrsim 10^{12}$ K (and $\gtrsim 10^{13}$ K)— assuming a scattering screen at 1 kpc. (2) The variations are unlikely to be intrinsic due to the strong correlations and the short variation timescale, as explained in Section 3.3.1.

We calculate the modulation indices of the above four sets of flux density measurements (Table 3.5, column 2) and find each of them more than 5σ lower than the predictions (error bar calculated from the statistical errors in the flux density measurements), though our observation spacings are longer than the predicted refractive time scale (Table 3.4). To conclude the comparison, we perform χ^2 tests for two hypotheses —

1. The flux density is constant.
2. The flux density measurements are drawn from a Gaussian distribution whose standard deviation is equal to the scattering theory prediction (Table 3.4, Section 3.4.1.1). A Gaussian distribution is used here to provide a conservative test, though galactic scattering has been observed to modulate intensity with one-side exponential functions (e.g., [48]).

We test the first hypothesis by fitting our measurements in each band with their weighted average and calculate the χ^2:

$$\chi^2 = \sum_i \frac{(f_i - \langle f \rangle_w)^2}{\sigma_{f_i}^2}. \tag{3.12}$$

Here, $\langle f \rangle_w$, f_i and σ_{f_i} are the weighted average flux density, the i-th epoch flux density and its measurement error, respectively. For example, in the K-band, the best-fit result of f3/f2 has a χ^2_{min} of 5.8 and a degree of freedom (dof) of 2, yielding a one-side P-value of 5.6% for obtaining a χ^2_{min} that is greater or equals to our observation if the flux density were constant. Other results are listed in Table 3.5. In both bands, the constant flux density hypothesis is questionable using the f3/f2 light curve, and is rejected to a level of at least 10^{-3} using the f3 light curve.

We test the second hypothesis by simulating 10^5 light curves for both bands, each with the same number of measurements and the same fractional uncertainties as our observations. For each light curve, the flux densities are drawn from the absolute values of a Gaussian distribution centered at unity and with a standard deviation of $m_p\sqrt{n/(n-1)}$, where m_p is the expected modulation index and n is the number of measurements. We calculate the χ^2_ν for each light curve and compare the smoothed distribution with our observations in each band. For example, using f3/f2 in the Ku-band, $\sim$ 3% of the simulated light curves have χ_ν values lower than or equals to our observation (2.9), questioning the second hypothesis. In both bands, the scintillation-variability-hypothesis is doubtful using the f3/f2 data.

3.4.1.3 Implications

We have found it questionable that our observation is consistent with refractive scintillation predictions for a point-like source. We will discuss the implications of the absence of refractive scintillation modulation in our observations.

First, scintillation variations would be smeared out if the angular size of the source is greater than that of the scattering disc. The lack of modulation implies a lower limit to the physical size of the source in each band (Fig. 3.6). Here, the scattering disc angular size lower limit is calculated assuming a range of distances from 100 pc to 10 kpc between the scattering screen and the observer. The physical size limit of the source is obtained using the angular size limit and the host redshift (z = 0.19273). In the Ku-band, the scattering disc radius is 10 μas (Table 3.4) assuming a scattering screen distance of 1 kpc ($\sim$ galactic scale height), corresponding to a physical

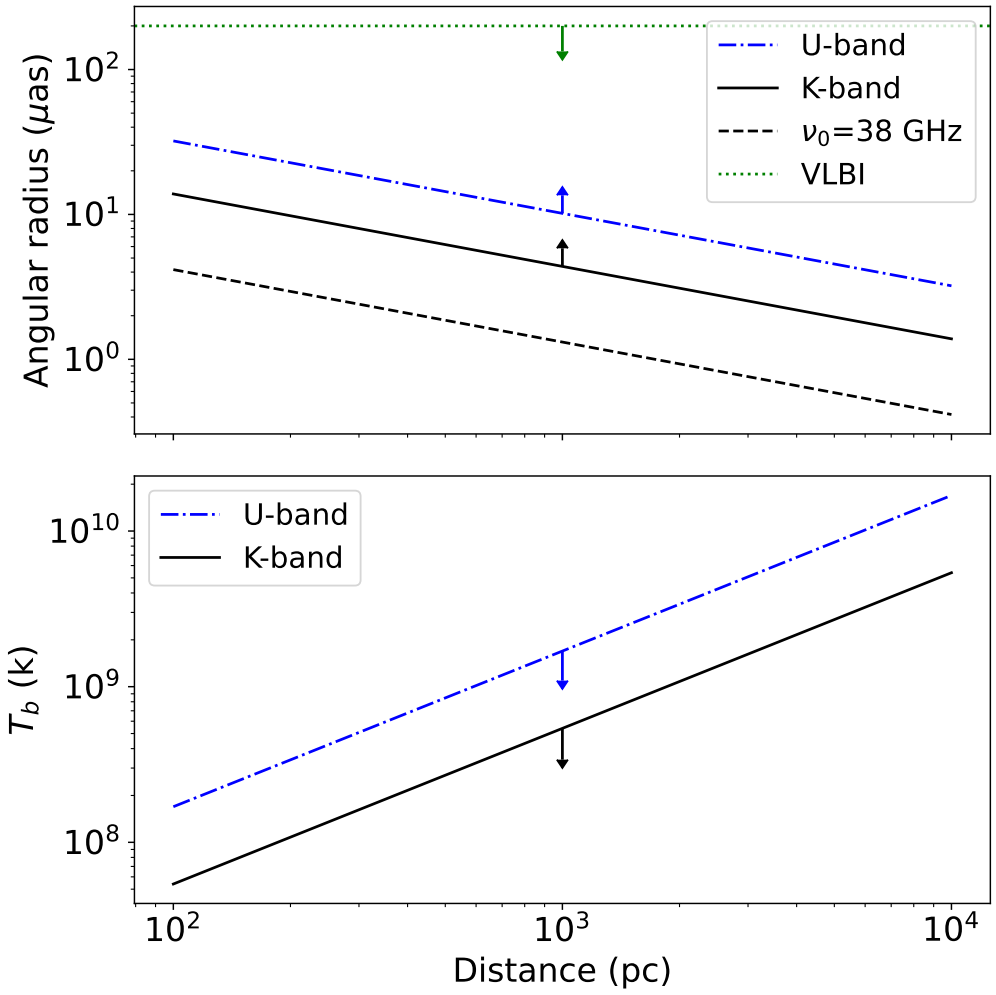

Figure 3.6: Implication from the lack of refractive scintillation modulation assuming a range of distances between the scattering screen and the observer. Upper panel: source radius lower limits in the Ku-band (dash-dot blue line) and the K-band (solid black line), the scattering disc radius at the transitional frequency ν_0, as well as the source radius upper limit from the unresolved VLBI image at 5 GHz. Lower panel: brightness temperature upper limits using the emission region size lower limit inferred from the Ku-band ($\theta_{\rm r} \gtrsim 10$ μas) and the weighted average flux densities measured in the Ku-band (dashed blue line) and the K-band (solid black line).

radius of $R \gtrsim 10^{17}$ cm (0.03 pc) at the host redshift. This together with the VLBI resolution at 5 GHz limit the emission radius to be between $\sim 10^{17}$ cm and $\sim 10^{18}$ cm. Alternatively, a rough estimation on the source radius could be made using the measured modulation index. When the angular radius of the source is larger than that of the refractive scattering disc, the variability would reduce and the source radius is given by $\theta_s \approx \theta_r(m_p/m'_p)^{6/7}$, where m_p is the expected scintillation modulation index, m'_p is the observed modulation index and θ_r is the refractive scintillation disc angular radius. This gives a source radius of 14 μas (1.4×10^{17} cm) in the K-band and 36 μas (3.7×10^{17} cm) in the Ku-band (using the host redshift and assuming a scattering screen at 1 kpc), within the above constraints of $10^{17\sim18}$ cm.

In addition, the constraint on source size rules out the scenario that the flux density modulation is intrinsic. The flux density varies significantly within a week in the Ku-band (e.g., epochs 3, 4, 5). If the modulations were intrinsic, the source radius would be $R \lesssim (1/2) \cdot (7 \text{ days}) \cdot c \sim 10^{14}$ cm, three orders of magnitude below the scintillation size limit. The source would also have scintillated more if the fast variations were intrinsic.

Moreover, the brightness temperature of the source can be constrained by its size limit and flux density measurement. Brightness temperature provides clues on the radio emission process. For example, a brightness temperature above 10^5 K may rule out star-forming galaxies (e.g., [49]), and a brightness temperature above 10^{12} K requires coherent processes or relativistic boosting (e.g., [26]). The brightness temperature is given by:

$$T_b \lesssim \frac{fc^2}{2\pi\theta^2_{r,15GHz} k_b \nu^2}. \tag{3.13}$$

Here, $\theta_{r,15GHz}$ is the radius lower limit implied by the lack of scintillation modulation in the Ku-band, and ν is the frequency at which the flux density f is measured. Assuming a scattering screen distance of 1 kpc (Table 3.6), we find $T_b \lesssim 5 \times 10^8$ K using our average flux density measured in the K-band (ν_c = 22 GHz, $\langle f_\nu \rangle \approx 61.3 \pm 5.0$ μJy, weighted by the statistical errors in the flux density measurements) and $T_b \lesssim 2 \times 10^9$ K using the weighted average flux density measured in the Ku-band (ν_c = 15 GHz, $\langle f_\nu \rangle \approx 61.3 \pm 5.0$ μJy). A more complete result assuming a range of scattering screen distances is shown in Fig. 3.6.

3.4.2 Optical

3.4.2.1 Implications of Constraint on Potential supermassive BH Mass

We have estimated the mass of the potential supermassive BH to be $10^{4\sim5}$ $M_\odot$ using the velocity dispersion measured from the Hα emission line width (section 3.3.2). We will test the AGN hypothesis by comparing its mass, radio luminosity and X-ray luminosity with the AGN population.

The radio luminosity of QRS121102 is several orders of magnitude higher than expected given $M_{BH} \approx 10^{4\sim5} M_\odot$, based on results from a large sample of AGN with higher BH masses [50]. However, it may not be rare in a sample of bright radio emissions detected in dwarf galaxies at intermediate redshifts [17], and is only slightly brighter than those detected in some nearby dwarf galaxies [16]. For the general AGN population, the BH mass (M_{BH}), radio luminosity (L_{5GHz}), and the ratio of bolometric luminosity to the Eddington limit (L/L_{Edd}) has been reported to be correlated. For example, Lacy et al. [50] measure a relation based on a sample of 60 AGN with BH masses of $10^{6.5\sim10}$ $M_\odot$: $\log_{10}(L_{5GHz}) = 1.9 \log_{10}(M_{BH}/M_\odot) + x \log_{10}(L/L_{Edd}) + 7.9$ (with a scatter of 1.1 dex), where L_{5GHz} is in a unit of W Hz^{-1} sr^{-1}, $x \approx 1$ for a typical (L/L_{Edd}) of 0.1 and $x \approx 0.3$ for a low (L/L_{Edd}) of 10^{-5}. The specific radio luminosity of QRS121102 is $L_{5GHz} \approx 10^{21.2}$ W Hz^{-1} sr^{-1}, as calculated using the host redshift and the flux density of ≈ 200 μJy at 3GHz and 6 GHz [12]. This is three orders of magnitude greater than calculated from the relation (scatter included) even if $L/L_{Edd} = 100\%$ and $M_{BH} = 10^5$ $M_\odot$. However, we note that the relation reported in Lacy et al. [50] is derived from a sample of more massive BHs ($10^{6.5\sim10}$ $M_\odot$).

It is intriguing that the radio luminosity of QRS121102 is consistent with a sample of bright radio emissions detected in dwarf galaxies at intermediate redshifts [17]. The specific radio luminosity of QRS121102 at 3 GHz is $L_{3GHz} \sim 2.3 \times 10^{22}$ W Hz^{-1}, as calculated using the host redshift and the flux density at 3 GHz (206 ± 17 μJy; [12]). This lies within the broad luminosity range ($L_{3GHz} \approx 10^{21.5\sim24.2}$ W Hz^{-1}) observed in a sample of 35 dwarf galaxies ($10^7 < M_* < 10^{9.5}$) at intermediate redshifts (0.13 to 3.4) hosting compact radio sources from the VLA-COSMOS 3 GHz Large Project catalog [17]. These sources are suspected to be AGN mainly because they are significantly more luminous ($\geq 2\sigma$) than expected from star formation processes. In particular, a few objects in their sample show similar radio luminosities, host stellar masses, BH mass estimations and redshifts with QRS121102, although the constraints on their X-ray luminosities are weaker (Table 1, 2 of [17]). Similarly,

the specific luminosity at 10 GHz ($\sim 1.9 \times 10^{22}$ W Hz^{-1}) is only slightly above the observed range ($10^{18.5\sim22}$ W Hz^{-1}) from 13 nearby (z < 0.055) dwarf galaxies hosting bright radio sources that are too bright to be star formation processes or supernova remnants [16]. We suggest that the nature of several of these radio sources, including QRS121102, remains uncertain [e.g., 51].[2]

In addition, we estimate the minimum average radio luminosity of QRS121102 during its past life span and find it uncomfortably high given constraints on the X-ray luminosity. We assume possible source radii of 10^{17} cm (lower limit from this work) and 10^{18} cm (upper limit from the previous VLBI observation; [8]) and calculate the minimum energy (equipartition energy) based on section 2.3 of [53]. Assuming a power-law electron energy distribution of index -1.5 (to enable direct comparison with [53] and to account for the flat spectrum), the minimum total energies required to power a synchrontron source with the observed radio luminosity at these two size limits are $E_q \approx 10^{48.9}$ ergs ($B_{eq} \approx 27$ mG) and $\approx 10^{50.2}$ ergs ($B_{eq} \approx 190$ mG), respectively (e.g., Chapter 5 of [54]). Adopting a conservative expansion speed of ~ 0.01c [53], the average radio luminosity during its past lifespan would be 2×10^{40} erg s^{-1} (5×10^{40} erg s^{-1}), about 0.2% (0.5%) of the Eddington limit for a $10^5 M_\odot$ BH. This is uncomfortably high, accounting for typical amounts ($\sim 10\%$) of energy deposited into relativistic electrons, given the upper limit on X-ray emission of 4% of the Eddington limit for a $10^5 M_\odot$ BH [12].

The radio and X-ray observations of QRS121102 can also be compared with the radio / X-ray luminosity correlation in accreting BH systems (e.g., [55]). In particular, the AGN BH mass has been found to be correlated with its radio and X-ray luminosity (e.g., [56, 57]). A recent report based on a sample of 30 AGN with independent dynamical mass measurements shows that $\log\left(M/10^8\ M_\odot\right) = 0.55 + 1.09 \log\left(L_R/10^{38}\text{erg s}^{-1}\right) - 0.59 \log\left(L_X/10^{40}\text{erg s}^{-1}\right)$ [58], with a 1σ scatter of 1 dex assuming a log-normal mass distribution. Here, L_R and L_x are the luminosity at 5 GHz and 2 to 10 keV, respectively, observed within close epochs ($\Delta t \lesssim 2 + M/10^6 M_\odot$ days). We adopt a 5 GHz flux density of $f_R \approx 5\ \text{GHz} \cdot 200\mu\text{Jy} \sim 10^{-17}$erg s^{-1} cm^{-2} measured by VLA and an X-ray flux upper limit of $f_x \lesssim 5 \times 10^{-15}$erg s^{-1} cm^{-2} inferred from the non-detection in the XMM-Newton and Chandra images [12]. We convert the flux density to isotropic luminosity using the host redshift and have $L_R \approx 10^{39}$erg s^{-1} and $L_x \lesssim 5 \times 10^{37}$erg s^{-1}, giving a BH mass of $\sim 10^{11}\ M_\odot$, $6 \sim 7$ orders of magnitude greater than our measurement. Therefore the persistent radio

[2] Although see [52] for an example of an unambiguous AGN in a dwarf galaxy.

source does not follow the AGN BH mass-luminosity relation measured in Gültekin et al. [58].

3.4.2.2 AGN in an Isolated Dwarf Galaxy

A fraction (8% to 32%) of supermassive BH have been estimated to reside within high mass ultra-compact dwarf galaxies, suggesting that some of those galaxies could be the stripped cores of larger galaxies through tidal interactions with their companions [59]. We find that this scenario is not supported for QRS121102 for two reasons. First, the low BH mass estimated from the gas velocity dispersion is consistent with a typical dwarf galaxy instead of a more massive galaxy (section 3.3.2). Second, member(s) from the same galaxy group are expected to be associated with QRS121102 if the host had been dynamically stripped by nearby companions. From the low resolution LRIS spectra, we found that the three nearby bright sources are likely to have different redshift values from the host (section 3.3.3).

We extend this argument by searching the PanSTARRS catalog for potential companions that are likely to belong to the same galaxy group. We search the PanSTARRS catalog for sources within 5 arcmin (~1 Mpc, the virial radius of a galaxy group with a typical mass of $\sim 10^{13}$ $M_\odot$ and velocity of 200 km/s) and have consistent photometric redshift measurements with the host. One object (PSO J082.9850+33.0967) was found at 3' from QRS121102 but only detected in a stacked image and have no valid magnitude measurement available in the catalog. Another object (PSO J082.9961+33.0895) was ignored due to the large uncertainty in its photomatric redshift (0.20 ± 0.18). We find no promising group member candidate from the PanSTARRs catalog. Moreover, we compare the PanSTARRS galaxy number density within this area with the galaxy number density calculated from the deep VRI images in the R-band produced by the Keck Telescope [60]. In that work, they estimate a galaxy number density of $\approx 7 \times 10^5$ deg^{-2} with a magnitude range of $20.5 \lesssim m_R \lesssim 27.2$. In the PanSTARRS DS1 catalog, 2705 objects are found within a radius of 5 arcmin around FRB121102, and 30 of them are classified as galaxies above a confidence level of 90% [61]. The limiting magnitude of PanSTARRS is $m_r \approx 23.2$, six times shallower than that of the deep VRI images, predicting ≈ 60 galaxies within the searched area at a limiting magnitude of 23.2. The galaxy number density near QSR121102 is not overdense compare to an average sky region. We find no evidence that the host belongs to a galaxy group.

3.4.3 What Else Could the Source Be

We have found that QRS121102 is unlikely to be an AGN based on the low inferred BH mass ($\lesssim 10^{4\sim5} M_\odot$), high radio-to-X-ray luminosity ratio and the absence of companions from the same galaxy group. In this section, we discuss other possible sources for the compact persistent radio emission.

The size of the persistent radio emission could be explained by an isolated young neutron star with luminous synchrotron emission produced in a pulsar wind nebula (PWN), or plerion. The pulsar wind forms a terminal shock at a radius where the wind momentum flux and the confining pressure reach a balance, and forms a PWN further out. The shock radius is given by: $r_w = \sqrt{\dot{E}/(4\pi\eta cp)}$ [62], where $\dot{E}$ is the pulsar energy injection rate into the wind, η is the fraction of area covered by the wind, c is the speed of light, p is the confining pressure outside the shock and is proportional to the electron number density n_e for medium with the same components. The relation gives a radius of ~ 0.1 pc for a canonical isolated radio pulsar, and is confirmed to be $\approx 3 \times 10^{17}$ cm from the X-ray images of the Crab nebula [63]. For the Crab pulsar, the spin down energy rate is $\dot{E} \sim 4.5 \times 10^{38}$ ergs s^{-1} [64], and the confining pressure outside the shock is proportional to the density of the medium, which can be approximated as a typical ISM ($n_e \sim 10^{-1}$ to 10^{-2} cm^{-3}; e.g., [27]). In comparison, the energy ejection rate of FRB 121102 by the flares and the wind into the surrounding medium is estimated to be $\dot{E} \sim 10^{39}$ to 10^{40} ergs s^{-1} (Fig. 5 of [65]), and the medium ahead of the termination shock is likely denser than a typical ISM, as indicated from the high RM of FRB 121102 [66].

One example of the PWN emission model that produce the observed radio luminosities and the size of QRS121102 is presented in Margalit and Metzger [22], where the authors explain the persistent emission using a concordance FRB model. On a large scale ($\sim 10^{15}$ cm, Eqn. 4 of [67]), the train of ion-electron shells merge into a steady wind and feed into a nebula via a terminal shock, which heats up electrons in the nebula and produces the persistent synchrotron radio source. Based on the lack of self-absorption feature down to 6.0 GHz in the spectrum of the persistent source [12], Margalit and Metzger [22] estimate that the emission region's radius $R \gtrsim 0.46 \times 10^{17}$ cm adopting the observed luminosity at 6 GHz. Moreover, Resmi et al. [13] report the lack of self-absorption down to 400 MHz in their GMRT observations. Using their flux density measurement at 400 MHz and the scaling relation $R \propto L_{\nu,\mathrm{obs}}^{4/11} \nu_{\mathrm{obs}}^{-10/11}$ (Eqn. 21 in [22]), we find that $R \gtrsim 5.4 \times 10^{17}$ cm. This emission size is consistent with the constraint implied by the lack of refractive scintillation in

the Ku-band.

Among the more unique features of QRS121102 is its unusually flat radio spectrum at GHz frequencies [12]. As we have noted, several examples of compact radio sources of similar luminosities exist in dwarf galaxies. Indeed, two recent discoveries of *transient* radio sources not associated with BHs also reached similar radio luminosities. The first, FIRST J141918.9+394036, had a peak radio luminosity of 2×10^{29} erg d^{-1} Hz^{-1} at 1.4 GHz, and is hosted by a star-forming dwarf galaxy [68]. FIRST J141918.9+394036 is most likely the afterglow of an off-axis long-duration GRB [69]. The second, VT J121001+495647, had a peak radio luminosity of 1.5×10^{29} erg s^{-1} Hz^{-1} at 5 GHz, was associated with a star-forming region, and was ascribed to interaction with a dense circum-stellar medium ejected through binary interaction [20]. In both cases, however, classical synchrotron spectral shapes were observed together with secular time-evolution, unlike in the case of QRS121102. We urge continued wideband monitoring of QRS121102, together with more detailed evaluation of potential empirical analogs.

Finally, we rule out a few other possible origins of QRS121102 based on our observations. First, the source cannot be a supernova remnant (SNR) due to its high luminosity. We have calculated the specific luminosity of QSR121102 at 3 GHz and 10 GHz as $L_\nu \sim 10^{22}$ W Hz^{-1}. Varenius et al. [70] and Ulvestad [71] recently report the radio luminosities (5 GHz and 8.4 GHz) of 102 SNRs in the merging galaxies Arp 220 and Arp 229. The brightest SNR in the sample is $L_\nu < 10^{21}$ W Hz^{-1}, over one order of magnitude lower than that of QSR121102. Moreover, the luminosity is inconsistent with the star formation rate (SFR) of the host galaxy if the source were SNR(s). The brightest SNR and the SFR of a galaxy have been reported to be related [72] as: $L_{1.4}^{\rm max} = 95^{+31}_{-23}\ {\rm SFR}^{0.98\pm0.12}$, where $L_{1.4}^{\rm max}$ is in a unit of 10^{24} erg s^{-1} Hz^{-1} and SFR is in $M_\odot$ year^{-1}. Adopting the SFR upper limit of 0.4 $M_\odot$ year^{-1} based on the host Hα emission flux [9], the brightest SNR in the host would be $L_{1.4}^{\rm max} \approx 10^{18.6}$ W Hz^{-1}, over 3 orders of magnitude lower than that of QSR121102. The persistent source is too bright to be an SNR. Second, the source is too bright for a long-duration GRB (LGRB) radio afterglow. Adopting a typical LGRB peak radio luminosity of $L_{\nu,8.5{\rm GHz}} \sim 2 \times 10^{31}$ erg^{-1} s^{-1} Hz^{-1} and a decay rate of $\propto t^{-2}$ from day 10 after the GRB (e.g., [21]), the radio luminosity would have reached the level of QRS121102 ($L_{\nu,10{\rm GHz}} \approx 2 \times 10^{29}$ erg^{-1} s^{-1} Hz^{-1}) within 3 weeks, while the radio luminosity of QRS121102 have been nearly constant below 10 GHz for years (e.g., [9, 13]).

3.5 Conclusion

In this work, we investigated the origin of the persistent radio source, QRS121102, associated with FRB 121102. We present new VLA monitoring data (12 to 26 GHz) and new spectra from Keck/LRIS. The main results are summarized as follows:

1. We constrained the emission radius to be $10^{17\sim18}$ cm based on the low level of scintillation variability in our VLA observations and the previous VLBI observation. A few compact radio sources (e.g., AGN, PWNs, very young SNRs and GRB afterglows) could fall into these size limits. Most interpretations with the exception of an AGN would have been in tension with a converse finding of significant scintillation in QRS121102.

2. To further investigate the hypothesis that the source is an AGN, we roughly constrained the mass of the potential BH to be $\lesssim 10^{4\sim5} M_\odot$ using the Hα velocity dispersion. The radio luminosity ($L_\nu \sim 2 \times 10^{22}$ W Hz^{-1} from 400 MHz to 10 GHz) is possibly too high at this BH mass compared to the general AGN population, although similarly bright radio emissions have been reported in several dwarf galaxies. The source is also unlikely to be an AGN because it is too faint in the X-ray for its low BH mass and bright radio emission.

3. A significant fraction of dwarf galaxies hosting supermassive BHs may be the stripped cores of massive galaxies during tidal interactions with their nearby companion(s). From our LRIS spectra and the PanSTARRS catalog, we found no promising companion galaxy near the host to support an environment for a tidal stripping event history.

4. We briefly discussed possible origins other than AGN. QRS121102 is too luminous in the radio band to be an SNR and too old to be a typical GRB afterglow. The isolated young neutron star models for FRBs might be able to account for both the size and the luminosity of the persistent source as synchrotron emission produced in the PWN (e.g., [67]).

In conclusion, the persistent radio emission associated with FRB 121102 is likely not an AGN, and its nature remains interesting for FRB emission models involving extreme neutron stars.

References

[1] Ge Chen, Vikram Ravi, and Gregg W. Hallinan. A Comprehensive Observational Study of the FRB 121102 Persistent Radio Source. *ApJ*, 958(2):185, December 2023. doi: 10.3847/1538-4357/ad02f3.

[2] D. R. Lorimer, M. Bailes, M. A. McLaughlin, D. J. Narkevic, and F. Crawford. A Bright Millisecond Radio Burst of Extragalactic Origin. *Science*, 318(5851): 777, November 2007. doi: 10.1126/science.1147532.

[3] The CHIME/FRB Collaboration, :, Mandana Amiri, Bridget C. Andersen, Kevin Bandura, Sabrina Berger, Mohit Bhardwaj, Michelle M. Boyce, P. J. Boyle, Charanjot Brar, Daniela Breitman, Tomas Cassanelli, Pragya Chawla, Tianyue Chen, J. F. Cliche, Amanda Cook, Davor Cubranic, Alice P. Curtin, Meiling Deng, Matt Dobbs, Fengqiu, Dong, Gwendolyn Eadie, Mateus Fandino, Emmanuel Fonseca, B. M. Gaensler, Utkarsh Giri, Deborah C. Good, Mark Halpern, Alex S. Hill, Gary Hinshaw, Alexander Josephy, Jane F. Kaczmarek, Zarif Kader, Joseph W. Kania, Victoria M. Kaspi, T. L. Landecker, Dustin Lang, Calvin Leung, Dongzi Li, Hsiu-Hsien Lin, Kiyoshi W. Masui, Ryan Mckinven, Juan Mena-Parra, Marcus Merryfield, Bradley W. Meyers, Daniele Michilli, Nikola Milutinovic, Arash Mirhosseini, Moritz Münchmeyer, Arun Naidu, Laura Newburgh, Cherry Ng, Chitrang Patel, Ue-Li Pen, Emily Petroff, Tristan Pinsonneault-Marotte, Ziggy Pleunis, Masoud Rafiei-Ravandi, Mubdi Rahman, Scott M. Ransom, Andre Renard, Pranav Sanghavi, Paul Scholz, J. Richard Shaw, Kaitlyn Shin, Seth R. Siegel, Andrew E. Sikora, Saurabh Singh, Kendrick M. Smith, Ingrid Stairs, Chia Min Tan, S. P. Tendulkar, Keith Vanderlinde, Haochen Wang, Dallas Wulf, and A. V. Zwaniga. The First CHIME/FRB Fast Radio Burst Catalog. *arXiv e-prints*, art. arXiv:2106.04352, June 2021.

[4] L. G. Spitler, P. Scholz, J. W. T. Hessels, S. Bogdanov, A. Brazier, F. Camilo, S. Chatterjee, J. M. Cordes, F. Crawford, J. Deneva, R. D. Ferdman, P. C. C. Freire, V. M. Kaspi, P. Lazarus, R. Lynch, E. C. Madsen, M. A. McLaughlin, C. Patel, S. M. Ransom, A. Seymour, I. H. Stairs, B. W. Stappers, J. van Leeuwen, and W. W. Zhu. A repeating fast radio burst. *Nature*, 531(7593): 202–205, March 2016. doi: 10.1038/nature17168.

[5] P. Scholz, L. G. Spitler, J. W. T. Hessels, S. Chatterjee, J. M. Cordes, V. M. Kaspi, R. S. Wharton, C. G. Bassa, S. Bogdanov, F. Camilo, F. Crawford, J. Deneva, J. van Leeuwen, R. Lynch, E. C. Madsen, M. A. McLaughlin, M. Mickaliger, E. Parent, C. Patel, S. M. Ransom, A. Seymour, I. H. Stairs, B. W. Stappers, and S. P. Tendulkar. The Repeating Fast Radio Burst FRB 121102: Multi-wavelength Observations and Additional Bursts. *ApJ*, 833(2): 177, December 2016. doi: 10.3847/1538-4357/833/2/177.

[6] M. Cruces, L. G. Spitler, P. Scholz, R. Lynch, A. Seymour, J. W. T. Hessels, C. Gouiffés, G. H. Hilmarsson, M. Kramer, and S. Munjal. Repeating be-

haviour of FRB 121102: periodicity, waiting times, and energy distribution. *MNRAS*, 500(1):448–463, January 2021. doi: 10.1093/mnras/staa3223.

[7] C. G. Bassa, S. P. Tendulkar, E. A. K. Adams, N. Maddox, S. Bogdanov, G. C. Bower, S. Burke-Spolaor, B. J. Butler, S. Chatterjee, J. M. Cordes, J. W. T. Hessels, V. M. Kaspi, C. J. Law, B. Marcote, Z. Paragi, S. M. Ransom, P. Scholz, L. G. Spitler, and H. J. van Langevelde. FRB 121102 Is Coincident with a Star-forming Region in Its Host Galaxy. *ApJ*, 843(1):L8, July 2017. doi: 10.3847/2041-8213/aa7a0c.

[8] B. Marcote, Z. Paragi, J. W. T. Hessels, A. Keimpema, H. J. van Langevelde, Y. Huang, C. G. Bassa, S. Bogdanov, G. C. Bower, S. Burke-Spolaor, B. J. Butler, R. M. Campbell, S. Chatterjee, J. M. Cordes, P. Demorest, M. A. Garrett, T. Ghosh, V. M. Kaspi, C. J. Law, T. J. W. Lazio, M. A. McLaughlin, S. M. Ransom, C. J. Salter, P. Scholz, A. Seymour, A. Siemion, L. G. Spitler, S. P. Tendulkar, and R. S. Wharton. The Repeating Fast Radio Burst FRB 121102 as Seen on Milliarcsecond Angular Scales. *ApJ*, 834(2):L8, January 2017. doi: 10.3847/2041-8213/834/2/L8.

[9] S. P. Tendulkar, C. G. Bassa, J. M. Cordes, G. C. Bower, C. J. Law, S. Chatterjee, E. A. K. Adams, S. Bogdanov, S. Burke-Spolaor, B. J. Butler, P. Demorest, J. W. T. Hessels, V. M. Kaspi, T. J. W. Lazio, N. Maddox, B. Marcote, M. A. McLaughlin, Z. Paragi, S. M. Ransom, P. Scholz, A. Seymour, L. G. Spitler, H. J. van Langevelde, and R. S. Wharton. The Host Galaxy and Redshift of the Repeating Fast Radio Burst FRB 121102. *ApJ*, 834(2):L7, January 2017. doi: 10.3847/2041-8213/834/2/L7.

[10] Planck Collaboration, N. Aghanim, Y. Akrami, M. Ashdown, J. Aumont, C. Baccigalupi, M. Ballardini, A. J. Banday, R. B. Barreiro, N. Bartolo, S. Basak, R. Battye, K. Benabed, J. P. Bernard, M. Bersanelli, P. Bielewicz, J. J. Bock, J. R. Bond, J. Borrill, F. R. Bouchet, F. Boulanger, M. Bucher, C. Burigana, R. C. Butler, E. Calabrese, J. F. Cardoso, J. Carron, A. Challinor, H. C. Chiang, J. Chluba, L. P. L. Colombo, C. Combet, D. Contreras, B. P. Crill, F. Cuttaia, P. de Bernardis, G. de Zotti, J. Delabrouille, J. M. Delouis, E. Di Valentino, J. M. Diego, O. Doré, M. Douspis, A. Ducout, X. Dupac, S. Dusini, G. Efstathiou, F. Elsner, T. A. Enßlin, H. K. Eriksen, Y. Fantaye, M. Farhang, J. Fergusson, R. Fernandez-Cobos, F. Finelli, F. Forastieri, M. Frailis, A. A. Fraisse, E. Franceschi, A. Frolov, S. Galeotta, S. Galli, K. Ganga, R. T. Génova-Santos, M. Gerbino, T. Ghosh, J. González-Nuevo, K. M. Górski, S. Gratton, A. Gruppuso, J. E. Gudmundsson, J. Hamann, W. Handley, F. K. Hansen, D. Herranz, S. R. Hildebrandt, E. Hivon, Z. Huang, A. H. Jaffe, W. C. Jones, A. Karakci, E. Keihänen, R. Keskitalo, K. Kiiveri, J. Kim, T. S. Kisner, L. Knox, N. Krachmalnicoff, M. Kunz, H. Kurki-Suonio, G. Lagache, J. M. Lamarre, A. Lasenby, M. Lattanzi, C. R. Lawrence, M. Le Jeune, P. Lemos, J. Lesgourgues, F. Levrier, A. Lewis, M. Liguori, P. B. Lilje, M. Lilley, V. Lindholm, M. López-Caniego, P. M. Lubin, Y. Z. Ma, J. F. Macías-Pérez, G. Mag-

gio, D. Maino, N. Mandolesi, A. Mangilli, A. Marcos-Caballero, M. Maris, P. G. Martin, M. Martinelli, E. Martínez-González, S. Matarrese, N. Mauri, J. D. McEwen, P. R. Meinhold, A. Melchiorri, A. Mennella, M. Migliaccio, M. Millea, S. Mitra, M. A. Miville-Deschênes, D. Molinari, L. Montier, G. Morgante, A. Moss, P. Natoli, H. U. Nørgaard-Nielsen, L. Pagano, D. Paoletti, B. Partridge, G. Patanchon, H. V. Peiris, F. Perrotta, V. Pettorino, F. Piacentini, L. Polastri, G. Polenta, J. L. Puget, J. P. Rachen, M. Reinecke, M. Remazeilles, A. Renzi, G. Rocha, C. Rosset, G. Roudier, J. A. Rubiño-Martín, B. Ruiz-Granados, L. Salvati, M. Sandri, M. Savelainen, D. Scott, E. P. S. Shellard, C. Sirignano, G. Sirri, L. D. Spencer, R. Sunyaev, A. S. Suur-Uski, J. A. Tauber, D. Tavagnacco, M. Tenti, L. Toffolatti, M. Tomasi, T. Trombetti, L. Valenziano, J. Valiviita, B. Van Tent, L. Vibert, P. Vielva, F. Villa, N. Vittorio, B. D. Wandelt, I. K. Wehus, M. White, S. D. M. White, A. Zacchei, and A. Zonca. Planck 2018 results. VI. Cosmological parameters. *A&A*, 641:A6, September 2020. doi: 10.1051/0004-6361/201833910.

[11] C. H. Niu, K. Aggarwal, D. Li, X. Zhang, S. Chatterjee, C. W. Tsai, W. Yu, C. J. Law, S. Burke-Spolaor, J. M. Cordes, Y. K. Zhang, S. Ocker, J. M. Yao, P. Wang, Y. Feng, Y. Niino, C. Bochenek, M. Cruces, L. Connor, J. A. Jiang, S. Dai, R. Luo, G. D. Li, C. C. Miao, J. R. Niu, R. Anna-Thomas, J. Sydnor, D. Stern, W. Y. Wang, M. Yuan, Y. L. Yue, D. J. Zhou, Z. Yan, W. W. Zhu, and B. Zhang. A repeating FRB in a dense environment with a compact persistent radio source. *arXiv e-prints*, art. arXiv:2110.07418, October 2021.

[12] S. Chatterjee, C. J. Law, R. S. Wharton, S. Burke-Spolaor, J. W. T. Hessels, G. C. Bower, J. M. Cordes, S. P. Tendulkar, C. G. Bassa, P. Demorest, B. J. Butler, A. Seymour, P. Scholz, M. W. Abruzzo, S. Bogdanov, V. M. Kaspi, A. Keimpema, T. J. W. Lazio, B. Marcote, M. A. McLaughlin, Z. Paragi, S. M. Ransom, M. Rupen, L. G. Spitler, and H. J. van Langevelde. A direct localization of a fast radio burst and its host. *Nature*, 541(7635):58–61, January 2017. doi: 10.1038/nature20797.

[13] L Resmi, J Vink, and C H Ishwara-Chandra. Implications of the lowest frequency detection of the persistent counterpart of FRB121102. *arXiv e-prints*, art. arXiv:2010.14334, October 2020.

[14] R. W. Romani, R. Narayan, and R. Blandford. Refractive effects in pulsar scintillation. *MNRAS*, 220:19–49, May 1986. doi: 10.1093/mnras/220.1.19.

[15] Mark A. Walker. Interstellar scintillation of compact extragalactic radio sources. *MNRAS*, 294:307–311, February 1998. doi: 10.1046/j.1365-8711.1998.01238.x.

[16] Amy E. Reines, James J. Condon, Jeremy Darling, and Jenny E. Greene. A New Sample of (Wandering) Massive Black Holes in Dwarf Galaxies from High-resolution Radio Observations. *ApJ*, 888(1):36, January 2020. doi: 10.3847/1538-4357/ab4999.

[17] M. Mezcua, H. Suh, and F. Civano. Radio jets from AGNs in dwarf galaxies in the COSMOS survey: mechanical feedback out to redshift ∼3.4. *MNRAS*, 488(1):685–695, September 2019. doi: 10.1093/mnras/stz1760.

[18] J. A. Baldwin, M. M. Phillips, and R. Terlevich. Classification parameters for the emission-line spectra of extragalactic objects. *PASP*, 93:5–19, February 1981. doi: 10.1086/130766.

[19] J. Sabater, P. N. Best, M. J. Hardcastle, T. W. Shimwell, C. Tasse, W. L. Williams, M. Brüggen, R. K. Cochrane, J. H. Croston, F. de Gasperin, K. J. Duncan, G. Gürkan, A. P. Mechev, L. K. Morabito, I. Prandoni, H. J. A. Röttgering, D. J. B. Smith, J. J. Harwood, B. Mingo, S. Mooney, and A. Saxena. The LoTSS view of radio AGN in the local Universe. The most massive galaxies are always switched on. *A&A*, 622:A17, February 2019. doi: 10.1051/0004-6361/201833883.

[20] D. Z. Dong, G. Hallinan, E. Nakar, A. Y. Q. Ho, A. K. Hughes, K. Hotokezaka, S. T. Myers, K. De, K. P. Mooley, V. Ravi, A. Horesh, M. M. Kasliwal, and S. R. Kulkarni. A transient radio source consistent with a merger-triggered core collapse supernova. *Science*, 373(6559):1125–1129, September 2021. doi: 10.1126/science.abg6037.

[21] E. Berger, S. R. Kulkarni, G. Pooley, D. A. Frail, V. McIntyre, R. M. Wark, R. Sari, A. M. Soderberg, D. W. Fox, S. Yost, and P. A. Price. A common origin for cosmic explosions inferred from calorimetry of GRB030329. *Nature*, 426 (6963):154–157, November 2003. doi: 10.1038/nature01998.

[22] Ben Margalit and Brian D. Metzger. A Concordance Picture of FRB 121102 as a Flaring Magnetar Embedded in a Magnetized Ion-Electron Wind Nebula. *ApJ*, 868(1):L4, November 2018. doi: 10.3847/2041-8213/aaedad.

[23] D. S. Briggs. High Fidelity Interferometric Imaging: Robust Weighting and NNLS Deconvolution. In *American Astronomical Society Meeting Abstracts*, volume 187 of *American Astronomical Society Meeting Abstracts*, page 112.02, December 1995.

[24] Thomas M. O. Franzen, Matthew L. Davies, Rod D. Davies, Richard J. Davis, Farhan Feroz, Ricardo Génova-Santos, Keith J. B. Grainge, David A. Green, Michael P. Hobson, Natasha Hurley-Walker, Anthony N. Lasenby, Marcos López-Caniego, Malak Olamaie, Carmen P. Padilla-Torres, Guy G. Pooley, Rafael Rebolo, Carmen Rodríguez-Gonzálvez, Richard D. E. Saunders, Anna M. M. Scaife, Paul F. Scott, Timothy W. Shimwell, David J. Titterington, Elizabeth M. Waldram, Robert A. Watson, and Jonathan T. L. Zwart. Follow-up observations at 16 and 33GHz of extragalactic sources from WMAP 3-yr data: II - Flux density variability. *MNRAS*, 400(2):995–1005, December 2009. doi: 10.1111/j.1365-2966.2009.15673.x.

[25] Daniel A. Perley. Fully Automated Reduction of Longslit Spectroscopy with the Low Resolution Imaging Spectrometer at the Keck Observatory. *PASP*, 131(1002):084503, August 2019. doi: 10.1088/1538-3873/ab215d.

[26] George B. Rybicki and Alan P. Lightman. *Radiative processes in astrophysics*. 1979.

[27] Bruce T. Draine. *Physics of the Interstellar and Intergalactic Medium*. 2011.

[28] Dana Simard and Vikram Ravi. Measuring interstellar turbulence in fast radio burst host galaxies. *arXiv e-prints*, art. arXiv:2107.11334, July 2021.

[29] Jenny E. Greene and Luis C. Ho. The M_{BH}-σ_* Relation in Local Active Galaxies. *ApJ*, 641(1):L21–L24, April 2006. doi: 10.1086/500507.

[30] Ting Xiao, Aaron J. Barth, Jenny E. Greene, Luis C. Ho, Misty C. Bentz, Randi R. Ludwig, and Yanfei Jiang. Exploring the Low-mass End of the M $_{BH}$-σ_* Relation with Active Galaxies. *ApJ*, 739(1):28, September 2011. doi: 10.1088/0004-637X/739/1/28.

[31] Kayhan Gültekin, Douglas O. Richstone, Karl Gebhardt, Tod R. Lauer, Scott Tremaine, M. C. Aller, Ralf Bender, Alan Dressler, S. M. Faber, Alexei V. Filippenko, Richard Green, Luis C. Ho, John Kormendy, John Magorrian, Jason Pinkney, and Christos Siopis. The M-σ and M-L Relations in Galactic Bulges, and Determinations of Their Intrinsic Scatter. *ApJ*, 698(1):198–221, June 2009. doi: 10.1088/0004-637X/698/1/198.

[32] Laura Ferrarese and Holland Ford. Supermassive Black Holes in Galactic Nuclei: Past, Present and Future Research. *Space Sci. Rev.*, 116(3-4):523–624, February 2005. doi: 10.1007/s11214-005-3947-6.

[33] Nicholas J. McConnell and Chung-Pei Ma. Revisiting the Scaling Relations of Black Hole Masses and Host Galaxy Properties. *ApJ*, 764(2):184, February 2013. doi: 10.1088/0004-637X/764/2/184.

[34] Thomas Wevers, Nicholas C. Stone, Sjoert van Velzen, Peter G. Jonker, Tiara Hung, Katie Auchettl, Suvi Gezari, Francesca Onori, Daniel Mata Sánchez, Zuzanna Kostrzewa-Rutkowska, and Jorge Casares. Black hole masses of tidal disruption event host galaxies II. *MNRAS*, 487(3):4136–4152, August 2019. doi: 10.1093/mnras/stz1602.

[35] Thomas Wevers, Sjoert van Velzen, Peter G. Jonker, Nicholas C. Stone, Tiara Hung, Francesca Onori, Suvi Gezari, and Nadejda Blagorodnova. Black hole masses of tidal disruption event host galaxies. *MNRAS*, 471(2):1694–1708, October 2017. doi: 10.1093/mnras/stx1703.

[36] Mitsuru Kokubo, Kazuma Mitsuda, Hajime Sugai, Shinobu Ozaki, Yosuke Minowa, Takashi Hattori, Yutaka Hayano, Kazuya Matsubayashi, Atsushi Shimono, Shigeyuki Sako, and Mamoru Doi. Hα Intensity Map of the Repeating

Fast Radio Burst FRB 121102 Host Galaxy from Subaru/Kyoto 3DII AO-assisted Optical Integral-field Spectroscopy. *ApJ*, 844(2):95, August 2017. doi: 10.3847/1538-4357/aa7b2d.

[37] Luis C. Ho, Marc Sarzi, Hans-Walter Rix, Joseph C. Shields, Greg Rudnick, Alexei V. Filippenko, and Aaron J. Barth. An Efficient Strategy to Select Targets for Gasdynamical Measurements of Black Hole Masses Using the Hubble Space Telescope. *PASP*, 114(792):137–143, February 2002. doi: 10.1086/338546.

[38] Bradley M. Peterson. Reverberation Mapping of Active Galactic Nuclei. *PASP*, 105:247, March 1993. doi: 10.1086/133140.

[39] Amy E. Reines and Marta Volonteri. Relations between Central Black Hole Mass and Total Galaxy Stellar Mass in the Local Universe. *ApJ*, 813(2):82, November 2015. doi: 10.1088/0004-637X/813/2/82.

[40] Amy E. Reines, Jenny E. Greene, and Marla Geha. Dwarf Galaxies with Optical Signatures of Active Massive Black Holes. *ApJ*, 775(2):116, October 2013. doi: 10.1088/0004-637X/775/2/116.

[41] Mareki Honma, Takumi Nagayama, Kazuma Ando, Takeshi Bushimata, Yoon Kyung Choi, Toshihiro Handa, Tomoya Hirota, Hiroshi Imai, Takaaki Jike, Mi Kyoung Kim, Osamu Kameya, Noriyuki Kawaguchi, Hideyuki Kobayashi, Tomoharu Kurayama, Seisuke Kuji, Naoko Matsumoto, Seiji Manabe, Takeshi Miyaji, Kazuhito Motogi, Akiharu Nakagawa, Hiroyuki Nakanishi, Kotaro Niinuma, Chung Sik Oh, Toshihiro Omodaka, Tomoaki Oyama, Nobuyuki Sakai, Katsuhisa Sato, Mayumi Sato, Katsunori M. Shibata, Satoshi Shiozaki, Kazuyoshi Sunada, Yoshiaki Tamura, Yuji Ueno, and Aya Yamauchi. Fundamental Parameters of the Milky Way Galaxy Based on VLBI astrometry. *PASJ*, 64:136, December 2012. doi: 10.1093/pasj/64.6.136.

[42] J. W. Armstrong, B. J. Rickett, and S. R. Spangler. Electron Density Power Spectrum in the Local Interstellar Medium. *ApJ*, 443:209, April 1995. doi: 10.1086/175515.

[43] J. M. Cordes and B. J. Rickett. Diffractive Interstellar Scintillation Timescales and Velocities. *ApJ*, 507(2):846–860, November 1998. doi: 10.1086/306358.

[44] Ramesh Narayan. The Physics of Pulsar Scintillation. *Philosophical Transactions of the Royal Society of London Series A*, 341(1660):151–165, October 1992. doi: 10.1098/rsta.1992.0090.

[45] J. M. Cordes and T. J. W. Lazio. NE2001.I. A New Model for the Galactic Distribution of Free Electrons and its Fluctuations. *arXiv e-prints*, art. astro-ph/0207156, July 2002.

[46] J. M. Cordes and T. J. W. Lazio. NE2001. II. Using Radio Propagation Data to Construct a Model for the Galactic Distribution of Free Electrons. *arXiv e-prints*, art. astro-ph/0301598, January 2003.

[47] B. J. Rickett, A. Quirrenbach, R. Wegner, T. P. Krichbaum, and A. Witzel. Interstellar scintillation of the radio source 0917+624. *A&A*, 293:479–492, January 1995.

[48] James M. Cordes. Pulsar Observations I. – Propagation Effects, Searching Distance Estimates, Scintillations and VLBI. In Snezana Stanimirovic, Daniel Altschuler, Paul Goldsmith, and Chris Salter, editors, *Single-Dish Radio Astronomy: Techniques and Applications*, volume 278 of *Astronomical Society of the Pacific Conference Series*, pages 227–250, December 2002.

[49] J. J. Condon. Radio emission from normal galaxies. *ARA&A*, 30:575–611, January 1992. doi: 10.1146/annurev.aa.30.090192.003043.

[50] Mark Lacy, Sally A. Laurent-Muehleisen, Susan E. Ridgway, Robert H. Becker, and Richard L. White. The Radio Luminosity-Black Hole Mass Correlation for Quasars from the FIRST Bright Quasar Survey and a "Unification Scheme" for Radio-loud and Radio-quiet Quasars. *ApJ*, 551(1):L17–L21, April 2001. doi: 10.1086/319836.

[51] C. J. Law, L. Connor, and K. Aggarwal. On the Fast Radio Burst and Persistent Radio Source Populations. *arXiv e-prints*, art. arXiv:2110.15323, October 2021.

[52] Mallory Molina, Amy E. Reines, Jenny E. Greene, Jeremy Darling, and James J. Condon. Outflows, Shocks, and Coronal Line Emission in a Radio-selected AGN in a Dwarf Galaxy. *ApJ*, 910(1):5, March 2021. doi: 10.3847/1538-4357/abe120.

[53] H. K. Vedantham and V. Ravi. Faraday conversion and magneto-ionic variations in fast radio bursts. *MNRAS*, 485(1):L78–L82, May 2019. doi: 10.1093/mnrasl/slz038.

[54] James J. Condon and Scott M. Ransom. *Essential Radio Astronomy*. 2016.

[55] D. C. Hannikainen, R. W. Hunstead, D. Campbell-Wilson, and R. K. Sood. MOST radio monitoring of GX 339-4. *A&A*, 337:460–464, September 1998.

[56] H. Falcke, E. Körding, and S. Markoff. A scheme to unify low-power accreting black holes. Jet-dominated accretion flows and the radio/X-ray correlation. *A&A*, 414:895–903, February 2004. doi: 10.1051/0004-6361:20031683.

[57] Andrea Merloni, Sebastian Heinz, and Tiziana di Matteo. A Fundamental Plane of black hole activity. *MNRAS*, 345(4):1057–1076, November 2003. doi: 10.1046/j.1365-2966.2003.07017.x.

[58] Kayhan Gültekin, Ashley L. King, Edward M. Cackett, Kristina Nyland, Jon M. Miller, Tiziana Di Matteo, Sera Markoff, and Michael P. Rupen. The Fundamental Plane of Black Hole Accretion and Its Use as a Black Hole-Mass Estimator. *ApJ*, 871(1):80, January 2019. doi: 10.3847/1538-4357/aaf6b9.

[59] Karina T. Voggel, Anil C. Seth, Holger Baumgardt, Steffen Mieske, Joel Pfeffer, and Alexander Rasskazov. The Impact of Stripped Nuclei on the Supermassive Black Hole Number Density in the Local Universe. *ApJ*, 871 (2):159, February 2019. doi: 10.3847/1538-4357/aaf735.

[60] Ian Smail, David W. Hogg, Lin Yan, and Judith G. Cohen. Deep Optical Galaxy Counts with the Keck Telescope. *ApJ*, 449:L105, August 1995. doi: 10.1086/309647.

[61] Yutaro Tachibana and A. A. Miller. A Morphological Classification Model to Identify Unresolved PanSTARRS1 Sources: Application in the ZTF Realtime Pipeline. *PASP*, 130(994):128001, December 2018. doi: 10.1088/1538-3873/aae3d9.

[62] Patrick Slane. The devil is in the details: Compact structures in pulsar wind nebulae. *Advances in Space Research*, 35(6):1092–1098, January 2005. doi: 10.1016/j.asr.2005.04.029.

[63] Martin C. Weisskopf, J. Jeff Hester, Allyn F. Tennant, Ronald F. Elsner, Norbert S. Schulz, Herman L. Marshall, Margarita Karovska, Joy S. Nichols, Douglas A. Swartz, Jeffery J. Kolodziejczak, and Stephen L. O'Dell. Discovery of Spatial and Spectral Structure in the X-Ray Emission from the Crab Nebula. *ApJ*, 536(2):L81–L84, June 2000. doi: 10.1086/312733.

[64] David H. Staelin and III Reifenstein, Edward C. Pulsating Radio Sources near the Crab Nebula. *Science*, 162(3861):1481–1483, December 1968. doi: 10.1126/science.162.3861.1481.

[65] Ben Margalit, Brian D. Metzger, and Lorenzo Sironi. Constraints on the engines of fast radio bursts. *MNRAS*, 494(4):4627–4644, June 2020. doi: 10.1093/mnras/staa1036.

[66] D. Michilli, A. Seymour, J. W. T. Hessels, L. G. Spitler, V. Gajjar, A. M. Archibald, G. C. Bower, S. Chatterjee, J. M. Cordes, K. Gourdji, G. H. Heald, V. M. Kaspi, C. J. Law, C. Sobey, E. A. K. Adams, C. G. Bassa, S. Bogdanov, C. Brinkman, P. Demorest, F. Fernandez, G. Hellbourg, T. J. W. Lazio, R. S. Lynch, N. Maddox, B. Marcote, M. A. McLaughlin, Z. Paragi, S. M. Ransom, P. Scholz, A. P. V. Siemion, S. P. Tendulkar, P. van Rooy, R. S. Wharton, and D. Whitlow. An extreme magneto-ionic environment associated with the fast radio burst source FRB 121102. *Nature*, 553(7687):182–185, January 2018. doi: 10.1038/nature25149.

[67] Brian D. Metzger, Ben Margalit, and Lorenzo Sironi. Fast radio bursts as synchrotron maser emission from decelerating relativistic blast waves. *MNRAS*, 485(3):4091–4106, May 2019. doi: 10.1093/mnras/stz700.

[68] C. J. Law, B. M. Gaensler, B. D. Metzger, E. O. Ofek, and L. Sironi. Discovery of the Luminous, Decades-long, Extragalactic Radio Transient FIRST J141918.9+394036. *ApJ*, 866(2):L22, October 2018. doi: 10.3847/2041-8213/aae5f3.

[69] K. P. Mooley, B. Margalit, C. J. Law, D. A. Perley, A. T. Deller, T. J. W. Lazio, M. F. Bietenholz, T. Shimwell, H. T. Intema, B. M. Gaensler, B. D. Metzger, D. Z. Dong, G. Hallinan, E. O. Ofek, and L. Sironi. Late-Time Evolution and Modeling of the Off-Axis Gamma-ray Burst Candidate FIRST J141918.9+394036. *arXiv e-prints*, art. arXiv:2107.04703, July 2021.

[70] E. Varenius, J. E. Conway, F. Batejat, I. Martí-Vidal, M. A. Pérez-Torres, S. Aalto, A. Alberdi, C. J. Lonsdale, and P. Diamond. The population of SNe/SNRs in the starburst galaxy Arp 220. A self-consistent analysis of 20 years of VLBI monitoring. *A&A*, 623:A173, March 2019. doi: 10.1051/0004-6361/201730631.

[71] James S. Ulvestad. Radio Emission from Young Supernovae and Supernova Remnants in Arp 299. *AJ*, 138(5):1529–1538, November 2009. doi: 10.1088/0004-6256/138/5/1529.

[72] Laura Chomiuk and Eric M. Wilcots. A Universal Luminosity Function for Radio Supernova Remnants. *ApJ*, 703(1):370–389, September 2009. doi: 10.1088/0004-637X/703/1/370.

Table 3.1: VLA Observations and Results.

Obs.	Epoch (YYYY-MM-DD hh:mm)	Band	3C147 (f0) (Jy)	J0555+3948 (f1) (mJy)	J0518+3306 (f2) (mJy)	QRS121102 (f3) (μJy)
1	2017-05-29 16:09	K	1.994 ± 0.010	1956.5 ± 2.5	153.1 ± 5.3	56.6 ± 8.2
2	2017-06-03 16:43	K	2.010 ± 0.013	2135.8 ± 3.4	143.9 ± 2.5	52.4 ± 7.0
3	2017-06-08 08:19	U	2.82 ± 0.11	2242 ± 15	200.2 ± 1.7	67 ± 13
4	2017-06-10 21:25	U	2.857 ± 0.010	2565 ± 30	214.5 ± 5.7	118.0 ± 5.5
5	2017-06-11 16:32	U	2.799 ± 0.018	2431.2 ± 6.4	158.2 ± 2.5	82.1 ± 6.4
6	2017-08-10 12:31	K	2.050 ± 0.026	2148.4 ± 7.5	193.6 ± 5.4	109 ± 14
	2017-08-10 06:04	U	2.804 ± 0.026	2217.7 ± 6.0	144.0 ± 4.3	63.5 ±6.3

Table 3.2: VLA Targets.

Field	Target	RA	DEC	Intention	Single Scan Duration (Minutes)
0	J0542+4951 (3C147)	$05^h42^m36.1^s$	$+49^o51'07.2''$	Flux and Bandpass Calibrator	6
1	J0555+3948	$05^h55^m30.8^s$	$+39^o48'49.2''$	Phase Calibrator 1 [a]	1.5
2	J0518+3306	$05^h18^m05.1^s$	$+33^o06'13.4''$	Phase Calibrator 2 [b]	1.5
3	QRS121102	$05^h31^m58.7^s$	$+33^o08'52.5''$	Science	10

a Used as the phase calibrator during our CASA imaging process.
b Treated as a science target during our CASA imaging process.

Table 3.3: Summary of Optical Observations.

Date (YYYY-MM-DD)	Instrument	Grating, Grism (Red, Blue)	λ (Red, Blue; Å)	Slit	Resolution (1σ) (Å)	Exposure (Minutes)
2018-10-12	LRIS	1200/7500, 400/3400	NA	long 1.0"	~ 1	80 [a]
2017-01-26	LRIS	400/8500, 600/4000	5462 ~ 10318, 3122 ~ 5603	long 1.5"	~ 4	50

a Each exposure is 20 minutes. The total exposure time is 80 minutes when combining all four exposures, and 40 minutes after excluding the two exposures polluted by cosmic rays (see Section 3.3.2).

Table 3.4: Predicted Galactic Refractive Scintillation Properties of QRS121102 Assuming a Point Source and Kolmogorov Turbulence.

Band (ν_c)	m_p	t_r (Hour)	θ_r [a] (μas)
K (22 GHz)	73%	~ 7	4
U (15 GHz)	59%	~ 16	10

a Assuming a nominal distance between the scattering screen and the observer to be 1 kpc.

Table 3.5: VLA Flux Density Modulation Indices Results and Statistical Tests.

Data (band)	m'_p (Observed)	χ^2_{min} (dof)	Constant $P(\geq \chi^2_{min}; \nu)$	Refractive Scintillation $P(\leq \chi^2_\nu; m_p)$
f3/f2[a](K)	(19.3 ± 7.1)%	5.8 (2)	5.6%	~ 9%
f3/f2 (U)	(13.3 ± 4.8)%	10.9 (3)	1.2%	~ 3%
f3[b](K)	(30.2 ± 5.8)%	13.9 (2)	10^{-3}	~ 20%
f3 (U)	(26.1 ± 4.4)%	48.5 (3)	10^{-10}	~ 23%

a The flux density measurements of QRS121102 divided by those of J0518+3306 and then normalized to an average of unity.
b The normalized flux density measurements of QRS121102.

Table 3.6: Implications of the Lack of Refractive Scintillation.

Observation	$\langle f_\nu \rangle$ [a] (μJy)	Radio Luminosity [b] (erg s^{-1})	Radius[c] (cm)	T_b[c] (k)
VLA K-band (22 GHz)	61.3 ± 5.0	1.5×10^{39}	$\gtrsim 4 \times 10^{16}$	$\lesssim 5 \times 10^8$
VLA Ku-band (15 GHz)	89.4 ± 3.4	1.5×10^{39}	$\gtrsim 10^{17}$	$\lesssim 2 \times 10^9$

a Weighted Average Flux Density
b Isotropic Luminosity $L \approx \nu_c \langle f_\nu \rangle 4\pi D_L^2$, where ν_c is the band central frequency.
c Assuming a nominal distance of 1 kpc between the scattering screen and the observer.

Chapter 4

THE BURST MORPHOLOGY OF A SAMPLE OF DSA-110 FRBS

The work presented in this chapter has been adapted from:

- Radio morphology of a sample of 21 DSA-110 FRBs. *In preparation*, 2023.

4.1 Introduction

Fast Radio Bursts (FRBs) are short ($\sim \mu$s to several ms), luminous ($10^{40\sim46}$ erg s^{-1}) transients detected in the radio band (110 MHz to 8 GHz). By the end of 2022, nearly 700 FRB sources have been reported by the Canadian Hydrogen Intensity Mapping Experiment (CHIME) [1], the Australian Square Kilometre Array Pathfinder (ASKAP) (e.g., [2], add more recent papers), the Parkes Radio Telescope, the Deep Synoptic Array (DSA-10), the Five hundred meter Aperture Spherical Telescope (FAST), the APERture Tile In Focus (Apertif), the European VLBI Network (EVN) and Arecibo. Those samples illustrate the diversity in burst properties such as fluence, width, multi-path scattering, temporal-spectral complexities, repetitions and periodic activities, revealing a potentially non-uniform population of FRBs (e.g., [1]). In particular, the temporal-spectral features are best resolved using the high resolution baseband voltage data.

Localized FRBs provide important clues on their progenitor formation channels. To begin with, the precise redshift measured from individual host galaxy spectrum makes it possible to calculate the burst energy, the volumetric rate and to explore the correlation between burst properties with host distance and cosmic evolution. Moreover, additional host properties, such as the galaxy type, age, star formation rate as well as the spatial offset between the FRB and the star-forming regions, help to distinguish different progenitor formation histories (e.g., [3]; [4]; [5]).

Localized FRBs could be used as cosmic tools. For example, the relation between redshift and extragalactic DM helps to explain the distribution of the cosmic baryon content (e.g., [6]). In addition, the redshift measurements could help to disentangle the DM, multi-path scattering and scintillation contributions from the Milky Way, the intergalactic medium (IGM), the host galaxy and potentially intervening systems such as galaxies, galaxy clusters or the cosmic web (e.g., [7]). What's more, if there were any correlation among the host properties such as the Hα luminosity, host DM

and host scattering, they would provide additional means to understand host-galaxy systematics in future studies.

By the end of 2022, about 25 FRBs have been associated with individual host galaxies (e.g., [3]). The diversity in host properties and FRBs locations within their hosts indicate the possibility of multiple formation channels for FRB progenitors. For example, FRB 20121102 has been localized to a dwarf galaxy with active star formation and a persistent radio counterpart (e.g., [8]), which could be explained by a young magnetar (e.g., [9]). The repeating FRB 20200120E in M81 has been associated within an old globular cluster that is unlikely to fit in with a young magnetar formed in a recent core-collapse supernovae, but could be explained by magnetar progenitor formed via accretion- or merger- induced collapse in a binary system (e.g., [10]; [11]). Recently, [12] report two FRBs within massive galaxy clusters with different host types: the host of FRB 20220914A is a late-type star-forming galaxy, while the host of FRB 20220509G is an early-type quiescent galaxy, requiring progenitor formation channels to accommodate different stellar population ages.

In this work, we report a sample of 21 FRBs detected by the Deep Synoptic Array-110 (DSA-110) from January to October of 2022 during the commissioning stage. We utilize the raw-resolution voltage data to best characterize their burst morphology and spectral features. In particular, hosts in some imaging data have been identified for 18 objects and 16 have optical spectra. The combination of the DSA-110 high-resolution voltage data and optical observations of the host provide an invaluable opportunity to explore any potential correlations between FRB features and host types.

In this paper, we describe the DSA commissioning observations in Section 4.2, present the burst morphology and spectral analyses method and results in Section 4.3, compare the DSA sample with other relatively large FRB samples and explore the correlation between burst and host properties in Section 4.4 and conclude in Section 4.5. Throughout this work, we use the cosmological constants reported by [13] for a flat universe, with a Hubble constant of $H_0 = 67.8$ km $s^{-1}Mpc^{-1}$, a dark matter energy density of $\Omega_{\Omega_0} = 0.691$, a matter density of $\Omega_{m_0} = 0.308$ and a baryon matter density of $\Omega_{b_0} = 0.0486$.

4.2 DSA-110

The DSA-110 is a radio interforometer sited at the Owens Valley Radio Observatory (OVRO). It is the only radio interforometer designed specifically to search for and localize FRBs. During the time period described in this work, DSA-110 is within a commissioning stage with a 63-antenna deployment (Ravi et al. in prep). The deployment is composed of 48 searching antennas aligned along the east-west direction with a maximum spacing of 400 m, and 15 outrigger antennas spread out at the site with a maximum baseline of 2.6 km. All of the dishes are 4.65 m in diameter, has a dual-polarization receiver with a system temperature of 25 K [14] and a system equivalent flux density (SEFD) for FRB searching of 140 Jy.

The real-time search system inspects the 256 fan-beams formed by the 48 searching antennas using a modified multi-beam `Heimdall` pipeline [15] within a DM range from 50 to 1500. The pulse candidates are then clustered by individual event and evaluated by a machine learning classifier to estimate the probability of being an astrophysical event. For events above a signal-to-noise-ratio (SNR) of 8.5, a 2s-long (or 4s-long) of voltage data from the 63 antennas are stored, with $\sim$ 0.5 s of data before the event and $\sim$ 1.5 s (or 3.5 s) of data afterwards. The 4-bit voltage data has a temporal resolution of 32.768 μs and spectral resolution of 6144 $\times$ 30.518 kHz from 1498.8 to 1211.3 MHz.

The voltage data are coherently combined towards the direction of each FRB candidate to initially verify the detection. Complex, frequency- and polarization-dependent calibration weights are applied to data from each antenna prior to combination. The weights are typically identical to those applied in real time for FRB searching. Total-intensity (Stokes I) time-frequency data sets at the native time and frequency resolutions are then saved for future analysis.

Table 4.1: DSA-110 Specifications during the Commissioning Period for Baseband Voltage Data

Parameters	
Dish diameter (m)	4.65
Antennas	63
Time resolution (μs)	32.768
Frequency resolution (kHz)	30.518
Effective band (MHz)	1498.8–1311.3
Bandwidth (MHz)	187.5
Central frequency (MHz)	1405.0
SEFD (Jy)	140

4.3 Data Analysis and Results

Baseband data reveal burst temporal and spectral features that would have been unresolvable at lower resolutions (e.g., [16]; [17]). In this work, we analyze the baseband data for 21 of the 24 FRB candidates detected from January to October 2022.

In this section, we first introduce our Bayesian burst modelling procedure, then present burst morphology analysis results on this DSA sample as well as on the simulated testing data, and finally show the spectral decorrelation analysis. All error bars are given at 1σ level unless specified otherwise.

4.3.1 Burst Morphology Analysis

We develop our burst morphology analysis routine based on *burstfit* [18] using a Bayesian approach. First, we pre-processed the filterbank produced from the full-intensity voltage data. We de-dispersed the filterbank using the initial DM estimation reported by `Heimdall`. We included data of width 1 to 3 times the `Heimdall` boxcar on each side of the burst as the burst morphology analysis data window. We found that the morphology analysis results did not change with different selections of data window widths as long as the windows were sufficiently wide to include the burst signal plus a portion of the baseline on both sides. We used data far from the burst signal (from 0.1 s to 0.45 s and from 0.6 s to 0.9 s) for baseline statistics calculations. We subtracted from the data the mean level of the baseline of each channel and then normalized the data using the frequency-averaged baseline's standard deviation. We binned the data evenly into 4 frequency channels to simplify the burst morphology model. We will use the baseband raw-resolution spectrum afterwards in the spectral analysis.

Second, we fit the de-dispersed, channel-by-channel mean-subtracted and normalized spectrogram to a few models using a Bayesian approach. For each model, we first fitted the spectrogram using the least-square method as an initial estimations of parameters values. We then took the estimations as the initial guesses in the following Markov chain Monte Carlo (MCMC) analysis using the *emcee* package to fully explore the parameters spaces and the errors. The spectrogram model is given by

$$\mathrm{f} = \mathrm{c}(\nu) \times \mathrm{T(t)}. \tag{4.1}$$

Here, $\mathrm{c}(\nu)$ is the normalized spectrum and T(t) is the temporal pulse profile.

For the spectrum, we do not assume any model, but estimate the relative spectral

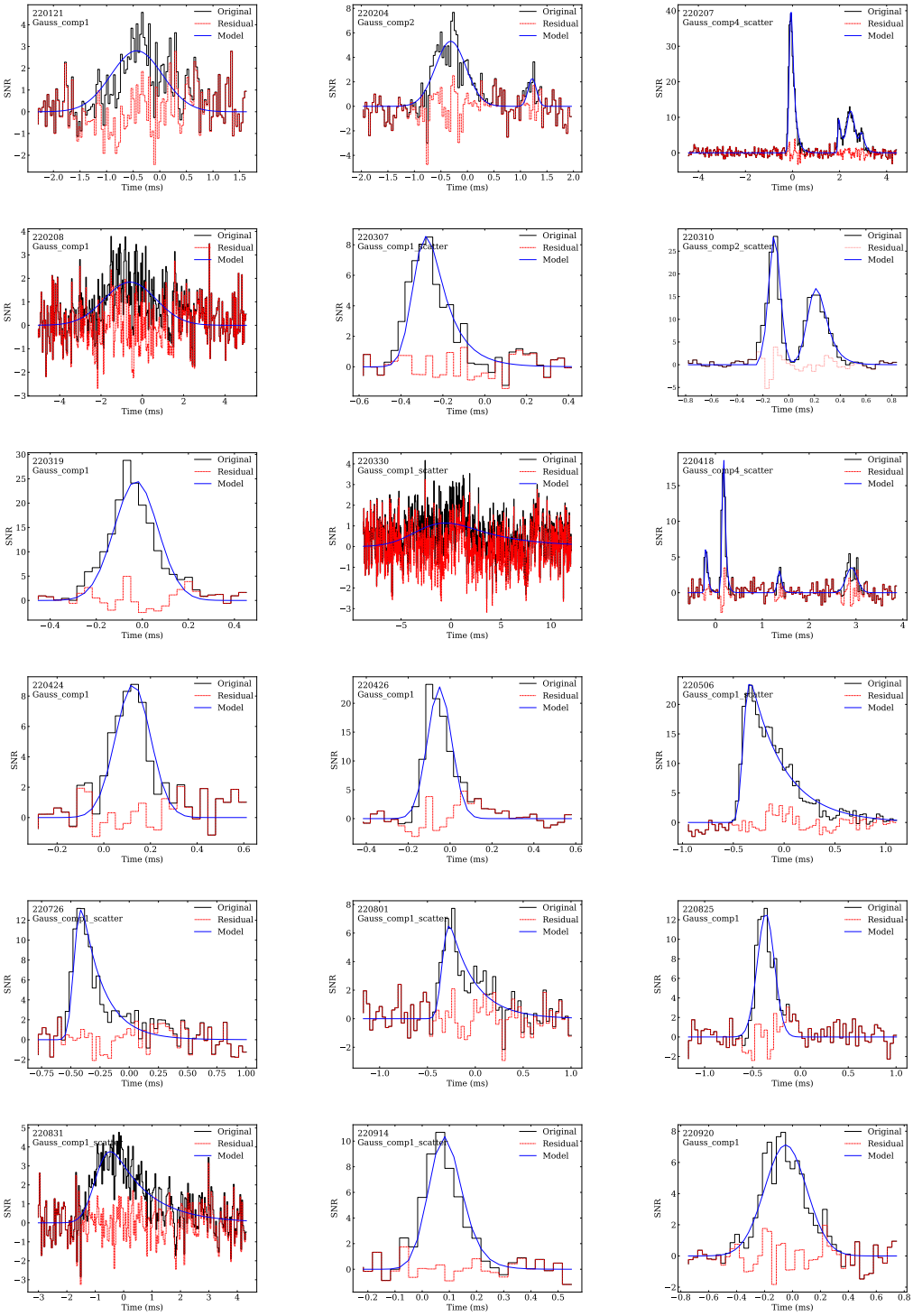
220121
Gauss_comp1
220204
Gauss_comp2
220207
Gauss_comp4_scatter
220208
Gauss_comp1
220307
Gauss_comp1_scatter
220310
Gauss_comp2_scatter
220319
Gauss_comp1
220330
Gauss_comp1_scatter
220418
Gauss_comp4_scatter
220424
Gauss_comp1
220426
Gauss_comp1
220506
Gauss_comp1_scatter
220726
Gauss_comp1_scatter
220801
Gauss_comp1_scatter
220825
Gauss_comp1
220831
Gauss_comp1_scatter
220914
Gauss_comp1_scatter
220920
Gauss_comp1
Original
Residual
Model
SNR
Time (ms)

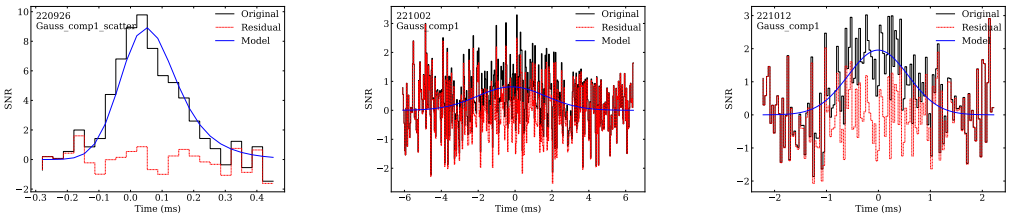

Figure 4.1: Frequency-averaged pulse profile data at raw resolution (solid black line), optimal model obtained by `burstfit` (blue curve) and residual (data – model; dashed red line). Data and model have been dedispersed at the optimal DM. The name of each FRB and its optimal model are shown on the sub-plot— "Gauss" means a simple Gaussian model, "scatter" means that the Gaussian model is convolved with an exponential scattering tail, and "comp" gives the total number of component(s) / sub-pulse(s) of the optimal model.

amplitudes c_i in four channels. The spectrum model is normalized to unity ($\sum_{i=1}^{4} c_i = 1$) such that the burst fluence can be measured from the pulse profile model directly.

For the pulse profile, the following models were used:

1. We started with a Gaussian model without scattering:

$$f1 = \frac{S \cdot c_i}{\sigma_{i,DM}\sqrt{2\pi}} \exp\left[-\frac{(t - t_0 - t_{i,DM})^2}{2\sigma_{i,DM}^2}\right]. \tag{4.2}$$

Here, c_i is the relative spectral amplitudes in the i-th channel. t_0 is the burst arrival time at the highest frequency channel. S is the fluence of the spectrogram that has been normalized by the baseline noise level. However, we choose to report S measured directly from the de-dispersed data to reduce errors introduced by modeling. S (in ms) could be converted to burst fluence F (in Jy ms) by $F = 1.26\ \text{Jy} \times S$, where the flux density noise of 1.26 Jy was estimated by $\text{SEFD}/\sqrt{2 \cdot 187.5\ \text{MHz} \cdot 32.768\ \mu\text{s}}$ using a SEFD of 140 Jy at boresight, an effective bandwidth of 187.5 MHz, a time resolution of 32.768 μs and two polarizations. $t_{i,DM}$ is the relative time delay in the i-th channel due to the residual DM (DM_{fit}) not modeled accurately by the initial `Heimdall` estimation ($DM_{tot} = DM_{init} + DM_{fit}$):

$$t_{i,DM} = 4.15\ \text{ms}\ DM_{fit}(\nu_{i,GHz}^{-2} - \nu_{0,GHz}^{-2}). \tag{4.3}$$

$\sigma_{i,DM}$ is the burst standard deviation measured in the i-th channel and is given by the intrinsic burst standard deviation w added in quadrature to the dispersion smearing in the i-th channel. We note that the constant of 4.15 ms is used for convention, and that the results can be scaled as needed [19].

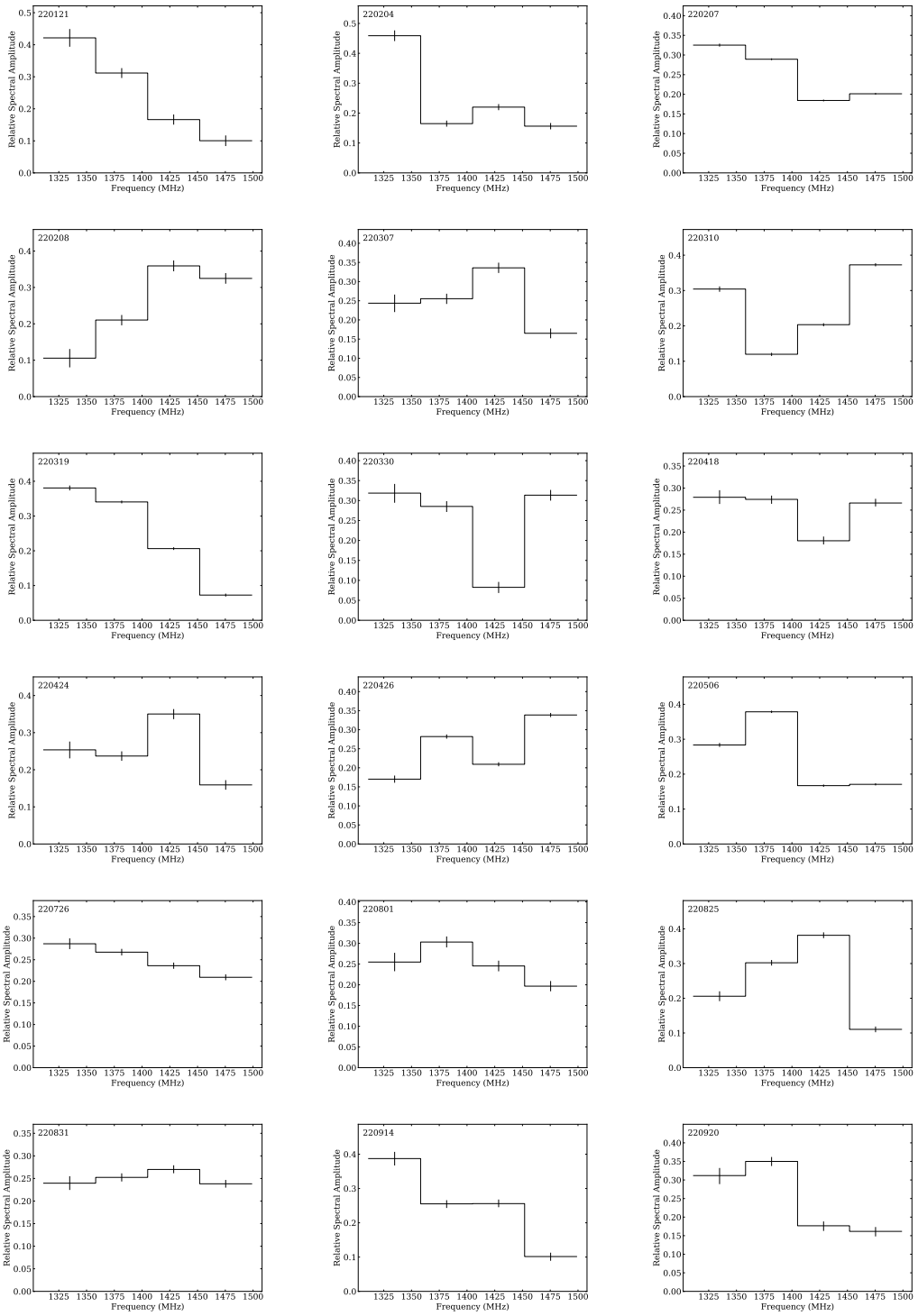

We represent the dispersion smearing using a Gaussian function whose standard deviation is given by:

$$w_{i,DM} = 8.30 \text{ ms } DM_{tot} \, \nu_{i,GHz}^{-3} \, \Delta\nu_{MHz}. \tag{4.4}$$

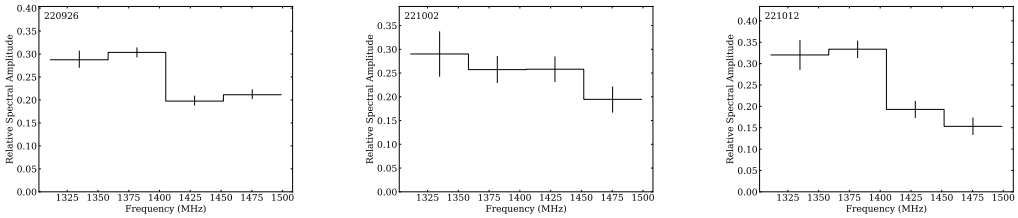

Figure 4.2: Normalized spectra obtained from `burstfit`. The data has been binned to 4 channels to simplify the fitting process and the summation of the 4 channels is normalized to unity. FRB names are shown on the upper left of each sub-plot and the order of the sub-plots is the same with those of Fig. 4.1.

Here, $\Delta\nu_{\rm MHz}$ is the channel width in MHz. In this model, there are seven free parameters: DM, c_1, c_2, c_3, S, w, and t_0.

2. We then consider the effect of multi-path scattering by convolving the Gaussian function with a one-sided exponential scattering tail:

$$s(t) = \begin{cases} \exp\left[-\frac{t-t_0}{\tau_{1.5}(\nu_i/1.5\mathrm{GHz})^{-4}}\right], & (t \geq t_0), \\ 0, & \text{otherwise.} \end{cases}$$

Here, $\tau_{1.5}$ is the e-fold scatter broadening timescale at the highest frequency channel (1498.75 MHz). The power index of 4 was adopted assuming Gaussian homogeneity in the galactic ISM, though a wide range of power index values may exist for FRBs (e.g., [20]).

The convolution is (Eqn. 3 of [18]):

$$f2 = \frac{S \cdot c_i}{2\tau_{i,sc}} \left[1 + \mathrm{erf}\left[\frac{t - t_0 - t_i - \sigma^2_{i,DM}/\tau_{i,sc}}{\sigma_{i,DM}\sqrt{2}}\right]\right] \times \exp\left(\frac{\sigma^2_{i,DM}}{2\tau^2_{i,sc}}\right) \exp\left(\frac{t - t_0 - t_i}{\tau_{i,sc}}\right). \quad (4.5)$$

Here, $\tau_{i,sc}$ is the e-fold scattering broadening timescale in the i-th channel assuming an index of –4. This model includes eight free parameters: $\tau_{1.5}$ in addition to the seven parameters used in the simple Gaussian model.

3. In a few cases, the pulse profiles were multi-component as judged by humans and we used multi-peak Gaussian functions with and without scattering in the fitting process. In these cases, we model each peak using the same DM, scattering timescale and relative spectral amplitudes. Sub-pulses from one

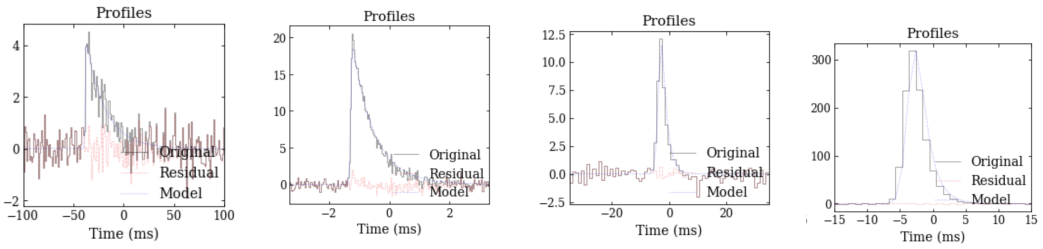

Figure 4.3: Burst morphology tests using simulated pulses with scattering tails. Frequency-averaged pulse profile data at the search resolution (solid black line), optimal model obtained by `burstfit` (blue curve) and residual (data – model; dashed red line). Data and model have been dedispersed at the optimal DM.

FRB should have the same scattering timescale due to the small temporal separations ($\lesssim$ a few ms) between sub-pulses (e.g., [21]). The similarities of spectra from sub-pulses will be confirmed in the spectral analysis afterwards. For a n-component spectrogram model with no scattering, there are (4 + 3n) free parameters: DM, c_1, c_2, c_3, and n sets of S, w and t_0. For a n-component spectrogram model with scattering, there are (5 + 3n) free parameters: DM, τ, c_1, c_2, c_3, and n sets of S, w and t_0.

Finally, we select the best model using the Bayesian information criterion (BIC):

$$\mathrm{BIC} = k \cdot \ln N - 2 \ln L. \tag{4.6}$$

Here, k is the number of free parameters in a model, N is the data size and L is the likelihood of the estimation. The first term penalizes model complexity and the second term favors higher likelihood. For each FRB, the BIC value of all models used in the fitting were calculated and compared. A model is selected if (1) it has the lowest BIC that is at least 3 units lower than that of any other model, or (2) it has the second lowest BIC that is no more than 3 units greater than the lowest BIC and the model has fewer free parameters than the model with the lowest BIC. The best model results for each FRB is listed in Table 4.2 and the burst morphology profiles are displayed in Fig 4.1. All error bars are at the 1σ level.

In addition, we test the analysis routine using four simulated pulses (Fig. 4.3). Each of the test pulses was simulated with the DSA search parameters (262.144 μs time resolution, and 1024 channels between 1280–1530 MHz), the same burst width, two different scattering timescales and different signal to noise ratios. In all cases, the correct model is selected and parameters are correctly recovered.

4.3.2 Spectral Characterizations

The high-resolution of baseband data enables detailed FRB spectral studies to understand the intrinsic emission model. For example, the spectra of repeating FRBs have been reported to be relatively narrow-banded, more variable and display characteristic temporal revolutions as compared to the one-off FRBs spectra [22]. In addition, high-resolution FRB spectra help to understand the medium along the path of the FRB. For example, spectral modulation can be used to estimate scintillation from propagation medium.

In this section, we present our measurement of the spectral decorrelation bandwidth following the method used in [23]. The implications on scintillation will be discussed in Section 4.4.

For each FRB, we extracted the normalized pulse spectrum (spectra) in the following the steps:

- De-disperse the raw-resolution filterbank (30.5 KHz, 32.8 ms) using the optimal DM value found in the previous burst morphology analysis.
- Extract data within the FWHM of the pulse profile (or the FWHM of each sub-pulse for FRBs with multi-peak profile models) using the best burst profile model obtained from the burst morphology analysis above.
- For each pulse (or sub-pulse), the data were averaged over time and weighted using the square of the profile amplitude and then normalized to unit area to generate the normalized spectrum.

For FRBs with multi-peak profile models, we compared the spectrum of each sub-pulse by calculating the cross-correlation coefficient (CCC) of each pair of them. Table 4.3 lists the CCC and the p-value of each pair of spectra being uncorrelated. The components of FRBs 220207 and 220310 are correlated as indicated by the low p-values. For FRB 220418, the comparison remains unclear due to the low SNR of some of the components.

We then calculated the autocorrelation function (ACF) of the normalized pulse spectrum as follow:

$$\mathrm{ACF}(\Delta\nu) = \frac{\sum_i \mathrm{S}(\nu_i)\mathrm{S}(\nu_i + \Delta\nu)}{\sqrt{\sum_i \mathrm{S}(\nu)^2 \sum_i \mathrm{S}(\nu_i + \Delta\nu)^2}}. \tag{4.7}$$

Here, $\Delta\nu$ is the offset frequency, $S(\nu_i)$ is the spectral value at the i-th frequency channel and $S(\nu_i + \Delta\nu)$ is the spectral value at the frequency of $\nu_i + \Delta\nu$.

We fitted the first peak of the ACF with a Lorenzian model and estimated the spectral de-correlation bandwidth ν_d using the half width at half maximum (HWHM) of the model. The scintillation bandwidth τ_d is given by:

$$2\pi\Delta\nu_d\tau_d = C_1. \tag{4.8}$$

Here, we used $C_1 = 1.16$ for a Kolmogorov scattering media [24]. We list the decorrelation bandwidth ($\Delta\nu_d$) and the scintillation bandwidth at 1.4 GHz ($\tau_{d,1.4}$)in Table 4.4. We will not include the scintillation timescale measurements of the following FRBs in the discussion since their spectra are likely too noisy for accurate estimations: FRBs 220121, 220330, 220726, 220831, 220926, 221002, 221012. Finally, we note that the short scintillation timescale for FRB 220920 needs further validation since its spectral autocorrelation function is relatively noisy.

4.4 Discussion

4.4.1 Comparison with the large Samples

Over 600 FRBs have been reported by the end of 2022. To understand whether or not each instrument features the same FRB population, we compare the burst morphology of this DSA sample with those of the first CHIME catalog and the ASKAP sample reported by [2] in Fig. 4.4. We choose to compare with these two samples since each of them contains a large sample size that was observed under a consistent instrumental status.

The first CHIME catalog consists of about 600 events [1]. The data has a temporal resolution of 0.98304 ms and 16, 384×24.3 kHz frequency channels from 400 to 800 MHz. Their spectrogram morphology is characterized using the least square method following the `fitburst` routine. They model their burst profile with a Gaussian function smeared by dispersion and potentially convolved with a scattering tail and model the spectra using an empirical function. They assume a frequency dependency of $\tau \propto \nu^{-4}$ for the scattering timescale as we do in our analysis. For FRBs with multi-component, they model each component with the same DM and scattering timescale τ but independent widths. Their model selection criterion is unknown to us (e.g., [1]).

The ASKAP population [2] consists of 33 FRBs. The data has a temporal resolution of 0.86– 1.73 ms and 336×1 MHz channel within the band of 700– 1800 MHz. The

Table 4.2: Burst Morphology Results.

FRB		DM	Component	σ	τ
	(Jy ms)	(pc cm^{-3})		(ms)	(ms)
220121aaat	5.885	$314.04^{+0.22}_{-0.21}$	1	$0.4823^{+0.027}_{-0.029}$	< 0.7
220204aaai	5.543	$612.72^{+0.048}_{-0.049}$	1	$0.2853^{+0.0088}_{-0.0094}$	< 0.17
			2	$0.07768^{+0.011}_{-0.011}$	< 0.17
220207aabh	25.33	$262.34^{+0.005}_{-0.0046}$	1	$0.05902^{+0.0012}_{-0.0013}$	$0.1063^{+0.0022}_{-0.0022}$
			2	$0.02515^{+0.0039}_{-0.0045}$	$0.1063^{+0.0022}_{-0.0022}$
			3	$0.1392^{+0.0061}_{-0.0059}$	$0.1063^{+0.0022}_{-0.0022}$
			4	$0.07106^{+0.0097}_{-0.012}$	$0.1063^{+0.0022}_{-0.0022}$
220208aaaa	11.88	$436.24^{+0.59}_{-0.6}$	1	$1.25^{+0.073}_{-0.075}$	< 2.2
220307aaae	1.883	$499.25^{+0.028}_{-0.032}$	1	$0.04971^{+0.0056}_{-0.0057}$	$0.07593^{+0.0098}_{-0.0099}$
220310aaam	20.249	$462.24^{+0.004}_{-0.0035}$	1	$0.04395^{+0.0017}_{-0.0014}$	$0.007343^{+0.00033}_{-0.0023}$
			2	$0.05703^{+0.003}_{-0.0036}$	$0.007343^{+0.00033}_{-0.0023}$
220319aaeb	7.79	$110.98^{+0.01}_{-0.01}$	1	$0.09274^{+0.0013}_{-0.0013}$	< 0.057
220330aaan	19.23	$472.1^{+0.84}_{-0.91}$	1	$2.378^{+0.16}_{-0.17}$	$3.768^{+0.46}_{-0.48}$
220418aaai	5.824	$623.24^{+0.0061}_{-0.0068}$	1	$0.01578^{+0.0052}_{-0.0056}$	$0.03003^{+0.0036}_{-0.0036}$
			2	$0.02372^{+0.0025}_{-0.0024}$	$0.03003^{+0.0036}_{-0.0036}$
			3	$0.03577^{+0.021}_{-0.44}$	$0.03003^{+0.0036}_{-0.0036}$
			4	$0.1122^{+0.0099}_{-0.011}$	$0.03003^{+0.0036}_{-0.0036}$
220424aabq	2.983	$863.48^{+0.022}_{-0.036}$	1	$0.07468^{+0.004}_{-0.0045}$	< 0.081
220506aabd	13.08	$396.97^{+0.011}_{-0.0097}$	1	$0.03987^{+0.002}_{-0.002}$	$0.2662^{+0.0044}_{-0.0045}$
220426aaaw	5.407	$269.53^{+0.0071}_{-0.0071}$	1	$0.0243^{+0.0014}_{-0.0014}$	$0.08048^{+0.0028}_{-0.0029}$
220726aabn	5.408	$686.73^{+0.013}_{-0.014}$	1	$0.03939^{+0.003}_{-0.0032}$	$0.1509^{+0.0078}_{-0.0084}$
220801aabd	3.21	$412.64^{+0.04}_{-0.042}$	1	$0.0461^{+0.0054}_{-0.0055}$	$0.2133^{+0.017}_{-0.018}$
220825aaad	4.63	$651.38^{+0.015}_{-0.015}$	1	$0.0888^{+0.0024}_{-0.0025}$	< 0.11
220831aaaj	11.06	$1146.7^{+0.17}_{-0.16}$	1	$0.3762^{+0.038}_{-0.038}$	$1.042^{+0.079}_{-0.085}$
220914aabz	2.987	$631.26^{+0.016}_{-0.024}$	1	$0.0507^{+0.0057}_{-0.0081}$	$0.03335^{+0.016}_{-0.009}$
220920aacl	3.494	$315.0^{+0.059}_{-0.036}$	1	$0.1492^{+0.0065}_{-0.0057}$	< 0.056
220926aaeu	3.374	$441.55^{+0.029}_{-0.028}$	1	$0.0689^{+0.0075}_{-0.0068}$	$0.06378^{+0.012}_{-0.013}$
221002aaab	6.644	$321.53^{+0.98}_{-1.0}$	1	$1.843^{+0.22}_{-0.31}$	< 0.68
221012aaab	3.622	$441.09^{+0.26}_{-0.26}$	1	$0.5774^{+0.031}_{-0.033}$	< 0.86

FRBs were detected in a single-dish fly's eye mode and the multi-dish interferometric mode using 7 or 36 antennas. The single-dish mode has a sensitivity of $\sim 25\sqrt{w}$ Jy ms and the interforometric mode has a sensitivity of $\sim 25\sqrt{w}/\sqrt{N}$ Jy ms. Here, w is the burst width in ms and N is the number of dishes / antennas used. We choose not to include the ASKAP FRBs reported after [2] as they were observed with a range

Table 4.3: Multi-peak FRBs Spectra Comparison.

FRB	components	CCC	p-value
220204	1&2	0.007	0.6
220207	1&2	0.03	2×10^{-2}
	1&3	0.1	2×10^{-17}
	1&4	0.04	3×10^{-3}
	2&3	0.03	6×10^{-3}
	2&4	0.03	3×10^{-2}
	3&4	0.02	0.1
220310	1&2	0.06	10^{-6}
220418	1&2	0.005	0.7
	1&3	-0.02	0.1
	1&4	0.006	0.7
	2&3	-0.008	0.5
	2&4	0.008	0.5
	3&4	0.002	0.8

Table 4.4: Spectral Analysis Results.

FRB	$\Delta\nu_{\rm d}$ (MHz)	$\tau_{\rm d,1.4}$ (10^{-5} ms)
220121	NA	NA
220204	6.06 ± 0.75	3.05 ± 0.38
220207	1.02 ± 0.07	18.14 ± 1.26
220208	2.38 ± 0.76	7.75 ± 2.47
220307	0.79 ± 0.25	23.4 ± 7.4
220310	22.20 ± 0.79	0.83 ± 0.03
220319	2.07 ± 0.10	8.91 ± 0.42
220330	NA	NA
220418	8.80 ± 4.20	2.10 ± 1.00
220424	10.65 ± 4.80	1.73 ± 0.78
220506	2.83 ± 0.06	6.54 ± 0.14
220426	3.48 ± 0.12	5.31 ± 0.18
220726	NA	NA
220801	8.63 ± 1.80	2.14 ± 0.45
220825	6.98 ± 4.20	2.64 ± 1.59
220831	NA	NA
220914	3.68 ± 0.52	5.02 ± 0.71
220920	0.19 ± 0.08	96 ± 39
220926	NA	NA
221002	NA	NA
221012	NA	NA

of different antenna numbers and therefore various fluence threshold, which would make the ASKAP sample less uniform. [2] extract the spectrogram morphology using a Bayesian method. They model the pulse profile with a Gaussian function that is convolved with an exponential scattering decay kernel. The models with and without scattering is then selected using their Bayes factors. For the scattering timescale τ, they adopt a frequency dependency of $\tau \propto \nu^{-4}$ for all FRBs except FRB 180110, where the power law index is a free parameter.

For this DSA sample, in all cases except FRB 220319, the extragalactic dispersion measurement is estimated by

$$\mathrm{DM_{Ex}} = \mathrm{DM_{tot}} - \mathrm{DM_{Ne2001}} - \mathrm{DM_{MW\ halo}} \quad \mathrm{pc\ cm^{-3}}. \tag{4.9}$$

Here, $\mathrm{DM_{tot}}$ is the total DM measured from the burst morphology analysis, $\mathrm{DM_{Ne2001}}$ is the galactic ISM DM predicted by the `Ne2001` model along the LoS of the FRB [25] and $\mathrm{DM_{MW\ halo}}$ is the Milky Way halo DM which is typically between $\sim$ 20 and $\sim$ 80 pc cm^{-3} (e.g. [26, 27]). In this work, we adopt a typical value of $\mathrm{DM_{MW,halo}} = 50$ pc cm^{-3} for all FRBs. The uncertainty of $\mathrm{DM_{Ex}}$ is estimated by

$$\Delta_{\mathrm{DM_{Ex}}} = \sqrt{\Delta^2_{\mathrm{DM_{tot}}} + \Delta^2_{\mathrm{DM_{Ne2001}}} + \Delta^2_{\mathrm{DM_{MW,halo}}}} \quad \mathrm{pc\ cm^{-3}}. \tag{4.10}$$

Here, $\Delta_{\mathrm{DM_{tot}}}$ is found from the burst morphology analysis. We assume an uncertainty of 20% for $\mathrm{DM_{Ne2001}}$, as estimated by most models [25, 28]. For $\Delta_{\mathrm{DM_{MW,halo}}}$, we adopt a value of 30 pc cm^{-3}, though the distribution of the halo DM has not been well measured in observations. We note that it is in principle more correct to characterize the probability distribution function (PDF) of $\mathrm{DM_{Ex}}$ by calculation the convolution of the PDF's of each of the DM component. In practice, however, it may not be a significant improvement, since the PDF of $\mathrm{DM_{Ex}}$ is dominated by the PDF's of $\mathrm{DM_{Ne2001}}$ and $\mathrm{DM_{MW\ halo}}$, while neither of them have been well characterized in observations. Therefore we simplify the calculations using Eqn's 4.9 and 4.10.

For FRB 220319, [27] report that the $\mathrm{DM_{ISM}}$ along the LoS of 220319 are overestimated using the `Ne2001` and the `YMW16` models. They estimate the $\mathrm{DM_{ISM}}$ using nearby pulsars and find an $\mathrm{DM_{Ex}}$ between 45.7 and 64.3 pc cm^{-3}. We adopt the mean $\mathrm{DM_{Ex}}$ value of 55 pc cm^{-3} in this work. The width is defined as the standard deviation of the simple Gaussian pulse profile model. The exponential scattering timescale τ has been converted from 600 MHz (CHIME) or 1.3 GHz (ASKAP) to 1498.75 MHz using $\tau \propto \nu^{-4}$ to compare with the DSA sample. We note the followings in the population comparison (Fig. 4.4):

- The extragalactic DM median value of this DSA sample (363 ± 0.26 pc cm^{-3}) is 13% lower than that of the first CHIME catalog sample (419 pc cm^{-3}), and is less than 1% lower than that of this ASKAP sample (366 pc cm^{-3}). As discussed in the CHIME catalog paper [1], different surveys may have different DM selection functions. The selection function of DSA-110 is likely flat, as verified through injection tests, but is affected at high DMs during periods of increased RFI.

- The fluence distribution (Fig. 4.4 top panel) of this DSA sample is not distinguishable from the CHIME sample, and is fainter than the ASKAP sample, which is expected from the detection threshold. For a burst of width 1 ms, the DSA sensitivity is $\sim$ 1.7 Jy ms with a SNR cutoff of 7.5, and the ASKAP fluence thresholds are 25 Jy ms (fly's eye mode), 9.4 Jy ms (interferometric mode using 7 antennas) and 4.2 Jy ms (interferometric mode using 36 antennas).

- This DSA sample of FRBs contains narrower bursts than the CHIME and the ASKAP samples as expected, since the search system of DSA uses a sampling rate of 262.144 μs, while the CHIME and the ASKAP samples used for comparison in this work have temporal resolutions of $\sim$ 1 ms and thus are less sensitive to narrower bursts.

- Similarly, this DSA sample contains shorter scattering time scales than the ASKAP sample. In addition, 11 out of the 21 DSA FRBs have scattering, while only 2 out of the 33 ASKAP sample are scattered if using the same Bayesian model selection criterion. This is also expected since the higher time resolution of our baseband data makes it possible to resolve narrower scattering tail. We do not compare with the CHIME scattering timescale since their model selection criterion is unclear to us.

4.4.2 Comparison with the localized samples

FRBs that are localized to individual host galaxies help to understand their progenitor formation history as well as to use them as cosmic tools. In this work, we have expanded the population of localized FRBs with optical spectra from the previously reported size of about 25 to over 40. The combination of high-resolution voltage data with optical host observations enable a detailed correlation study between the

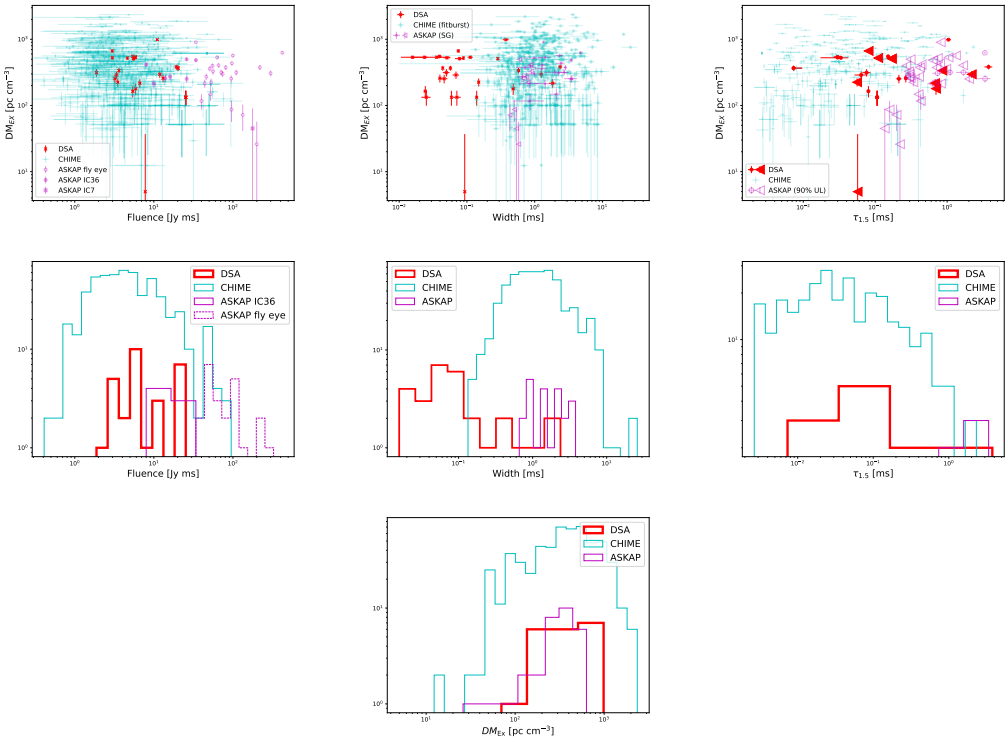

Figure 4.4: Comparison of this DSA sample (red), the CHIME first catalog sample (cyan) and the ASKAP samples (magenta). The triangular marks represent the upper limits measured from the pulse morphology models with the confidence level indicated in the figures legends, and the circular or square marks are the results reported in the pulse morphology analysis with an error bar of 68% confidence level. We distinguish the ASKAP FRBs observed in the single-dish fly's eye model (open magenta circles / dashed magenta histogram), the interferometric mode using 36 antennas (IC36; solid magenta circles / solid magenta histogram) and using 7 antennas (IC7; solid magenta squares) since they have different fluence thresholds. Width is defined as the standard deviation of the simple Gaussian (SG) pulse profile model. $\tau_{1.5}$ is the exponential scattering timescale converted to 1498.75 MHz using a frequency-dependency of $\tau \propto \nu^{-4}$. All error bars are at 1-σ level unless specified otherwise.

burst features and the host properties of this DSA sample and a comparison study with other localized FRB samples.

In this subsection, we take the first steps in this direction by exploring potential correlations between the burst properties measured in Section 4.3 and the host redshift and Hα luminosity. Several host spectra are presented in [29]. In the correlation analyse below (Figs. 4.5 to 4.13), we first calculate the Pearson correlation coefficient (PCC) of each pair of burst-host feature and compute the p-value that they were log-linearly correlated. We then fit each pair of burst-host data with a log-linear model $\log_{10} y = m \cdot \log_{10} x + b$ using the least square method and show the results

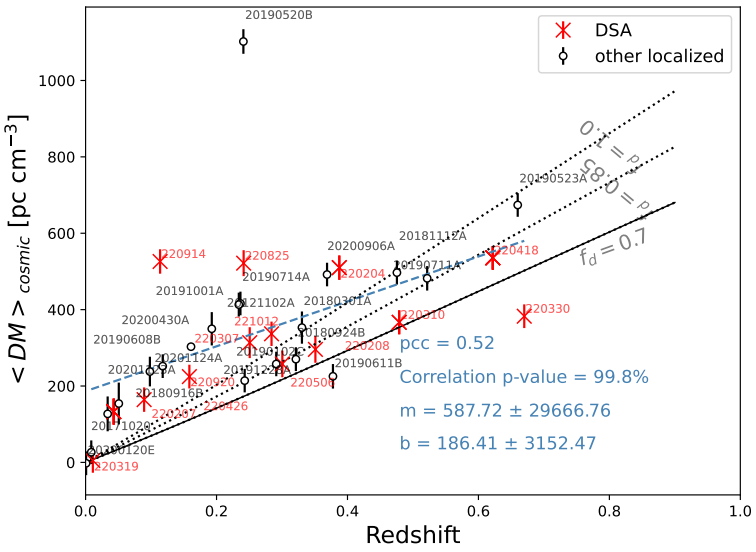

Figure 4.5: Extragalactic DM (DM_{Ex}) of the localized FRBs compare with the average cosmic DM ($\langle DM_{cosmic} \rangle$) predicted by the Macquart relation using a cosmic baryon fraction f_d of 70%, 85% and 100%.

on each plot and discuss their implications.

4.4.2.1 Redshift and Burst Properties

This DSA sample spans the second nearest extragalactic FRB (220319, z = 0.0111(4), next to the nearest extragalactic FRB 20200120E detected in M81) and the second-highest redshift (220330, z = 0.67) among all localized extragalactic FRBs that have been reported. This expands the parameter space to explore the correlation between the host distance and the burst properties. Here, we explore the relation between the host redshift with the FRBs' cosmic DM, extragalactic scattering, width, burst fluence and radio luminosities.

The Macquart relation predicts the average cosmic DM for a flat universe at redshift z (e.g., [6]):

$$\langle DM_{cosmic} \rangle = \int_0^{z_{FRB}} \frac{c\bar{n_e}(z)dz}{H_0(1+z)^2\sqrt{\Omega_m(1+z)^3+\Omega_\Lambda}}. \tag{4.11}$$

Here, the mean ion density $\bar{n_e} = f_d \rho_d(z) m_p^{-1}(1 - Y_{He}/2)$, where f_d is the fraction of cosmic baryons in ionized diffuse gas, $\rho_d(z) = \Omega_b \rho_{c,0}(1+z)^3$ is the baryon mass density at redshift z for a critical universe whose mass density today is $\rho_{c,0} =$

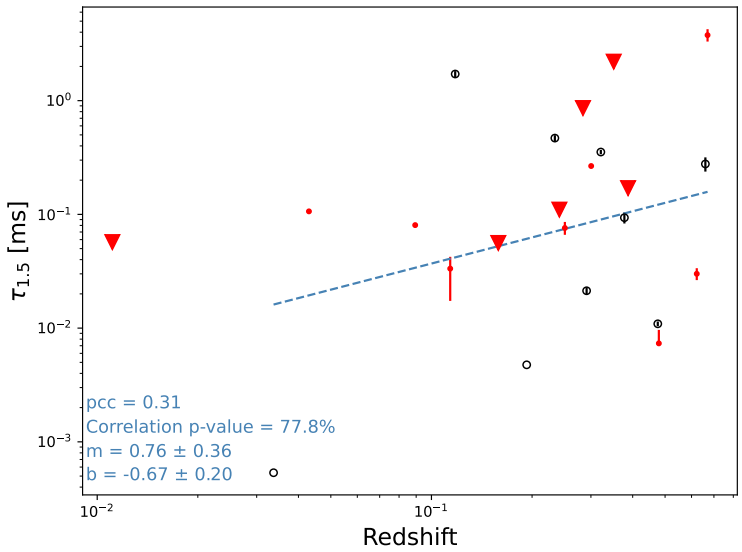

Figure 4.6: Extragalactic scattering timescale (scaled to 1498.75 MHz) of the localized FRBs and their redshifts.

$3H_0^2/8\pi G$, m_p is the mass of proton and $Y_{He} = 0.25$ is the Helium mass fraction. $\Omega_b = 0.0486$, $\Omega_m = 0.3075$ and $\Omega_\Lambda = 0.6910$ are the mass fraction of baryon, matter and dark energy, respectively [13]. In Fig. 4.5, we compare the extragalactic DM (DM_{Ex}, see Eqn. 4.9) of the localized FRBs of this DSA sample and other samples with the Macquart relation using a typical cosmic baryon fraction of 70% (solid line) as well as 85% and 100% (dotted lines) for comparison. The observed DM_{Ex} is highly correlated with redshift as expected. The majority of DM_{Ex} in these localized FRB samples lie above the predicted average IGM DM as expected due, for example, to the additional DM contributions from the FRB host. We fit the FRB data with a function $y = k \cdot x + b$, where the slope k could be compared with the slope of the DM-z relation and b could represent the averaged DM contribution from the host. However, the linear model does not fit well with the localized FRB sample. This might be caused by redshift-dependent scatter due to the cosmic foreground structure, the uncertainties of the ISM DM near the galactic plane, and the various host DM contribution from different progenitors local environments and host types.

The multi-path scattering could come from the ionized gas within the Milky Way, the host, and the intervening galaxies. The contribution is maximum if the scattering screen were half way through between the Milky way and the host. The scattering would be positively correlated with the redshift if intervening galaxies contribution

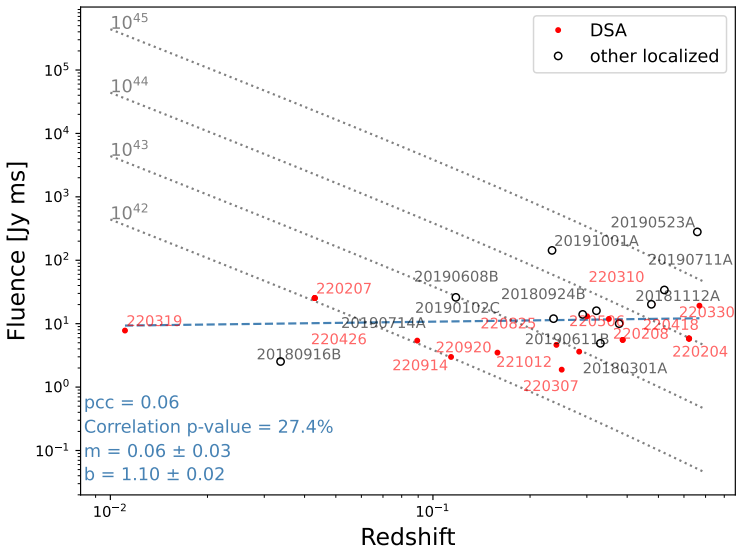

Figure 4.7: Fluence and redshift of the localized FRB samples. Dashed grey curves have constant radio luminosities whose values are marked along each line in erg s^{-1}.

were significant to the total scattering [30], since the chance of intersection increases with the redshift. We find that the extragalactic scattering timescale and the host redshifts are not strongly correlated (Fig. 4.6). Here, the scattering timescale of the other localized FRBs are converted to 1498.75 MHz by $\tau \propto \nu^{-4}$. We ignore the scattering contribution from the galactic ISM (predicted by the Ne2001 model at 30 kpc alone the LoS of each FRB; [25]) to the total scattering, since the former is at least two orders of magnitude lower than the later. The lack of clear correlation could be explained by— (1) The contribution from the scattering screen in the intervening galaxy depends strongly on the geometry of the host-screen-observer system, causing large scatter in the linear correlation. (2) Alternatively, intervening galaxies may not contribute significantly to the scattering in most FRBs.

Previous studies have concluded that FRBs are not standard candles (e.g., [31]). We compare the fluence of these localized FRB samples at different redshift with that of radio sources with constant luminosity. As shown in Fig. 4.7, this sample of FRBs do not follow the curves of constant luminosities. Here, we calculate the radio fluence F from the luminosity L by F = w L/ν_1 $4\pi d_L(z)^2$, where we assume a typical burst width of w = 1 ms, typical FRB luminosity values from 10^{42} to 10^{45} erg s^{-1}, lowest channel of the radio instrument of $\sim$ 1 GHz and calculate the luminosity distance d_L from the redshift z. In addition, we do not find strong

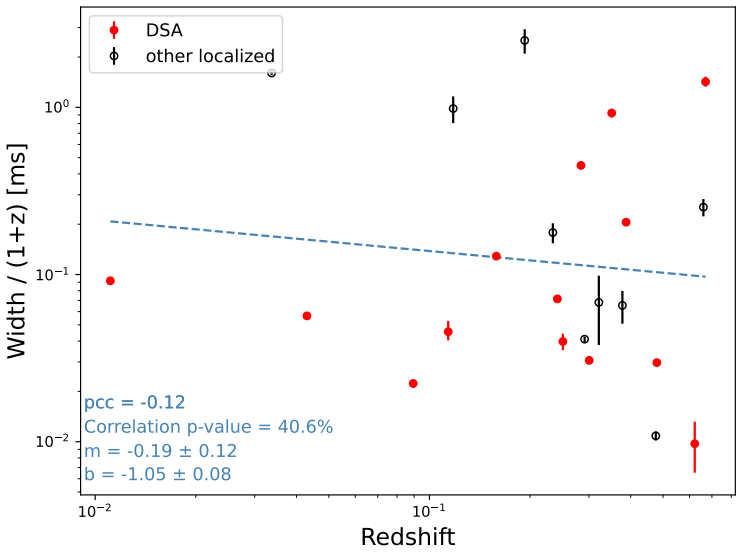

Figure 4.8: Redshift-corrected pulse width of the localized FRBs and their redshifts.

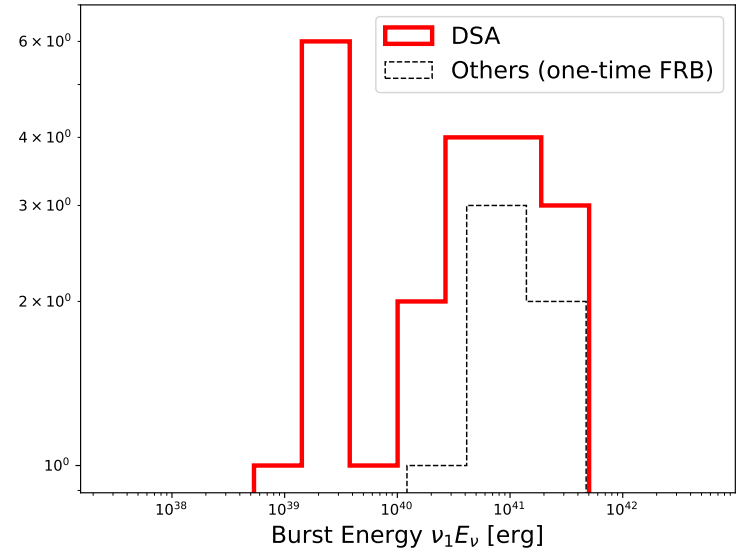

Figure 4.9: Energy distribution of localized FRBs.

correlation between the fluence and the redshift.

The observed burst is broadened by a factor of (1 + z) due to time dilation for a FRB at redshift z. Fig 4.8 shows that the redshift-corrected burst width (1σ) of the localized samples are not correlated with the redshift.

In Fig. 4.9, we compare the burst energy of the localized DSA FRBs with the

other localized samples by $E = \nu_1 F_\nu 4\pi d_L^2(z)$, where ν_1 is the lowest frequency of the instrument, F_ν is the specific fluence of the burst, and $d_L^2(z)$ is the luminosity distance at redshift z. The burst energy distribution of this DSA sample is lower than that of the other localized sample.

4.4.2.2 Hα Luminosity and Burst Properties

The host galaxy's Hα luminosity ($L_{H\alpha}$), together with its initial mass function, can be used to estimate its current star formation rate (SFR). This helps to understand the global stellar population of the host and its relation to the formation history of the FRB progenitor. In addition, any potential correlations of the host Hα luminosity with other host properties such as DM_{host} and τ_{host}, or with any burst properties such as fluence and radio luminosity, would provide an independent estimation of those properties based on the $L_{H\alpha}$ measurement [27]. For the FRBs in our sample with spectroscopic data on host galaxies, we obtain Hα luminosities where possible [29].

We estimate the host DM by

$$DM_{host} = (1 + z_{host}) \left(DM - DM_{Ne2001} - DM_{MW,halo} - \langle DM_{cosmic} \rangle\right). \quad (4.12)$$

Here, z_{host} is the host redshift, DM_{Ne2001} is the galactic ISM DM predicted by the Ne2001 model [25] at 30 kpc along the line of sight of each FRB, $DM_{MW,halo}$ is the galactic halo DM which we assume to be 50 pc cm^{-3} as in Eqn.4.9 and $\langle DM_{cosmic}(z) \rangle$ is the average extragalactic DM (Eqn. 4.11). The uncertainty on the host DM is calculated by

$$\Delta_{DM_{host}} = (1 + z_{host}) \sqrt{\Delta^2_{DM_{tot}} + \Delta^2_{DM_{Ne2001}} + \Delta^2_{DM_{MW,halo}}} \text{ pc cm}^{-3}. \quad (4.13)$$

Here, the same values are used as in Eqn. 4.10 and the same argument applies.

The host $L_{H\alpha}$ and DM_{host} could be correlated if the majority of the ionized gas in the host ISM comes from the star-forming regions along the LoS of the FRB. We find no correlation between $L_{H\alpha}$ and DM_{host} (Fig. 4.10). This could be caused by any of the followings— (1) $L_{H\alpha}$ is determined by the global star-forming rate of the host, while DM_{host} only measures ionized gas along the LoS. They may not represent the same region since some FRBs have been found outside the star-forming regions of their host galaxy. For example, FRB 20200120E has been localized to an aged globular cluster in the spiral galaxy M81. In such a case, the observed

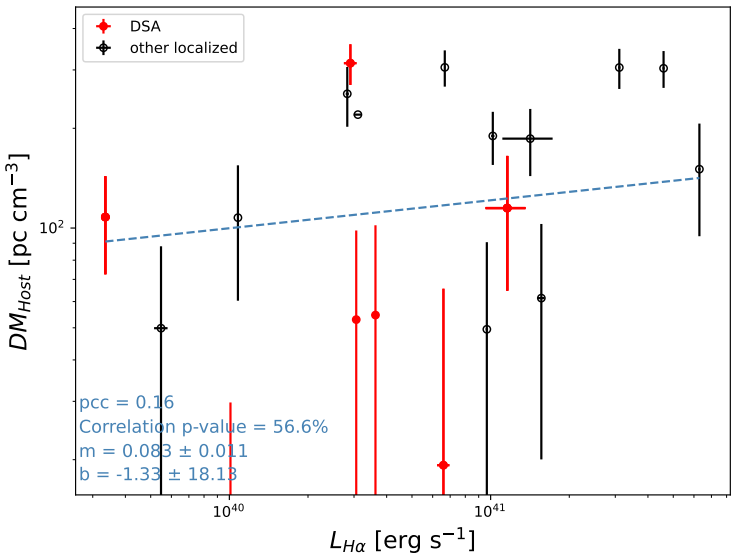

Figure 4.10: The host DM and the host Hα luminosity.

$L_{H\alpha}$ is expected to be uncorrelated with the DM_{host} measured along the LoS of FRB 20200120E since the globular cluster is not a star forming region. (2) The DM_{host} estimation may be compromised by the larger scatter in the extragalactic DM-z relation (Fig. 4.5). (3) The ionized gas in the host ISM could be produced by non star-forming processes along the LoS such as AGN radiations and supervovea explosions.

The host $L_{H\alpha}$ could also be correlated with the host scattering timescale τ_{host} if the multi-path scattering within the host is primarily due to the star-forming regions. The rest-frame host scattering timescale is estimated by (e.g., [32]):

$$\tau_{host,1.5} = (1+z)^3(\tau_{1.5} - \tau_{MW,1.5}). \tag{4.14}$$

Here, z is the host redshift, $\tau_{1.5}$ is the observed total scattering timescale converted to 1498.75 MHz, and $\tau_{Ne2001,1.5}$ is the galactic scattering at 30 kpc converted to 1498.75 MHz, as described before. We find $L_{H\alpha}$ and $\tau_{host,1.5}$ not strongly correlated (Fig. 4.11). We note two uncertainties in this analysis. (1) The $\tau_{host,1.5}$ estimation assumes no intervening galaxy. Intervening galaxies could contribute significantly to the total scattering depending on the geometry, but this is beyond the scope of this work. (2) $L_{H\alpha}$ is determined by the global star-forming rate, while τ_{host} only measures scattering medium along the LoS.

The host $L_{H\alpha}$ and burst energy are highly correlated (Fig. 4.12, p = 99%). The burst

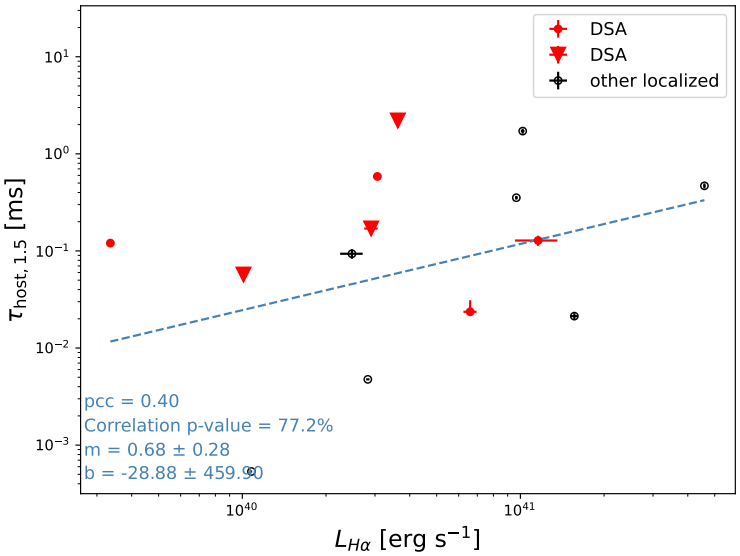

Figure 4.11: The host scattering timescale and Hα luminosity.

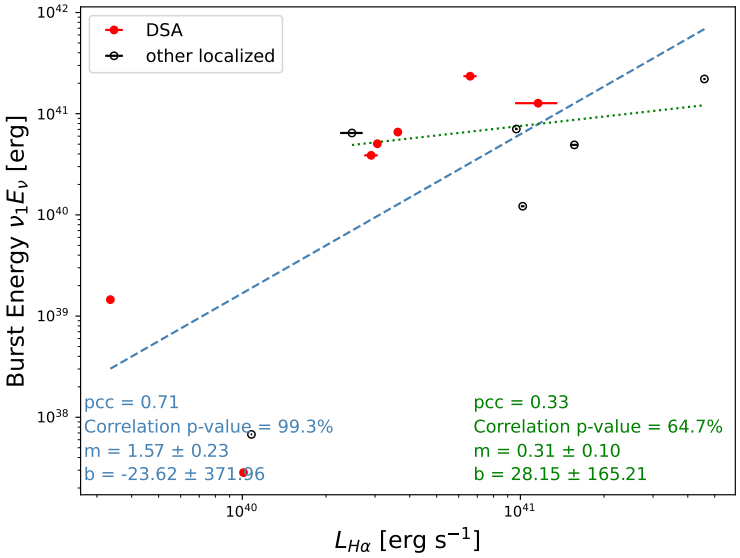

Figure 4.12: The burst energy and host Hα luminosity of the entire sample are strongly correlated (dashed blue line and the blue texts, correlation p-value = 99%). However, they are not correlated after excluding the lowest three points (dotted green line and green texts, correlation p-value = 65%).

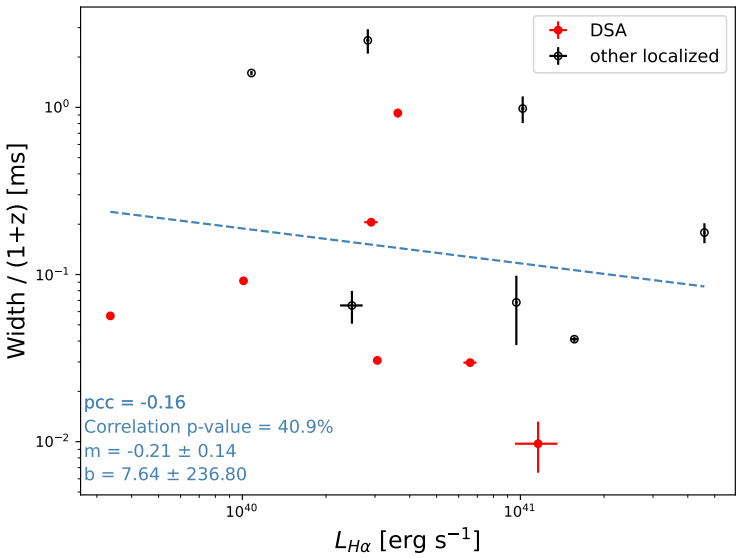

Figure 4.13: Redshift-corrected burst widths and the host Hα luminosities.

energies are calculated by $E = \nu_1 E_\nu = \nu_1 4\pi d_L^2 S$, where ν_1 is the lowest frequency of the instrument, $d_L^2(z)$ is the luminosity distance at redshift z and S is the burst fluence. This correlation is expected due to apparent-brightness limited selections on both the FRB and host-galaxy samples (spectra are typically only obtained for brighter hosts). We note that the correlation is dominated by the three FRBs with the lowest energies in this sample and does not retain when they are excluded (Fig. 4.12, p = 65%).

The redshift-correlated burst width and the host luminosity are not correlated (Fig. 4.13).

4.4.2.3 Which media dominate the scattering and the scintillation?

Most previous radio surveys show that scattering is dominated by extragalactic medium while scintillation mostly comes from the Milky Way (e.g., [33]), though extraglactic scintillation has been reported (e.g. FRB 150807 [34]). For this DSA sample (Fig. 4.14), we compare the scattering timescales from the burst morphology, the decorrelation timescales (τ_d) calculated from the spectral decorrelation bandwidth (Eqn. 4.8) and the scattering timescales predicted by the *Ne2001* model along the LoS at 30 kpc ($\tau_{Ne2001,1.5}$). All timescales have been scaled to 1498.75 MHz for comparison. We note the followings.

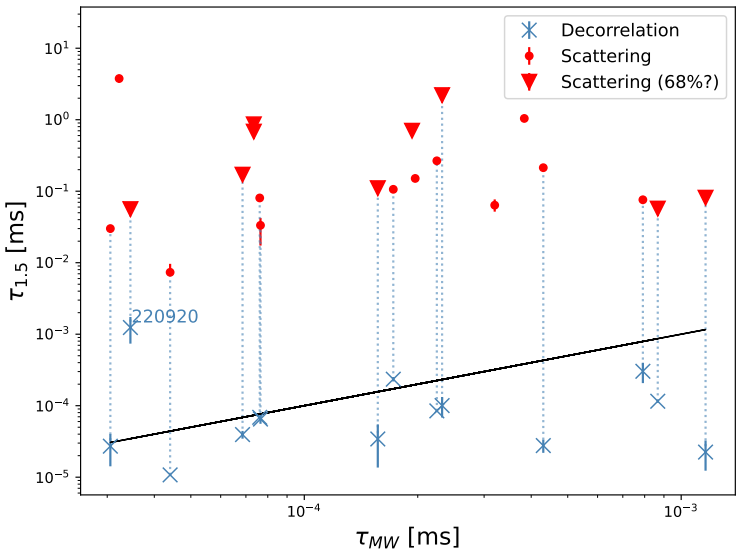

Figure 4.14: Measured scattering timescales (circles) and upper limits (triangles), scintillation timescales measured from the spectral decorrelation bandwidths (crosses) and the galactic scattering timescale (solid black line) predicted by the Ne2001 model at 30 kpc alone the line of sight of each FRB. All timescales have been converted to 1498.75 MHz for comparison.

- The total scattering timescales (red circles or triangles) are over two orders of magnitude greater than the Milky way ISM scattering timescale prediction $\tau_{\mathrm{Ne2001,1.5}}$ (solid black line), indicating additional sources of scattering, such as the ISM of the host and / or the intervening galaxies (e.g., [30]).

- Some of the spectral decorrelation timescales (blue crosses) lies closely on $\tau_{\mathrm{Ne2001,1.5}}$, meaning that galactic scattering is likely the main source of scintillation for those FRBs.

- However, in some cases, τ_{d} lies below the galactic scattering predictions. This is unexpected since Ne2001 is unlikely to overestimate scintillation timescales along several directions.

- The decorrelation timescale of FRB 220920 (z = 0.16) is over one order of magnitude greater than the galactic scattering timescale, implying additional source of scintillation, although the structure of its ACF may be ambiguous.

The DM is proportional to the electron density along the line of sight, while the scattering is caused by the electron density inhomogeneity. It is unclear whether

or not the FRB DM and scattering come from the same ionized medium. The host redshift makes it possible to separate the DM and scattering contributions from the host and from the cosmic mediums. We discuss the relation between DM and scattering in the following hypothetical scenarios.

1. Extragalactic scattering were dominated by the host (Fig. 4.15a). In this case, the host scattering timescale can be estimated by Eq. 4.14. The galactic DM and scattering timescale have been found to be correlated as measured from galactic radio pulsars (e.g., [35]). Similarly, $\mathrm{DM_{Host}}$ and τ_{Host} could be correlated if the ISM of the host were similar with that of the Milky Way. We find $\mathrm{DM_{Host}}$ and τ_{Host} not strongly correlated (Fig. 4.15a). This could be due to (1) extragalactic scattering were not dominated by the host so the estimation on τ_{Host} were incorrect, or (2) although extragalactic scattering were dominated by the host, the host ISM has different turbulent states with the Milky Way and a significant portion of the host ISM does not contribute to scattering.

2. Extragalactic scattering were dominated by the cosmic medium between the Milky Way and the host. In this situation, a correlation between $\langle \mathrm{DM_{cosmic}} \rangle$ (Eq. 4.11) and $\tau_{1.5,\mathrm{Ex}}$ coule be expected. In Fig. 4.15b, we find them uncorrelated and discuss two types of scenarios. (1) If there were no intervening galaxy, they are likely uncorrelated since the IGM is usually not turbulent (cite) and so they contribute to the DM but not the scattering. (2) If there were intervening galaxies, their contribution to the cosmic DM would be linear and independent of their locations, while their contributions to the scattering would be strongly related to their locations. In the second case, the DM and scattering contributions need to be analyzed on a case-by-case basis (e.g., [7]).

3. Both the host and the cosmic medium contributed to the scattering significantly. In this case, the total extragalactic contributions, $\tau_{1.5,\mathrm{Ex}}$ and $\mathrm{DM_{Ex}}$, are expected to be correlated. We find them not strongly correlated (Fig. 4.15c). This is consistent with the reasons discussed in the previous two scenarios.

4.5 Summary

We have reported the burst morphology and spectral features of a sample of 21 FRBs discovered and localized by DSA-110 during the commissioning stage be-

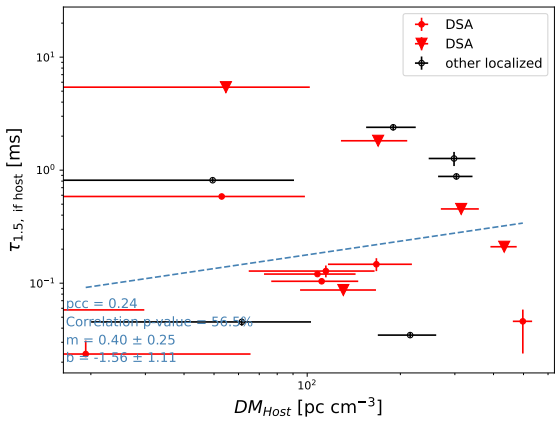

(a)

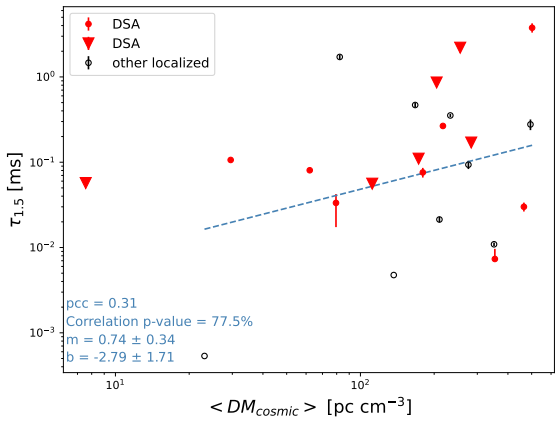

(b)

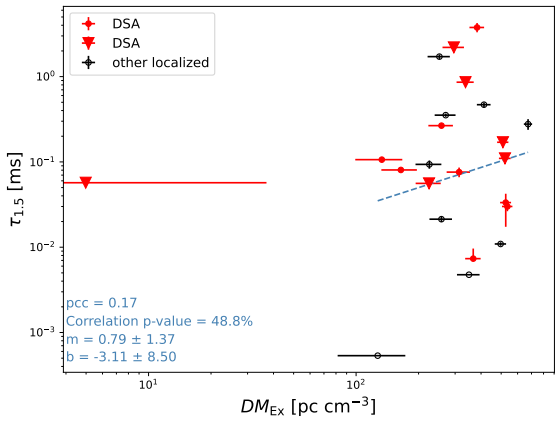

(c)

Figure 4.15: Dashed line shows the linear model fitting results using data with scattering measurements. (a) Assuming that the scattering were dominated by the host ISM. (b) Assuming that the scattering were dominated by the medium between the host the the Milky Way. (c) Assuming both contributions were significant.

tween January and October 2022. We used the raw-resolution baseband data and characterized the burst morphology using a Bayesian procedure.

1. We have compared this DSA sample with two other relatively large FRB samples and found that this DSA sample spans comparable DM_{EX} and fluence values to the CHIME sample, a fainter fluence range than the ASKAP sample, and is able to resolve narrower burst widths and shorter scattering tails due to the high time resolution. When comparing these samples, we note that the CHIME and the ASKAP samples are not from raw-resolution baseband data. A future comparison with samples from those instruments using the baseband data would be more informative once they become published.

2. We have explored correlations between burst and host properties for part of this DSA sample that have been optically observed as well as the other localized FRBs that have been published. (1) We have found a strong correlation between the burst energy and the host $L_{H\alpha}$ (p = 99%), likely caused by observational selection effects. We note that the correlation is dominated by the three lowest energy FRBs and does not retain when the three points are excluded in the correlation analysis. (2) In addition, we have found that the extragalactic DM of most of the FRBs lie above the $\langle DM \rangle$-z relation predicted by, e.g., [6], as expected due to the DM contribution from the host. For the next step, we could extend the burst- host correlation study by including some of the relevant host properties that are closely related to the progenitor formation history, such as the host color, age, SFR, sSFR, metallicity, offset distance of the FRB source with the star forming regions, location on the BPT diagram, and so on.

3. Our analyses agree with previous findings that FRB scintillation mostly come from the Milky Way, with the exception of FRB 220920, whose scintillation may be dominated by extragalactic medium though the accuracy of the result is debatable due to the relatively noisy spectrum. A more detailed study of intervening medium along its LoS could help to understand the source of the additional scattering. Our results is also consistent with previous reports that FRB scattering is dominated by extragalactic medium, although it remains unclear if it is dominated by the host, the intervening galaxies or in rare cases the IGM.

References

[1] CHIME/FRB Collaboration, Mandana Amiri, Bridget C. Andersen, Kevin Bandura, Sabrina Berger, Mohit Bhardwaj, Michelle M. Boyce, P. J. Boyle, Charanjot Brar, Daniela Breitman, Tomas Cassanelli, Pragya Chawla, Tianyue Chen, J. F. Cliche, Amanda Cook, Davor Cubranic, Alice P. Curtin, Meiling Deng, Matt Dobbs, Fengqiu Adam Dong, Gwendolyn Eadie, Mateus Fandino, Emmanuel Fonseca, B. M. Gaensler, Utkarsh Giri, Deborah C. Good, Mark Halpern, Alex S. Hill, Gary Hinshaw, Alexander Josephy, Jane F. Kaczmarek, Zarif Kader, Joseph W. Kania, Victoria M. Kaspi, T. L. Landecker, Dustin Lang, Calvin Leung, Dongzi Li, Hsiu-Hsien Lin, Kiyoshi W. Masui, Ryan McKinven, Juan Mena-Parra, Marcus Merryfield, Bradley W. Meyers, Daniele Michilli, Nikola Milutinovic, Arash Mirhosseini, Moritz Münchmeyer, Arun Naidu, Laura Newburgh, Cherry Ng, Chitrang Patel, Ue-Li Pen, Emily Petroff, Tristan Pinsonneault-Marotte, Ziggy Pleunis, Masoud Rafiei-Ravandi, Mubdi Rahman, Scott M. Ransom, Andre Renard, Pranav Sanghavi, Paul Scholz, J. Richard Shaw, Kaitlyn Shin, Seth R. Siegel, Andrew E. Sikora, Saurabh Singh, Kendrick M. Smith, Ingrid Stairs, Chia Min Tan, S. P. Tendulkar, Keith Vanderlinde, Haochen Wang, Dallas Wulf, and A. V. Zwaniga. The First CHIME/FRB Fast Radio Burst Catalog. *ApJS*, 257(2):59, December 2021. doi: 10.3847/1538-4365/ac33ab.

[2] Hao Qiu, Ryan M. Shannon, Wael Farah, Jean-Pierre Macquart, Adam T. Deller, Keith W. Bannister, Clancy W. James, Chris Flynn, Cherie K. Day, Shivani Bhandari, and Tara Murphy. A population analysis of pulse broadening in ASKAP fast radio bursts. *MNRAS*, 497(2):1382–1390, September 2020. doi: 10.1093/mnras/staa1916.

[3] Alexa C. Gordon, Wen-fai Fong, Charles D. Kilpatrick, Tarraneh Eftekhari, Joel Leja, J. Xavier Prochaska, Anya E. Nugent, Shivani Bhandari, Peter K. Blanchard, Manisha Caleb, Cherie K. Day, Adam T. Deller, Yuxin Dong, Marcin Glowacki, Kelly Gourdji, Alexandra G. Mannings, Elizabeth K. Mahoney, Lachlan Marnoch, Adam A. Miller, Kerry Paterson, Jillian C. Rastinejad, Stuart D. Ryder, Elaine M. Sadler, Danica R. Scott, Huei Sears, Ryan M. Shannon, Sunil Simha, Benjamin W. Stappers, and Nicolas Tejos. The Demographics, Stellar Populations, and Star Formation Histories of Fast Radio Burst Host Galaxies: Implications for the Progenitors. *arXiv e-prints*, art. arXiv:2302.05465, February 2023. doi: 10.48550/arXiv.2302.05465.

[4] Shivani Bhandari, Kasper E. Heintz, Kshitij Aggarwal, Lachlan Marnoch, Cherie K. Day, Jessica Sydnor, Sarah Burke-Spolaor, Casey J. Law, J. Xavier Prochaska, Nicolas Tejos, Keith W. Bannister, Bryan J. Butler, Adam T. Deller, R. D. Ekers, Chris Flynn, Wen-fai Fong, Clancy W. James, T. Joseph W. Lazio, Rui Luo, Elizabeth K. Mahony, Stuart D. Ryder, Elaine M. Sadler, Ryan M. Shannon, JinLin Han, Kejia Lee, and Bing Zhang. Characterizing the Fast Radio Burst Host Galaxy Population and its Connection to Transients

in the Local and Extragalactic Universe. *AJ*, 163(2):69, February 2022. doi: 10.3847/1538-3881/ac3aec.

[5] Kasper E. Heintz, J. Xavier Prochaska, Sunil Simha, Emma Platts, Wen-fai Fong, Nicolas Tejos, Stuart D. Ryder, Kshitij Aggerwal, Shivani Bhandari, Cherie K. Day, Adam T. Deller, Charles D. Kilpatrick, Casey J. Law, Jean-Pierre Macquart, Alexandra Mannings, Lachlan J. Marnoch, Elaine M. Sadler, and Ryan M. Shannon. Host Galaxy Properties and Offset Distributions of Fast Radio Bursts: Implications for Their Progenitors. *ApJ*, 903(2):152, November 2020. doi: 10.3847/1538-4357/abb6fb.

[6] J. P. Macquart, J. X. Prochaska, M. McQuinn, K. W. Bannister, S. Bhandari, C. K. Day, A. T. Deller, R. D. Ekers, C. W. James, L. Marnoch, S. Osłowski, C. Phillips, S. D. Ryder, D. R. Scott, R. M. Shannon, and N. Tejos. A census of baryons in the Universe from localized fast radio bursts. *Nature*, 581(7809): 391–395, May 2020. doi: 10.1038/s41586-020-2300-2.

[7] Liam Connor, Vikram Ravi, Morgan Catha, Ge Chen, Jakob T. Faber, James W. Lamb, Gregg Hallinan, Charlie Harnach, Greg Hellbourg, Rick Hobbs, David Hodge, Mark Hodges, Casey Law, Paul Rasmussen, Jack Sayers, Kritti Sharma, Myles B. Sherman, Jun Shi, Dana Simard, Jean Somalwar, Reynier Squillace, Sander Weinreb, David P. Woody, and Nitika Yadlapalli. Deep Synoptic Array science: Two fast radio burst sources in massive galaxy clusters. *arXiv e-prints*, art. arXiv:2302.14788, February 2023. doi: 10.48550/arXiv.2302.14788.

[8] S. P. Tendulkar, C. G. Bassa, J. M. Cordes, G. C. Bower, C. J. Law, S. Chatterjee, E. A. K. Adams, S. Bogdanov, S. Burke-Spolaor, B. J. Butler, P. Demorest, J. W. T. Hessels, V. M. Kaspi, T. J. W. Lazio, N. Maddox, B. Marcote, M. A. McLaughlin, Z. Paragi, S. M. Ransom, P. Scholz, A. Seymour, L. G. Spitler, H. J. van Langevelde, and R. S. Wharton. The Host Galaxy and Redshift of the Repeating Fast Radio Burst FRB 121102. *ApJ*, 834(2):L7, January 2017. doi: 10.3847/2041-8213/834/2/L7.

[9] Ben Margalit and Brian D. Metzger. A Concordance Picture of FRB 121102 as a Flaring Magnetar Embedded in a Magnetized Ion-Electron Wind Nebula. *ApJ*, 868(1):L4, November 2018. doi: 10.3847/2041-8213/aaedad.

[10] M. Bhardwaj, B. M. Gaensler, V. M. Kaspi, T. L. Landecker, R. Mckinven, D. Michilli, Z. Pleunis, S. P. Tendulkar, B. C. Andersen, P. J. Boyle, T. Cassanelli, P. Chawla, A. Cook, M. Dobbs, E. Fonseca, J. Kaczmarek, C. Leung, K. Masui, M. Mnchmeyer, C. Ng, M. Rafiei-Ravandi, P. Scholz, K. Shin, K. M. Smith, I. H. Stairs, and A. V. Zwaniga. A Nearby Repeating Fast Radio Burst in the Direction of M81. *ApJ*, 910(2):L18, April 2021. doi: 10.3847/2041-8213/abeaa6.

[11] F. Kirsten, B. Marcote, K. Nimmo, J. W. T. Hessels, M. Bhardwaj, S. P. Tendulkar, A. Keimpema, J. Yang, M. P. Snelders, P. Scholz, A. B. Pearlman,

C. J. Law, W. M. Peters, M. Giroletti, Z. Paragi, C. Bassa, D. M. Hewitt, U. Bach, V. Bezrukovs, M. Burgay, S. T. Buttaccio, J. E. Conway, A. Corongiu, R. Feiler, O. Forssén, M. P. Gawroński, R. Karuppusamy, M. A. Kharinov, M. Lindqvist, G. Maccaferri, A. Melnikov, O. S. Ould-Boukattine, A. Possenti, G. Surcis, N. Wang, J. Yuan, K. Aggarwal, R. Anna-Thomas, G. C. Bower, R. Blaauw, S. Burke-Spolaor, T. Cassanelli, T. E. Clarke, E. Fonseca, B. M. Gaensler, A. Gopinath, V. M. Kaspi, N. Kassim, T. J. W. Lazio, C. Leung, D. Z. Li, H. H. Lin, K. W. Masui, R. Mckinven, D. Michilli, A. G. Mikhailov, C. Ng, A. Orbidans, U. L. Pen, E. Petroff, M. Rahman, S. M. Ransom, K. Shin, K. M. Smith, I. H. Stairs, and W. Vlemmings. A repeating fast radio burst source in a globular cluster. *Nature*, 602(7898):585–589, February 2022. doi: 10.1038/s41586-021-04354-w.

[12] Kritti Sharma, Jean Somalwar, Casey Law, Vikram Ravi, Morgan Catha, Ge Chen, Liam Connor, Jakob T. Faber, Gregg Hallinan, Charlie Harnach, Greg Hellbourg, Rick Hobbs, David Hodge, Mark Hodges, James W. Lamb, Paul Rasmussen, Myles B. Sherman, Jun Shi, Dana Simard, Reynier Squillace, Sander Weinreb, David P. Woody, and Nitika Yadlapalli. Deep Synoptic Array science: A massive elliptical host among two galaxy-cluster fast radio bursts. *arXiv e-prints*, art. arXiv:2302.14782, February 2023. doi: 10.48550/arXiv.2302.14782.

[13] Planck Collaboration, P. A. R. Ade, N. Aghanim, M. Arnaud, M. Ashdown, J. Aumont, C. Baccigalupi, A. J. Banday, R. B. Barreiro, J. G. Bartlett, N. Bartolo, E. Battaner, R. Battye, K. Benabed, A. Benoît, A. Benoit-Lévy, J. P. Bernard, M. Bersanelli, P. Bielewicz, J. J. Bock, A. Bonaldi, L. Bonavera, J. R. Bond, J. Borrill, F. R. Bouchet, F. Boulanger, M. Bucher, C. Burigana, R. C. Butler, E. Calabrese, J. F. Cardoso, A. Catalano, A. Challinor, A. Chamballu, R. R. Chary, H. C. Chiang, J. Chluba, P. R. Christensen, S. Church, D. L. Clements, S. Colombi, L. P. L. Colombo, C. Combet, A. Coulais, B. P. Crill, A. Curto, F. Cuttaia, L. Danese, R. D. Davies, R. J. Davis, P. de Bernardis, A. de Rosa, G. de Zotti, J. Delabrouille, F. X. Désert, E. Di Valentino, C. Dickinson, J. M. Diego, K. Dolag, H. Dole, S. Donzelli, O. Doré, M. Douspis, A. Ducout, J. Dunkley, X. Dupac, G. Efstathiou, F. Elsner, T. A. Enßlin, H. K. Eriksen, M. Farhang, J. Fergusson, F. Finelli, O. Forni, M. Frailis, A. A. Fraisse, E. Franceschi, A. Frejsel, S. Galeotta, S. Galli, K. Ganga, C. Gauthier, M. Gerbino, T. Ghosh, M. Giard, Y. Giraud-Héraud, E. Giusarma, E. Gjerløw, J. González-Nuevo, K. M. Górski, S. Gratton, A. Gregorio, A. Gruppuso, J. E. Gudmundsson, J. Hamann, F. K. Hansen, D. Hanson, D. L. Harrison, G. Helou, S. Henrot-Versillé, C. Hernández-Monteagudo, D. Herranz, S. R. Hildebrandt, E. Hivon, M. Hobson, W. A. Holmes, A. Hornstrup, W. Hovest, Z. Huang, K. M. Huffenberger, G. Hurier, A. H. Jaffe, T. R. Jaffe, W. C. Jones, M. Juvela, E. Keihänen, R. Keskitalo, T. S. Kisner, R. Kneissl, J. Knoche, L. Knox, M. Kunz, H. Kurki-Suonio, G. Lagache, A. Lähteenmäki, J. M. Lamarre, A. Lasenby, M. Lattanzi, C. R. Lawrence, J. P. Leahy, R. Leonardi,

J. Lesgourgues, F. Levrier, A. Lewis, M. Liguori, P. B. Lilje, M. Linden-Vørnle, M. López-Caniego, P. M. Lubin, J. F. Macías-Pérez, G. Maggio, D. Maino, N. Mandolesi, A. Mangilli, A. Marchini, M. Maris, P. G. Martin, M. Martinelli, E. Martínez-González, S. Masi, S. Matarrese, P. McGehee, P. R. Meinhold, A. Melchiorri, J. B. Melin, L. Mendes, A. Mennella, M. Migliaccio, M. Millea, S. Mitra, M. A. Miville-Deschênes, A. Moneti, L. Montier, G. Morgante, D. Mortlock, A. Moss, D. Munshi, J. A. Murphy, P. Naselsky, F. Nati, P. Natoli, C. B. Netterfield, H. U. Nørgaard-Nielsen, F. Noviello, D. Novikov, I. Novikov, C. A. Oxborrow, F. Paci, L. Pagano, F. Pajot, R. Paladini, D. Paoletti, B. Partridge, F. Pasian, G. Patanchon, T. J. Pearson, O. Perdereau, L. Perotto, F. Perrotta, V. Pettorino, F. Piacentini, M. Piat, E. Pierpaoli, D. Pietrobon, S. Plaszczynski, E. Pointecouteau, G. Polenta, L. Popa, G. W. Pratt, G. Prézeau, S. Prunet, J. L. Puget, J. P. Rachen, W. T. Reach, R. Rebolo, M. Reinecke, M. Remazeilles, C. Renault, A. Renzi, I. Ristorcelli, G. Rocha, C. Rosset, M. Rossetti, G. Roudier, B. Rouillé d'Orfeuil, M. Rowan-Robinson, J. A. Rubiño-Martín, B. Rusholme, N. Said, V. Salvatelli, L. Salvati, M. Sandri, D. Santos, M. Savelainen, G. Savini, D. Scott, M. D. Seiffert, P. Serra, E. P. S. Shellard, L. D. Spencer, M. Spinelli, V. Stolyarov, R. Stompor, R. Sudiwala, R. Sunyaev, D. Sutton, A. S. Suur-Uski, J. F. Sygnet, J. A. Tauber, L. Terenzi, L. Toffolatti, M. Tomasi, M. Tristram, T. Trombetti, M. Tucci, J. Tuovinen, M. Türler, G. Umana, L. Valenziano, J. Valiviita, F. Van Tent, P. Vielva, F. Villa, L. A. Wade, B. D. Wandelt, I. K. Wehus, M. White, S. D. M. White, A. Wilkinson, D. Yvon, A. Zacchei, and A. Zonca. Planck 2015 results. XIII. Cosmological parameters. *A&A*, 594:A13, September 2016. doi: 10.1051/0004-6361/201525830.

[14] Sander Weinreb and Jun Shi. Low Noise Amplifier With 7-K Noise at 1.4 GHz and 25 °C. *IEEE Transactions on Microwave Theory Techniques*, 69(4): 2345–2351, April 2021. doi: 10.1109/TMTT.2021.3061459.

[15] B. R. Barsdell, M. Bailes, D. G. Barnes, and C. J. Fluke. Accelerating incoherent dedispersion. *MNRAS*, 422(1):379–392, May 2012. doi: 10.1111/j.1365-2966.2012.20622.x.

[16] K. Nimmo, J. W. T. Hessels, A. Keimpema, A. M. Archibald, J. M. Cordes, R. Karuppusamy, F. Kirsten, D. Z. Li, B. Marcote, and Z. Paragi. Highly polarized microstructure from the repeating FRB 20180916B. *Nature Astronomy*, 5:594–603, June 2021. doi: 10.1038/s41550-021-01321-3.

[17] Walid A. Majid, Aaron B. Pearlman, Thomas A. Prince, Robert S. Wharton, Charles J. Naudet, Karishma Bansal, Liam Connor, Mohit Bhardwaj, and Shriharsh P. Tendulkar. A Bright Fast Radio Burst from FRB 20200120E with Sub-100 Nanosecond Structure. *ApJ*, 919(1):L6, September 2021. doi: 10.3847/2041-8213/ac1921.

[18] Kshitij Aggarwal, Devansh Agarwal, Evan F. Lewis, Reshma Anna-Thomas, Jacob Cardinal Tremblay, Sarah Burke-Spolaor, Maura A. McLaughlin, and

Duncan R. Lorimer. Comprehensive Analysis of a Dense Sample of FRB 121102 Bursts. *ApJ*, 922(2):115, December 2021. doi: 10.3847/1538-4357/ac2577.

[19] S. R. Kulkarni. Dispersion measure: Confusion, Constants & Clarity. *arXiv e-prints*, art. arXiv:2007.02886, July 2020. doi: 10.48550/arXiv.2007.02886.

[20] Vikram Ravi. The observed properties of fast radio bursts. *MNRAS*, 482(2): 1966–1978, January 2019. doi: 10.1093/mnras/sty1551.

[21] Dana Simard and Vikram Ravi. Scintillation Can Explain the Spectral Structure of the Bright Radio Burst from SGR 1935+2154. *ApJ*, 899(1):L21, August 2020. doi: 10.3847/2041-8213/abaa40.

[22] Ziggy Pleunis, Deborah C. Good, Victoria M. Kaspi, Ryan Mckinven, Scott M. Ransom, Paul Scholz, Kevin Bandura, Mohit Bhardwaj, P. J. Boyle, Charanjot Brar, Tomas Cassanelli, Pragya Chawla, Fengqiu (Adam) Dong, Emmanuel Fonseca, B. M. Gaensler, Alexander Josephy, Jane F. Kaczmarek, Calvin Leung, Hsiu-Hsien Lin, Kiyoshi W. Masui, Juan Mena-Parra, Daniele Michilli, Cherry Ng, Chitrang Patel, Masoud Rafiei-Ravandi, Mubdi Rahman, Pranav Sanghavi, Kaitlyn Shin, Kendrick M. Smith, Ingrid H. Stairs, and Shriharsh P. Tendulkar. Fast Radio Burst Morphology in the First CHIME/FRB Catalog. *ApJ*, 923(1):1, December 2021. doi: 10.3847/1538-4357/ac33ac.

[23] L. Connor, J. van Leeuwen, L. C. Oostrum, E. Petroff, Y. Maan, E. A. K. Adams, J. J. Attema, J. E. Bast, O. M. Boersma, H. Dénes, D. W. Gardenier, J. E. Hargreaves, E. Kooistra, I. Pastor-Marazuela, R. Schulz, A. Sclocco, R. Smits, S. M. Straal, D. van der Schuur, D. Vohl, B. Adebahr, W. J. G. de Blok, W. A. van Cappellen, A. H. W. M. Coolen, S. Damstra, G. N. J. van Diepen, B. S. Frank, K. M. Hess, B. Hut, A. Kutkin, G. Marcel Loose, D. M. Lucero, Á. Mika, V. A. Moss, H. Mulder, T. A. Oosterloo, M. Ruiter, H. Vedantham, N. J. Vermaas, S. J. Wijnholds, and J. Ziemke. A bright, high rotation-measure FRB that skewers the M33 halo. *MNRAS*, 499(4):4716–4724, December 2020. doi: 10.1093/mnras/staa3009.

[24] J. M. Cordes and B. J. Rickett. Diffractive Interstellar Scintillation Timescales and Velocities. *ApJ*, 507(2):846–860, November 1998. doi: 10.1086/306358.

[25] J. M. Cordes and T. J. W. Lazio. NE2001.I. A New Model for the Galactic Distribution of Free Electrons and its Fluctuations. *arXiv e-prints*, art. astro-ph/0207156, July 2002. doi: 10.48550/arXiv.astro-ph/0207156.

[26] J. Xavier Prochaska and Yong Zheng. Probing Galactic haloes with fast radio bursts. *MNRAS*, 485(1):648–665, May 2019. doi: 10.1093/mnras/stz261.

[27] Vikram Ravi, Morgan Catha, Ge Chen, Liam Connor, James M. Cordes, Jakob T. Faber, James W. Lamb, Gregg Hallinan, Charlie Harnach, Greg Hellbourg, Rick Hobbs, David Hodge, Mark Hodges, Casey Law, Paul Rasmussen,

Kritti Sharma, Myles B. Sherman, Jun Shi, Dana Simard, Jean J. Somalwar, Reynier Squillace, Sander Weinreb, David P. Woody, and Nitika Yadlapalli. Deep Synoptic Array science: a 50 Mpc fast radio burst constrains the mass of the Milky Way circumgalactic medium. *arXiv e-prints*, art. arXiv:2301.01000, January 2023. doi: 10.48550/arXiv.2301.01000.

[28] J. M. Yao, R. N. Manchester, and N. Wang. A New Electron-density Model for Estimation of Pulsar and FRB Distances. *ApJ*, 835(1):29, January 2017. doi: 10.3847/1538-4357/835/1/29.

[29] C. J. Law, K. Sharma, V. Ravi, G. Chen, M. Catha, L. Connor, J. T. Faber, G. Hallinan, C. Harnach, G. Hellbourg, R. Hobbs, D. Hodge, M. Hodges, J. W. Lamb, P. Rasmussen, M. B. Sherman, J. Shi, D. Simard, R. Squillace, S. Weinreb, D. P. Woody, and N. Yadlapalli. Deep Synoptic Array Science: First FRB and Host Galaxy Catalog. *arXiv e-prints*, art. arXiv:2307.03344, July 2023. doi: 10.48550/arXiv.2307.03344.

[30] H. K. Vedantham and E. S. Phinney. Radio wave scattering by circumgalactic cool gas clumps. *MNRAS*, 483(1):971–984, February 2019. doi: 10.1093/mnras/sty2948.

[31] M. Caleb, C. Flynn, M. Bailes, E. D. Barr, R. W. Hunstead, E. F. Keane, V. Ravi, and W. van Straten. Are the distributions of fast radio burst properties consistent with a cosmological population? *MNRAS*, 458(1):708–717, May 2016. doi: 10.1093/mnras/stw175.

[32] J. M. Cordes, Stella Koch Ocker, and Shami Chatterjee. Redshift Estimation and Constraints on Intergalactic and Interstellar Media from Dispersion and Scattering of Fast Radio Bursts. *ApJ*, 931(2):88, June 2022. doi: 10.3847/1538-4357/ac6873.

[33] Dan R. Stinebring, Barney J. Rickett, Anthony H. Minter, Alex S. Hill, Adam P. Jussila, Lele Mathis, Maura A. McLaughlin, Stella Koch Ocker, and Scott M. Ransom. A Scintillation Arc Survey of 22 Pulsars with Low to Moderate Dispersion Measures. *ApJ*, 941(1):34, December 2022. doi: 10.3847/1538-4357/ac8ea8.

[34] V. Ravi, R. M. Shannon, M. Bailes, K. Bannister, S. Bhandari, N. D. R. Bhat, S. Burke-Spolaor, M. Caleb, C. Flynn, A. Jameson, S. Johnston, E. F. Keane, M. Kerr, C. Tiburzi, A. V. Tuntsov, and H. K. Vedantham. The magnetic field and turbulence of the cosmic web measured using a brilliant fast radio burst. *Science*, 354(6317):1249–1252, December 2016. doi: 10.1126/science.aaf6807.

[35] J. M. Cordes, R. S. Wharton, L. G. Spitler, S. Chatterjee, and I. Wasserman. Radio wave propagation and the provenance of fast radio bursts, 2016.

Chapter 5

CONCLUSIONS

This thesis focused on the use of observational data for FRB progenitor and environment studies. FRB studies has been developing rapidly around the time period of this thesis. For example, from 2018 to early 2023, the number of reported FRB sources has increased from about 60 to over 600, the number of localized FRBs have grown from a few to around 40. Those observations have helped to narrow down nearly 50 competing progenitor models to a few that are commonly discussed recently, though observations have not been able to completely rule out many of the other models. In this thesis, I explored three different methods to study the FRB progenitor models using radio and multiwavelength data.

Multiwavelength transient FRB counterparts have only been detected with the FRB-like event from the galactic Magnetar SGR 1935+2154. In Chapter 2, we demonstrate a technique to estimate the energy ratio emitted by the FRBs' multiwavelength transient counterparts to the FRBs themselves. We combined the FRB population fluence distribution with the existing multiwavelength transient blind surveys. Our technique provides tighter constraints on the energy ratio compared to most of the targeted surveys by 2020. For the "far-away" class of models, where FRBs are created through synchrotron masers process initiated by shocks driven by young-magnetar flares at regions that are far-away above the magnetar surface, our results implied that high energy surveys like Fermi and Swift are unlikely to have detected FRB counterparts, and Gaia could have detected a few FRB counterparts in some cases. For the "close-in" class of model, where FRBs are created within the magnetosphere via, for example, curvature radiation, our result for the X-ray / radio band energy ratio is consistent with some of the models (e.g., [1]). If no multiwavelength FRB transient were detected in the near future, our technique is valuable in continuing to tighten the constraint, especially when combined with sensitive surveys with short cadence and large FoV. However, with the detection of more local FRBs (e.g., FRB 20200120E in M81, 200428 from galactic magnetar SGR 1935+2154), based on the energy ratio estimated from this work, it would be possible to catch high energy transient associated with individual FRBs like those X-ray bursts from SGR 1935+2154, and thus directly measuring the energy ratio. This would relies on sensitive, fast surveys that covers sufficient sky areas near the galactic plane and

the nearby groups.

Unlike the multiwavelength transient counterpart that is difficult to capture, two FRB persistent radio sources (PRSs) have been spatially associated with FRBs 121102 [2] and 20190520B [3], providing opportunities for detailed, long-term studies of their progenitors and environments. In Chapter 3, we presented a detailed case study on the possible progenitors of FRB 121102 using the VLA monitoring data (12 to 26 GHz) and the new Keck optical spectrum and found that the emission source was unlikely an AGN. We constrained the radius of the emission to be $> 10^{17}$ cm based on the low level of flux density variability as compared to the galactic scintillation prediction, and $< 10^{18}$ cm since the source was reported to be unresolvable in the previous VLBI observation. The emission size is too big for an AGN. In addition, we estimated that the mass of the potential black hole at the center of the host to be $\lesssim 10^{4\sim5}$ $M_\odot$ based on the line width of the H emission in the Keck/LRIS spectrum, and found the mass too low for its radio luminosity as compared to the general AGN population. We concluded that the size and the luminosity of the emission could be explained by isolated neutron star FRB models, where the persistent source is produced by synchrontron radiation in the PWN. Detailed case studies like this work would be important for all future FRB PSRs to study their progenitor, environment and evolution channel as a potential different population as compared to other FRBs. Currently, only two FRBs that have been associated with PRSs have several similarities– both have been highly active repeaters, have very high RMs that varies with time, have very high host DM contribution, and are detected within star-forming dwarf galaxies. These features requires extreme and dynamic magneto-ionic environment, which could be related to dynamic formation channels or young age of their progenitors. It might be interesting to monitor FRBs that share similar characteristics and host type with thoses two but have not been associated with any PRSs.

Localized FRBs enables the studies of their progenitor's environments and formation histories. The potential correlations between the FRBs burst morphology and their host properties could help to distinguish potential FRB sub-populations produced by progenitors formed in different channels. In Chapter 4, we presented the burst morphology of a sample of 21 FRBs detected during the commissioning observations of DSA-110 in 2022, including 16 FRBs with host galaxy optical spectra. This DSA sample has a comparable extragalactic DM range with first CHIME catalog sample and is fainter than the ASKAP sample. We conducted preliminary correla-

tion studies between the burst and the host features. We found a potential correlation between the host DM and the host Hα luminosity, and noted a strong correlation between the FRB energy and the host Hα luminosity that is likely due to observational selection effects. We also found that galactic scattering is the major source of scintillation for most of the FRBs, with the obvious exception of FRB 220920, whose scintillation timescale is over one order of magnitude above the predicted galactic scattering timescale. To expand the correlation study between burst features (e.g., energy, width) and the host features, it could be interesting to include a few host properties that are closely related to the progenitor formation history, such as the delay time between the star formation period and the FRB event (e.g., [4], [5]), the SFR, the sSFR and the offset between the FRB and the star formation region when they become available. Although the correlation study remains inconclusive in this work, with a larger localized FRB sample, it could be a good starting point to reveal sub-populations of FRB produced by progenitors with different formation channels and / or reside in different environments.

References

[1] Wenbin Lu, Pawan Kumar, and Bing Zhang. A unified picture of Galactic and cosmological fast radio bursts. *MNRAS*, 498(1):1397–1405, October 2020. doi: 10.1093/mnras/staa2450.

[2] S. Chatterjee, C. J. Law, R. S. Wharton, S. Burke-Spolaor, J. W. T. Hessels, G. C. Bower, J. M. Cordes, S. P. Tendulkar, C. G. Bassa, P. Demorest, B. J. Butler, A. Seymour, P. Scholz, M. W. Abruzzo, S. Bogdanov, V. M. Kaspi, A. Keimpema, T. J. W. Lazio, B. Marcote, M. A. McLaughlin, Z. Paragi, S. M. Ransom, M. Rupen, L. G. Spitler, and H. J. van Langevelde. A direct localization of a fast radio burst and its host. *Nature*, 541(7635):58–61, January 2017. doi: 10.1038/nature20797.

[3] C. H. Niu, K. Aggarwal, D. Li, X. Zhang, S. Chatterjee, C. W. Tsai, W. Yu, C. J. Law, S. Burke-Spolaor, J. M. Cordes, Y. K. Zhang, S. K. Ocker, J. M. Yao, P. Wang, Y. Feng, Y. Niino, C. Bochenek, M. Cruces, L. Connor, J. A. Jiang, S. Dai, R. Luo, G. D. Li, C. C. Miao, J. R. Niu, R. Anna-Thomas, J. Sydnor, D. Stern, W. Y. Wang, M. Yuan, Y. L. Yue, D. J. Zhou, Z. Yan, W. W. Zhu, and B. Zhang. A repeating fast radio burst associated with a persistent radio source. *Nature*, 606(7916):873–877, June 2022. doi: 10.1038/s41586-022-04755-5.

[4] C. J. Law, K. Sharma, V. Ravi, G. Chen, M. Catha, L. Connor, J. T. Faber, G. Hallinan, C. Harnach, G. Hellbourg, R. Hobbs, D. Hodge, M. Hodges, J. W. Lamb, P. Rasmussen, M. B. Sherman, J. Shi, D. Simard, R. Squillace, S. Weinreb, D. P. Woody, and N. Yadlapalli. Deep Synoptic Array Science: First FRB and Host Galaxy Catalog. *arXiv e-prints*, art. arXiv:2307.03344, July 2023. doi: 10.48550/arXiv.2307.03344.

[5] Kritti Sharma, Jean Somalwar, Casey Law, Vikram Ravi, Morgan Catha, Ge Chen, Liam Connor, Jakob T. Faber, Gregg Hallinan, Charlie Harnach, Greg Hellbourg, Rick Hobbs, David Hodge, Mark Hodges, James W. Lamb, Paul Rasmussen, Myles B. Sherman, Jun Shi, Dana Simard, Reynier Squillace, Sander Weinreb, David P. Woody, and Nitika Yadlapalli. Deep Synoptic Array science: A massive elliptical host among two galaxy-cluster fast radio bursts. *arXiv e-prints*, art. arXiv:2302.14782, February 2023. doi: 10.48550/arXiv.2302.14782.

LIST OF ILLUSTRATIONS

Appendix A

CHANGES TO THE SOFTWARE HEIMDALL FOR MULTI-BEAM PROCESSING FOR DSA-110

This work is done by Christopher Bochenek and Ge Chen as part of the DSA-110 searching software development. The final subsection is concluded by simulations of Liam Conner. The simulations and results are not included in this appendix since Ge Chen did not contribute to them.

The default version of heimdall cannot process multiple beams simultaneously. The DSA-110 will produce 256 fan beams for the first stage of the project, with 64 beams being processed on one node. We have modified heimdall to process any number of beams. We describe the assumptions made about the input data, the modifications to the code, and the structure of the output.

A.1 Input Data

We assume that data will be structured as follows:

{beam 1 [time 1 (freq 1 ... freq n) ... time m (freq 1 ... freq n)] ... beam k [time 1 (freq 1 ... freq n) ... time m (freq 1 ... freq n)]}

Each beam must have the same number of time samples, and each time sample the same number of frequency samples.

A.2 Signal Flow Logic

The pipeline reads in 4 seconds of data from each beam at once (called a 'gulp'). Each beam is processed independently. Firstly, the data is de-dispersed using a series of DM trails and averaged over all channels. Then, the pipeline searches for pulses (called 'giants') in each of the frequency-averaged time series using a list of boxcar filters. The pipeline records every pulse whose signal-to-noise ratio (SNR) is above a detection threshold, and print results to a file. *Finally, the pipeline groups together pulse candidates that are considered to come from the same event and save possible FRB candidates into filterbank files. However, we will use some other software to group and select candidates later.*

A.3 Changes to the Code

Most of the changes happen in the code `Heimdall.C` and `pipeline.CU`.

A.3.1 Add the Multi-beam Option

In `Pipeline/`, we add a 'nbeams' option in `default_params.c`, `hd/params.h` and `parse_command_line.C`.

A.3.2 Allocate Memory for Multi-beam Data

In the single-beam version, the pipeline each time processes a 'gulp' of data. In this version, it processes a 'gulp' of data from each beam in parallel. We allocate more memory accordingly at the following steps .

- In `Heimdall.C`, we allocate nbeams · (gulp + overlap) of memory for the filterbank data vector. Here, nbeams is the number of beams, and overlap is the length of data that cannot be processed correctly in the current reading due to the de-dispersion delay and the width of the boxcar filter. We choose to read in the overlap in each beam to avoid mixing data from different beams.

- The overlap can only be processed in the next reading with data at later times. In each reading, we copy the overlap from the previous reading and put them at the beginning of each beam before reading in data from the next 'gulp' (called 'rewind').

- We initialize a overlap of randon numbers at the beginning of the filterbank to equalize the length of each reading. Otherwise, the first reading would be shorter than the rest since there is no data from a previous 'gulp' to put at its beginning. Consequently, the first reading takes longer due to the time required to initialize the vector. In addition, previous experience with the single-beam version shows that the first a couple of readings cannot be processed correctly anyways.

- In `Pipeline.CU`, we allocate more memory for the followings: `nbytes`, `dm_series`, `time_series`, `filtered_series`, `cur_nsamps`, `offset`.

A.3.3 Add Beam Label

We transfer all the raw pulse above the detection threshold from device (`d_giant`) to host (`h_giant`), and calculate their beam labels and filterbank indices. Results are printed to the file `giant.cand`

A.3.4 Other Changes

- In `Pipeline.CU`, we remove the lines that clean the filterbank RFI since we will use some other software to do it (what software?).

- `Pipeline.CU` produces two new output text files: `heimdall.cand` and `giants.cand` and saves each possible FRB candidate into a filterbank file.

- The pipeline selects possible FRBs from the grouped candidates and save each of them into a candidate filterbank file.

A.4 Code Management

The code is available at:

```
https://github.com/dsa110/
    dsa110-mbheimdall
```

and the version described here is right after the commit '87a3159' (Mar 6, 2020) on the master branch.

The code can be ran by

```
heimdall -{options}
```

. For example,

```
heimdall -f fakedata.fil
    -output_dir my_output_path
    -dm 10 3000 -dm_tol 1.25
    -nsamps_gulp 4096
    -detect_thresh 10
    -boxcar_max 512 -nbeams 32 -v
```

A complete list of option choices can be found by running "`heimdall -h`". More details on how to run the code are given in section A.6.

The code searches for pulses with SNR above the give detection threshold and produces the following outputs (more details in section A.5):

- giant.out: contains information about every pulse.
- heimdall.out: contains information about every event after grouping together pulses that belong to the same event.
- FRB candidates filterbank files.

In particular, one could test the code by checking the contents of `giant.out`.

A.5 Output

A.5.1 `giant.cand`

The file contains the following columns:

(0) SNR (float).

(1) Filterbank index (int). Note that this is different from the time sample index, since there are multiple beams.

(2) Time sample index (int). One time sample integration is 1.048 ms.

(3) The MJD time in seconds (float).

(4) Boxcar filter index (int).

(5) DM trail index (int).

(6) The DM value (float).

(7) Beam label (int), starting from 0.

A.5.2 `heimdall.out`

The file records parameters of the giant with the highest SNR in each candidate group. Note that we will use some other software to group candidates, so this output file will not be useful. Here, columns (0) to (6) are the same with those of `giant.out`, column (7) is the number of members in each group (int), and column (8) is beam label (int), starting from 0.

A.5.3 Candidates Filterbank Files

`Pipeline.CU` saves each of the FRB candidate into a filterbank. The filterbank is names after the time sample index at which the pulse reaches its peak SNR.

A.6 Test on multi-beam fake data

A.6.1 Fake Data

We test the pipeline using simulated multi-beam fake pulsar time series with Gaussian noise. The fake data is produced by running (on `dsamaster`)

```
/usr/local/sigproc/src/fake
    -{options} >path/file.fil
```

. Specifically, to match the DSA-110 data format, the fake data should satisfy the followings:

- The pulse width should be ms-scale. For example, if the `period` is 10^4 (in ms), the `width` should be ~ 0.01 (in percentage).

- Bits per time sample (`nbits`) is 8, total channel number (`nchans`) is 2048, sampling time (`tsamp`) is 1048 (in μs), channel 1 (`fch1`) is 1530 (in MHz), channel bandwidth (`foff`) is 0.1220703125 (in MHz), and the total beam number processed (`nbeams`) is 32.

- The samples per block (`nsblk`) is a tunable parameter that determines how many time samples to read in from each beam at once. For example, here the sampling time of the filterbank is 1048 μs, so one 'gulp' of data is 1048 $\mu\text{s} \cdot 4096 \approx 4\text{s}$. Note that (`nsblk`) must match with the `heimdall` command line option `nsamps_gulp`.

For example, the command could be:

```
/usr/local/sigproc/src/fake
    -period 10000 -width 0.01
    -snrpeak 20 -dm 600 -nbits 8
    -nchans 2048 -tsamp 1048
    -tstart 55000 -fch1 1530
```

```
    -foff 0.1220703125 -tobs 60
    -nbeams 32 -nsblk 4096
    > fakedata.fil
```

A.6.2 Heimdall Options

We test heimdall with the following options:

- DM from 10 to 1000, and SNR loss tolerance between each DM trial (`dm_tol`) 1.25.
- Each gulp takes 4096 time samples per beam. (Note that this should match with the `nsblk` option in the fake data.) The pipeline also get the time sampling rate from the data header.
- Detection threshold is 10.
- The maximum boxcar filter width (`boxcar_max`) is 512 time samples.
- The `-v` option enables the pipeline to print out more.

For example, the command could be:

```
heimdall -f fakedata.fil
    -output_dir my_output_path
    -dm 10 3000 -dm_tol 1.25
    -nsamps_gulp 4096
    -detect_thresh 10
    -boxcar_max 512
    -nbeams 32 -v
```

A.6.3 Output Analysis

In this test, we created a 32-beam fake pulsar data filterbank using the following command:

```
/usr/local/sigproc/src/fake
    -period 45000 -width 0.1
```

```
-snrpeak 20 -dm 600
-nbits 8 -nchans 2048
-tsamp 1048.576 -tstart 55000
-fch1 1530 -foff 0.1220703125
-tobs 60 -nbeams 32
-nsblk 4096 >
test_32beams_45speriod.fil.
```

The pulsar period is 45 s, the pulse width is 45 ms, the SNR peaks at 20, the DM value is 600, each time sample is 1.048576 ms, the observation lasts for 60 s, and the number of beams is 32.

We test the mbheimdall pipeline with the following command:

```
heimdall -f
    test_32beams_45speriod.fil
    -output_dir my_output_path
    -dm 10 3000 -dm_tol 1.25
    -nsamps_gulp 4096
    -detect_thresh 10
    -boxcar_max 512 -nbeams 32 -v
```

We then show the output in Figures 1 to 3. All pulses were detected with the maximum signal to noise at the correct DM, width, and time. However, the peak SNR of each pulse varies significantly from beam to beam, even though the fake data has the same SNR (with small noise) for each beam (Fig. A.1).

A.6.4 Real Time

The pipeline should be able to process 32 beams in 'real time' (see details in section A.7 and Figs. A.4, A.5). For example, it takes ~ 4– 5 s to run on 32 beams and a gulp size of 4s with approximately 1890 DM steps (from 5 to 3000 pc cm^{-3} with a pulse width smearing tolerance of 25%) and 10 boxcar width steps (from the minimum to 2^9). However, the length of a 'gulp' and the processing time cut-off are to be determined by future experiments.

A.6.5 Output Issue

The output text files contains a few lines with incorrect formats. This will be fixed in the future**, as the giants will be sent via socket connections, rather than writing**

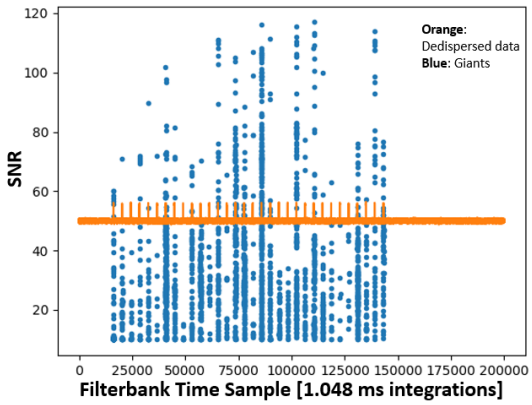

Figure A.1: SNR of the giants vs the sample number the giants were found at in the filterbank file. The orange series shows the frequency averaged dedispersed filterbank. Giants were found for every beam at the correct time samples.

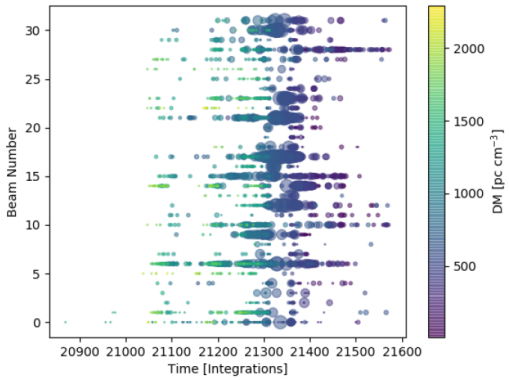

Figure A.2: The time samples that each giant was found at in each beam. The color corresponds to the DM of the giant and the size of the marker is proportional the the SNR squared.

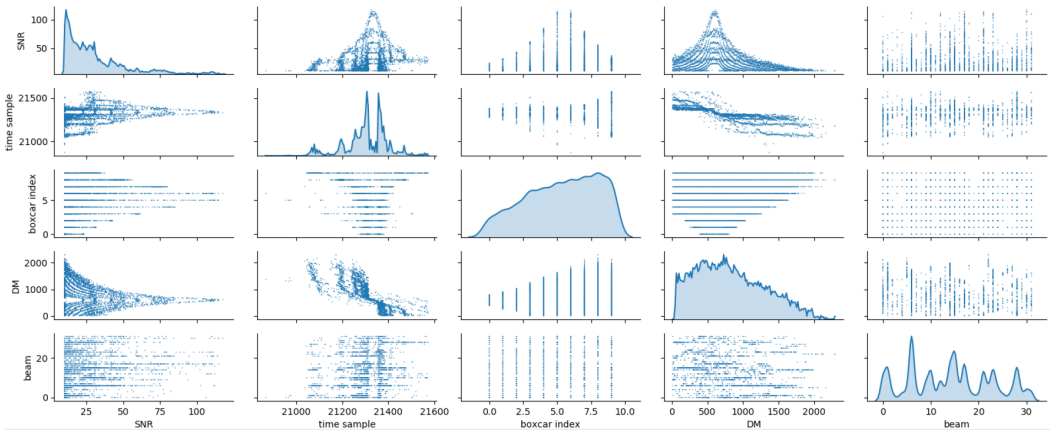

Figure A.3: Pair plot of SNR, time sample, filterbank width, DM, and beam number. The diagonals are KDEs of the parameters with a kernel width of 0.5.

to a text file..

A.7 Benchmark

We test the total processing time using the same fake pulsar time series and the same *heimdall* command as in Section A.6, and show results in Figs. A.4. The test first loops over a range of DM upper bounds, then a few DM tolerance values (`DM_tol`), and finally some maximum boxcar widths (`boxcar_max`). In particular, we only include gulps that detect no giant event to calculate the mean and the standard deviation of the total process time in each test.

A.7.1 Double the Boxcar Width in each trail

In these tests, the boxcar filter width doubles from the narrowest time resolution up to `boxcar_max` (Fig. A.4).

A.7.2 Linearly Boxcar Increments tests

In these tests, we add a new `heimdall` parameter `n_boxcar_inc` and let the boxcar filter width has `n_boxcar_inc` linear increments from the narrowest time resolution up to `boxcar_max` (Fig. A.5).

A.7.3 Completeness Tests

A.8 Single-beam Crab data test

on going test:

```
heimdall -f
    /home/user/vikram/
    scratch/fil_B0531+21_1.fil
    -output_dir my_output_dir
    -dm 10 1000 -dm_tol 1.25
    -nsamps_gulp 4096
    -detect_thresh 10
    -boxcar_max 256
    -nbeams 1 -v
```

A.9 Optimal Searching Parameters

This section estimates the detection rate using different beam forming parameters (time and frequency resolutions) and different searching parameters (DM upper limits, boxcar widths and beam number). The goal is to increase the detection rate

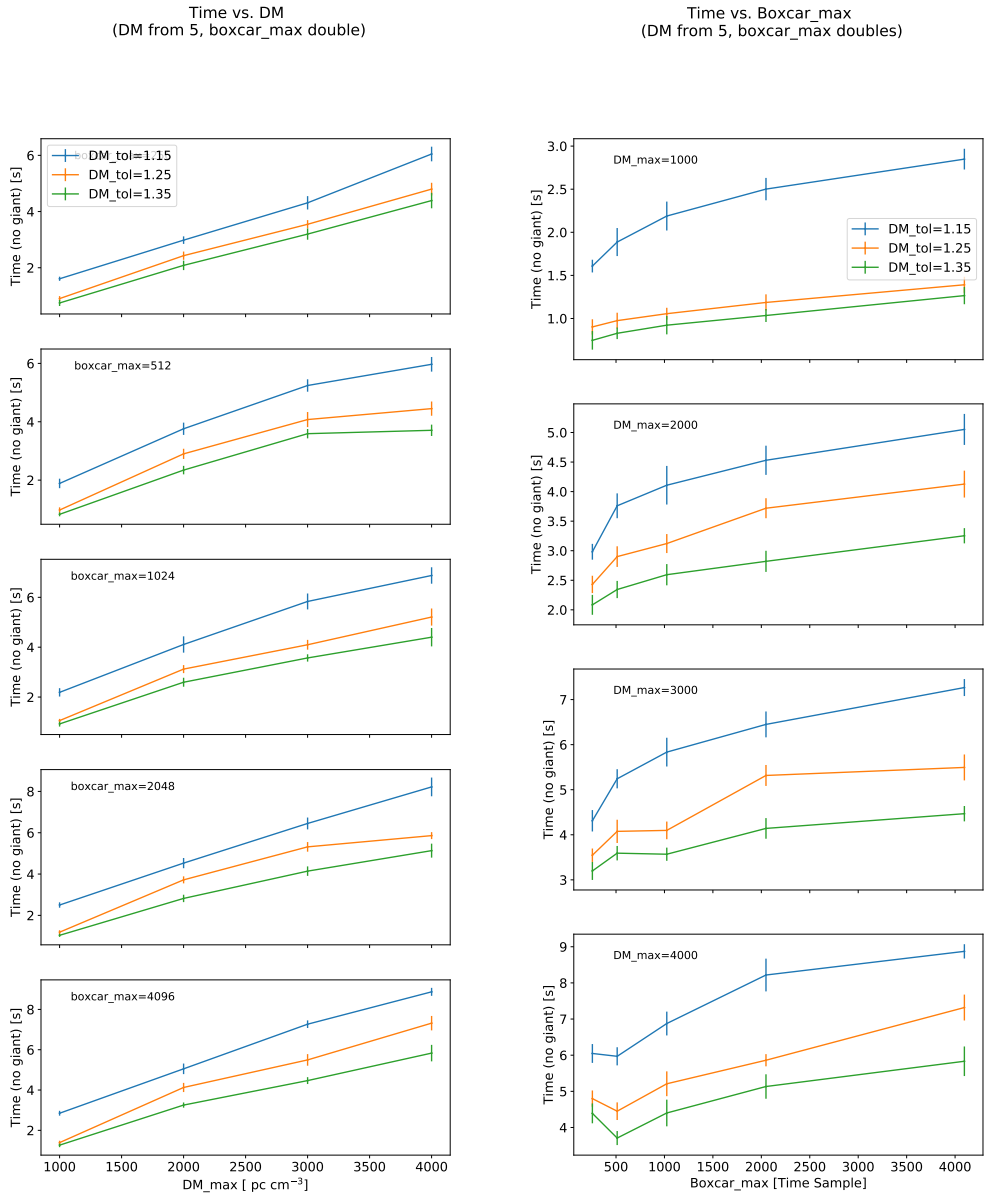

(a) Total process time vs. DM

(b) Total process time vs. Maximum boxcar width

Figure A.4: Total processing time for a range of maximum DM, DM tolerance, and maximum boxcar width. The boxcar width doubles in each trail. DM trail starts from 5.

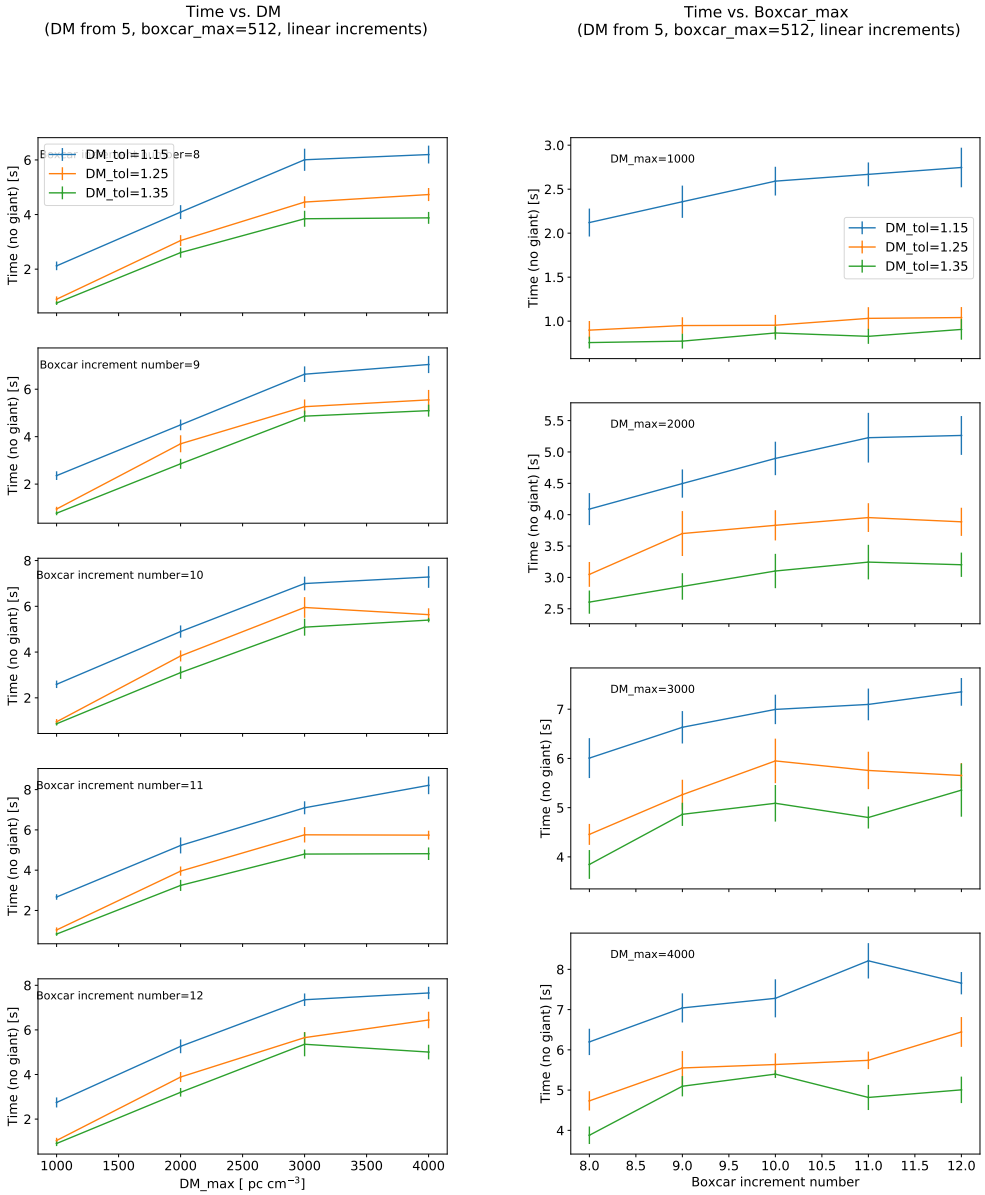

(a) Total process time vs. DM **(b)** Total process time vs. Maximum boxcar width

Figure A.5: Total processing time for a range of maximum DM, DM tolerance, and maximum boxcar width. The boxcar width has linear increments in each trail. DM trail starts from 5.

while keeping the searching pipeline in real time. All results are summarized in Table A.1.

I will calculate the detection rate by beam forming for now, and probably by imaging later.

A.9.1 Heimdall Search Parameters

This subsection investigates the detection rate at different `Heimdall` search parameters. Assume for now that the beam former time resolution is $\Delta t = 0.131073$ ms and the channel width is $\Delta\nu = 250/2048 = 0.122$ MHz.

To begin with, I approximated the FRB population's DM and width (limited to ≤ 1000 ms) distributions by fitting Gaussian functions to the FRBCAT.org catalog data in 2019 summer– the DM has a mean of 563 ± 13 pc cm^{-3} and a standard deviation of 442 ± 21, and the width has a mean of 1.85 ± 0.17 ms and a standard deviation of 3.03 ± 0.29 ms. Other population distributions will be discussed at the end of this section.

In addition, I adopt the broken power-law specific-fluence cumulative distribution function (CDF) estimated using the Australian Square Kilometre Array Pathfinder (ASKAP) and Parkes FRB samples [26]:

$$R(F_\nu) = \int_F^\infty r(F'_\nu)dF'_\nu, \tag{A.1a}$$

$$= R_0 \left(\frac{F_\nu}{F_{\nu,0}}\right)^{\alpha_1} \quad (F_{\nu,\min} < F_\nu < F_{\nu,b}), \tag{A.1b}$$

$$= R_b \left(\frac{F_\nu}{F_{\nu,b}}\right)^{\alpha_2} \quad (F_\nu > F_{\nu,b}). \tag{A.1c}$$

Here, $R(F_\nu)$ is the FRB rate (in the usual units of sky^{-1} day^{-1}) above a given fluence threshold F_ν in the radio band, $r(F_\nu)$ is the differential fluence distribution function, $\alpha_1 = -1.18$, $\alpha_2 = -2.2$, $F_{\nu,\min}$ is the (observationally unconstrained) fluence cut-off in the radio-band, $F_{\nu,0} \sim 2$ Jy ms is the fluence completeness threshold for the Parkes FRB searches [27], $R_0 \approx 1.7 \times 10^3$ sky^{-1} day^{-1} is the estimated rate above $F_{\nu,0}$ [2], $F_{\nu,b}$ is the fluence break which we choose to be 15 Jy ms, and $R_b \approx 171$ sky^{-1} day^{-1} is the rate above F_b calculated from Eq. (A.1b).

A pulse with an intrinsic width of w_{int} is broadened during incoherent de-dispersion. The dispersion delay of a signal (ν GHz) relative to a signal at some reference frequency (ν_{ref} GHz) is:

$$\tau = 4.15 \times 10^6 (\nu^{-2} - \nu_{ref}^{-2}) DM \quad \text{ms}. \tag{A.2}$$

The pulse is first broadened due to the finite frequency resolution:

$$w_{DM} = \frac{\partial \tau}{\partial \nu} \Delta\nu \approx 8.3 \times 10^6 \text{ DM } \nu^{-3} \ \Delta\nu \quad \text{ms}. \tag{A.3}$$

Here, DM is in pc cm^{-3}, $\Delta\nu$ and ν_c are the channel width and channel frequency in MHz, respectively, and I used the lower bound $\nu_1 = 1280$ MHz since it produces the largest smearing. Moreover, the pulse is further smeared by the discrete DM trails in de-dispersion. Across the entire band, the error becomes:

$$\begin{aligned} w_{\Delta DM} &= \frac{\partial \tau}{\partial DM} \Delta DM|_{\nu 1} - \frac{\partial \tau}{\partial DM} \Delta DM|_{\nu 2} \\ &= 4.15 \cdot 10^6 (\nu_1^{-2} - \nu_2^{-2}) \Delta DM \\ &= 4.15 \cdot 10^6 \nu_c^{-2} \left((1 + \frac{N\Delta\nu}{2\nu_c})^{-2} - (1 - \frac{N\Delta\nu}{2\nu_c})^{-2} \right) \Delta DM \\ &\approx 8.3 \cdot 10^6 N \cdot \Delta\nu \cdot \nu_c^{-3} \cdot \Delta DM \quad \text{ms}. \end{aligned} \tag{A.4}$$

Here, $\nu_1 = 1280$ MHz and $\nu_2 = 1530$ MHz are the band limits, $N \cdot \Delta\nu = 250$ MHz is the entire bandwidth, ΔDM is the step size between DM trails, and $\nu_c = 1405$ MHz is the central frequency of the entire band. The DM trail steps are determined such that it results in a smearing of $\leq 25\%$ (heimdall argument *dm_tol 1.25*). **Note that the DM trail step size increases at larger DM values, so the step number grows slightly sub-linearly with DM$_{max}$.** Finally, the effective pulse width is (ignore scattering):

$$w_{eff} = \sqrt{w_{int}^2 + \Delta t^2 + w_{DM}^2 + w_{\Delta DM}}. \tag{A.5}$$

Here, w_{int} is the intrinsic pulse width and $\Delta t = 0.131073$ ms is the tentative beam forming time resolution (may improve later).

The rms fluctuation on a flux density measurement is given by the radiometer equation:

$$\sigma_{s_\nu} = \frac{1}{\sqrt{n_{box}}} \frac{2k_b T_{sys}}{A_e \sqrt{N_{pol} B \Delta t}}. \tag{A.6}$$

Here, $N_{pol} = 2$ is the number of polarization, $B = 250$ MHz is the entire bandwidth and $\Delta t = 0.131073$ ms is the current beam forming time resolution. The effective area $A_e = \eta \cdot n_{dish} \pi R^2 \approx 938$ m^2 for an effiency of $\eta = 0.65$, dish number of $n_{dish} = 85$, and single dish radius of $R = 2.325$ m. The number of independent reading n_{box} is the searching boxcar width in the unit of Δt).

The detection fluence threshold is given by:

$$F_0 = \sigma_{s_\nu} * SNR_{min} * \max\{w_{eff}, b\}. \tag{A.7}$$

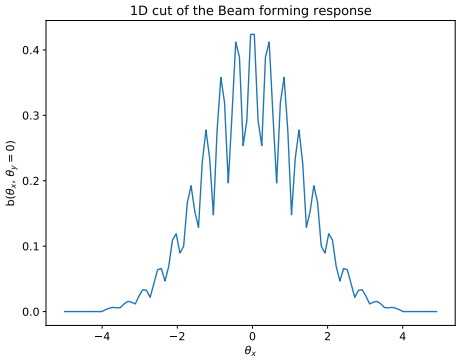

(a) 1D cut of the Beam Forming Response Function

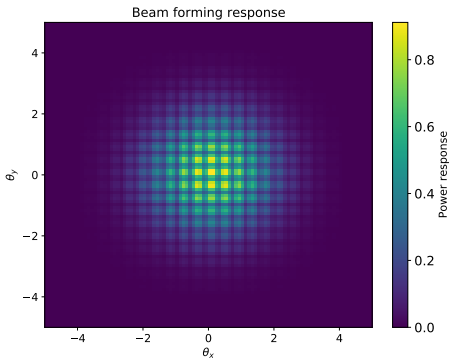

(b) Beam Forming Response Function

Figure A.6: Beam forming response function using 256 beams. Each main lobes are approximated with a narrow Gaussian with $\sigma_m \approx 0.012$ degree, and the prime beam as a broad Gaussian with $\sigma_p \approx 1.65$ degrees. The function is approximated by evenly placing all 256 main lobes within the prime beam's FWHM and scaling their peaks by the prime beam's envelope.

Here, $\sigma_{s\nu}$ is the flux noise (Eqn. A.6), SNR_{min} is the detection SNR threshold, w_{eff} is the effective width (Eqn. A.5), and $b = \Delta t * n_{box}$ is the boxcar width (the observed flux in further smeared out if the boxcar were wider than the effective pulse width).

In the beam forming method, the detection rate is further reduced by the beam response function B. In this calculation, side lobes are ignored. Each main lobe is approximated as a narrow Gaussian with $\sigma_m \approx 0.012$ degrees, and the prime beam as a broad Gaussian with $\sigma_p \approx 1.65$ degrees and peak normalized to unity. The beam response function B is approximated by evenly placing all main lobes within the prime beam's FWHM and scaling their peaks by the prime beam's envelope. For example, each main lobe would be spaced by $\approx 0.5\sigma_m$ if 256 beams were used (Fig. A.6). The integrated response rate within a small angle r around the boresight is given by:

$$B = \frac{1}{4\pi} \int_0^r \int_0^\theta b(r, \theta) r d\theta dr. \tag{A.8}$$

Here the spherical sky surface is approximated as flat since we're only interested in a small angle around the boresight (we use r = 5 degrees here). The response is normalized such that a perfect response function gives B = 1 over the entire sky.

Putting the above together, the detection rate is calculated by integrating the cumulative fluence distribution R above a fluence threshold F_0 that satisfies a desired

SNR_{min} over all possible DM and intrinsic width range:

$$B * \int_0^\infty \int_0^\infty R(F_0) * P(DM) * P(w)\ dDM\ dw. \tag{A.9}$$

As shown in Table A.1, one might consider a beam number of 256, a boxcar width that increments linearly from 1 to 8 at a step size of 1 and doubles from 8 to 32, a maximum DM of 2000. The relative detection rate are calculated using a beam former resolution of 0.13 ms and a channel width of 0.12 MHz.

A.9.2 Choosing back-end parameters (beam former)

Data rate	N_{beam}	$t_{s,opt}$ (ms)	ν_{opt} (MHz)	N_{box} (linear, +1)	DM_{max} (tolerance=25%)
1x	5% (32)	– (0.13)	– (0.24)	66% (2)	37% (500)
2x	6% (64)	– (0.066)	– (0.12)	92% (4)	80% (1000)
4x	37% (128)	– (0.033)	– (0.06)	99.8% (8)	99.9% (2000)
8x	100% (256)	– (0.016)	– (0.03)	100% (16)	100% (4000)
16x	–	–	–	100% (32)	–

Table A.1: Optimal search parameters– relative detection rate using different parameter. Results in the Columns N_{beam}, N_{box} and DM_{max} are calculated assuming a beam forming time resolution of 0.13 ms and a channel width of 0.12 MHz.

Liam Conner concluded this test using simulations (not included in this appendix).